



July 1996 • NREL/TP-442-8168

Effects of Grit Roughness and Pitch Oscillations on the S813 Airfoil

Airfoil Performance Report, Revised (12/99)

R. Reuss Ramsay
G.M. Gregorek
The Ohio State University
Columbus, Ohio

National Renewable Energy Laboratory
1617 Cole Boulevard
Golden, Colorado 80401-3393
A national laboratory of the U.S. Department of Energy
Managed by Midwest Research Institute
for the U.S. Department of Energy
under contract No. DE-AC36-83CH10093

Foreword

Airfoils for wind turbines have been selected by comparing data from different wind tunnels, tested under different conditions, making it difficult to make accurate comparisons. Most wind tunnel data sets do not contain airfoil performance in stall commonly experienced by turbines operating in the fields. Wind turbines commonly experience extreme roughness for which there is very little data. Finally, recent tests have shown that dynamic stall is a common occurrence for most wind turbines operating in yawed, stall or turbulent conditions. Very little dynamic stall data exists for the airfoils of interest to a wind turbine designer. In summary, very little airfoil performance data exists which is appropriate for wind turbine design.

Recognizing the need for a wind turbine airfoil performance data base, the National Renewable Energy Laboratory (NREL), funded by the U.S. Department of Energy, awarded a contract to the Ohio State University (OSU) to conduct a wind tunnel test program. Under this program, OSU tested a series of popular wind turbine airfoils. A standard test matrix was developed to assure that each airfoil was tested under the same conditions. The test matrix was developed in partnership with industry and is intended to include all of the operating conditions experienced by wind turbines. These conditions include airfoil performance at high angles of attack, rough leading edge (bug simulation), steady and unsteady angles of attack.

Special care has been taken to report as much of the test conditions and raw data as practical so that designers can make their own comparisons and focus on details of the data relevant to their design goals. Some of the airfoil coordinates are proprietary to NREL or an industry partner. To protect the information which defines the exact shape of the airfoil, the coordinates have not been included in the report. Instructions of how to obtain these coordinates may be obtained by contacting C.P.(Sandy) Butterfield at NREL.

C.P. (Sandy) Butterfield
Wind Technology Division
National Renewable Energy Laboratory
1617 Cole Blvd.
Golden, Colorado, 80401 USA
Internet Address: Sandy_Butterfield@NREL.GOV
Phone: 303-384-6902
FAX: 303-384-6901

Preface

The Ohio State University Aeronautical and Astronautical Research Laboratory is conducting a series of steady state and unsteady wind tunnel tests on a set of airfoils that have been or will be used for horizontal axis wind turbines. The purpose of these tests is to investigate the effect of pitch oscillations and leading edge grit roughness (LEGR) on airfoil performance. The study of pitch oscillation effects can help to understand the behavior of horizontal axis wind turbines in yaw. The results of these tests will aid in the development of new airfoil performance codes that account for unsteady behavior and also aid in the design of new airfoils for wind turbines. The application of LEGR simulates surface irregularities that occur on wind turbine blades. These irregularities are due to the accumulation of insect debris, ice, and/or the aging process and can significantly reduce the output of the horizontal axis wind turbines. The experimental results from the application of leading edge grit roughness will help develop airfoils that are less sensitive to roughness.

The present work was made possible by the efforts and financial support of the National Renewable Energy Laboratory which provided major funding and technical monitoring, the U.S. Department of Energy is credited for its funding of this document through the National Renewable Energy Laboratory under contract number DE-AC36-83CH10093. The staff of The Ohio State University Aeronautical and Astronautical Research Laboratory appreciate the contributions made by personnel from that organization. In addition, the authors would like to recognize the efforts of the following graduate and undergraduate student research assistants, Jolanta M. Janiszewska, Fernando Falasca, and Mònica Angelats I Coll.

Summary

An S813 airfoil model was tested in The Ohio State University Aeronautical and Astronautical Research Laboratory 3×5 subsonic wind tunnel under steady state and unsteady conditions. The test defined baseline conditions for steady state angles of attack from -20° to $+40^\circ$ and examined unsteady behavior by oscillating the model about its pitch axis for three mean angles, three frequencies, and two amplitudes. For all cases, Reynolds numbers of 0.75, 1, 1.25 and 1.4 million were used. In addition, the above conditions were repeated after the application of leading edge grit roughness (LEGR) to determine contamination effects on the airfoil performance.

Typical baseline steady state results of the S813 testing showed a maximum lift coefficient of 1.16 at 14.3° angle of attack. The application of LEGR reduced the maximum lift coefficient by 9.5% and increased the 0.0062 minimum drag coefficient value by 113%. The zero lift pitching moment of -0.0723 showed a 13% reduction in magnitude to -0.0626 with LEGR applied.

Data were also obtained for two pitch oscillation amplitudes, $\pm 5.5^\circ$ and $\pm 10^\circ$. The larger amplitude consistently gave a higher maximum lift coefficient than the smaller amplitude, and both sets of unsteady maximum lift coefficients were greater than the steady state values. Stall was delayed on the airfoil while the angle of attack was increasing, thereby causing an increase in maximum lift coefficient. A hysteresis behavior was exhibited for all the unsteady test cases. The hysteresis loops were larger for the higher reduced frequencies and for the larger amplitude oscillations. In addition to the hysteresis behavior, an unusual feature of these data was a sudden increase in the lift coefficient in some cases where the onset of stall was expected. As in the steady case, the effect of LEGR in the unsteady case was to reduce the lift coefficient at high angles of attack.

In general, the unsteady maximum lift coefficient was as much as 82% higher than the steady state maximum lift coefficient, and variation in the quarter chord pitching moment coefficient magnitude was as much as 340% larger than the steady state values at high angles of attack. These findings indicate the importance of considering the unsteady flow behavior occurring in wind turbine operation because use of steady state results could greatly underestimate the loads.

Contents

Page

Preface	iv
Summary	v
List of Symbols	ix
Introduction	1
Experimental Facility	2
Wind Tunnel	2
Oscillation System	3
Model Details	4
Test Equipment and Procedures	6
Data Acquisition	6
Data Reduction	7
Test Matrix	8
Results and Discussion	10
Comparison with Theory	10
Steady State Data	11
Unsteady Data	13
Summary of Results	21
References	24
Appendix A: Surface Pressure Tap Coordinates	A-1
Appendix B: Steady State Data	B-1
Appendix C: Unsteady Integrated Coefficients	C-1

List of Figures

Page

1. 3x5 subsonic wind tunnel, top view.	2
2. 3x5 subsonic wind tunnel, side view.	2
3. 3x5 wind tunnel oscillation system.	3
4. S813 airfoil section.	4
5. Measured-to-desired model coordinates difference curves.	4
6. Roughness pattern.	5
7. Data acquisition schematic.	6
8. Comparison with theory, C_l vs α	10
9. Comparison with theory, C_m vs α	10
10. Comparison with theory, C_p vs x/c , $\alpha=0.2^\circ$	10
11. Comparison with theory, C_p vs x/c , $\alpha=6.1^\circ$	10
12. C_l vs α , clean.	11
13. C_l vs α , LEGR, $k/c=0.0019$	11
14. C_m vs α , clean.	11
15. C_m vs α , LEGR, $k/c=0.0019$	11
16. Clean, drag polar.	12
17. LEGR, drag polar.	12
18. Pressure distribution, $\alpha=2.2^\circ$	12
19. Pressure distribution, $\alpha=12.1^\circ$	12
20. Clean, C_l vs α , $\omega_{red}=0.027, \pm 10^\circ$	13
21. Clean, C_l vs α , $\omega_{red}=0.084, \pm 10^\circ$	13
22. Unsteady pressure dist., $\alpha=19.4^\circ$	14
23. Unsteady pressure dist., $\alpha=21.3^\circ$	14
24. Unsteady pressure dist., $\alpha=23.2^\circ$	14
25. Unsteady pressure dist., $\alpha=24.8^\circ$	14
26. Unsteady pressure distribution, clean, $\omega_{red}=0.082, 20\pm 10^\circ$	15
27. Clean, C_m vs α , $\omega_{red}=0.027, \pm 10^\circ$	15
28. Clean, C_m vs α , $\omega_{red}=0.084, \pm 10^\circ$	15
29. LEGR, C_l vs α , $\omega_{red}=0.027, \pm 10^\circ$	16
30. LEGR, C_l vs α , $\omega_{red}=0.082, \pm 10^\circ$	16
31. LEGR, C_m vs α , $\omega_{red}=0.027, \pm 10^\circ$	16
32. LEGR, C_m vs α , $\omega_{red}=0.082, \pm 10^\circ$	16
33. Unsteady pressure distribution, LEGR, $\omega_{red}=0.084, 14\pm 10^\circ$	17
34. Clean, C_l vs α , $\omega_{red}=0.026, \pm 5.5^\circ$	18
35. Clean, C_l vs α , $\omega_{red}=0.078, \pm 5.5^\circ$	18
36. Clean, C_m vs α , $\omega_{red}=0.026, \pm 5.5^\circ$	18
37. Clean, C_m vs α , $\omega_{red}=0.078, \pm 5.5^\circ$	18
38. Unsteady pressure distribution, clean, $\omega_{red}=0.078, 8\pm 5.5^\circ$	19
39. Unsteady pressure distribution, clean, $\omega_{red}=0.075, 20\pm 5.5^\circ$	19
40. LEGR, C_l vs α , $\omega_{red}=0.027, \pm 5.5^\circ$	19
41. LEGR, C_l vs α , $\omega_{red}=0.081, \pm 5.5^\circ$	19
42. LEGR, C_m vs α , $\omega_{red}=0.027, \pm 5.5^\circ$	20
43. LEGR, C_m vs α , $\omega_{red}=0.081, \pm 5.5^\circ$	20
44. $\pm 5.5^\circ$, unsteady C_{lmax} vs ω_{red}	22
45. $\pm 10^\circ$, unsteady C_{lmax} vs ω_{red}	22

List of Tables

Page

1. S813 Steady State Parameters Summary.	21
2. S813, Unsteady, Clean, $\pm 5.5^\circ$	21
3. S813, Unsteady, LEGR, $\pm 5.5^\circ$	22
4. S813, Unsteady, Clean, $\pm 10^\circ$	23
5. S813, Unsteady, LEGR, $\pm 10^\circ$	23

List of Symbols

AOA	Angle of attack
A/C, a.c.	Alternating current
c	Model chord length
C_d	Drag coefficient
C_{dmin}	Minimum drag coefficient
C_{dp}	Pressure drag coefficient
C_{dw}	Wake drag coefficient
C_{du}	Uncorrected drag coefficient
C_l	Lift coefficient
C_{lmax}	Maximum lift coefficient
C_{ldec}	Lift coefficient at angle of maximum lift, but with angle of attack decreasing
C_{lu}	Uncorrected lift coefficient
$C_m, C_{m\frac{1}{4}}$	Pitching moment coefficient about the quarter chord
C_{mdec}	Pitching moment coefficient at angle of maximum lift, but with angle of attack decreasing
$C_{m inc}$	Pitching moment coefficient at angle of maximum lift, but with angle of attack increasing
C_{mo}	Pitching moment coefficient about the quarter chord, at zero lift
$C_{m\frac{1}{4}u}$	Uncorrected pitching moment coefficient about the quarter chord
C_p	Pressure coefficient, $(p - p_\infty)/q_\infty$
C_{pmin}	Minimum pressure coefficient
f	Frequency
h	Wind tunnel test section height
hp, Hp, HP	Horsepower
Hz	Hertz
k	Grit particle size
k/c	Grit particle size divided by airfoil model chord length
p	Pressure
q	Dynamic pressure
q_u	Uncorrected dynamic pressure
q_w	Dynamic pressure through the model wake
q_∞	Free stream dynamic pressure
Re	Reynolds number
Re_u	Uncorrected Reynolds number
t	Time
U_∞	Corrected free stream velocity
V	Velocity
V_u	Uncorrected velocity
x	Axis parallel to model reference line

y	Axis perpendicular to model reference line
α	Angle of attack
α_{dec}	Decreasing angle of attack
α_{inc}	Increasing angle of attack
α_{m}	Median angle of attack
α_{mean}	Mean angle of attack
α_{u}	Uncorrected angle of attack
ϵ	Tunnel solid wall correction scalar
ϵ_{sb}	Solid blockage correction scalar
ϵ_{wb}	Wake blockage correction scalar
Λ	Body-shape factor (0.305 used)
π	3.1416
σ	Tunnel solid wall correction parameter
$\omega_{\text{red}}, \omega_{\text{reduced}}$	Reduced frequency, $\pi fc/U_{\infty}$

Introduction

Horizontal axis wind turbine rotors experience unsteady aerodynamics due to wind shear when the rotor is yawed, when rotor blades pass through the support tower wake, and when the wind is gusting. An understanding of this unsteady behavior is necessary to assist in the calculation of rotor performance and loads. The rotors also experience performance degradation due to surface roughness. These surface irregularities are due to the accumulation of insect debris, ice, and/or the aging process. Wind tunnel studies that examine both the steady and unsteady behavior of airfoils can help define pertinent flow phenomena, and the resultant data can also be used to validate analytical computer codes.

An S813 airfoil model was tested in The Ohio State University Aeronautical and Astronautical Research Laboratory (OSU/AARL) 3×5 subsonic wind tunnel (3×5) under steady flow with both stationary model conditions, and pitch oscillations. To study the extent of performance loss due to surface roughness, a standard grit pattern, leading edge grit roughness (LEGR), was used to simulate leading edge contamination. After baseline cases were completed, the LEGR was applied for both steady state and model pitch oscillation cases. The Reynolds numbers for steady state conditions were 0.75, 1, 1.25 and 1.4 million, while the angle of attack ranged from -20° to $+40^\circ$. With the model undergoing pitch oscillation, data were acquired at Reynolds numbers of 0.75, 1, 1.25, and 1.4 million, at frequencies of 0.6, 1.2, and 1.8 Hz. Two sine wave forcing functions $\pm 5.5^\circ$ and $\pm 10^\circ$ were used; at mean angles of attack of 8° , 14° , and 20° . For purposes herein, any reference to unsteady conditions means that the model was in pitch oscillation about the quarter chord.

Experimental Facility

Wind Tunnel

The OSU/AARL 3×5 was used to conduct tests on the S813 airfoil section. Schematics of the top and side views of the tunnel are shown in figures 1 and 2, respectively. This open-circuit tunnel has a velocity range of 0 - 55 m/s (180-ft/s) produced by a 2.4-m (8-ft) diameter, six-bladed fan. The fan is belt driven by a 93.2-

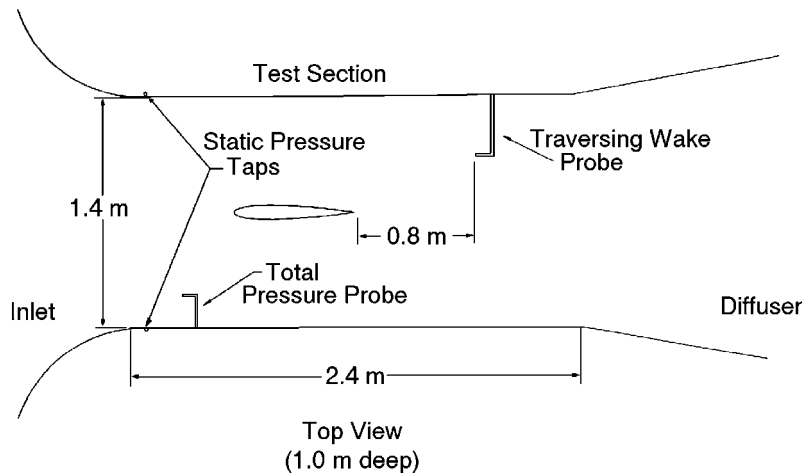


Figure 1. 3x5 subsonic wind tunnel, top view.

kw (125-hp) three phase a.c. motor connected to a variable frequency motor controller. Nominal test section dimensions are 1.0-m (39-in) high by 1.4-m (55-in) wide by a 2.4-m (96-in) long. The 457 mm (18 inch) chord airfoil model was mounted vertically in the test section. A steel tube through the quarter chord of the

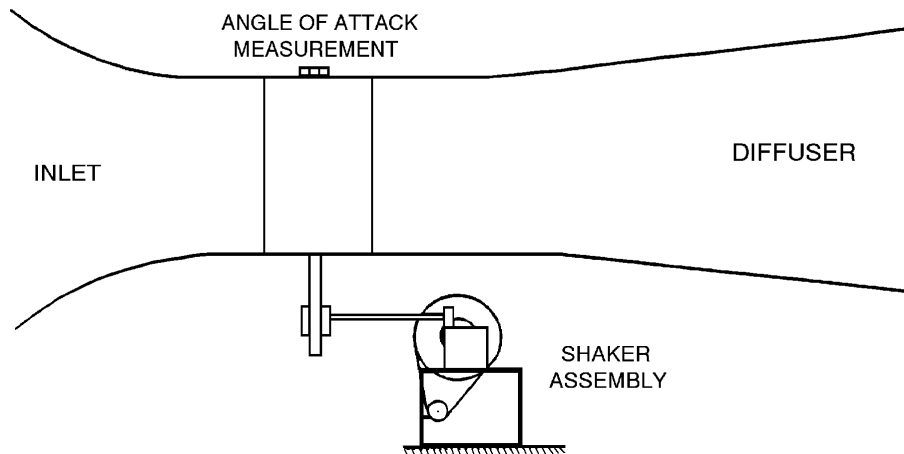


Figure 2. 3x5 subsonic wind tunnel, side view.

model was used to attach the model to the tunnel during testing. An angle of attack potentiometer was fastened to the model at the top of the tunnel as shown in figure 2. The steady state angle of attack was adjusted with a worm gear drive attached to the model strut below the tunnel floor.

Oscillation System

Portions of the testing required the use of a reliable model pitch oscillation system. The OSU/AARL "shaker" system incorporated a face cam and follower arm attached to the model support tube below the wind tunnel floor, figure 3. The choice of cam governed the type and amplitude of the wave form produced. Sine wave forms having amplitudes of $\pm 5.5^\circ$ and $\pm 10^\circ$ were used for these tests. The wave form is defined by the equation

$$\alpha = \alpha_m + A \sin(2\pi ft)$$

where A is the respective amplitude. The shaker system was powered by a 5 hp a.c. motor with a variable line frequency controller. The usable oscillating frequency range was 0.1 - 2.0 Hz, and three frequencies were used for this test: 0.6, 1.2, and 1.8 Hz.

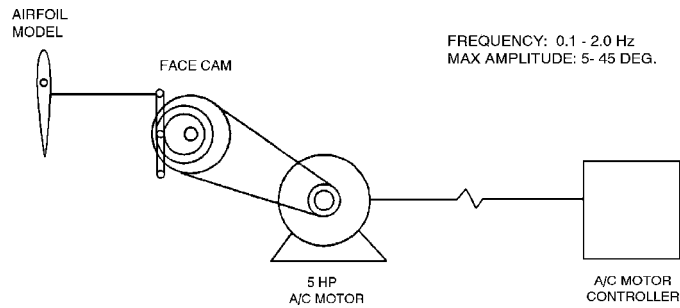


Figure 3. 3x5 wind tunnel oscillation system.

Model Details

A 457-mm (18-in) constant chord S813 airfoil model was designed and manufactured for this 3x5 wind tunnel test program. Figure 4 shows the airfoil section. Due to their proprietary nature, model coordinates are not presented in tabular form. The trailing edge was thickened to 1.25 mm (0.05 inch) for fabrication

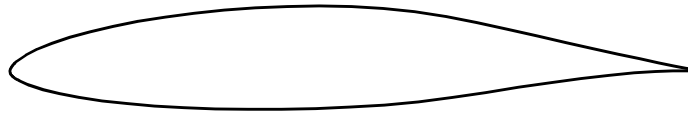


Figure 4. S813 airfoil section.

purposes. This thickness was added to the upper surface over the last 10% of the chord. The model was made of a nine layer composite lay up of alternating fiberglass and carbon fiber over ribs. The main load bearing member was a 38-mm (1.5-in) diameter steel tube that passed through the model quarter chord station. Ribs and end plates were used to transfer loads from the skin to the steel tube. The final surface was filled, painted and wet sanded to attain given coordinates within a requested tolerance of ± 0.25 -mm (± 0.01 -in). The completed model was measured at three spanwise locations using a Sheffield-Cordax RS-30 coordinate measuring machine. Measurements were made in English units and later converted to metric. Figure 5 shows the results of comparing measured-to-desired coordinates by calculating differences normal to the profiled surface at three stations on the model. The "spikes" apparent near the trailing and leading edge are due to the numerical method used and are not real. Although not all the surface was within tolerance, this model was accepted because this discrepancy was very small and the overall model construction was excellent.

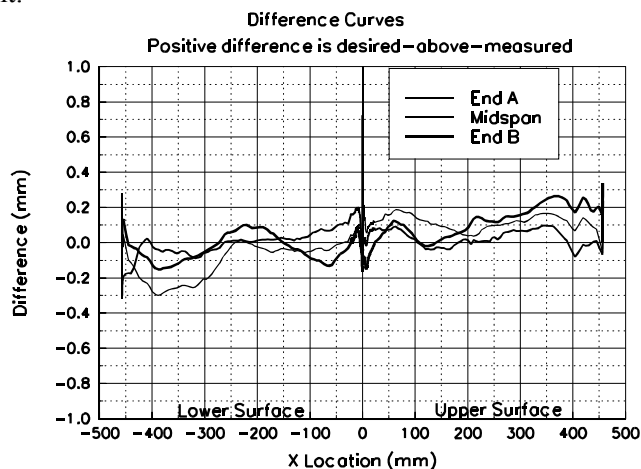


Figure 5. Measured-to-desired model coordinates difference curves.

To minimize pressure response times, which is important for the unsteady testing, the lengths of surface pressure tap lead-out lines had to be as short as possible. Consequently, a compartment was built into the model so that pressure scanning modules could be installed inside the model. This compartment was accessed through a panel door fitted flush with the model contour on the lower (pressure) surface.

For test cases involving roughness, a standard roughness pattern developed for the National Renewable Energy Laboratory airfoil test program was employed. The pattern was generated using a molded insect

pattern taken from a wind turbine in the field. The particle density was 5 particles per cm^2 (32 particles per square inch) in the middle of the pattern, thinning to 1.25 particles per cm^2 (8 particles per square inch) at the edge of the pattern. Figure 6 shows the pattern. To make a usable template, the pattern was repeatedly drilled into a thin steel plate 102 mm (4 inches) wide and 91 cm (3 ft) long with holes just large enough for one grain of grit. Based on average particle size from the field specimen, standard #40 lapidary grit was chosen for the roughness elements, giving $k/c=0.0019$ for a 457 mm (18 inch) chord model.

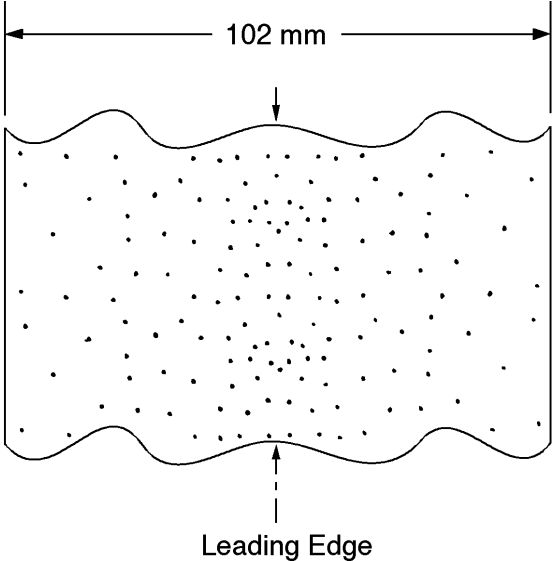


Figure 6. Roughness pattern.

To use the template, 102 mm (4 inch) wide double-sided tape was applied to one side of the template and grit was poured and brushed from the opposite side. The tape was then removed from the template and transferred to the model. This method allowed the same roughness pattern to be replicated for any test.

Test Equipment and Procedures

Data Acquisition

Data were acquired and processed from 60 surface pressure taps, four individual tunnel pressure transducers, an angle of attack potentiometer, a wake probe position potentiometer, and a tunnel thermocouple. The data acquisition system included an IBM PC compatible 80486-based computer connected to a Pressure Systems Incorporated (PSI) data scanning system. The PSI system included a 780B Data Acquisition and Control Unit (DACU), 780B Pressure Calibration Unit (PCU), 81-IFC scanning module interface, two 2.5 psid pressure scanning modules (ESPs), one 20" water column range pressure scanning module, and a 30 channel Remotely Addressed Millivolt Module (RAMM-30). Figure 7 shows the data acquisition system schematic.

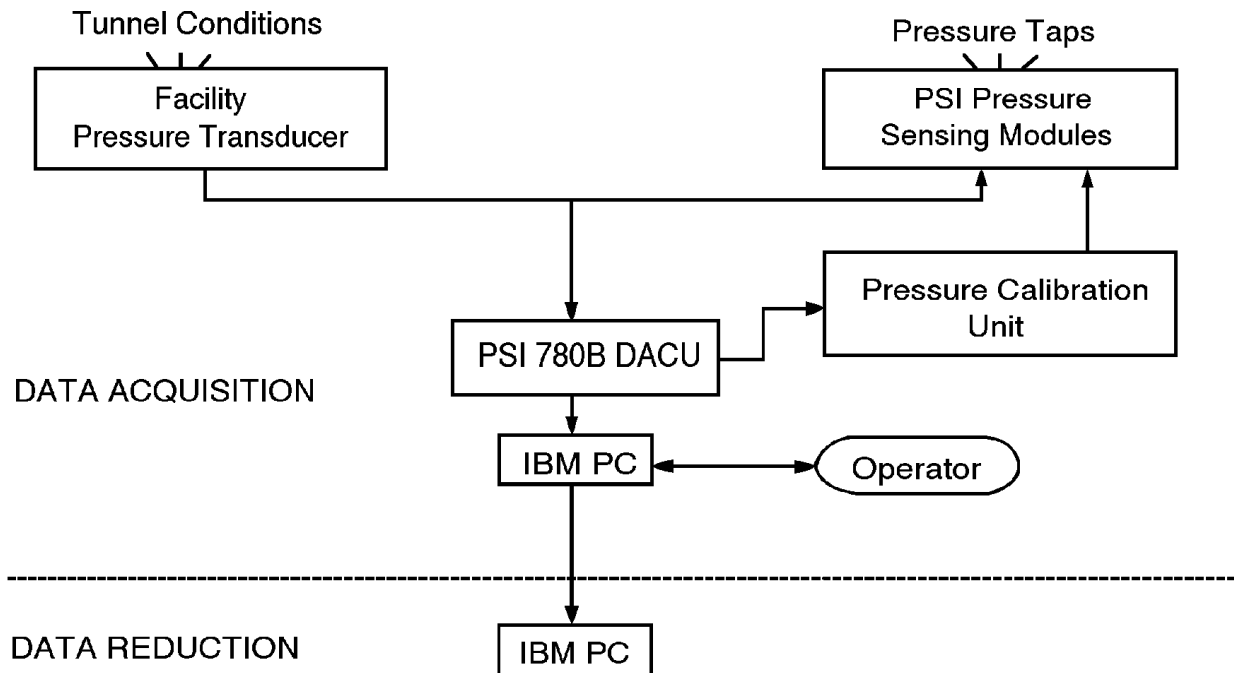


Figure 7. Data acquisition schematic.

Four individual pressure transducers read tunnel total pressure, tunnel north static pressure, tunnel south static pressure, and wake dynamic pressure. Before the test began, these transducers were bench calibrated using a water manometer to determine their sensitivities and offsets. Related values were entered into the data acquisition and reduction program so that the transducers could be shunt resistor calibrated before each series of wind tunnel runs.

The rotary angle of attack potentiometer of 0.5% linearity was regularly calibrated during the tunnel pressure transducers shunt calibration. The angle of attack calibration was accomplished by taking voltage readings at known values of set angle of attack. This calibration method gave angle of attack readings within $\pm 0.25^\circ$ over the entire angle range. The wake probe position potentiometer was a linear potentiometer, and it was also regularly calibrated during the shunt calibration of the tunnel pressure transducers.

Calibration of the three ESPs was done simultaneously by using the DACU and the PCU. At operator request, the DACU commanded the PCU to apply known regulated pressures to the ESPs and read the output voltages from each integrated pressure sensor. From these values, the DACU calculated the calibration

coefficients and stored them internally until the coefficients were requested by the controlling computer. This calibration was done several times during a run set because the ESPs were installed inside the model and their outputs tended to drift with temperature changes during a test sequence. Frequent on-line calibrations minimized the effect.

For steady state cases, the model was set to angle of attack, and the tunnel conditions were adjusted. At operator request, pressure measurements from the airfoil surface taps and all other channels of information were acquired and stored by the DACU and subsequently passed to the controlling computer for final processing. The angles of attack were always set in the same progression, from 0° to -20°, then from 0° to +40°.

For model oscillating cases, the tunnel conditions were set while the model was stationary at the desired mean angle of attack. The "shaker" was started, the model was allowed to oscillate through at least five cycles to set up the flow field, and then model surface pressure and tunnel condition data were acquired. Generally, 120 data scans were acquired over three model oscillation cycles. Since surface pressures were scanned sequentially, the data rate was set so the model rotated through less than 0.50° during any data burst. Finally, due to the unsteady and complex nature of the pitch oscillation cases, model wake surveys (for drag) were not conducted.

Data Reduction

The data reduction routine was included as a section of the data acquisition program. This combination of data acquisition and reduction routines allowed data to be reduced on-line during a test. By quickly reducing selected runs, integrity checks could be made to ensure the equipment was working properly and to allow timely decisions about the test matrix.

The ambient pressure was manually entered into the computer and was updated regularly. This value, as well as the measurements from the tunnel pressure transducers and the tunnel thermocouple, were used to calculate tunnel airspeed. As a continuous check of readings, the tunnel total and static pressures were read by both the tunnel individual pressure transducers and the 20-in water column ESP.

A typical steady state datum point was derived by acquiring 10 data scans of all channels over a 10 second window at each angle of attack and tunnel condition. The reduction portion of the program processed each data scan to coefficient forms (C_p , C_l , $C_{m\frac{1}{4}}$, and C_{dp}) using the measured surface pressure voltages, calibration coefficients, tap locations and wind tunnel conditions. Then, all scan sets for a given condition were ensemble averaged to provide one data set and that data set was then corrected for the effects of solid tunnel walls. All data were saved in electronic form.

Corrections due to solid tunnel sidewalls were applied to the wind tunnel data. As described by Pope and Harper (1966), tunnel conditions are represented by the following equations:

$$q = q_u(1 + 2\epsilon)$$

$$V = V_u(1 + \epsilon)$$

$$R_e = R_{e_u}(1 + \epsilon)$$

Airfoil aerodynamic characteristics are corrected by:

$$\alpha = \alpha_u + \frac{57.3\sigma}{2\pi} (C_{l_u} + 4C_{m\frac{1}{4}_u})$$

$$C_l = C_{l_u} (1 - \sigma - 2\epsilon)$$

$$C_{m_{\frac{1}{4}}} = C_{m_{\frac{1}{4}_u}} (1 - 2\epsilon) + \frac{\sigma C_l}{4}$$

$$C_d = C_{d_u} (1 - 3\epsilon_{sb} - 2\epsilon_{wb})$$

where

$$\sigma = \frac{\pi^2}{48} \left(\frac{c}{h} \right)^2$$

$$\epsilon = \epsilon_{sb} + \epsilon_{wb}$$

$$\epsilon_{sb} = \Lambda \sigma$$

$$\epsilon_{wb} = \frac{c}{h4} C_{d_u}$$

Model wake data were taken for steady state cases when the wake could be completely traversed. Pressures were acquired from a pitot-static probe which was connected to measure incompressible dynamic pressure through the wake. These pressure measurements were used to calculate drag coefficient using a form of the Jones equation derived from Schlichting (1979).

$$C_{dw} = \frac{2}{c} \int \sqrt{\frac{q_w}{q_\infty}} \left(1 - \sqrt{\frac{q_w}{q_\infty}} \right) dy$$

This method requires the standard transfer of the wake data to the true free stream pressure conditions. The integration was done automatically except the computer operator chose the end points of the integration from a plot of the wake survey displayed on the computer screen.

For pitch oscillation cases, model surface pressures were reduced to pressure coefficient form with subsequent integrations and angle of attack considerations giving lift, moment and pressure drag coefficients. There was no calibration available for unsteady model pitch conditions; therefore, the unsteady pressure data were not corrected for any possible effects due to time dependent pitching or solid tunnel walls. Also for these cases, the wind tunnel contraction pressures (used for steady state cases) could not be used to calculate instantaneous freestream conditions due to their slow response. The tunnel conditions were obtained from a total pressure probe, and the average of opposing static taps in the test section entrance; thereby giving near instantaneous flow pressure conditions for the pitching frequencies used.

Test Matrix

The test was designed to study steady state and unsteady pitch oscillation data. Steady state data were acquired at Reynolds numbers of 0.75, 1, 1.25, and 1.4 million with and without LEGR. Refer to the tabular data in Appendix B for the actual Reynolds number for each steady state angle of attack. The angle of attack increment was two degrees for $-20^\circ < \alpha < +10^\circ$ and $+20^\circ < \alpha < +40^\circ$, and one degree for $+10^\circ < \alpha < +20^\circ$. Wake surveys were conducted to find total airfoil drag over an approximate angle of attack range of -10° to $+10^\circ$. Unsteady data were taken for Reynolds numbers of 0.75, 1, 1.25, and 1.4 million. Sine wave cams having amplitudes $\pm 5.5^\circ$ and $\pm 10^\circ$ were used for pitch oscillations, and the mean angles for both these amplitudes

were 8° , 14° , and 20° . For all these conditions, the frequency was varied to 0.6 Hz, 1.2 Hz, and 1.8 Hz. All data points for the unsteady cases were acquired for both clean and LEGR cases.

Results and Discussion

The S813 airfoil model was tested under steady state and pitch oscillation conditions. A brief discussion of the results follows, including a comparison of experimental data and computational predictions, steady state results, and unsteady results.

Comparison with Theory

Comparisons were made between present wind tunnel steady state data and computed predictions made using the North Carolina State Airfoil Analysis Code. This analysis code has proven to be accurate for moderate angles of attack. The analysis was made with specifications set to allow free transition from laminar to turbulent flow, and the pressure distribution comparisons were matched to the same angle of attack as those of the wind tunnel cases.

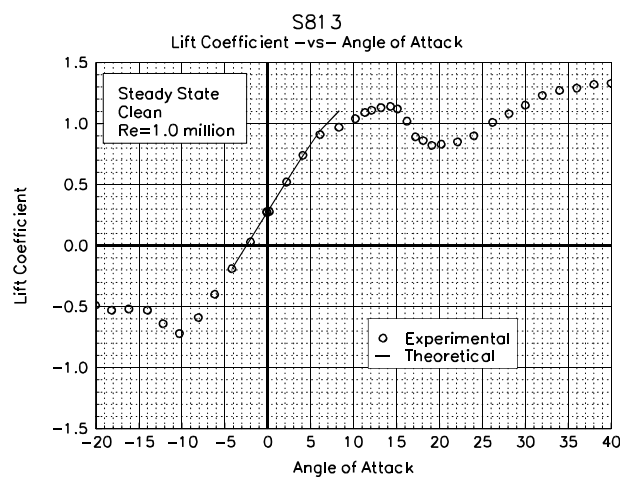


Figure 8. Comparison with theory, C_l vs α .

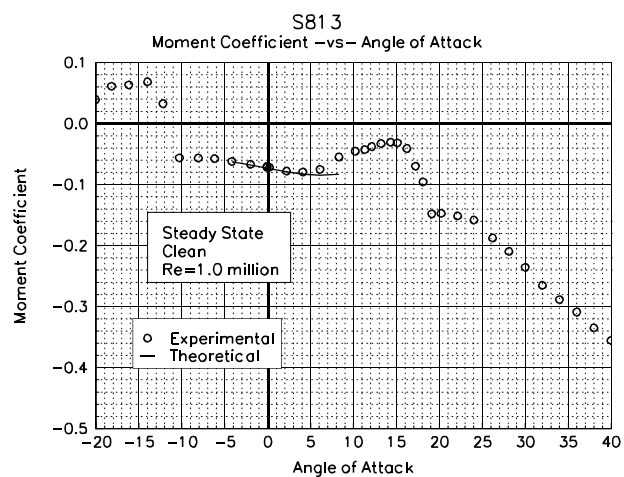


Figure 9. Comparison with theory, C_m vs α .

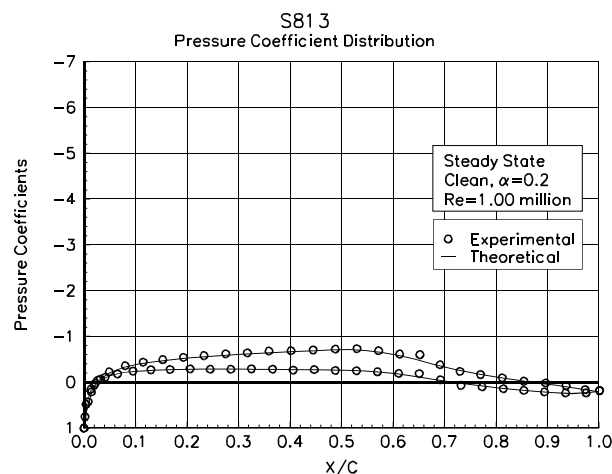


Figure 10. Comparison with theory, C_p vs x/c , $\alpha=0.2^\circ$.

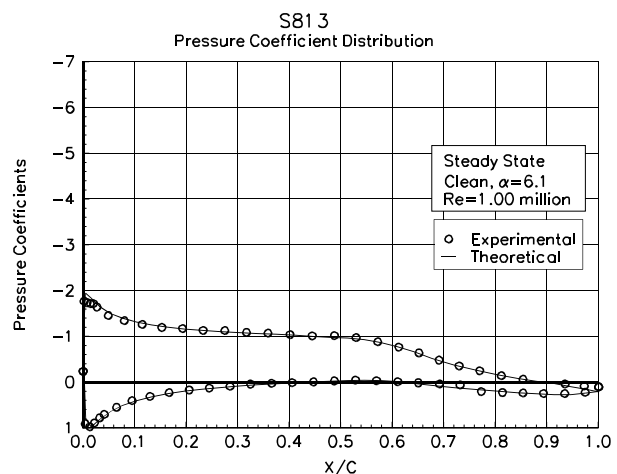


Figure 11. Comparison with theory, C_p vs x/c , $\alpha=6.1^\circ$.

Figure 8 shows the lift coefficient versus angle of attack for the 1 million Reynolds number case. For moderate angles of attack, in which the analysis code is valid, the comparison shows good agreement. The pitching moment about the quarter chord, figure 9, also shows good agreement for angles of attack from -4°

to $+5^\circ$. The pressure distributions shown in figures 10 and 11 are for angles of attack of 0.2° and 6.1° , respectively, and include clean and LEGR wind tunnel data as compared to computed, free transition pressure distributions. For both angles of attack, there is reasonable correlation between the experimental and the predicted values.

Steady State Data

The S813 airfoil model was tested at four Reynolds numbers at nominal angles of attack from -20° to $+40^\circ$. Figures 12 and 13 show lift coefficients for all tested Reynolds numbers both for the clean model and with

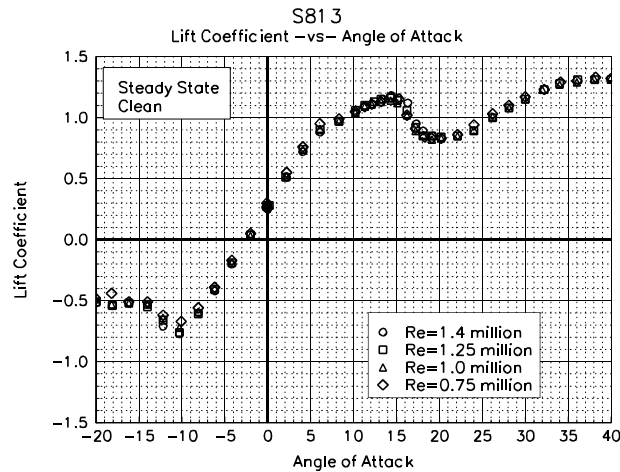


Figure 12. C_l vs α , clean.

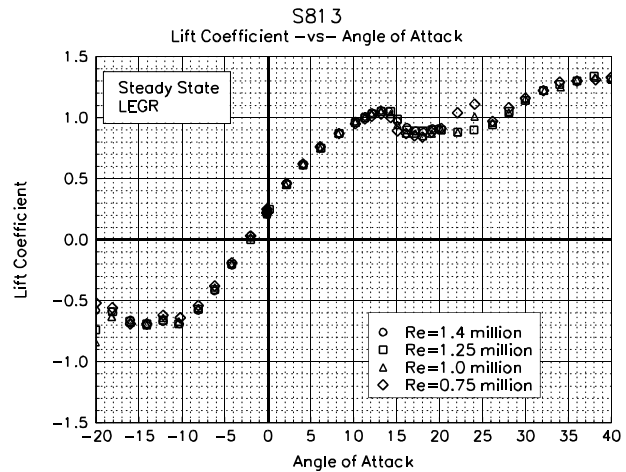


Figure 13. C_l vs α , LEGR, $k/c=0.0019$.

LEGR applied, respectively. The maximum positive lift coefficient for the 1.25 million Reynolds number, is 1.16 for the clean case and 1.05 for the LEGR cases, a 9.5% reduction. The clean cases have positive stall slightly beyond 14° angle of attack and the LEGR cases have stall near 13° angle of attack. In comparison, the clean data show a bend in the lift curve near 6° that occurs near 4° for the LEGR data. In addition, the clean data show a deeper stall than do the LEGR data. Finally, the average lift curve slope is about 0.112 for clean data and slightly lower at 0.098 for the LEGR case. The associated average lift coefficient at zero angle of attack is 0.27 for the clean case and 0.23 for the LEGR case.

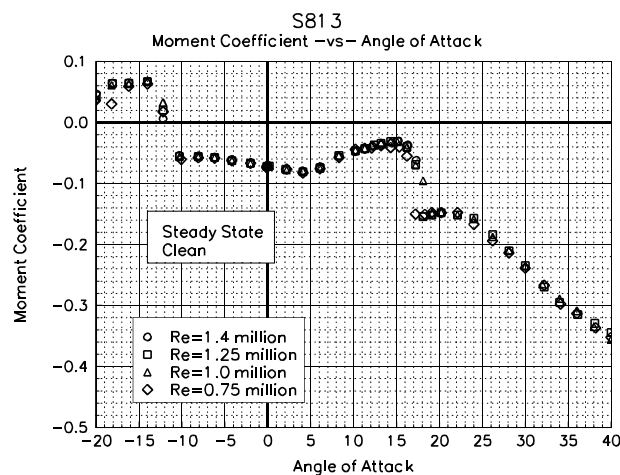


Figure 14. C_m vs α , clean.

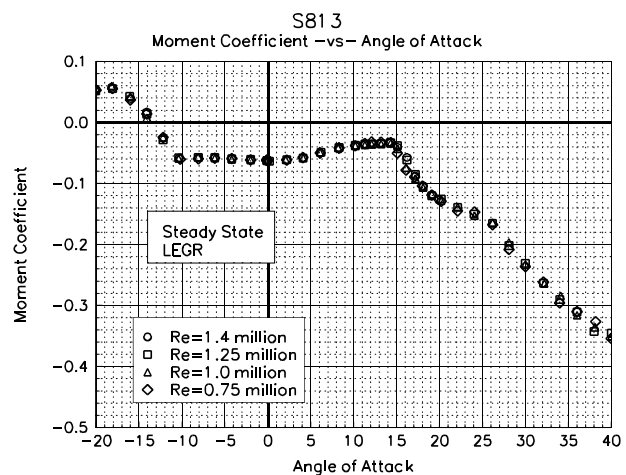


Figure 15. C_m vs α , LEGR, $k/c=0.0019$.

Figure 14 shows the pitching moment about the quarter chord for the clean cases, and figure15 shows the same for the LEGR cases. The magnitude of the zero lift pitching moment is 13% higher for the clean case than the LEGR case. The zero lift pitching moment coefficient about the quarter chord for the 1.25 million Reynolds number, is -0.0723 for clean case and -0.0626 for the LEGR case.

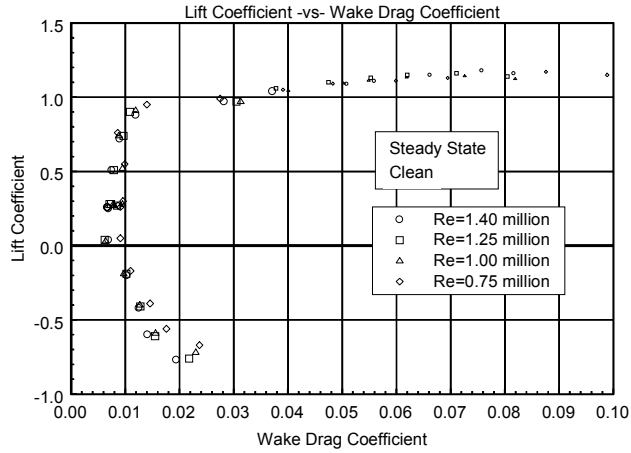


Figure 16. Clean, drag polar.

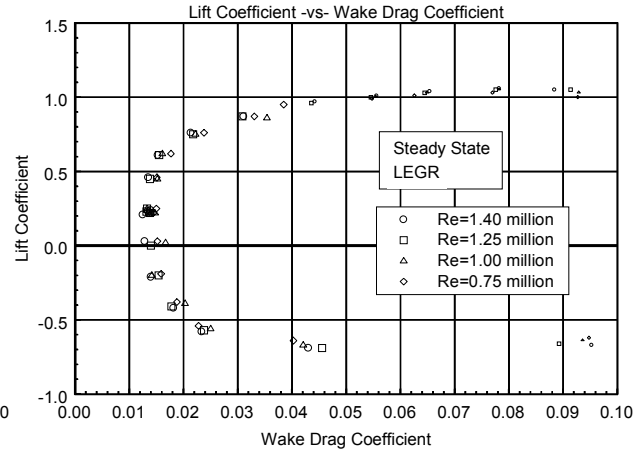


Figure 17. LEGR, drag polar.

Total wake drag data were obtained for the steady state cases over an angle of attack range of -10° to $+10^\circ$. A pitot-static probe was used to acquire the wake profile. This method is reliable when there is relatively low turbulence in the wake flow; therefore, only moderate angles of attack have reliable total drag coefficient data. At angles of attack other than those indicated above, surface pressure data were integrated to give C_{dp} and is shown in the drag polars as small symbols. The model clean drag data are shown in figure16 and the LEGR case is shown in figure 17. At 1.25 million Reynolds number, the minimum drag coefficient for the clean cases was measured as 0.0062 and for LEGR as 0.0132, a 113% increase, the highest percentage for all of the Reynolds number cases.

Two examples of the surface pressure distributions are shown in figures 18 and 19 for 2.2° and 12.1° , respectively, for 1 million Reynolds number. At the angles of attack close to zero degrees, LEGR does not appear to significantly change the pressure distribution in comparison with the clean case distribution; however, there is an effect apparent in the lift coefficient with values of 0.45 for the LEGR case and 0.52 for the clean case. For the higher angle of attack case, figure 19, the effect of LEGR is to reduce the

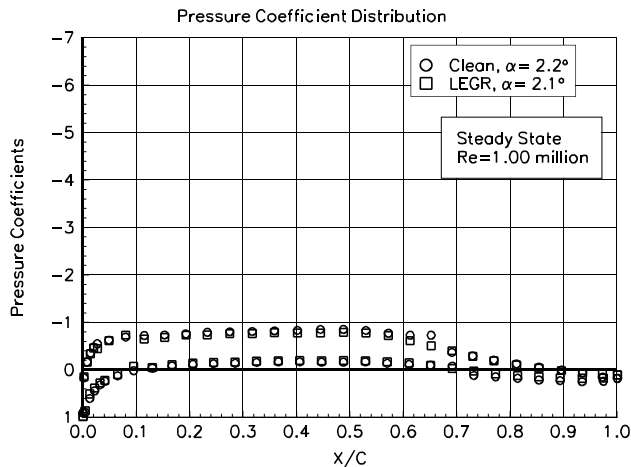


Figure 18. Pressure distribution, $\alpha=2.2^\circ$.

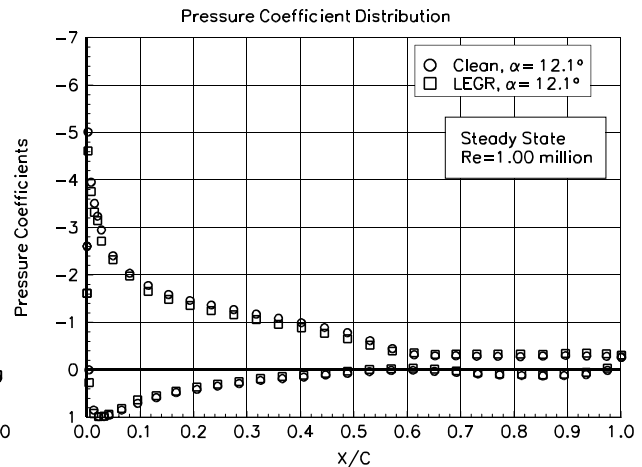


Figure 19. Pressure distribution, $\alpha=12.1^\circ$.

magnitude of the pressure peak from -5.0 to -4.6 and to slightly increase the pressures on the upper (suction) surface over the forward 60% of the chord. On the lower (pressure) surface, the LEGR and the clean cases are very similar. The net effect is a 7% reduction in lift coefficient from 1.11 to 1.03.

Unsteady Data

Unsteady experimental data were obtained for the S813 airfoil model undergoing sinusoidal pitch oscillations. As mentioned earlier, no calibration was available for the unsteady oscillating model conditions; the steady state tunnel calibration was used to set the flow conditions while the model was stationary at its mean angle of attack. A comprehensive set of test conditions was used to describe unsteady behavior of the S813 airfoil including: two angle of attack amplitudes, $\pm 5.5^\circ$ and $\pm 10^\circ$; four Reynolds numbers, 0.75, 1, 1.25, and 1.4 million; three pitch oscillation frequencies, 0.6, 1.2, and 1.8 Hz; and three mean angles of attack, 8° , 14° , and 20° .

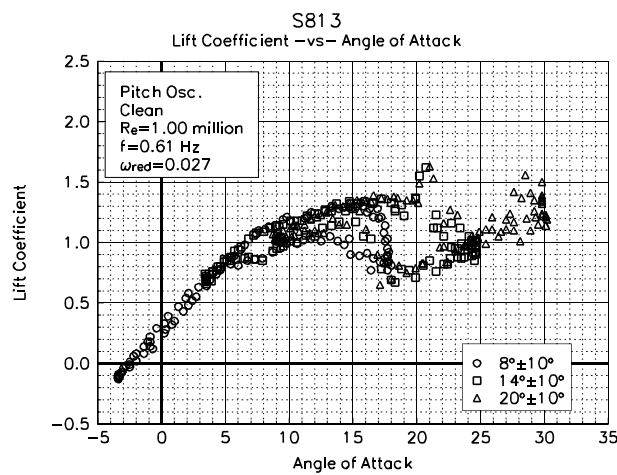


Figure 20. Clean, C_l vs α , $\omega_{red}=0.027$, $\pm 10^\circ$.

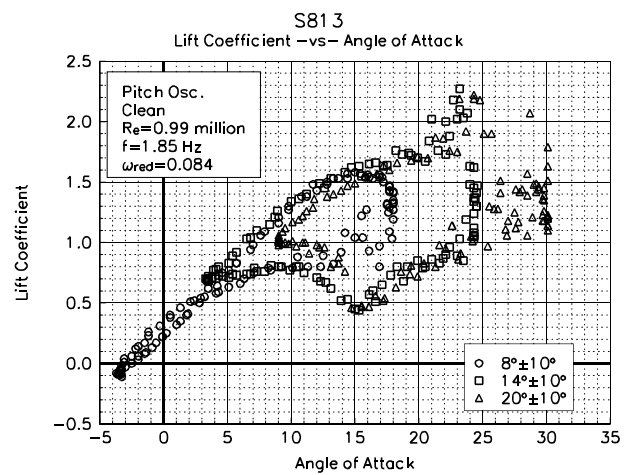


Figure 21. Clean, C_l vs α , $\omega_{red}=0.084$, $\pm 10^\circ$.

The lift coefficient versus angle of attack for the $\pm 10^\circ$ amplitude cases, clean, 1 million Reynolds number case are shown in figures 20 and 21 at reduced frequencies of 0.027 and 0.084, respectively. Note that all three mean angles of attack are plotted on the same figure. Hysteresis behavior was apparent for all unsteady cases. When the model is traveling through increasing angle of attack, the air flow tends to stay attached and, therefore, stall is delayed. In contrast, when the model is traveling through decreasing angles of attack, the stall recovery is delayed, and the lift coefficient is lower than what the steady state behavior predicts. In addition to hysteresis effects, a feature of the S813 airfoil data was the sudden increase in the lift coefficient close to where the onset of stall was expected. This phenomenon was observed in much of the clean unsteady data and in some of the LEGR data. It is important to note that this event occurs for both the $\pm 10^\circ$ and the $\pm 5.5^\circ$ amplitude cases even though the model is oscillating at a lower speed for the lower amplitude case. This indicates that the spike may be attributed to the model configuration.

To discover the cause of this spike, some preliminary analysis has been conducted. The following five figures show several individual unsteady pressure distributions, over time intervals concurrent with the lift spike, and a surface plot of the oscillating pressure distribution. When looking at the figures in time order, it appears that there is a slow moving wave traveling down the surface of the airfoil model at a speed approximately of the free stream velocity. This indicates that the phenomenon is related to the viscous forces on the model surface. One suggestion is that a laminar separation bubble forms near the leading edge and that the separation (stall) then expands downstream. It is noted that this airfoil has a very small leading edge radius and, therefore, might be susceptible to this behavior. A further speculation is that, as the

separated zone expands, it creates (impulsively) a low pressure region, evident in the pressure distributions, thus accounting for the momentarily high lift. Figure 26 shows a surface plot and the of the unsteady pressure coefficient from which the previous individual pressure distributions were taken. For plotting clarity, the model pressures were "unwrapped" about the trailing edge. The upper surface pressures are depicted on the right of the surface plot, lower surface values on the left. The trailing edge is then at the midpoint of the x-axis with the leading edge at each extreme. Additionally, the pressure coefficients were linearly interpolated to make an equally spaced grid. The time scale corresponds to angle of attack. The slow moving wave occurs four times in figure 26 corresponding to instances in which the model experiences the lift coefficient spike.

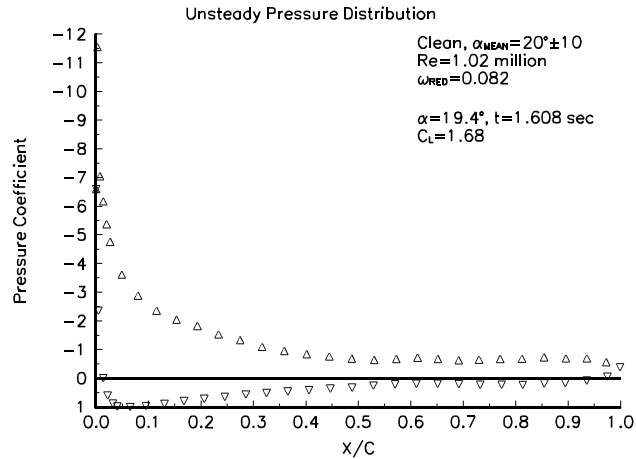


Figure 22. Unsteady pressure dist., $\alpha=19.4^\circ$.

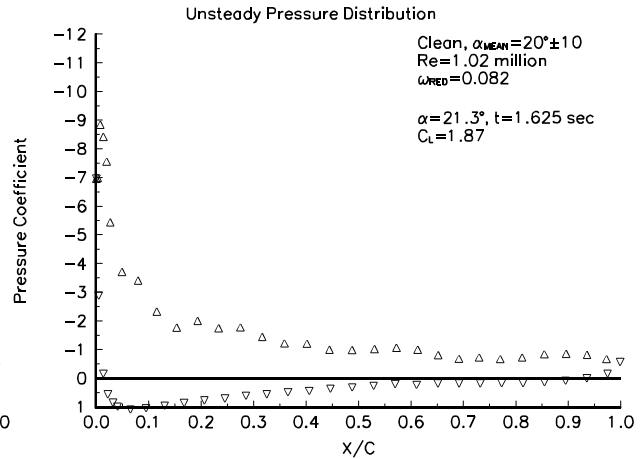


Figure 23. Unsteady pressure dist., $\alpha=21.3^\circ$.

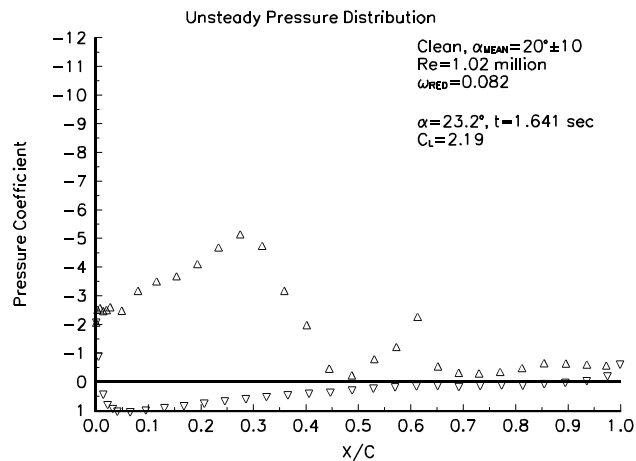


Figure 24. Unsteady pressure dist., $\alpha=23.2^\circ$.

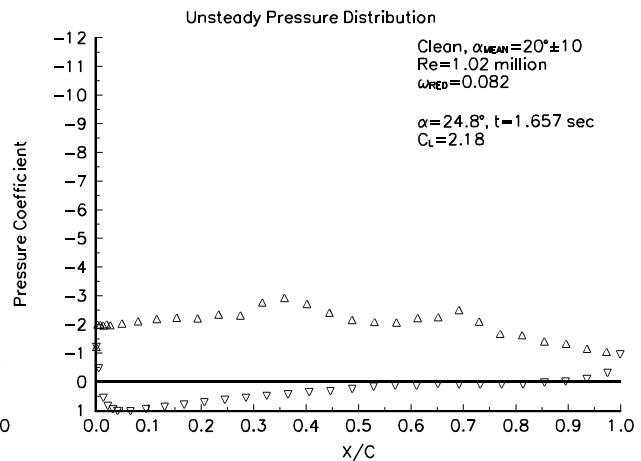


Figure 25. Unsteady pressure dist., $\alpha=24.8^\circ$.

Although this data spike are an notable phenomenon and should be the basis for further study, for comparison purposes, maximum lift coefficient values will be taken at a value prior to the lift coefficient spike. This approach is justified when the shortness of the time interval for which this event occurs and the inertia of a wind turbine system is considered.

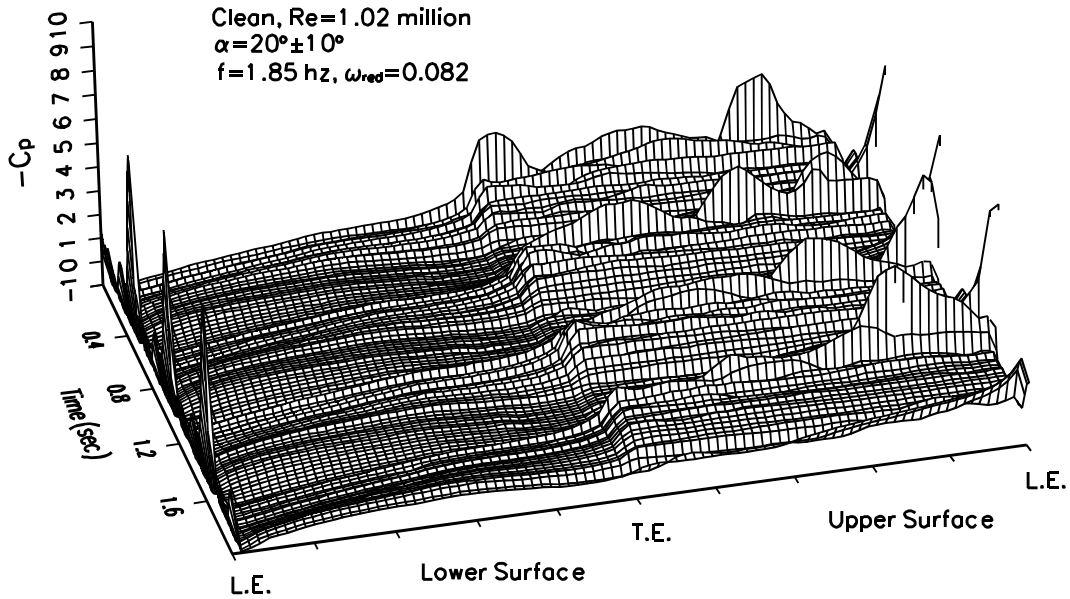


Figure 26. Unsteady pressure distribution, clean, $\omega_{red}=0.082$, $20\pm 10^\circ$.

Again considering figure 20 in which the reduced frequency is 0.027 the clean, maximum, lift coefficient is 1.34 and occurs at 15.9° angle of attack. To obtain some measure of the hysteresis behavior, the lift coefficient on the "return" portion of the curve, at the angle of attack where maximum lift coefficient occurs, can be used. For the case discussed here, the "hysteresis" lift coefficient is 1.05, a 22% decrease from the 1.34 unsteady maximum value. In comparison, the steady state maximum lift coefficient is 1.14. At the higher reduced frequency of 0.084, figure 21, the hysteresis behavior is more pronounced. In addition to greater hysteresis, the maximum lift coefficient increases to about 1.76, which is a 54% increase over the steady state value. The corresponding "hysteresis" lift coefficient is 0.80. This difference between steady state behavior and unsteady hysteresis behavior is a main reason why unsteady testing should be required for airfoils used in wind turbine applications.

The pitching moments in figures 27 and 28 correspond to the same conditions as do the two lift coefficient plots previously discussed. There is an indication that the hysteresis behavior is present, but it is not as apparent as in the lift coefficient plots. The higher reduced frequency case, however, does show hysteresis

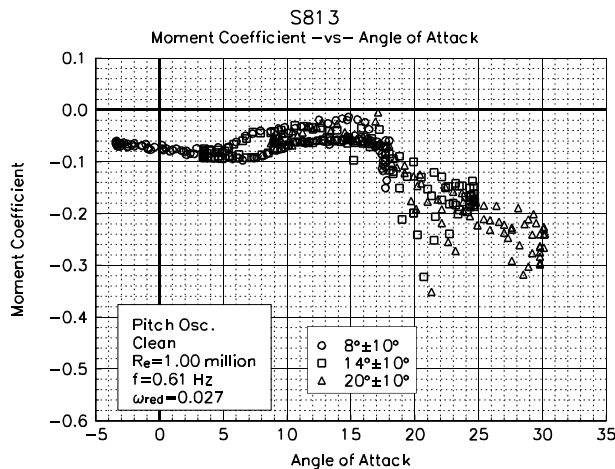


Figure 27. Clean, C_m vs α , $\omega_{red}=0.027$, $\pm 10^\circ$.

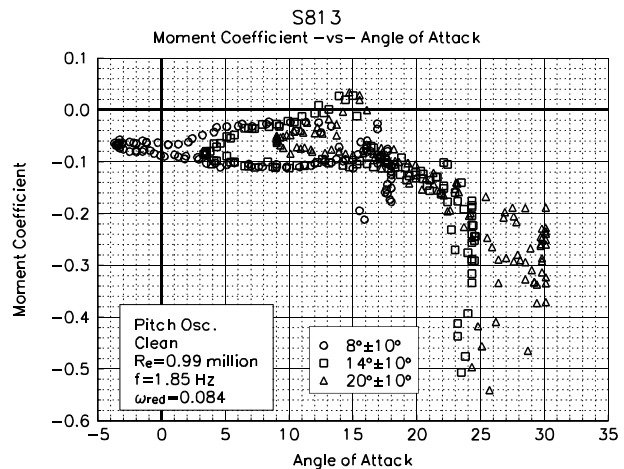


Figure 28. Clean, C_m vs α , $\omega_{red}=0.084$, $\pm 10^\circ$.

more than the lower reduced frequency case. For reference, the steady state maximum lift occurs near 14° angle of attack, and the steady state pitching moment at this maximum lift point is -0.0308 . In comparison, when the airfoil is undergoing pitch oscillation at the lower frequency, pitching moment varies from -0.0601 to -0.0356 (at 15.9° where unsteady maximum lift occurs), a 95% to 16% increase in magnitude from the steady state value. Note the angle of attack where the maximum unsteady lift coefficient occurs does not necessarily show the "greatest" hysteresis behavior but does give a relative indication of the effect.

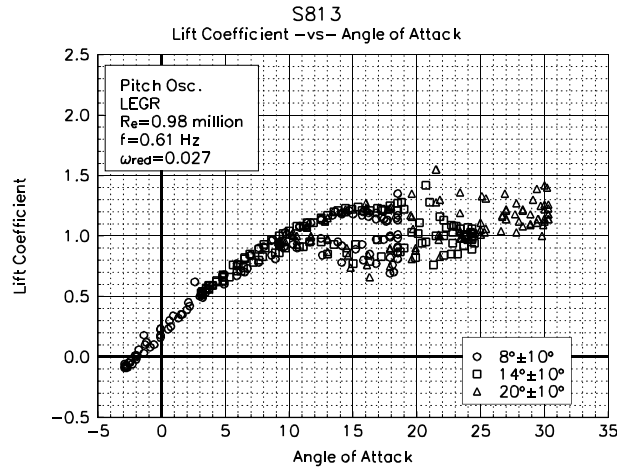


Figure 29. LEGR, C_l vs α , $\omega_{red}=0.027, \pm 10^\circ$.

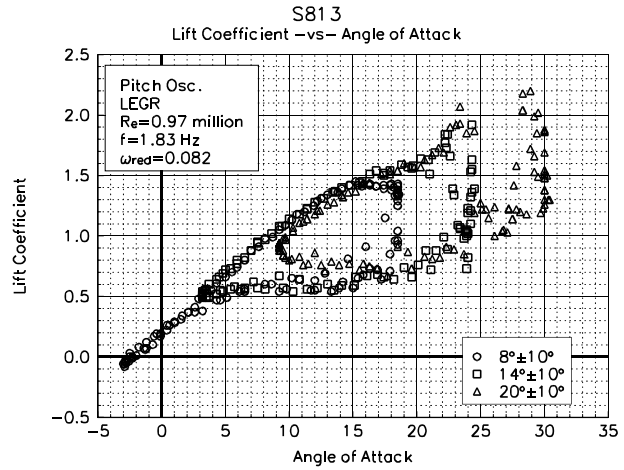


Figure 30. LEGR, C_l vs α , $\omega_{red}=0.082, \pm 10^\circ$.

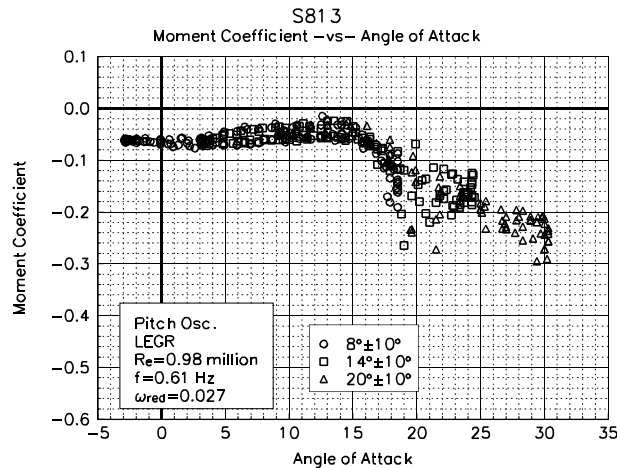


Figure 31. LEGR, C_m vs α , $\omega_{red}=0.027, \pm 10^\circ$.

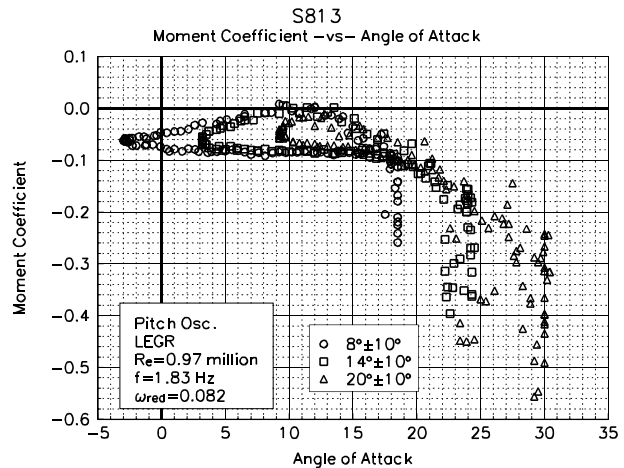


Figure 32. LEGR, C_m vs α , $\omega_{red}=0.082, \pm 10^\circ$.

In comparison to the clean data, the application of LEGR reduces the maximum lift coefficient in the pitch oscillation cases. Lift coefficient versus angle of attack with LEGR applied is shown in figure 29 for the 0.027 reduced frequency case. The 0.082 reduced frequency case is in figure 30. Both figures correspond to the same run conditions described earlier for the clean cases. For the lower reduced frequency, the maximum unsteady lift coefficient is reduced to 1.24 from the corresponding clean case of 1.34, a 7.5% decrease. Hysteresis behavior at this frequency is slightly less apparent than in the clean case; the corresponding "hysteresis" lift coefficient is 0.73 when LEGR is applied. The higher frequency LEGR case has a maximum lift coefficient of 1.58 while the model is increasing in angle of attack and the corresponding decreasing angle of attack lift coefficient is 0.66. In this case, the application of LEGR reduced the hysteresis loop behavior through the stall region compared with the clean case at the same run conditions.

Note that a spike in the lift coefficient does develop for the high frequency conditions even with LEGR applied.

The pitching moment coefficient shown in figure 31 is for a 0.027 reduced frequency with LEGR applied. At the angle of unsteady maximum lift (15.4°), the pitching moment ranges from -0.0597 to -0.0465, while the steady state LEGR pitching moment is -0.0353 at the steady state maximum lift angle of attack (13.2°). The higher reduced frequency of 0.082 with LEGR application is shown in figure 32. As was seen with the lift coefficient, pitching moment hysteresis is also more apparent at the higher reduced frequency than at the corresponding lower reduced frequency. Unsteady maximum lift angle of attack for this reduced frequency occurs at 19.7° , and the pitching moment ranges from -0.1130 to -0.0683 at that angle. Throughout the higher angle of attack range, the magnitude of the unsteady pitching moment can be very different from the steady state clean case (steady state pitching moment at maximum lift is -0.0308). It seems these differences can have significant impact on the fatigue life predictions of a wind turbine system.

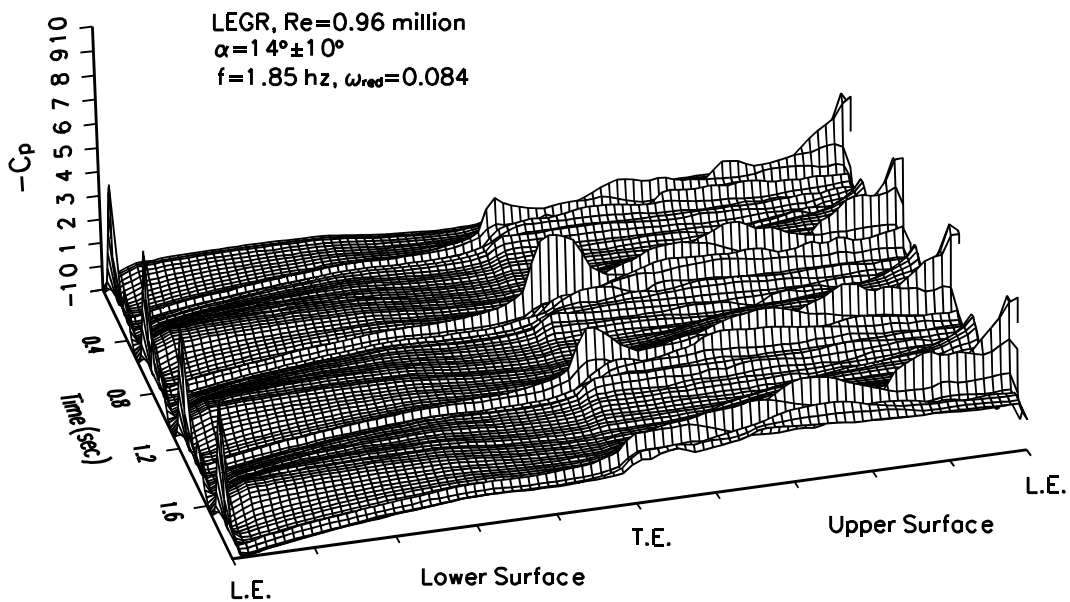


Figure 33. Unsteady pressure distribution, LEGR, $\omega_{red}=0.084$, $14^\circ \pm 10^\circ$.

Figure 33 shows a surface pressure distribution for the $14^\circ \pm 10^\circ$ LEGR case at 0.084 reduced frequency and 1 million Reynolds number, the same as the above case. These data show indications of a traveling wave as did the clean case in figure 26. Because the mean angle was 14° , the flow was able to recover from stall. (The minimum angle was 4° .) This recovery is observed as the stable flow region between the occurrences of the traveling waves.

In addition to the $\pm 10^\circ$ unsteady experimental data, $\pm 5.5^\circ$ unsteady data were obtained with and without LEGR. The data used were taken at 1 million Reynolds number using the same mean angles and frequencies as in the 10° amplitude cases. Figures 34 and 35 show the $\pm 5.5^\circ$, unsteady, clean, lift coefficients for the reduced frequencies of 0.026 and 0.078, respectively. The maximum lift coefficient for the lower frequency is 1.31 and occurs, as expected, when the airfoil is traveling through increasing angle of attack. The "hysteresis" lift coefficient (at 17.1°) is 0.80. At the higher reduced frequency, the lift coefficient spike is apparent, and the maximum lift coefficient prior to the data spike occurs at 17.7° and is 1.45. The corresponding "hysteresis" lift coefficient is 0.84. The difference between the maximum lift coefficient and

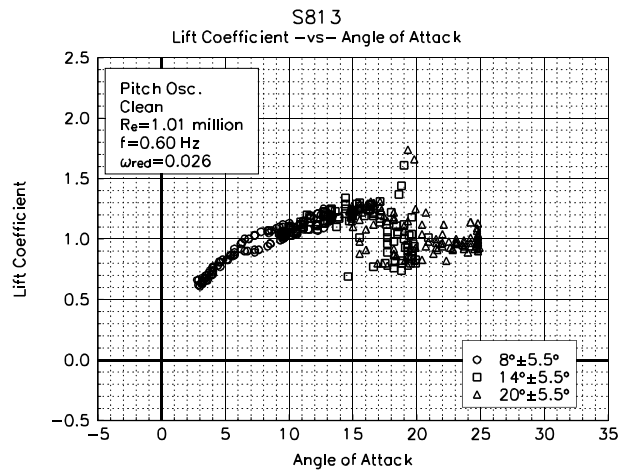


Figure 34. Clean, C_l vs α , $\omega_{red}=0.026$, $\pm 5.5^\circ$.

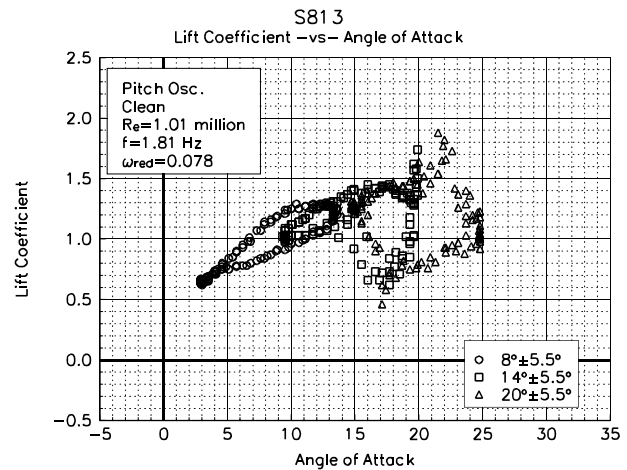


Figure 35. Clean, C_l vs α , $\omega_{red}=0.078$, $\pm 5.5^\circ$.

the "hysteresis" lift coefficient indicates a much greater hysteresis response than that experienced for the lower reduced frequency. The steady state, clean, maximum lift coefficient is 1.14; therefore, the unsteady behavior created lift coefficients more than 27% higher the steady state values.

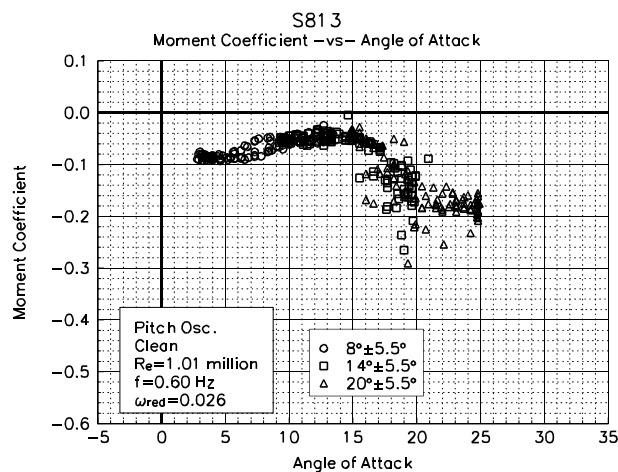


Figure 36. Clean, C_m vs α , $\omega_{red}=0.026$, $\pm 5.5^\circ$.

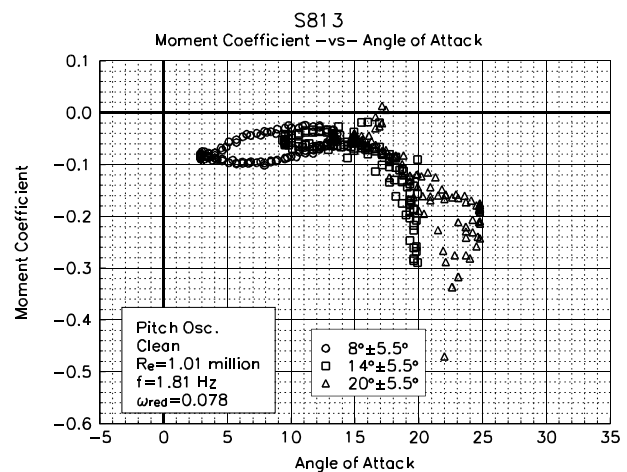


Figure 37. Clean, C_m vs α , $\omega_{red}=0.078$, $\pm 5.5^\circ$.

The quarter chord pitching moments having the same reduced frequencies as the preceding lift coefficient cases are shown in figure 36 and 37. The hysteresis behavior observed in the lift coefficient plots is also reflected in these pitching moment data. Near the maximum lift angle, 17.1° for the lower frequency, the pitching moment coefficient ranges from -0.0724 to -0.1298; whereas, the 0.078 reduced frequency case has maximum lift near 17.7° , and the pitching moment ranges from -0.0884 to -0.1346. In comparison, the steady state pitching moment is -0.0308 near the steady state maximum lift coefficient angle of attack of 14° . The higher reduced frequency again shows large hysteresis loops for all three mean angles of attack.

Figures 38 and 39 compare the effect of mean angle of attack on the surface pressure distributions for conditions corresponding to the 0.078 reduced frequency case described above. For an angle of attack range of $8^\circ \pm 5.5^\circ$, 38, the model does not exceed the unsteady stall angle of attack of 17.1° ; therefore, the pressure distributions are well behaved, reflecting the increase and decrease in angle of attack. On the other hand, for an angle of attack range of $20^\circ \pm 5.5^\circ$, the model does not have the opportunity to fully recover from stall, and a large portion of the upper surface appears to be stalled. In addition, traveling waves are observed

because the model is traveling through a range of angles that includes the angles for which the lift coefficient spike phenomenon occurs.

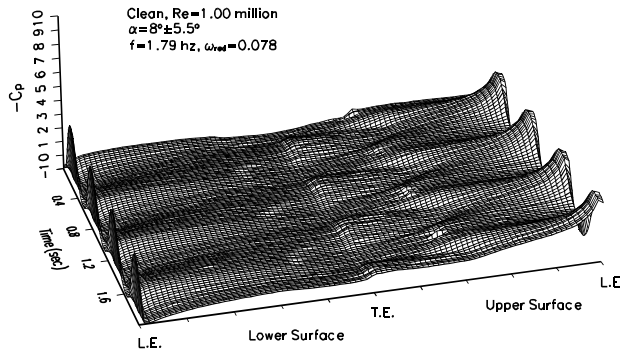


Figure 38. Unsteady pressure distribution, clean, $\omega_{red}=0.078$, $8\pm 5.5^\circ$.

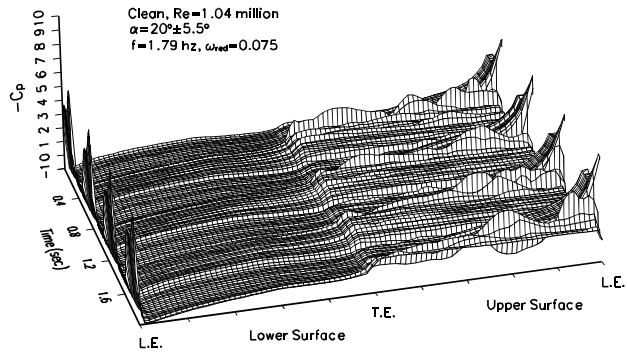


Figure 39. Unsteady pressure distribution, clean, $\omega_{red}=0.075$, $20\pm 5.5^\circ$.

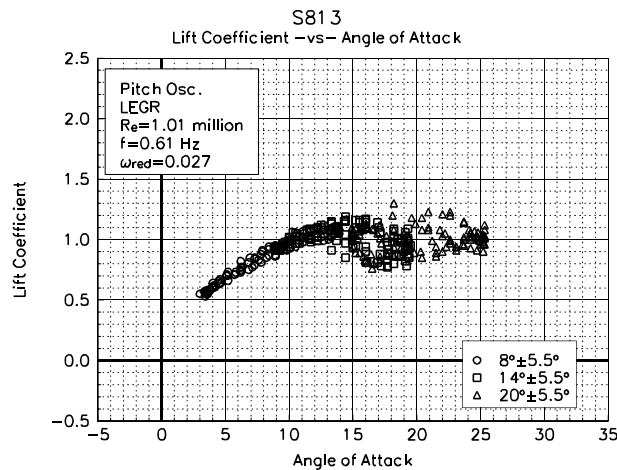


Figure 40. LEGR, C_l vs α , $\omega_{red}=0.027$, $\pm 5.5^\circ$.

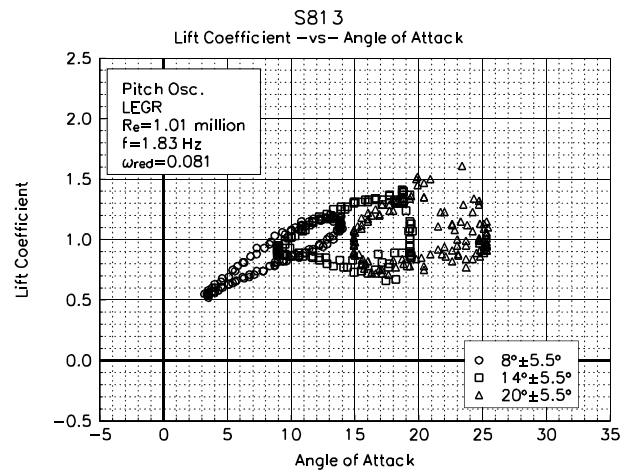


Figure 41. LEGR, C_l vs α , $\omega_{red}=0.081$, $\pm 5.5^\circ$.

The application of LEGR degrades the lift performance of the airfoil as would be expected from the results discussed previously. The LEGR lift coefficient data for reduced frequencies of 0.027 and 0.081 are shown in figures 40 and 41, respectively. The maximum lift coefficient is reduced to 1.19 from 1.31 for the low frequency clean case. Although there is a reduction, this value is still significantly higher than the LEGR steady state case, which has a maximum lift coefficient of 1.05 at 13.2° angle of attack. The higher reduced frequency has a maximum lift coefficient of 1.37, which occurs near 17.7° angle of attack. The corresponding lift coefficient at 17.7° for the airfoil traveling with decreasing angle of attack is 0.80, a 42% reduction from the unsteady maximum.

Figures 42 and 43 show the corresponding pitching moment coefficients for the LEGR cases at reduced frequencies of 0.027 and 0.081. For the 0.027 reduced frequency case, the pitching moment varies from -0.0555 to -0.0385 at 14.4° (where the maximum lift occurs). The hysteresis behavior is more pronounced for the higher reduced frequency case in which the range of pitching moments was from -0.0986 to -0.1058, at the maximum lift angle of 17.7° . These values can then be compared to the steady state LEGR value of -0.0353.

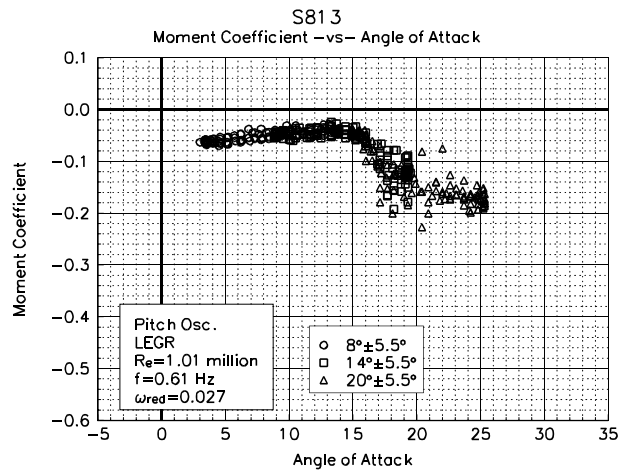


Figure 42. LEGR, C_m vs α , $\omega_{red}=0.027, \pm 5.5^\circ$.

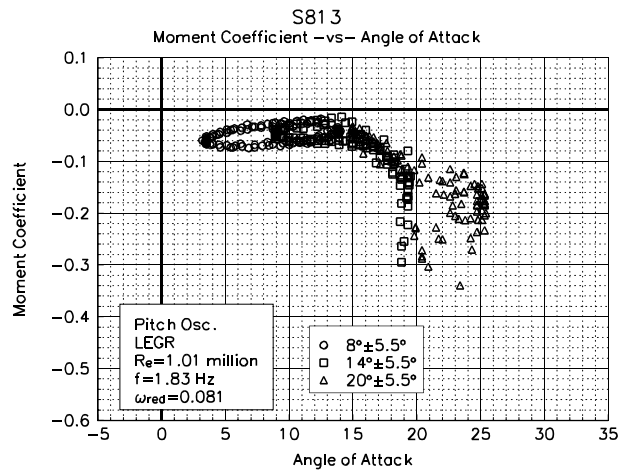


Figure 43. LEGR, C_m vs α , $\omega_{red}=0.081, \pm 5.5^\circ$.

Although all the unsteady data have not been discussed here, the previous discussion included typical examples of the wind tunnel data. The remaining cases of the $\pm 5.5^\circ$ and $\pm 10^\circ$ pitch oscillation data for all the Reynolds numbers are included in Appendix C.

Summary of Results

An S813 airfoil model was tested under steady state and pitch oscillation conditions. Baseline tests were made while the model was clean, and then corresponding tests were conducted with leading edge grit roughness (LEGR) applied.

A summary of the steady state aerodynamic parameters is shown in table 1. As observed, the application of LEGR reduced the maximum lift of the airfoil up to 12%, and the minimum drag coefficient increased up to 113%. The zero lift pitching moment coefficient was also affected from the application of LEGR which reduced the magnitude more than 14% in some cases.

Table 1. S813 Steady State Parameters Summary.

Grit Pattern	Re x 10 ⁻⁶	C _{lmax}	C _{dmin}	C _{mo}
Clean	0.75	1.17 @ 14.3	0.0086	-0.0717
LEGR	0.75	1.03 @ 13.2	0.0140	-0.0619
Clean	1.00	1.14 @ 14.3	0.0064	-0.0715
LEGR	1.00	1.05 @ 13.2	0.0133	-0.0618
Clean	1.25	1.16 @ 14.3	0.0062	-0.0723
LEGR	1.25	1.05 @ 13.2	0.0132	-0.0626
Clean	1.40	1.18 @ 14.4	0.0067	-0.0715
LEGR	1.40	1.06 @ 13.2	0.0125	-0.0633

Table 2. S813, Unsteady, Clean, ±5.5°.

ω_{red}	Re x 10 ⁻⁶	f	C _{lmax}	α_{max}	C _{l dec}	C _{m inc}	C _{m dec}
0.035	0.76	0.61	1.30	16.0	0.86	-0.0753	-0.1185
0.070	0.76	1.21	1.40	17.7	0.75	-0.1016	-0.0930
0.106	0.76	1.85	1.53	17.1	0.79	-0.0909	-0.1345
0.026	1.01	0.60	1.31	17.1	0.80	-0.0724	-0.1298
0.052	1.01	1.19	1.35	16.6	0.76	-0.0628	-0.0385
0.078	1.01	1.81	1.45	17.7	0.84	-0.0884	-0.1346
0.021	1.26	0.61	1.32	16.2	0.94	-0.0536	-0.0881
0.042	1.26	1.22	1.36	16.6	0.91	-0.0589	-0.1121
0.063	1.26	1.83	1.42	16.6	1.04	-0.0660	-0.0693
0.019	1.41	0.60	1.31	15.9	1.09	-0.0565	-0.0371
0.037	1.40	1.22	1.38	17.7	0.89	-0.0823	-0.1336
0.056	1.41	1.81	1.42	16.2	0.77	-0.0621	-0.1089

The pitch oscillation data can be divided into two groups, the ±5.5° amplitude and ±10° amplitude oscillations, which show similar trends. For both ±5.5° and ±10°, the unsteady test conditions and some parameters are in tables 2, 3, 4, and 5. Looking at the reduced frequency, which takes oscillation and tunnel speed into account, and comparing as this value is increased, it can be observed that the maximum lift

coefficient increases. The increase in maximum lift coefficient with reduced frequency is nearly linear for all the test cases as shown in figures 44 and 45. In addition, the hysteresis behavior becomes increasingly apparent with increased reduced frequency.

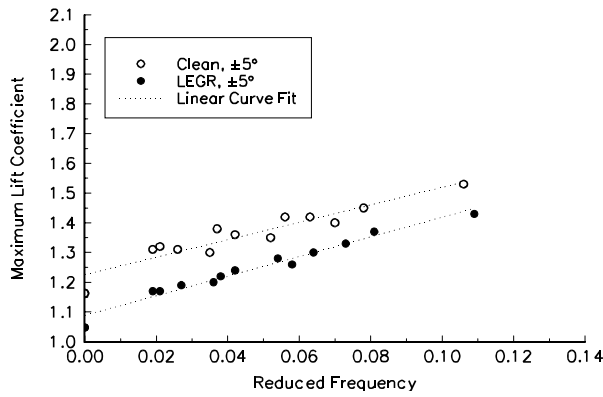


Figure 44. $\pm 5.5^\circ$, unsteady C_{lmax} vs ω_{red} .

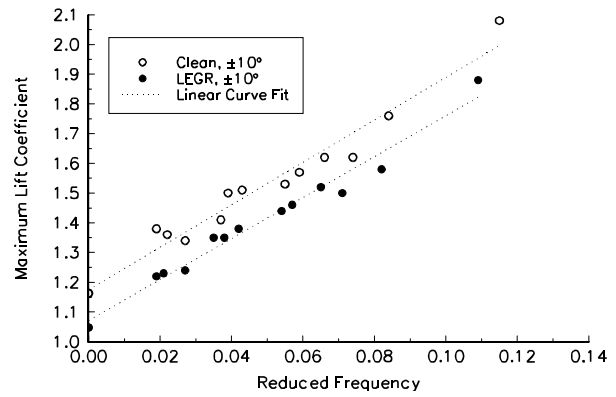


Figure 45. $\pm 10^\circ$, unsteady C_{lmax} vs ω_{red} .

Table 3. S813, Unsteady, LEGR, $\pm 5.5^\circ$.

ω_{red}	$Re \times 10^{-6}$	f	C_{lmax}	α_{max}	C_{ldec}	$C_{m inc}$	$C_{m dec}$
0.036	0.76	0.60	1.20	15.5	0.74	-0.0556	-0.0615
0.073	0.76	1.22	1.33	18.0	0.88	-0.1198	-0.1342
0.109	0.76	1.83	1.43	17.6	0.85	-0.1007	-0.1614
0.027	1.01	0.61	1.19	14.4	0.85	-0.0555	-0.0385
0.054	1.00	1.21	1.28	15.9	0.74	-0.0707	-0.0555
0.081	1.01	1.83	1.37	17.7	0.80	-0.0986	-0.1058
0.021	1.26	0.61	1.17	14.7	0.90	-0.0508	-0.0465
0.042	1.25	1.19	1.24	16.0	0.85	-0.0691	-0.0513
0.064	1.25	1.81	1.30	16.7	0.68	-0.0715	-0.0624
0.019	1.41	0.60	1.17	14.2	0.97	-0.0517	-0.0315
0.038	1.41	1.22	1.22	15.5	0.83	-0.0601	-0.0428
0.058	1.41	1.83	1.26	16.6	0.77	-0.0713	-0.0482

As expected, the application of LEGR reduces the aerodynamic performance of the airfoil. The maximum lift coefficient is reduced as much as 12% for both the $\pm 5.5^\circ$ and the $\pm 10^\circ$ cases. As well as following the same trends as the clean, unsteady data discussed previously, the LEGR causes the hysteresis behavior to persist into lower angles of attack than do the clean cases. Overall, the unsteady wind tunnel data show hysteresis behavior that becomes more apparent with increased, reduced frequency. The maximum unsteady lift coefficient can be as much as 82% higher than the steady state maximum lift coefficient. Variation in the quarter chord pitching moment coefficient can be as much as 340% greater than that indicated by steady state results. These findings indicate that it is very important to consider the unsteady loading that will occur in wind turbine operation because steady state results can greatly underestimate the forces.

Table 4. S813, Unsteady, Clean, $\pm 10^\circ$.

ω_{red}	$Re \times 10^{-6}$	f	C_{lmax}	α_{max}	C_{ldec}	$C_{m inc}$	$C_{m dec}$
0.037	0.74	0.60	1.41	17.6	0.64	-0.0900	-0.0981
0.074	0.73	1.19	1.62	16.5	0.57	-0.1125	-0.0685
0.115	0.72	1.83	2.08	21.8	1.14	-0.1014	-0.2309
0.027	1.00	0.61	1.34	15.9	1.05	-0.0601	-0.0356
0.055	0.99	1.21	1.53	17.4	0.63	-0.0892	-0.0934
0.084	0.99	1.85	1.76	18.2	0.80	-0.1052	-0.1110
0.022	1.25	0.60	1.36	17.2	1.01	-0.0677	-0.0971
0.043	1.24	1.19	1.51	19.4	0.67	-0.1383	-0.1020
0.066	1.24	1.81	1.62	19.1	0.76	-0.1089	-0.1261
0.019	1.41	0.60	1.38	18.2	0.84	-0.0727	-0.1166
0.039	1.39	1.21	1.50	18.3	0.71	-0.0825	-0.1002
0.059	1.40	1.85	1.57	18.8	0.70	-0.0997	-0.0845

Table 5. S813, Unsteady, LEGR, $\pm 10^\circ$.

ω_{red}	$Re \times 10^{-6}$	f	C_{lmax}	α_{max}	C_{ldec}	$C_{m inc}$	$C_{m dec}$
0.035	0.74	0.59	1.35	18.8	0.76	-0.1289	-0.0958
0.071	0.74	1.19	1.50	18.5	0.66	-0.1084	-0.1199
0.109	0.73	1.81	1.88	20.9	0.93	-0.1264	-0.1524
0.027	0.98	0.61	1.24	15.4	0.73	-0.0597	-0.0465
0.054	0.98	1.21	1.44	19.0	0.79	-0.0964	-0.0983
0.082	0.97	1.83	1.58	19.7	0.66	-0.1130	-0.0683
0.021	1.24	0.61	1.23	16.9	0.80	-0.0671	-0.0540
0.042	1.23	1.19	1.38	17.7	0.72	-0.0994	-0.0539
0.065	1.23	1.85	1.52	19.6	0.78	-0.1045	-0.0966
0.019	1.38	0.61	1.22	15.7	0.85	-0.0543	-0.0452
0.038	1.37	1.19	1.35	16.9	0.78	-0.0729	-0.0703
0.057	1.38	1.83	1.46	19.6	0.71	-0.1052	-0.1017

References

Pope, A.; Harper, J.J. 1966. *Low Speed Wind Tunnel Testing*. New York, NY: John Wiley & Sons, Inc.

Schlichting, H. 1979. *Boundary Layer Theory*. New York, NY: McGraw-Hill Inc.

Smetana, F. Summey, D., et-al. 1975. *Light Aircraft Lift, Drag, Moment Prediction - a Review and Analysis*. North Carolina State University. NASA-CR2523.

Appendix A: Surface Pressure Tap Coordinates

Table A1. S813 Surface Pressure Taps, Non-Dimensional Coordinates		
Tap Number	Chord Station	Ordinate
1	1.0012	--
2	0.9749	--
3	0.9352	--
4	0.8945	--
5	0.8542	--
6	0.8136	--
7	0.7729	--
8	0.7323	--
9	0.6919	--
10	0.6512	--
11	0.6106	--
12	0.5699	--
13	0.5287	--
14	0.4879	--
15	0.4465	--
16	0.4059	--
17	0.3656	--
18	0.3251	--
19	0.2853	--
20	0.2452	--
21	0.2059	--
22	0.1672	--
23	0.1304	--
24	0.0949	--
25	0.0650	--
26	0.0406	--
27	0.0316	--
28	0.0221	--
29	0.0134	--
30	0.0045	--
31	0.0000	--
32	0.0025	--
33	0.0076	--
34	0.0136	--

Table A1. S813 Surface Pressure Taps, Non-Dimensional Coordinates		
Tap Number	Chord Station	Ordinate
35	0.0198	--
36	0.0267	--
37	0.0489	--
38	0.0796	--
39	0.1151	--
40	0.1533	--
41	0.1932	--
42	0.2334	--
43	0.2746	--
44	0.3166	--
45	0.3589	--
46	0.4015	--
47	0.4446	--
48	0.4876	--
49	0.5304	--
50	0.5725	--
51	0.6130	--
52	0.6518	--
53	0.6915	--
54	0.7300	--
55	0.7703	--
56	0.8120	--
57	0.8540	--
58	0.8958	--
59	0.9356	--
60	0.9726	--
End of Table A1		

**Appendix B: Steady State Data
Integrated Coefficients and Pressure Distributions**

List of Figures

Page

Pressure Distributions, Steady State, Re = 0.75 million	B-20
1. $\alpha = -20.1^\circ$	B-21
2. $\alpha = -18.2^\circ$	B-21
3. $\alpha = -16.2^\circ$	B-21
4. $\alpha = -14.0^\circ$	B-21
5. $\alpha = -12.2^\circ$	B-22
6. $\alpha = -10.1^\circ$	B-22
7. $\alpha = -8.1^\circ$	B-22
8. $\alpha = -6.2^\circ$	B-22
9. $\alpha = -4.2^\circ$	B-23
10. $\alpha = -2.0^\circ$	B-23
11. $\alpha = -0.1^\circ$	B-23
12. $\alpha = 2.2^\circ$	B-23
13. $\alpha = 4.1^\circ$	B-24
14. $\alpha = 6.1^\circ$	B-24
15. $\alpha = 8.3^\circ$	B-24
16. $\alpha = 10.2^\circ$	B-24
17. $\alpha = 11.3^\circ$	B-25
18. $\alpha = 12.1^\circ$	B-25
19. $\alpha = 13.2^\circ$	B-25
20. $\alpha = 14.3^\circ$	B-25
21. $\alpha = 15.3^\circ$	B-26
22. $\alpha = 16.2^\circ$	B-26
23. $\alpha = 17.2^\circ$	B-26
24. $\alpha = 18.3^\circ$	B-26
25. $\alpha = 19.1^\circ$	B-27
26. $\alpha = 20.2^\circ$	B-27
27. $\alpha = 22.1^\circ$	B-27
28. $\alpha = 24.0^\circ$	B-27
29. $\alpha = 26.2^\circ$	B-28
30. $\alpha = 28.1^\circ$	B-28
31. $\alpha = 30.0^\circ$	B-28
32. $\alpha = 32.2^\circ$	B-28
33. $\alpha = 34.1^\circ$	B-29
34. $\alpha = 36.0^\circ$	B-29
35. $\alpha = 38.2^\circ$	B-29
36. $\alpha = 40.0^\circ$	B-29
Pressure Distributions, Steady State, Re = 1 million	B-30
37. $\alpha = -20.1^\circ$	B-31
38. $\alpha = -18.2^\circ$	B-31
39. $\alpha = -16.2^\circ$	B-31
40. $\alpha = -14.0^\circ$	B-31
41. $\alpha = -12.2^\circ$	B-32
42. $\alpha = -10.3^\circ$	B-32
43. $\alpha = -8.1^\circ$	B-32
44. $\alpha = -6.2^\circ$	B-32

45.	$\alpha = -4.2^\circ$	B-33
46.	$\alpha = -2.0^\circ$	B-33
47.	$\alpha = 0.2^\circ$	B-33
48.	$\alpha = 2.2^\circ$	B-33
49.	$\alpha = 4.1^\circ$	B-34
50.	$\alpha = 6.1^\circ$	B-34
51.	$\alpha = 8.3^\circ$	B-34
52.	$\alpha = 10.2^\circ$	B-34
53.	$\alpha = 11.3^\circ$	B-35
54.	$\alpha = 12.1^\circ$	B-35
55.	$\alpha = 13.2^\circ$	B-35
56.	$\alpha = 14.3^\circ$	B-35
57.	$\alpha = 15.1^\circ$	B-36
58.	$\alpha = 16.2^\circ$	B-36
59.	$\alpha = 17.2^\circ$	B-36
60.	$\alpha = 18.1^\circ$	B-36
61.	$\alpha = 19.1^\circ$	B-37
62.	$\alpha = 20.2^\circ$	B-37
63.	$\alpha = 22.1^\circ$	B-37
64.	$\alpha = 24.0^\circ$	B-37
65.	$\alpha = 26.2^\circ$	B-38
66.	$\alpha = 28.1^\circ$	B-38
67.	$\alpha = 30.0^\circ$	B-38
68.	$\alpha = 32.0^\circ$	B-38
69.	$\alpha = 34.0^\circ$	B-39
70.	$\alpha = 36.0^\circ$	B-39
71.	$\alpha = 38.0^\circ$	B-39
72.	$\alpha = 40.0^\circ$	B-39
Pressure Distributions, Steady State, Re = 1.25 million		B-40
73.	$\alpha = -20.0^\circ$	B-41
74.	$\alpha = -18.1^\circ$	B-41
75.	$\alpha = -16.2^\circ$	B-41
76.	$\alpha = -14.0^\circ$	B-41
77.	$\alpha = -12.2^\circ$	B-42
78.	$\alpha = -10.3^\circ$	B-42
79.	$\alpha = -8.1^\circ$	B-42
80.	$\alpha = -6.2^\circ$	B-42
81.	$\alpha = -4.2^\circ$	B-43
82.	$\alpha = -2.0^\circ$	B-43
83.	$\alpha = 0.2^\circ$	B-43
84.	$\alpha = 2.1^\circ$	B-43
85.	$\alpha = 4.1^\circ$	B-44
86.	$\alpha = 6.1^\circ$	B-44
87.	$\alpha = 8.3^\circ$	B-44
88.	$\alpha = 10.2^\circ$	B-44
89.	$\alpha = 11.3^\circ$	B-45
90.	$\alpha = 12.4^\circ$	B-45
91.	$\alpha = 13.2^\circ$	B-45
92.	$\alpha = 14.3^\circ$	B-45

93. $\alpha = 15.1^\circ$	B-46
94. $\alpha = 16.2^\circ$	B-46
95. $\alpha = 17.2^\circ$	B-46
96. $\alpha = 18.1^\circ$	B-46
97. $\alpha = 19.1^\circ$	B-47
98. $\alpha = 20.2^\circ$	B-47
99. $\alpha = 22.1^\circ$	B-47
100. $\alpha = 24.0^\circ$	B-47
101. $\alpha = 26.2^\circ$	B-48
102. $\alpha = 28.1^\circ$	B-48
103. $\alpha = 30.0^\circ$	B-48
104. $\alpha = 32.2^\circ$	B-48
105. $\alpha = 34.0^\circ$	B-49
106. $\alpha = 36.1^\circ$	B-49
107. $\alpha = 38.1^\circ$	B-49
108. $\alpha = 40.0^\circ$	B-49
Pressure Distributions, Steady State, Re = 1.4 million	B-50
109. $\alpha = -20.0^\circ$	B-51
110. $\alpha = -18.1^\circ$	B-51
111. $\alpha = -16.2^\circ$	B-51
112. $\alpha = -14.0^\circ$	B-51
113. $\alpha = -12.2^\circ$	B-52
114. $\alpha = -10.3^\circ$	B-52
115. $\alpha = -8.1^\circ$	B-52
116. $\alpha = -6.2^\circ$	B-52
117. $\alpha = -4.2^\circ$	B-53
118. $\alpha = -2.0^\circ$	B-53
119. $\alpha = 0.0^\circ$	B-53
120. $\alpha = 2.2^\circ$	B-53
121. $\alpha = 4.1^\circ$	B-54
122. $\alpha = 6.1^\circ$	B-54
123. $\alpha = 8.3^\circ$	B-54
124. $\alpha = 10.2^\circ$	B-54
125. $\alpha = 11.3^\circ$	B-55
126. $\alpha = 12.2^\circ$	B-55
127. $\alpha = 13.3^\circ$	B-55
128. $\alpha = 14.4^\circ$	B-55
129. $\alpha = 15.2^\circ$	B-56
130. $\alpha = 16.3^\circ$	B-56
131. $\alpha = 17.3^\circ$	B-56
132. $\alpha = 18.1^\circ$	B-56
133. $\alpha = 19.2^\circ$	B-57
134. $\alpha = 20.2^\circ$	B-57

List of Tables

Page

B1. S813, Clean, $Re = 0.75 \times 10^6$	B-6
B2. S813, Clean, $Re = 1.0 \times 10^6$	B-8
B3. S813, Clean, $Re = 1.25 \times 10^6$	B-10
B4. S813, Clean, $Re = 1.4 \times 10^6$	B-12
B5. S813, LEGR, $Re = 0.75 \times 10^6$	B-13
B6. S813, LEGR, $Re = 1.0 \times 10^6$	B-15
B7. S813, LEGR, $Re = 1.25 \times 10^6$	B-17
B8. S813, LEGR, $Re = 1.4 \times 10^6$	B-19

Table B1. S813, Clean, Re = 0.75 x 10⁶

RUN	AOA	C _l	C _{dp}	C _{m/4}	Re x 10 ⁻⁶	C _{dw}
87	-20.1	-0.48	0.2894	0.0359	0.75	--
86	-18.2	-0.44	0.2542	0.0303	0.75	--
85	-16.2	-0.51	0.2541	0.0592	0.75	--
84	-14.0	-0.51	0.2246	0.0630	0.76	--
83	-12.2	-0.62	0.1716	0.0178	0.75	--
82	-10.1	-0.67	0.0352	-0.0608	0.75	0.0237
81	-8.1	-0.56	0.0233	-0.0577	0.76	0.0176
80	-6.2	-0.39	0.0146	-0.0585	0.75	0.0146
79	-4.2	-0.17	0.0084	-0.0628	0.75	0.0110
78	-2.0	0.05	0.0055	-0.0671	0.75	0.0091
77	-0.1	0.26	0.0063	-0.0717	0.75	0.0091
88	-0.1	0.30	0.0044	-0.0736	0.75	0.0096
114	-0.1	0.27	0.0061	-0.0743	0.74	0.0087
89	2.2	0.55	0.0060	-0.0769	0.75	0.0099
90	4.1	0.76	0.0103	-0.0829	0.75	0.0086
91	6.1	0.95	0.0135	-0.0759	0.74	0.0149
92	8.3	0.99	0.0264	-0.0574	0.75	0.0275
93	10.2	1.05	0.0391	-0.0444	0.75	--
94	11.3	1.09	0.0483	-0.0426	0.75	--
95	12.1	1.11	0.0599	-0.0418	0.75	--
96	13.2	1.13	0.0695	-0.0383	0.75	--
97	14.3	1.17	0.0876	-0.0413	0.75	--
98	15.3	1.15	0.0989	-0.0403	0.76	--
99	16.2	1.02	0.1409	-0.0551	0.75	--
100	17.2	0.91	0.3162	-0.1504	0.75	--
101	18.3	0.84	0.3322	-0.1508	0.77	--
102	19.1	0.83	0.3468	-0.1478	0.76	--
103	20.2	0.83	0.3670	-0.1481	0.75	--

Table B1. S813, Clean, Re = 0.75 x 10 ⁶						
RUN	AOA	C _l	C _{dp}	C _{m/4}	Re x 10 ⁻⁶	C _{dw}
104	22.1	0.86	0.4102	-0.1477	0.76	--
105	24.0	0.94	0.4787	-0.1669	0.77	--
106	26.2	1.03	0.5708	-0.1941	0.75	--
107	28.1	1.10	0.6458	-0.2138	0.76	--
108	30.0	1.17	0.7349	-0.2388	0.75	--
109	32.2	1.23	0.8362	-0.2669	0.73	--
110	34.1	1.29	0.9364	-0.2979	0.75	--
111	36.0	1.30	1.0098	-0.3132	0.74	--
112	38.2	1.33	1.1054	-0.3366	0.74	--
113	40.0	1.32	1.1741	-0.3523	0.74	--
End of Table B1						

Table B2. S813, Clean, Re = 1.0 x 10 ⁶						
RUN	AOA	C _l	C _{dp}	C _{m^{1/4}}	Re x 10 ⁻⁶	C _{dw}
11	-20.1	-0.49	0.2936	0.0394	1.00	--
10	-18.2	-0.53	0.2864	0.0612	1.00	--
9	-16.2	-0.52	0.2581	0.0634	1.00	--
8	-14.0	-0.53	0.2283	0.0683	0.99	--
7	-12.2	-0.64	0.1784	0.0324	1.00	--
6	-10.3	-0.72	0.0384	-0.0562	0.99	0.0230
5	-8.1	-0.59	0.0232	-0.0564	1.00	0.0156
4	-6.2	-0.40	0.0141	-0.0576	0.99	0.0127
3	-4.2	-0.19	0.0077	-0.0621	1.00	0.0097
2	-2.0	0.03	0.0047	-0.0669	0.99	0.0064
12	-0.1	0.28	0.0029	-0.0715	1.00	0.0078
38	-0.1	0.27	0.0031	-0.0707	1.00	0.0079
1	0.2	0.28	0.0041	-0.0717	0.99	0.0095
13	2.2	0.52	0.0063	-0.0780	1.00	0.0095
14	4.1	0.74	0.0098	-0.0793	1.00	0.0088
15	6.1	0.91	0.0162	-0.0751	0.99	0.0119
16	8.3	0.97	0.0253	-0.0549	0.99	0.0313
17	10.2	1.04	0.0401	-0.0454	1.00	--
18	11.3	1.09	0.0503	-0.0427	0.99	--
19	12.1	1.11	0.0549	-0.0377	0.99	--
20	13.2	1.13	0.0619	-0.0330	0.99	--
21	14.3	1.14	0.0726	-0.0308	0.99	--
22	15.1	1.12	0.0819	-0.0316	1.00	--
23	16.2	1.02	0.1085	-0.0408	0.99	--
24	17.2	0.89	0.1616	-0.0698	0.99	--
25	18.1	0.86	0.2191	-0.0958	0.99	--
26	19.1	0.82	0.3431	-0.1481	1.00	--
27	20.2	0.83	0.3627	-0.1472	1.00	--

Table B2. S813, Clean, Re = 1.0 x 10 ⁶						
RUN	AOA	C _l	C _{dp}	C _{m/4}	Re x 10 ⁻⁶	C _{dw}
28	22.1	0.85	0.4046	-0.1515	1.00	--
29	24.0	0.90	0.4631	-0.1583	1.00	--
30	26.2	1.01	0.5578	-0.1875	1.00	--
31	28.1	1.08	0.6364	-0.2096	1.00	--
32	30.0	1.15	0.7273	-0.2355	1.01	--
33	32.0	1.23	0.8276	-0.2653	1.00	--
34	34.0	1.27	0.9174	-0.2887	1.00	--
35	36.0	1.29	1.0024	-0.3089	0.99	--
36	38.0	1.32	1.0963	-0.3349	0.98	--
37	40.0	1.33	1.1808	-0.3554	0.98	--
End of Table B2						

Table B3. S813, Clean, Re = 1.25 x 10 ⁶						
RUN	AOA	C _l	C _{dp}	C _{m/4}	Re x 10 ⁻⁶	C _{dw}
49	-20.0	-0.51	0.3000	0.0438	1.25	--
48	-18.1	-0.54	0.2885	0.0637	1.25	--
47	-16.2	-0.52	0.2556	0.0645	1.26	--
46	-14.0	-0.55	0.2268	0.0670	1.25	--
45	-12.2	-0.66	0.1708	0.0201	1.25	--
44	-10.3	-0.76	0.0360	-0.0558	1.25	0.0218
43	-8.1	-0.61	0.0213	-0.0556	1.25	0.0155
42	-6.2	-0.41	0.0131	-0.0572	1.25	0.0128
41	-4.2	-0.19	0.0078	-0.0627	1.25	0.0102
40	-2.0	0.04	0.0034	-0.0671	1.25	0.0062
50	-0.1	0.27	0.0029	-0.0722	1.25	0.0085
76	0.0	0.28	0.0028	-0.0723	1.25	0.0071
39	0.2	0.28	0.0039	-0.0717	1.25	0.0074
51	2.1	0.51	0.0071	-0.0771	1.25	0.0079
52	4.1	0.74	0.0099	-0.0809	1.25	0.0097
53	6.1	0.90	0.0161	-0.0743	1.25	0.0109
54	8.3	0.97	0.0253	-0.0543	1.25	0.0305
55	10.2	1.06	0.0378	-0.0466	1.25	--
56	11.3	1.10	0.0475	-0.0430	1.25	--
57	12.4	1.13	0.0553	-0.0373	1.26	--
58	13.2	1.15	0.0620	-0.0346	1.26	--
59	14.3	1.16	0.0711	-0.0314	1.26	--
60	15.1	1.14	0.0805	-0.0313	1.25	--
61	16.2	1.06	0.1061	-0.0398	1.25	--
62	17.2	0.92	0.1585	-0.0689	1.26	--
63	18.1	0.85	0.3309	-0.1544	1.22	--
64	19.1	0.85	0.3467	-0.1516	1.26	--
65	20.2	0.84	0.3644	-0.1482	1.27	--

Table B3. S813, Clean, Re = 1.25 x 10 ⁶						
RUN	AOA	C _l	C _{dp}	C _{m/4}	Re x 10 ⁻⁶	C _{dw}
66	22.1	0.85	0.4046	-0.1518	1.26	--
67	24.0	0.89	0.4575	-0.1570	1.25	--
68	26.2	1.00	0.5500	-0.1840	1.25	--
69	28.1	1.08	0.6380	-0.2102	1.24	--
70	30.0	1.15	0.7233	-0.2345	1.24	--
71	32.2	1.23	0.8370	-0.2696	1.23	--
72	34.0	1.28	0.9291	-0.2950	1.24	--
73	36.1	1.31	1.0174	-0.3147	1.23	--
74	38.1	1.31	1.0893	-0.3293	1.23	--
75	40.0	1.31	1.1569	-0.3442	1.21	--
End of Table B3						

Table B4. S813, Clean, Re = 1.4 x 10 ⁶						
RUN	AOA	C _l	C _{dp}	C _{m^{1/4}}	Re x 10 ⁻⁶	C _{dw}
141	-20.0	-0.52	0.3044	0.0469	1.40	--
140	-18.1	-0.54	0.2892	0.0641	1.40	--
139	-16.2	-0.52	0.2587	0.0650	1.41	--
138	-14.0	-0.53	0.2281	0.0674	1.41	--
137	-12.2	-0.71	0.1558	0.0059	1.42	--
136	-10.3	-0.77	0.0371	-0.0544	1.40	0.0194
135	-8.1	-0.60	0.0224	-0.0546	1.40	0.0141
134	-6.2	-0.42	0.0130	-0.0575	1.39	0.0125
133	-4.2	-0.20	0.0075	-0.0609	1.40	0.0103
132	-2.0	0.04	0.0035	-0.0673	1.40	0.0069
131	0.0	0.26	0.0035	-0.0706	1.40	0.0067
142	0.0	0.26	0.0036	-0.0715	1.40	0.0068
158	0.0	0.25	0.0037	-0.0719	1.40	0.0069
143	2.2	0.51	0.0072	-0.0770	1.40	0.0075
144	4.1	0.72	0.0116	-0.0797	1.41	0.0090
145	6.1	0.88	0.0188	-0.0727	1.40	0.0119
146	8.3	0.97	0.0286	-0.0558	1.40	0.0282
147	10.2	1.04	0.0418	-0.0478	1.40	0.0371
148	11.3	1.09	0.0508	-0.0437	1.41	--
149	12.2	1.11	0.0559	-0.0394	1.40	--
150	13.3	1.15	0.0661	-0.0367	1.40	--
151	14.4	1.18	0.0757	-0.0338	1.41	--
152	15.2	1.16	0.0816	-0.0307	1.41	--
153	16.3	1.12	0.1052	-0.0373	1.39	--
154	17.3	0.95	0.1504	-0.0620	1.39	--
155	18.1	0.89	0.3335	-0.1536	1.42	--
156	19.2	0.85	0.3483	-0.1518	1.43	--
157	20.2	0.83	0.3652	-0.1489	1.41	--
End of Table B4						

Table B5. S813, LEGR, Re = 0.75 x 10 ⁶						
RUN	AOA	C _l	C _{dp}	C _{m/4}	Re x 10 ⁻⁶	C _{dw}
309	-20.0	-0.52	0.3042	0.0527	0.75	--
308	-18.1	-0.56	0.2804	0.0553	0.75	--
307	-16.0	-0.69	0.2377	0.0366	0.75	--
306	-14.1	-0.69	0.1750	0.0138	0.76	--
305	-12.2	-0.62	0.0948	-0.0245	0.75	--
304	-10.2	-0.64	0.0425	-0.0603	0.75	0.0403
303	-8.1	-0.54	0.0271	-0.0596	0.75	0.0228
302	-6.2	-0.38	0.0163	-0.0586	0.75	0.0188
301	-4.2	-0.19	0.0100	-0.0590	0.75	0.0159
300	-2.0	0.03	0.0056	-0.0616	0.76	0.0152
299	-0.1	0.22	0.0048	-0.0618	0.75	0.0144
310	-0.1	0.25	0.0031	-0.0619	0.75	0.0150
336	-0.1	0.22	0.0049	-0.0626	0.75	0.0140
311	2.2	0.46	0.0054	-0.0618	0.75	0.0151
312	4.1	0.62	0.0104	-0.0576	0.74	0.0177
313	6.1	0.76	0.0158	-0.0501	0.75	0.0238
314	8.3	0.87	0.0282	-0.0418	0.74	0.0331
315	10.2	0.95	0.0441	-0.0383	0.75	0.0385
316	11.3	0.99	0.0548	-0.0345	0.75	--
317	12.1	1.01	0.0626	-0.0323	0.75	--
318	13.2	1.03	0.0770	-0.0328	0.75	--
319	14.3	1.00	0.0927	-0.0333	0.75	--
320	15.1	0.89	0.1254	-0.0503	0.75	--
321	16.1	0.87	0.1800	-0.0783	0.75	--
322	17.1	0.85	0.2137	-0.0897	0.76	--
323	18.0	0.84	0.2531	-0.1042	0.75	--
324	19.1	0.88	0.2961	-0.1189	0.76	--
325	20.2	0.91	0.3402	-0.1293	0.75	--

Table B5. S813, LEGR, Re = 0.75 x 10 ⁶						
RUN	AOA	C _l	C _{dp}	C _{m/4}	Re x 10 ⁻⁶	C _{dw}
326	22.1	1.04	0.4099	-0.1452	0.76	--
327	24.1	1.11	0.4634	-0.1469	0.76	--
328	26.2	0.97	0.5253	-0.1678	0.75	--
329	28.1	1.08	0.6379	-0.2081	0.75	--
330	30.0	1.16	0.7311	-0.2363	0.74	--
331	32.1	1.22	0.8266	-0.2618	0.74	--
332	34.0	1.29	0.9341	-0.2961	0.74	--
333	36.0	1.30	1.0067	-0.3104	0.73	--
334	38.2	1.31	1.0917	-0.3267	0.74	--
335	40.0	1.33	1.1805	-0.3542	0.74	--
End of Table B5						

Table B6. S813, LEGR, Re = 1 x 10 ⁶						
RUN	AOA	C _l	C _{dp}	C _{m/4}	Re x 10 ⁻⁶	C _{dw}
205	-20.1	-0.84	0.3544	0.0565	1.01	--
204	-18.2	-0.63	0.2873	0.0599	1.01	--
203	-16.0	-0.68	0.2393	0.0426	1.00	--
202	-14.1	-0.70	0.1665	0.0073	1.01	--
201	-12.2	-0.64	0.0936	-0.0245	1.01	--
200	-10.4	-0.67	0.0438	-0.0588	0.99	0.0421
199	-8.1	-0.56	0.0276	-0.0571	1.00	0.0250
198	-6.2	-0.39	0.0160	-0.0582	1.01	0.0203
197	-4.2	-0.20	0.0087	-0.0603	1.00	0.0142
196	-2.0	0.02	0.0044	-0.0615	1.00	0.0167
195	-0.1	0.21	0.0039	-0.0618	1.00	0.0138
206	-0.1	0.25	0.0032	-0.0628	1.00	0.0133
232	-0.1	0.22	0.0036	-0.0611	1.00	0.0148
207	2.1	0.45	0.0040	-0.0610	0.99	0.0152
208	4.1	0.62	0.0086	-0.0581	0.99	0.0161
209	6.1	0.75	0.0149	-0.0489	1.00	0.0222
210	8.2	0.87	0.0273	-0.0415	1.00	0.0354
211	10.2	0.96	0.0440	-0.0383	1.00	--
212	11.3	1.00	0.0555	-0.0370	0.99	--
213	12.1	1.03	0.0649	-0.0359	1.00	--
214	13.2	1.05	0.0782	-0.0353	1.00	--
215	14.3	1.03	0.0929	-0.0344	1.00	--
216	15.1	0.94	0.1141	-0.0430	1.00	--
217	16.1	0.87	0.1715	-0.0742	1.01	--
218	17.2	0.87	0.2174	-0.0924	1.00	--
219	18.1	0.85	0.2548	-0.1068	1.02	--
220	19.1	0.87	0.2924	-0.1178	1.00	--
221	20.2	0.90	0.3308	-0.1281	1.01	--

Table B6. S813, LEGR, Re = 1 x 10 ⁶						
RUN	AOA	C _l	C _{dp}	C _{m/4}	Re x 10 ⁻⁶	C _{dw}
222	22.1	0.88	0.3895	-0.1380	1.01	--
223	24.1	1.01	0.4655	-0.1531	1.01	--
224	26.2	0.96	0.5173	-0.1639	1.00	--
225	28.1	1.04	0.6122	-0.1963	1.01	--
226	30.0	1.15	0.7237	-0.2329	1.00	--
227	32.2	1.22	0.8307	-0.2642	1.00	--
228	34.1	1.25	0.9112	-0.2843	0.99	--
229	36.0	1.31	1.0157	-0.3158	1.00	--
230	38.1	1.33	1.1067	-0.3356	0.99	--
231	40.0	1.32	1.1759	-0.3508	1.00	--
End of Table B6						

Table B7. S813, LEGR, Re = 1.25 x 10 ⁶						
RUN	AOA	C _l	C _{dp}	C _{m/4}	Re x 10 ⁻⁶	C _{dw}
243	-20.1	-0.74	0.3390	0.0516	1.25	--
242	-18.1	-0.59	0.2801	0.0555	1.26	--
241	-16.1	-0.67	0.2409	0.0427	1.26	--
240	-14.1	-0.69	0.1721	0.0137	1.26	--
239	-12.2	-0.66	0.0893	-0.0287	1.26	--
238	-10.4	-0.69	0.0456	-0.0577	1.26	0.0456
237	-8.1	-0.57	0.0280	-0.0575	1.25	0.0238
236	-6.2	-0.41	0.0163	-0.0576	1.25	0.0178
235	-4.2	-0.20	0.0089	-0.0596	1.25	0.0154
234	-2.0	0.00	0.0046	-0.0607	1.26	0.0140
233	-0.1	0.22	0.0034	-0.0626	1.24	0.0138
270	-0.1	0.23	0.0024	-0.0628	1.25	0.0132
244	0.2	0.25	0.0033	-0.0635	1.25	0.0133
245	2.2	0.45	0.0040	-0.0613	1.25	0.0138
246	4.1	0.61	0.0090	-0.0582	1.25	0.0155
247	6.2	0.75	0.0165	-0.0492	1.25	0.0218
248	8.3	0.87	0.0270	-0.0412	1.25	0.0309
249	10.2	0.96	0.0436	-0.0375	1.26	--
250	11.3	1.00	0.0546	-0.0354	1.25	--
251	12.2	1.03	0.0645	-0.0355	1.25	--
252	13.2	1.05	0.0776	-0.0347	1.25	--
253	14.3	1.05	0.0914	-0.0334	1.25	--
254	15.1	0.99	0.1082	-0.0381	1.26	--
255	16.2	0.90	0.1543	-0.0615	1.26	--
256	17.2	0.89	0.2061	-0.0853	1.26	--
257	18.1	0.89	0.2545	-0.1064	1.27	--
258	19.1	0.90	0.2950	-0.1204	1.27	--
259	20.2	0.90	0.3255	-0.1255	1.26	--

Table B7. S813, LEGR, Re = 1.25 x 10 ⁶						
RUN	AOA	C _l	C _{dp}	C _{m/4}	Re x 10 ⁻⁶	C _{dw}
260	22.1	0.88	0.3881	-0.1391	1.26	--
261	24.0	0.90	0.4440	-0.1501	1.25	--
262	26.2	0.94	0.5154	-0.1655	1.25	--
263	28.1	1.05	0.6221	-0.2018	1.25	--
264	30.0	1.14	0.7193	-0.2309	1.25	--
265	32.1	1.22	0.8289	-0.2633	1.23	--
266	34.0	1.27	0.9227	-0.2906	1.23	--
267	36.0	1.30	1.0083	-0.3109	1.23	--
268	38.0	1.34	1.1130	-0.3424	1.22	--
269	40.0	1.31	1.1633	-0.3453	1.22	--
End of Table B7						

Table B8. S813, LEGR, Re = 1.4 x 10 ⁶						
RUN	AOA	C _l	C _{dp}	C _{m^{1/4}}	Re x 10 ⁻⁶	C _{dw}
281	-20.1	-0.58	0.3132	0.0543	1.41	--
280	-18.2	-0.59	0.2852	0.0575	1.40	--
279	-16.0	-0.66	0.2370	0.0390	1.41	--
278	-14.1	-0.70	0.1790	0.0171	1.41	--
277	-12.2	-0.67	0.0952	-0.0258	1.40	--
276	-10.3	-0.69	0.0453	-0.0582	1.41	0.0430
275	-8.1	-0.58	0.0275	-0.0578	1.41	0.0234
274	-6.2	-0.42	0.0158	-0.0578	1.41	0.0182
273	-4.2	-0.21	0.0089	-0.0595	1.41	0.0140
272	-2.0	0.03	0.0034	-0.0614	1.41	0.0129
282	-0.1	0.24	0.0023	-0.0632	1.40	0.0140
298	-0.1	0.21	0.0029	-0.0624	1.40	0.0125
271	0.0	0.23	0.0025	-0.0633	1.40	0.0135
283	2.2	0.46	0.0038	-0.0619	1.40	0.0135
284	4.1	0.61	0.0092	-0.0583	1.40	0.0153
285	6.1	0.76	0.0149	-0.0499	1.40	0.0214
286	8.3	0.87	0.0287	-0.0435	1.40	0.0311
287	10.2	0.97	0.0442	-0.0386	1.40	--
288	11.3	1.01	0.0556	-0.0363	1.40	--
289	12.1	1.04	0.0654	-0.0354	1.40	--
290	13.2	1.06	0.0782	-0.0342	1.40	--
291	14.1	1.05	0.0884	-0.0329	1.40	--
292	15.1	0.97	0.1113	-0.0407	1.39	--
293	16.2	0.92	0.1487	-0.0572	1.39	--
294	17.2	0.89	0.2107	-0.0885	1.40	--
295	18.1	0.88	0.2506	-0.1041	1.41	--
296	19.2	0.91	0.2932	-0.1189	1.42	--
297	19.9	0.91	0.3225	-0.1269	1.41	--
End of Table B8						

S813

Pressure Distributions, Steady State, $Re = 0.75$ million

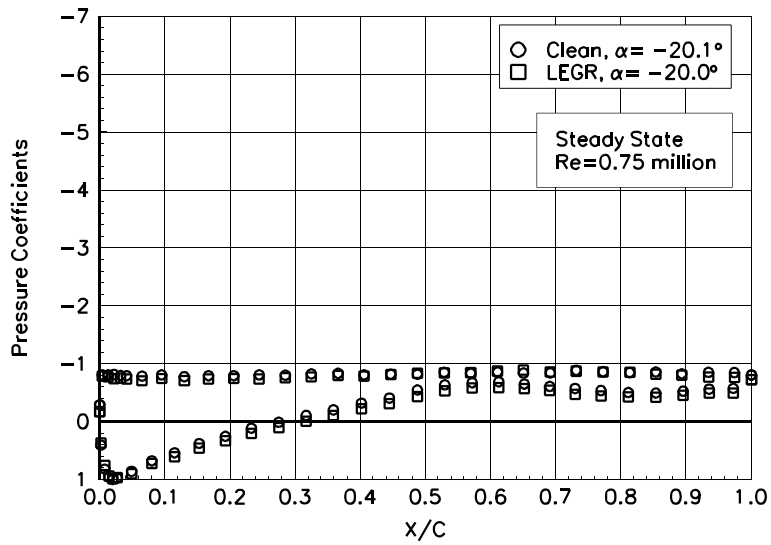


Figure 1. $\alpha = -20.1^\circ$

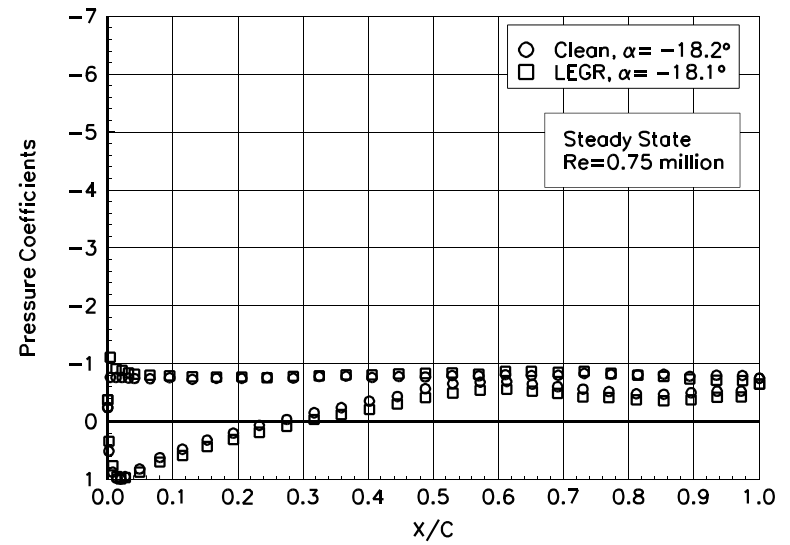


Figure 2. $\alpha = -18.2^\circ$

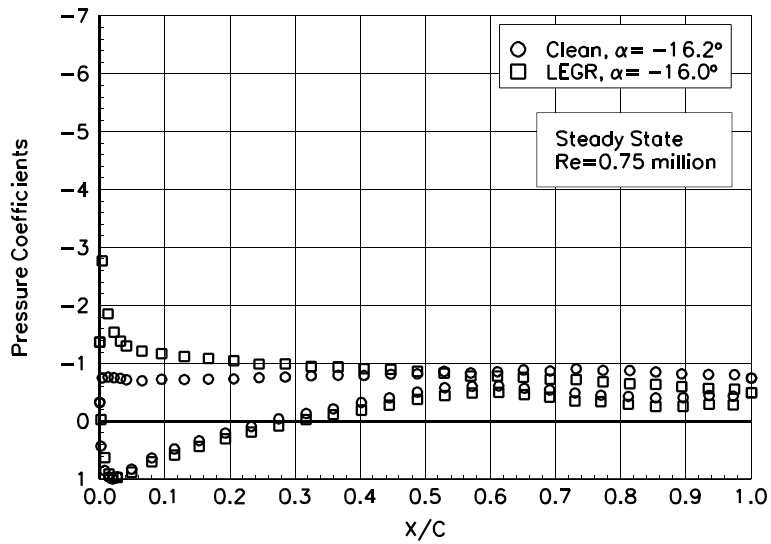


Figure 3. $\alpha = -16.2^\circ$

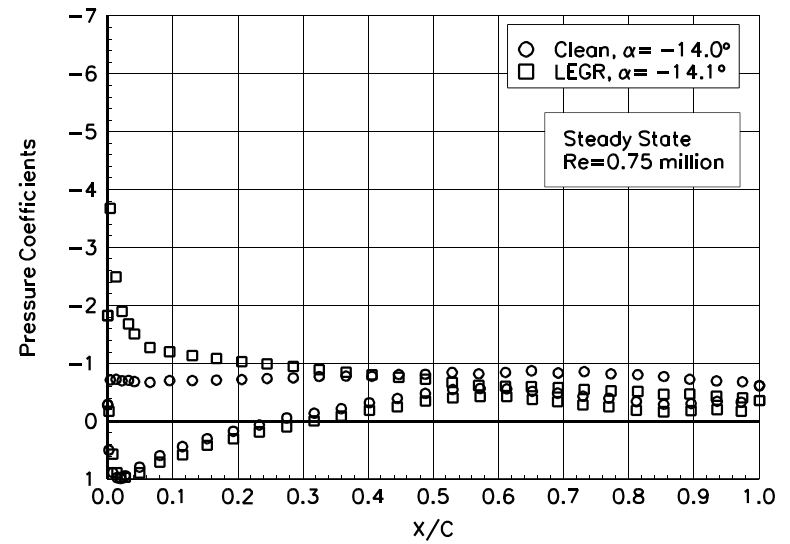


Figure 4. $\alpha = -14.0^\circ$

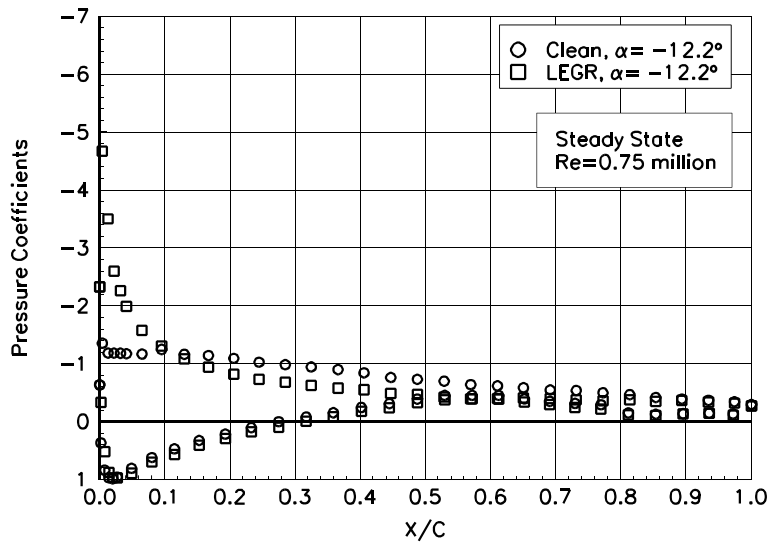


Figure 5. $\alpha = -12.2^\circ$

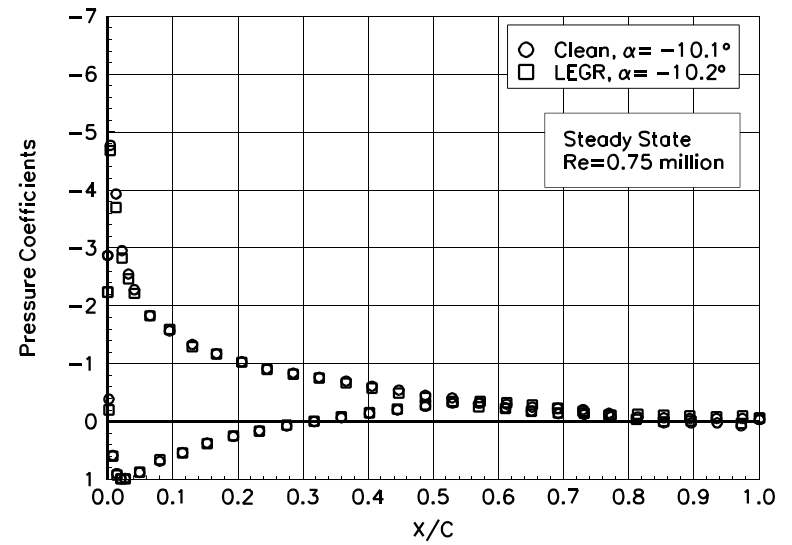


Figure 6. $\alpha = -10.1^\circ$

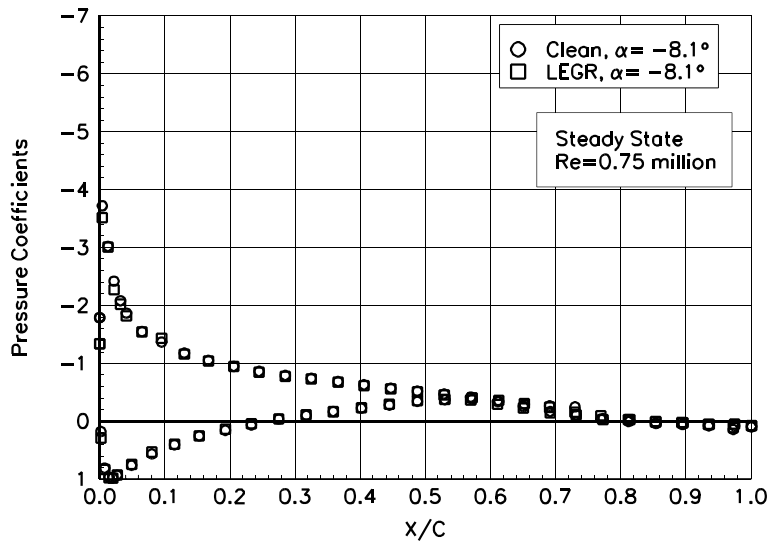


Figure 7. $\alpha = -8.1^\circ$

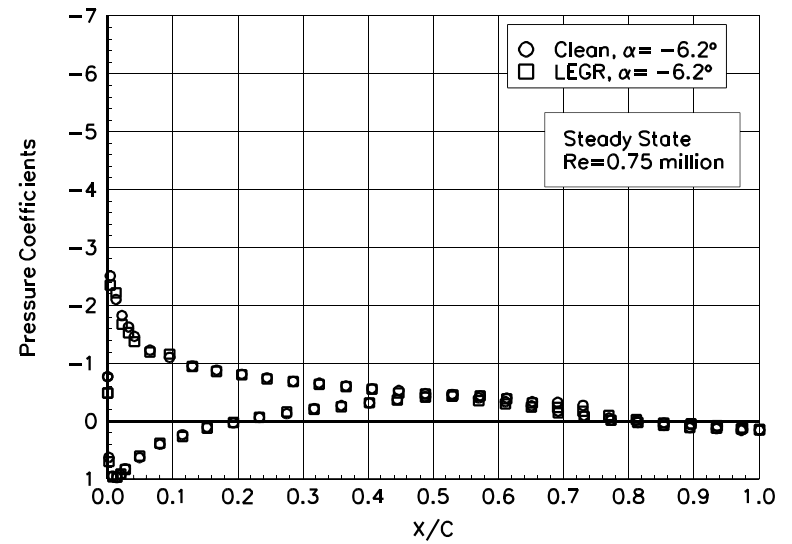


Figure 8. $\alpha = -6.2^\circ$

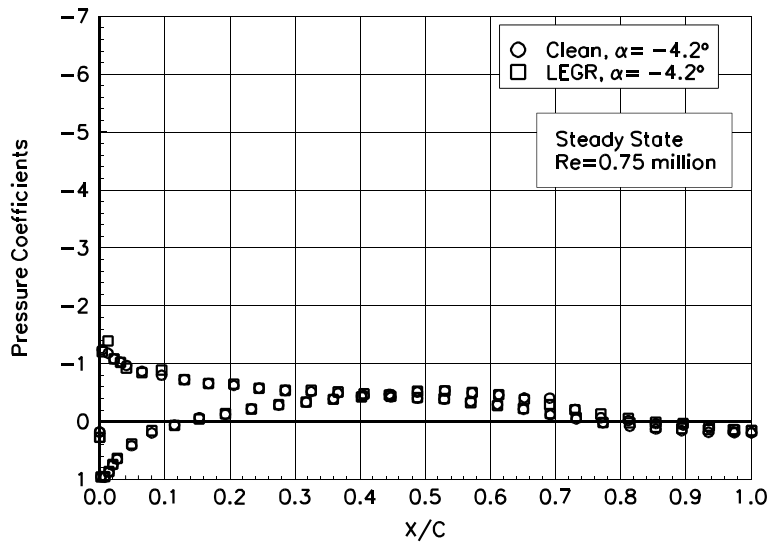


Figure 9. $\alpha = -4.2^\circ$

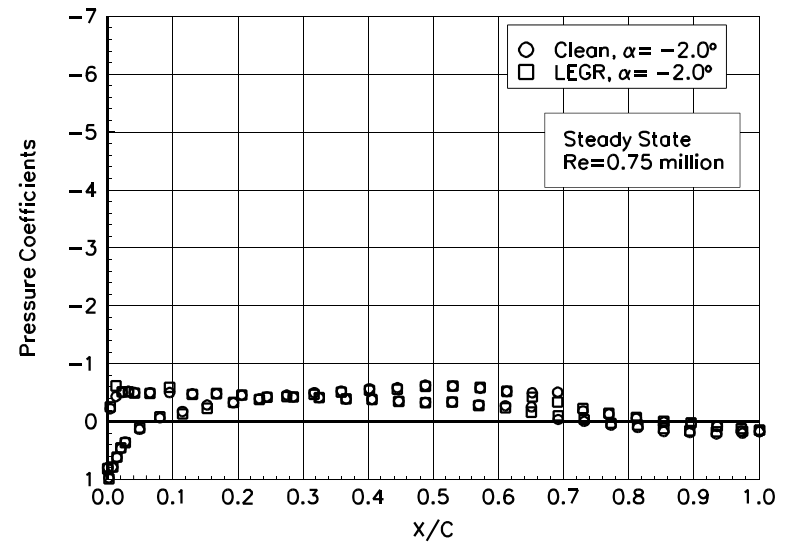


Figure 10. $\alpha = -2.0^\circ$

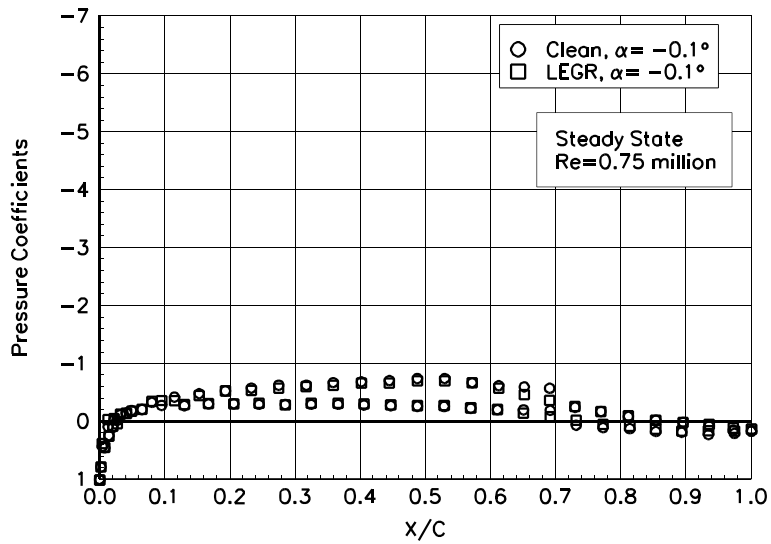


Figure 11. $\alpha = -0.1^\circ$

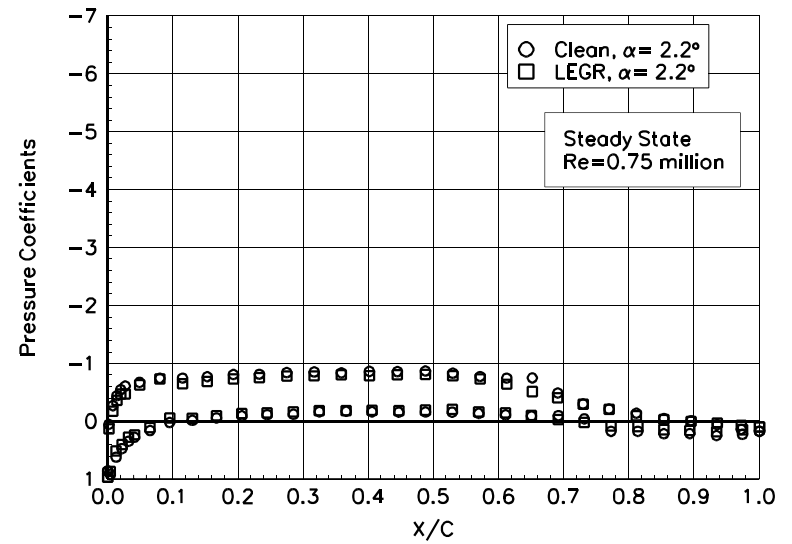


Figure 12. $\alpha = 2.2^\circ$

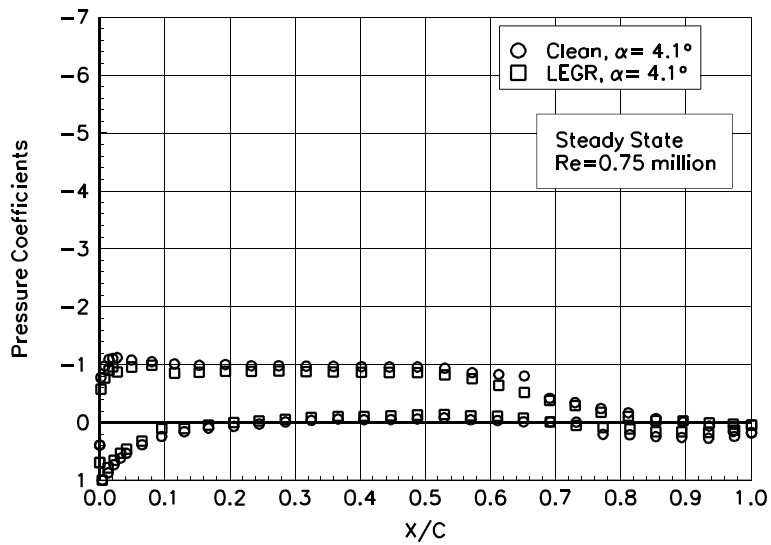


Figure 13. $\alpha = 4.1^\circ$

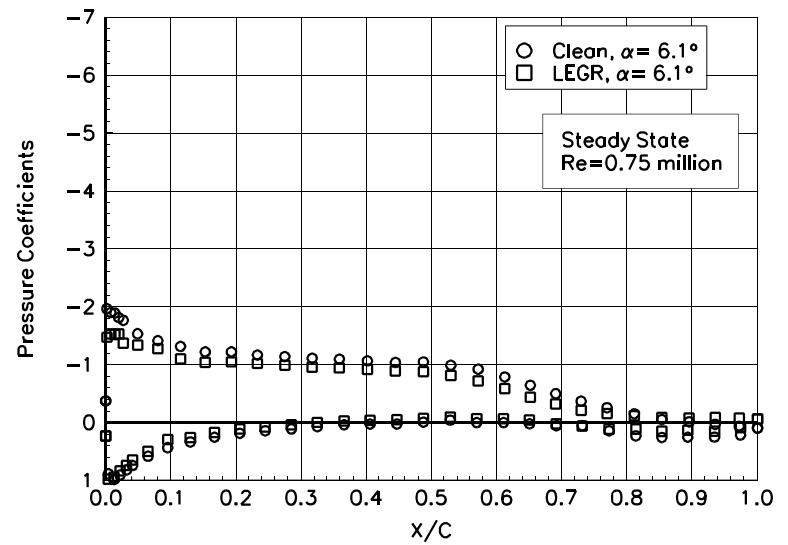


Figure 14. $\alpha = 6.1^\circ$

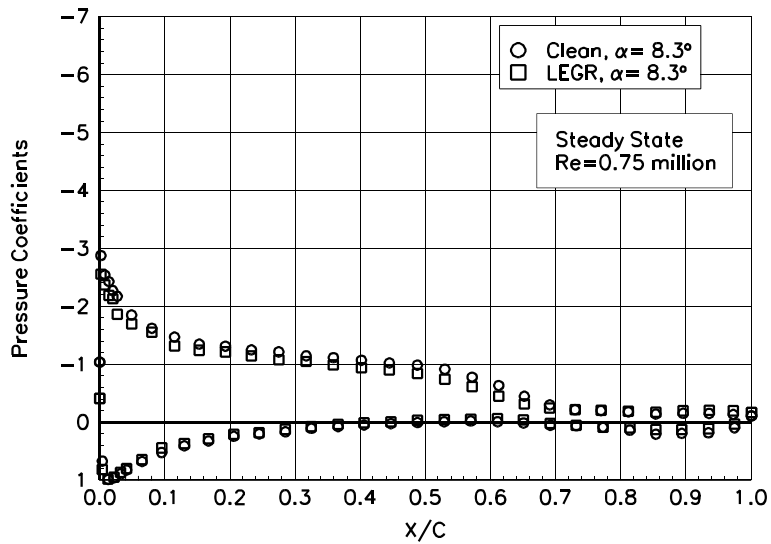


Figure 15. $\alpha = 8.3^\circ$

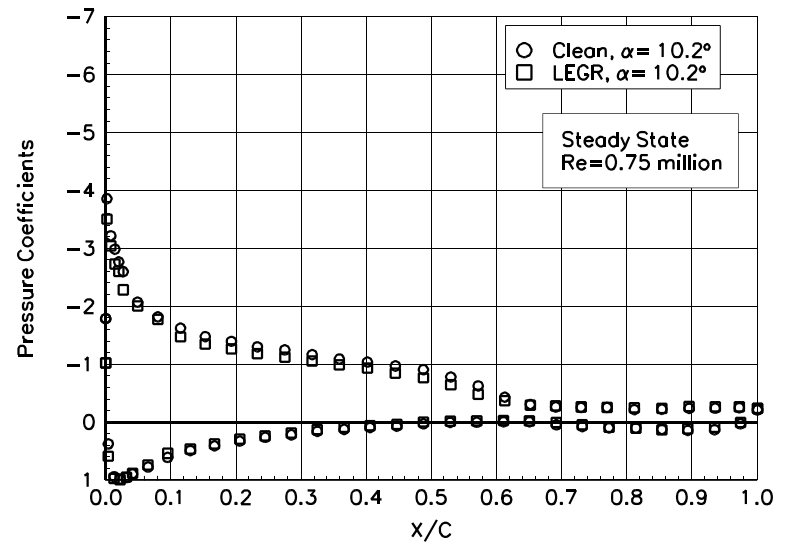


Figure 16. $\alpha = 10.2^\circ$

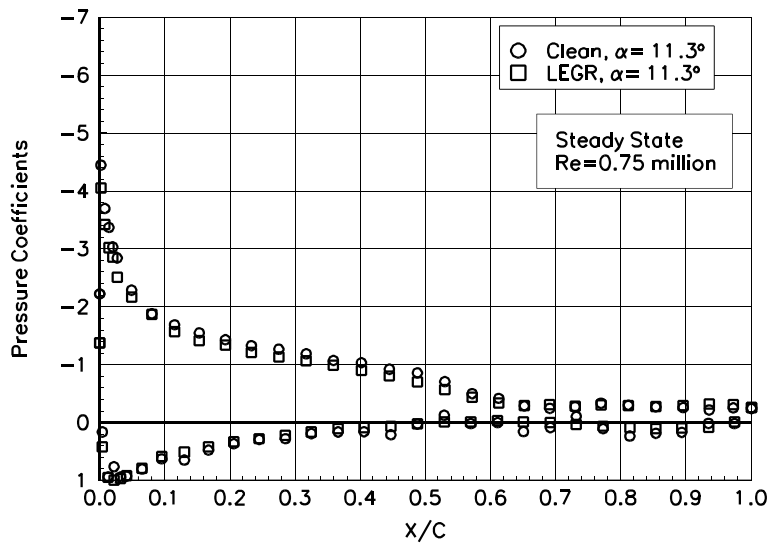


Figure 17. $\alpha = 11.3^\circ$

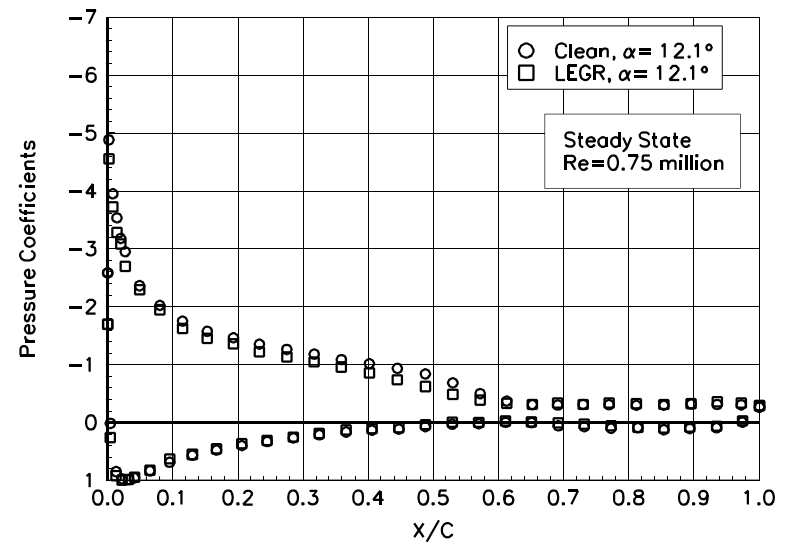


Figure 18. $\alpha = 12.1^\circ$

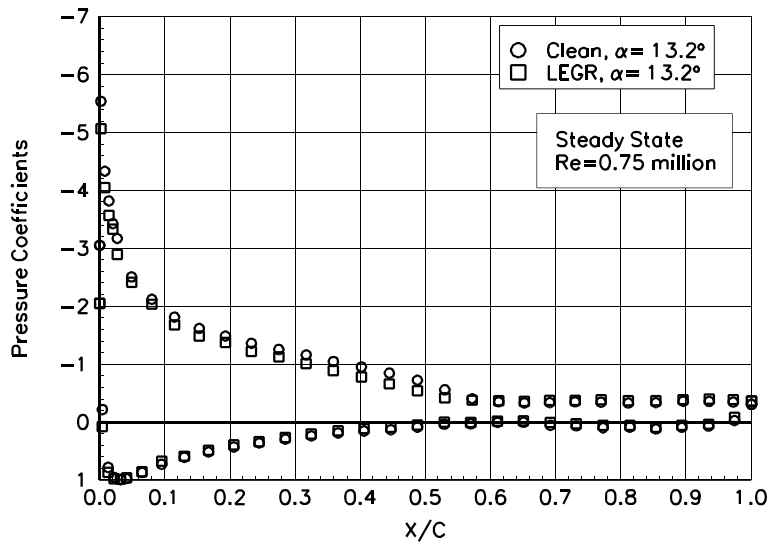


Figure 19. $\alpha = 13.2^\circ$

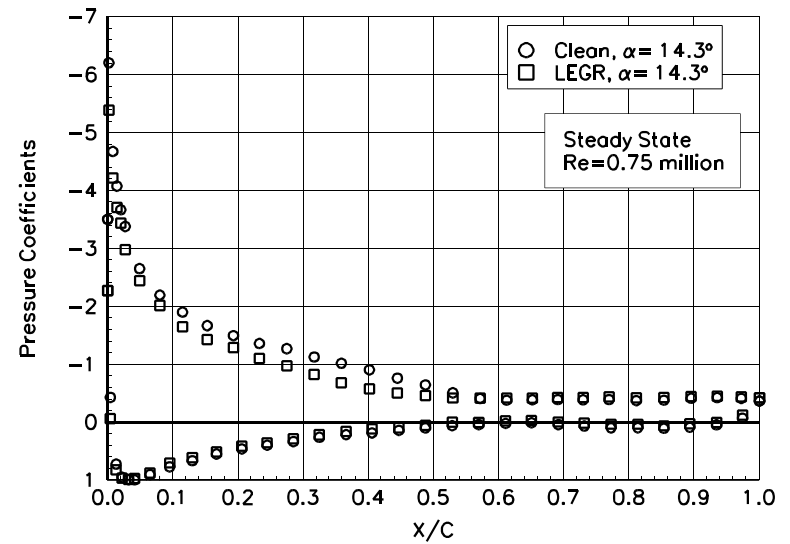


Figure 20. $\alpha = 14.3^\circ$

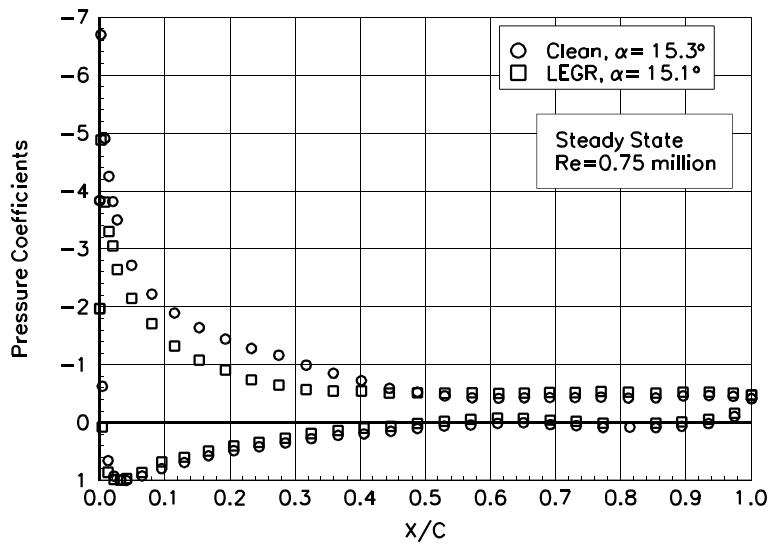


Figure 21. $\alpha = 15.3^\circ$

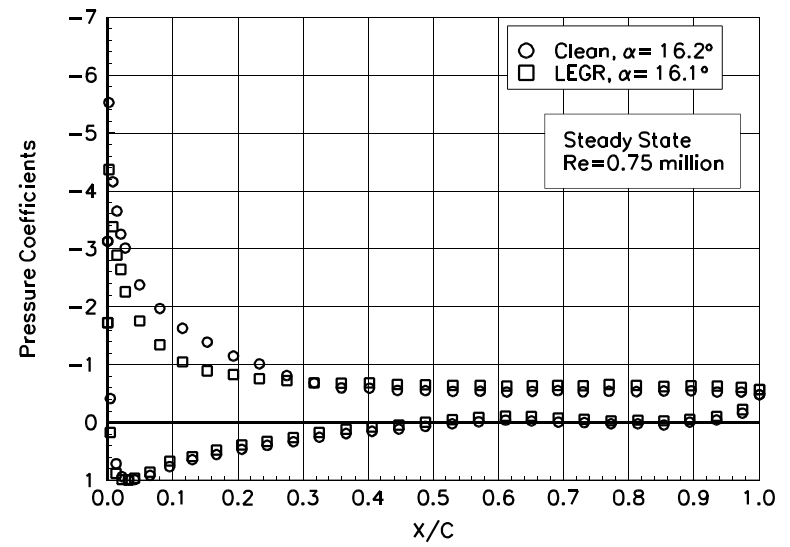


Figure 22. $\alpha = 16.2^\circ$

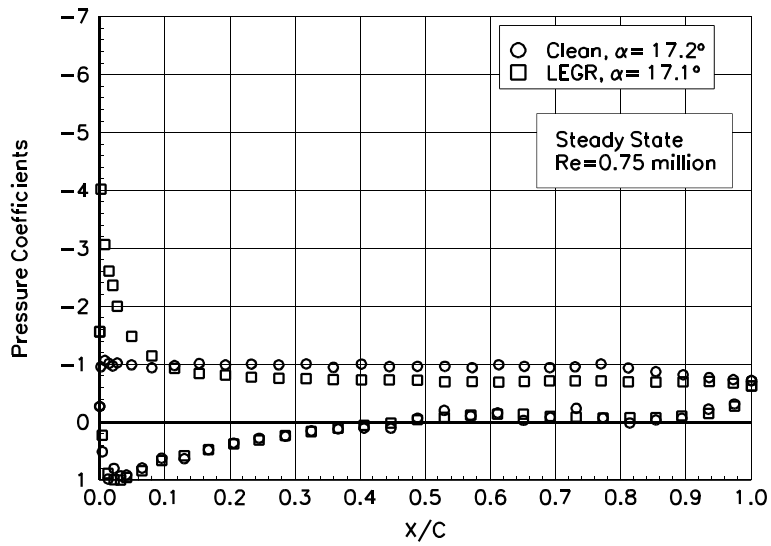


Figure 23. $\alpha = 17.2^\circ$

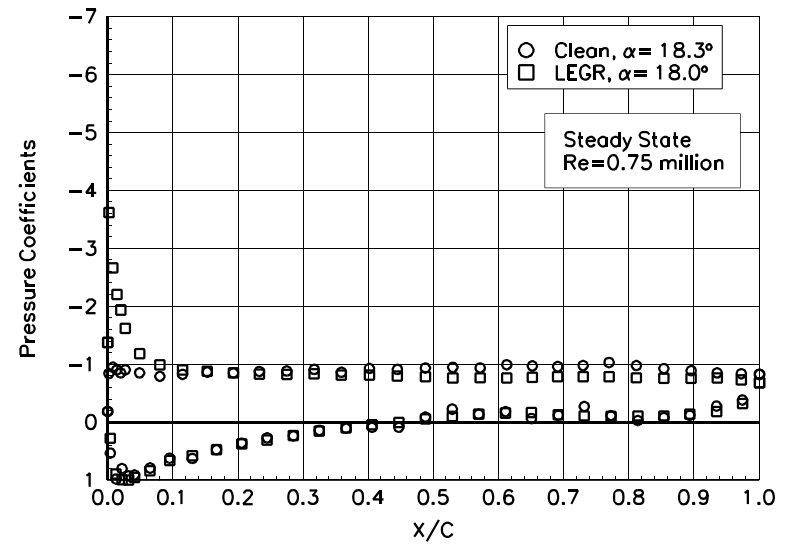


Figure 24. $\alpha = 18.3^\circ$

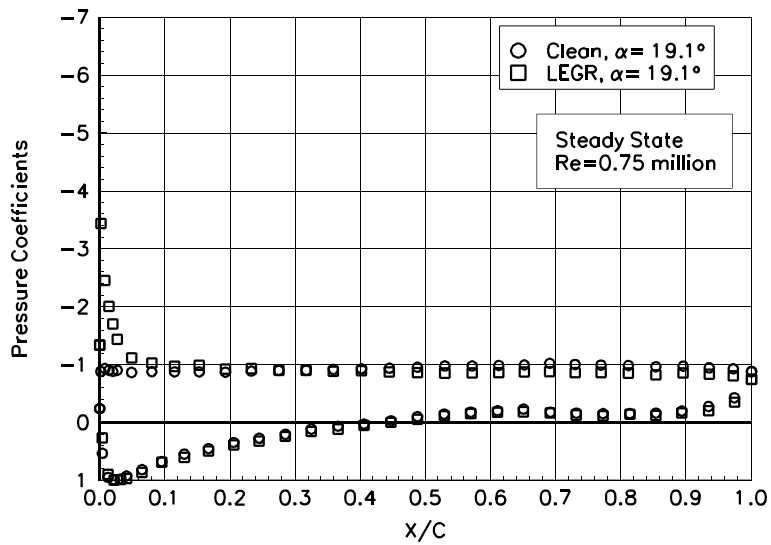


Figure 25. $\alpha = 19.1^\circ$

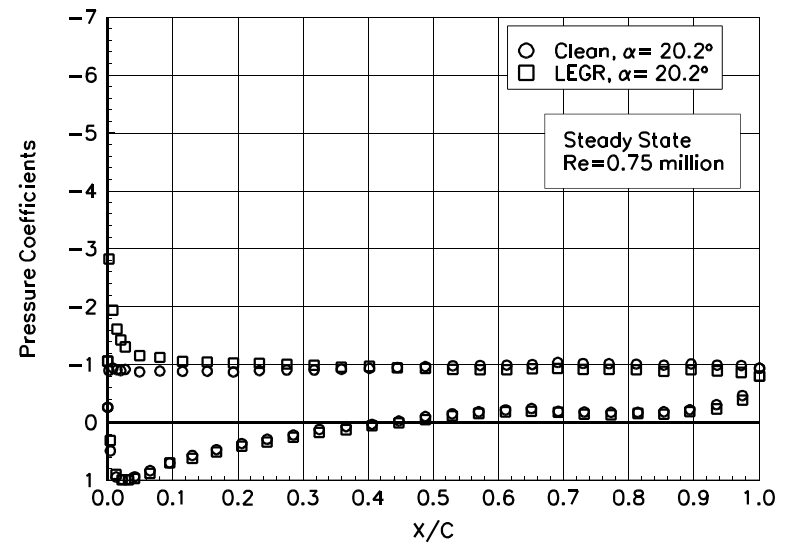


Figure 26. $\alpha = 20.2^\circ$

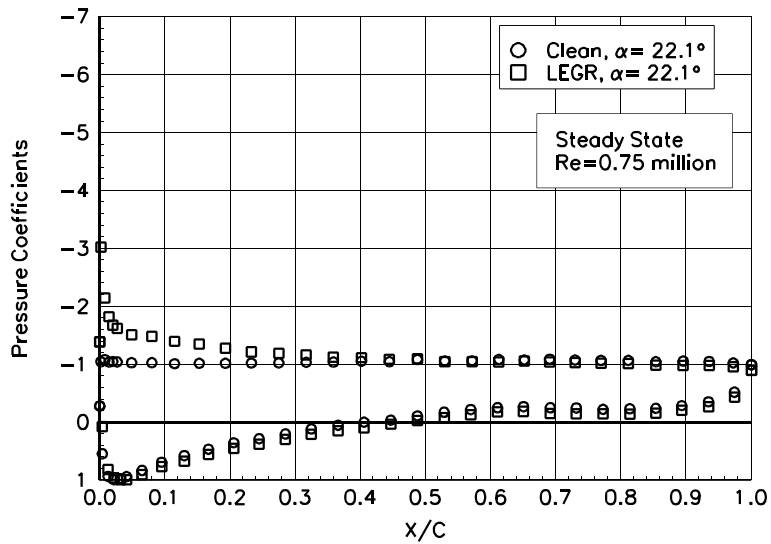


Figure 27. $\alpha = 22.1^\circ$

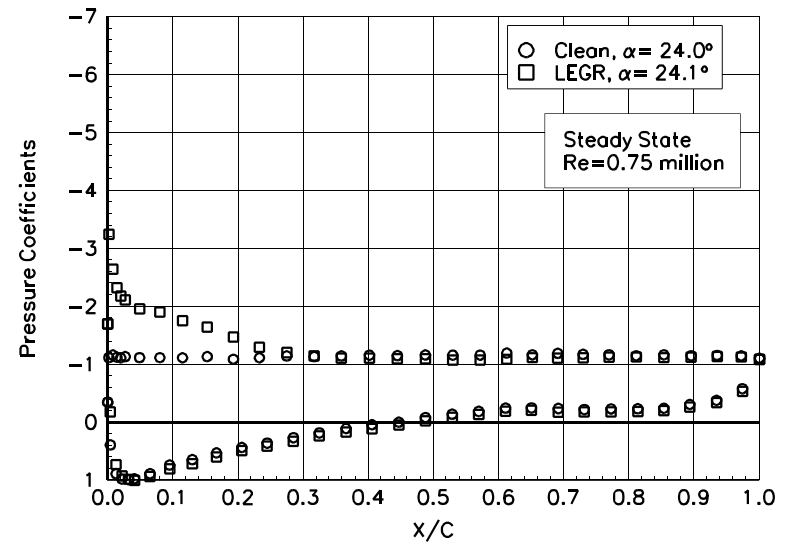


Figure 28. $\alpha = 24.0^\circ$

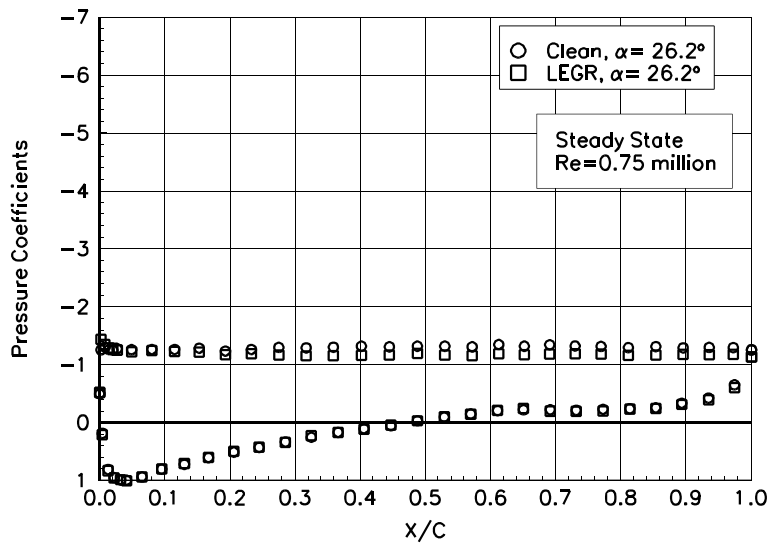


Figure 29. $\alpha = 26.2^\circ$

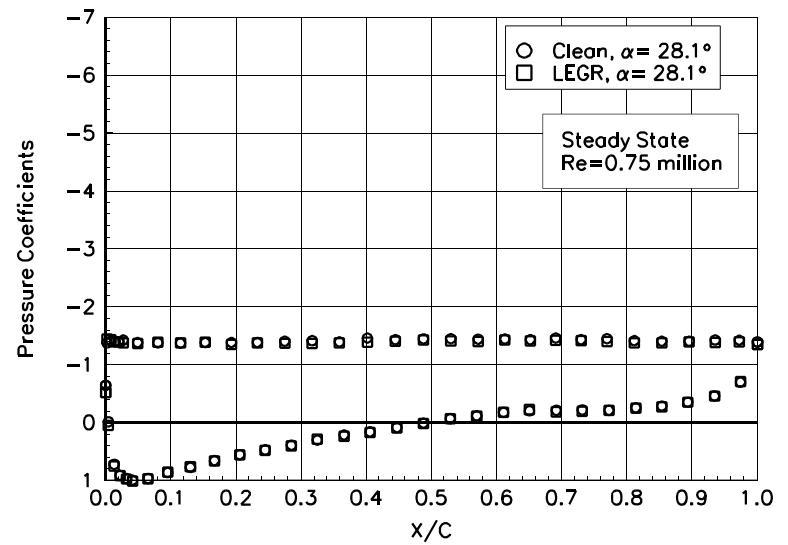


Figure 30. $\alpha = 28.1^\circ$

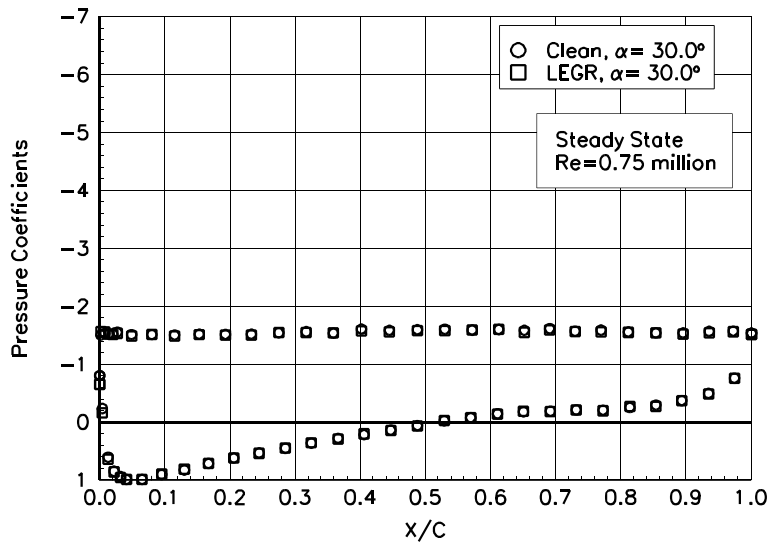


Figure 31. $\alpha = 30.0^\circ$

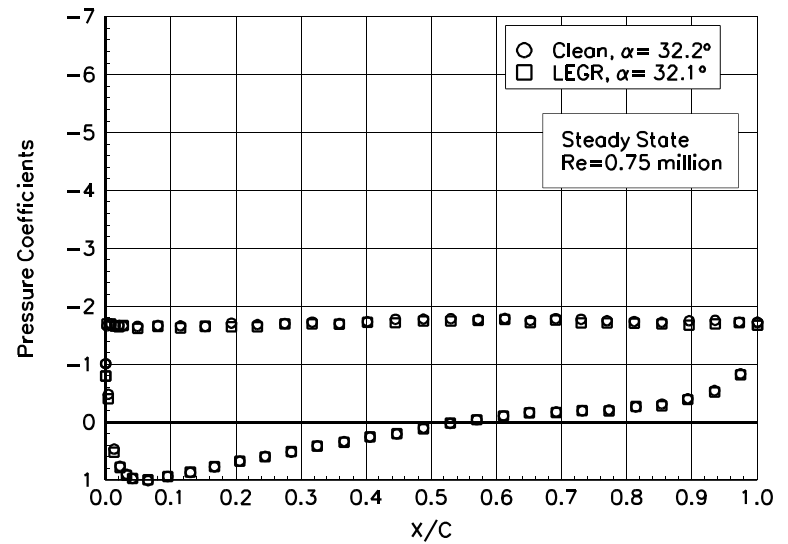


Figure 32. $\alpha = 32.2^\circ$

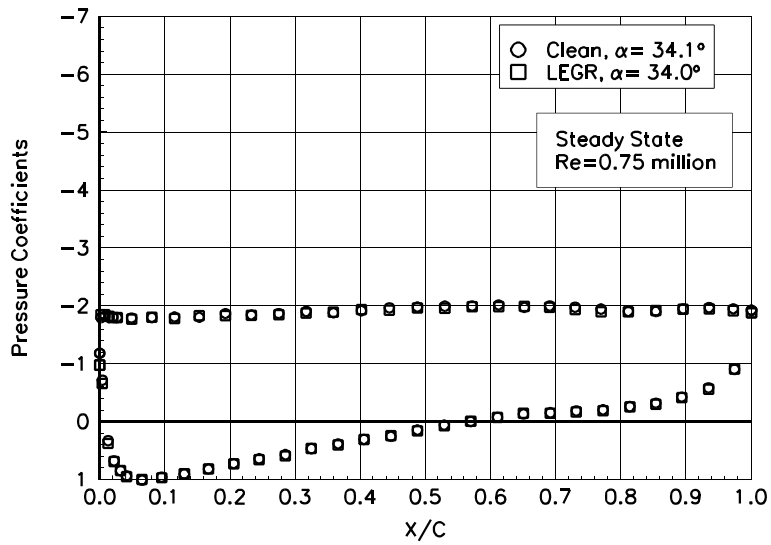


Figure 33. $\alpha = 34.1^\circ$

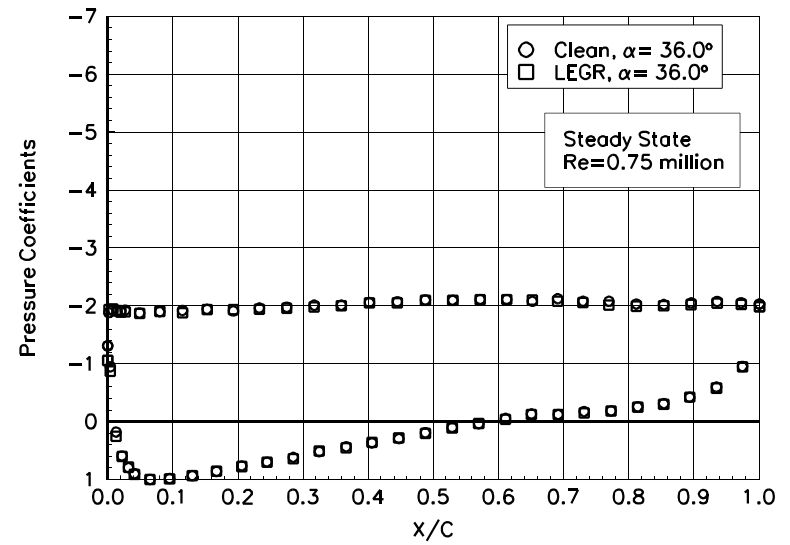


Figure 34. $\alpha = 36.0^\circ$

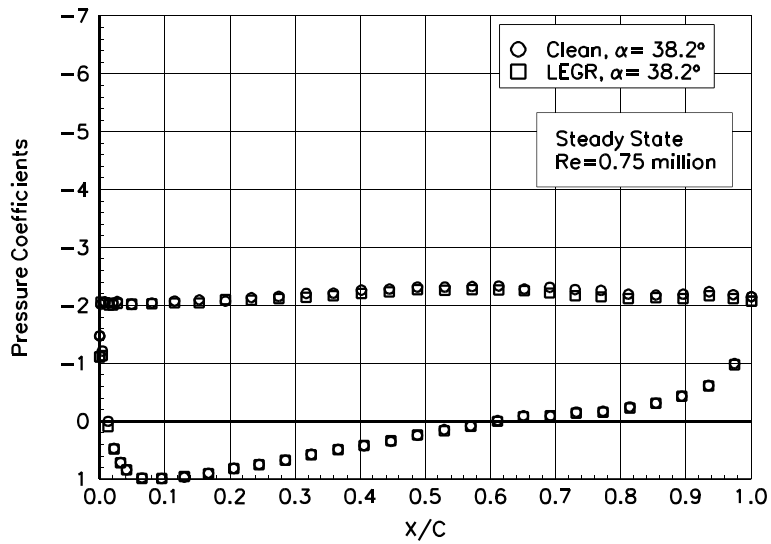


Figure 35. $\alpha = 38.2^\circ$

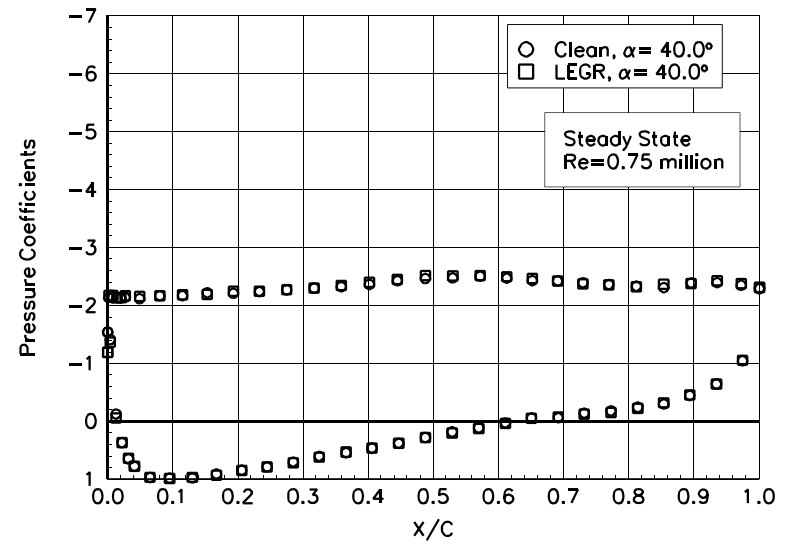


Figure 36. $\alpha = 40.0^\circ$

S813

Pressure Distributions, Steady State, Re = 1 million

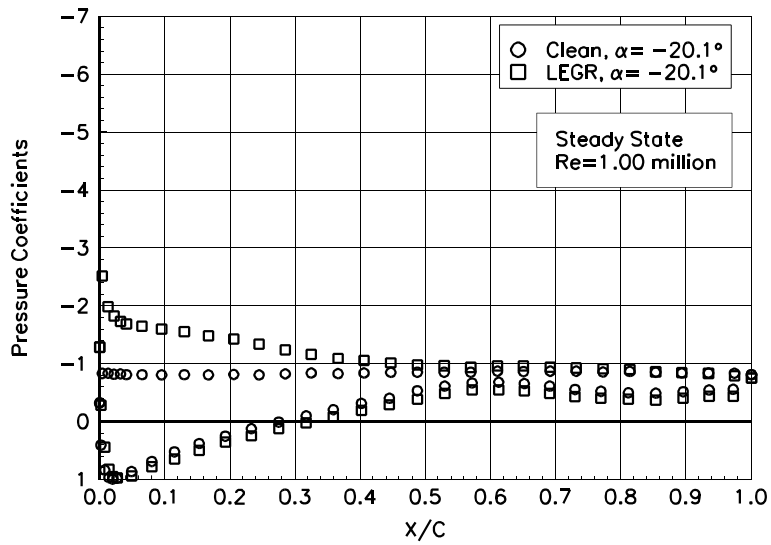


Figure 37. $\alpha = -20.1^\circ$

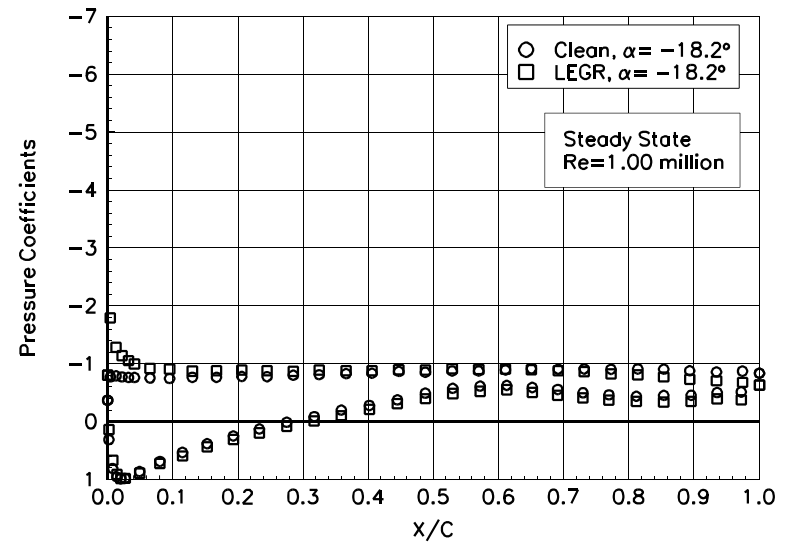


Figure 38. $\alpha = -18.2^\circ$

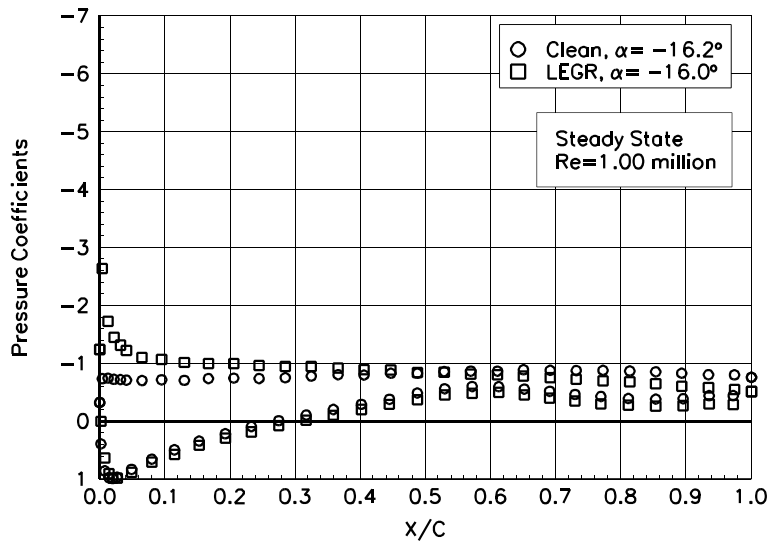


Figure 39. $\alpha = -16.2^\circ$

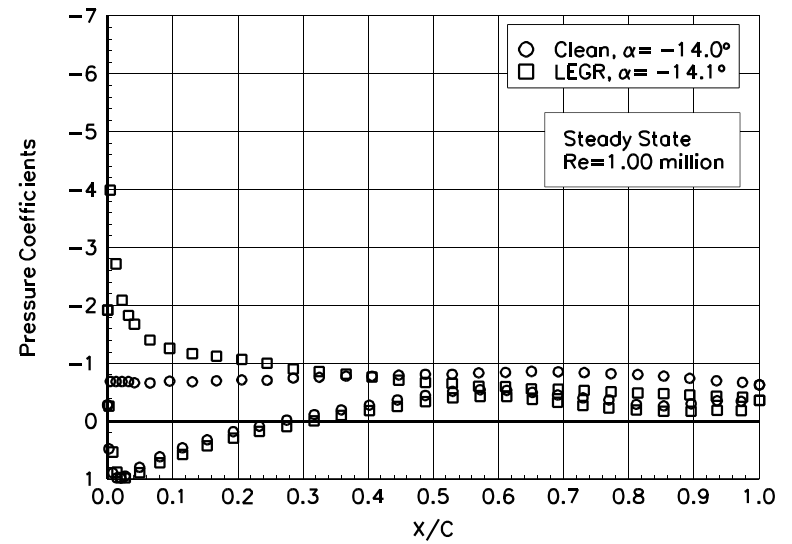


Figure 40. $\alpha = -14.0^\circ$

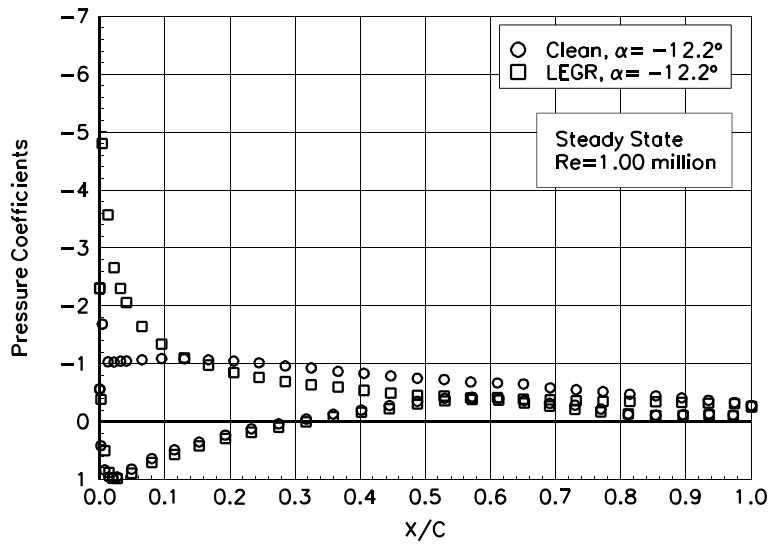


Figure 41. $\alpha = -12.2^\circ$

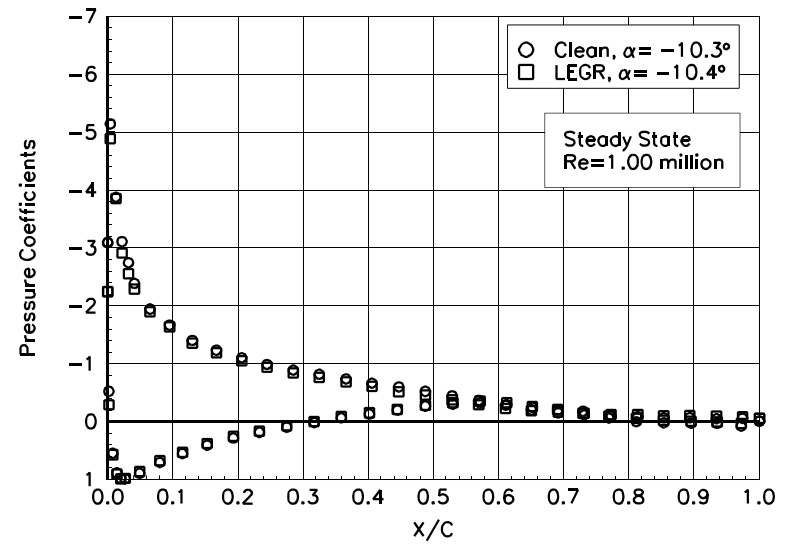


Figure 42. $\alpha = -10.3^\circ$

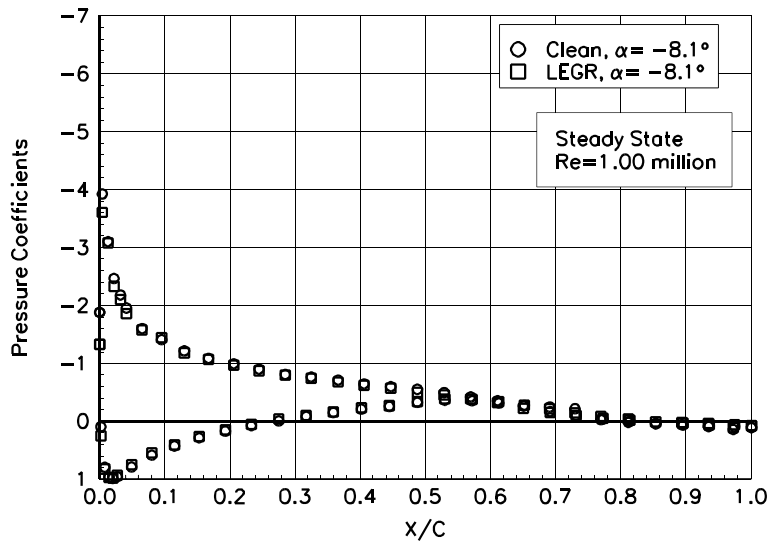


Figure 43. $\alpha = -8.1^\circ$

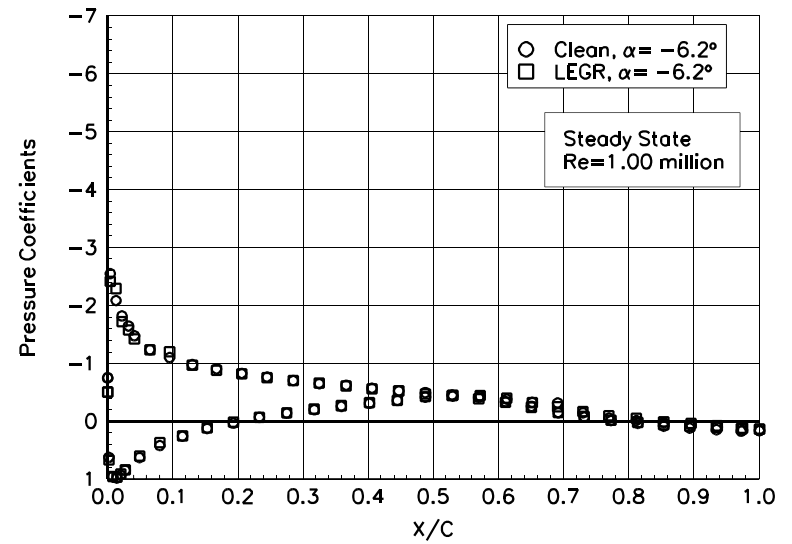


Figure 44. $\alpha = -6.2^\circ$

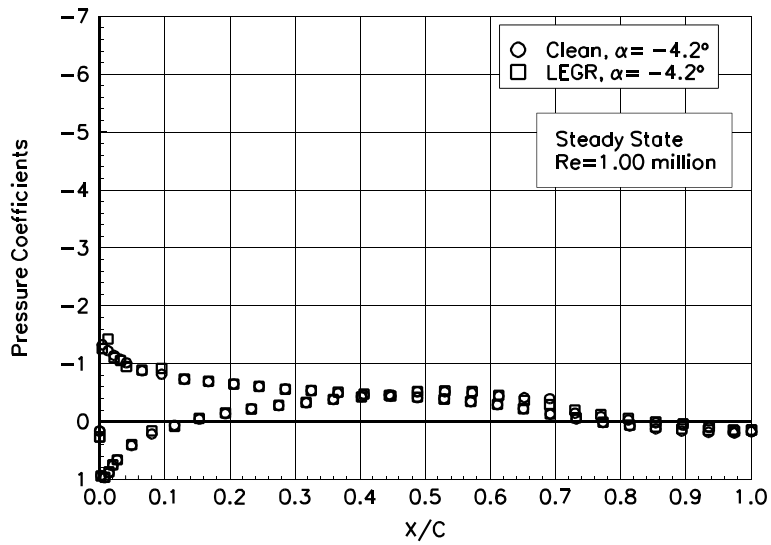


Figure 45. $\alpha = -4.2^\circ$

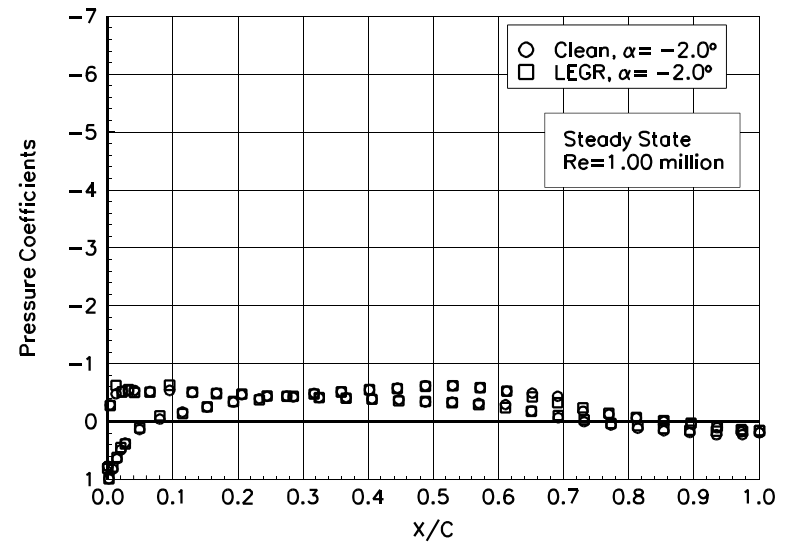


Figure 46. $\alpha = -2.0^\circ$

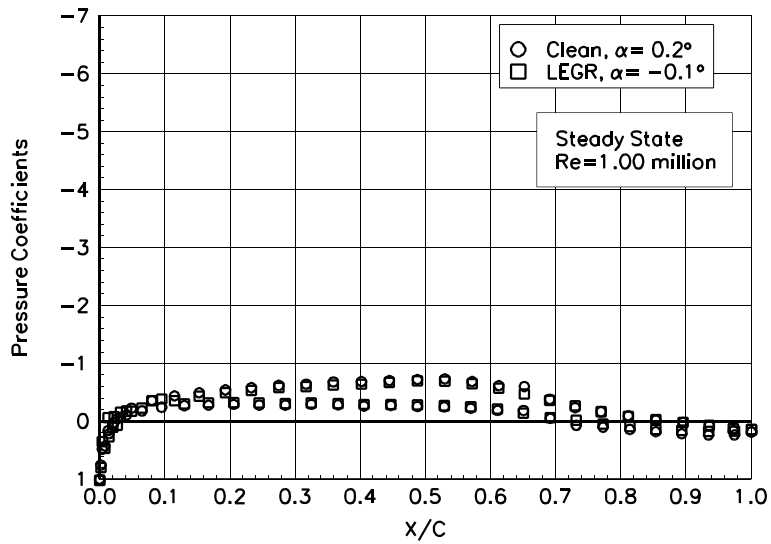


Figure 47. $\alpha = 0.2^\circ$

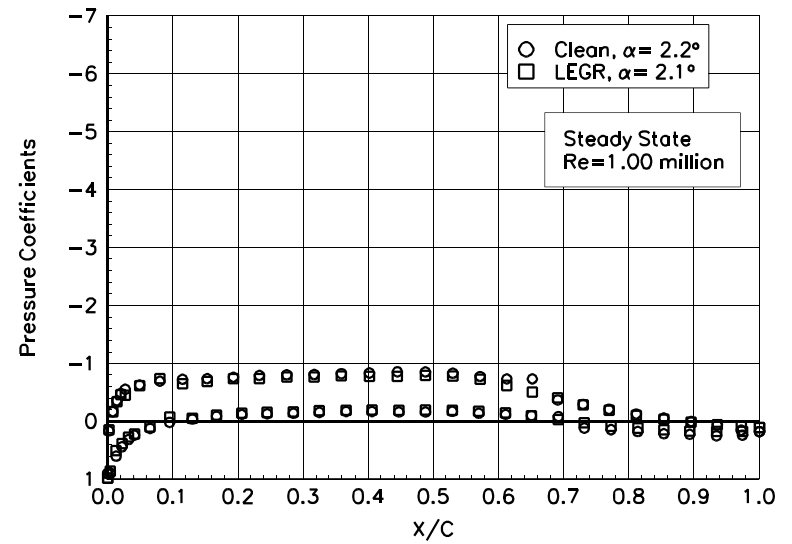


Figure 48. $\alpha = 2.2^\circ$

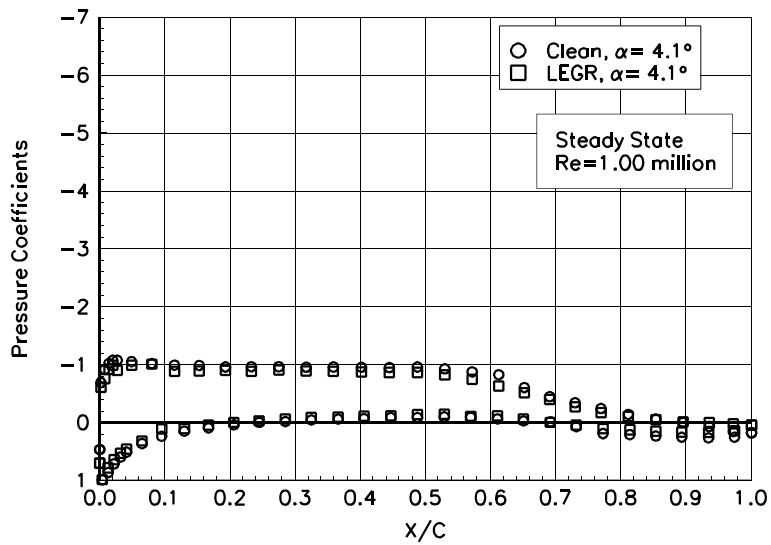


Figure 49. $\alpha = 4.1^\circ$

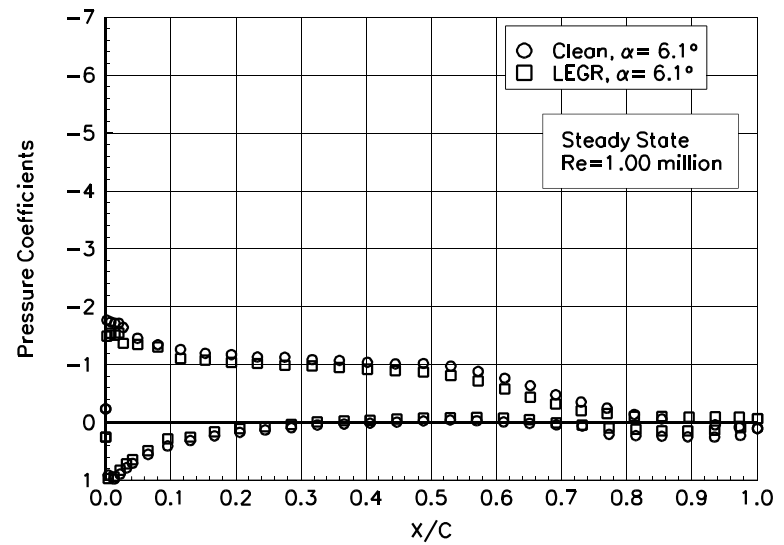


Figure 50. $\alpha = 6.1^\circ$

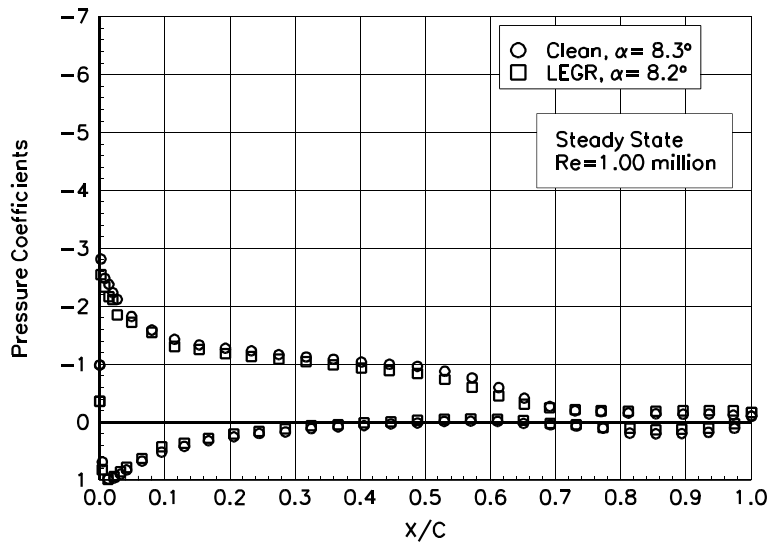


Figure 51. $\alpha = 8.3^\circ$

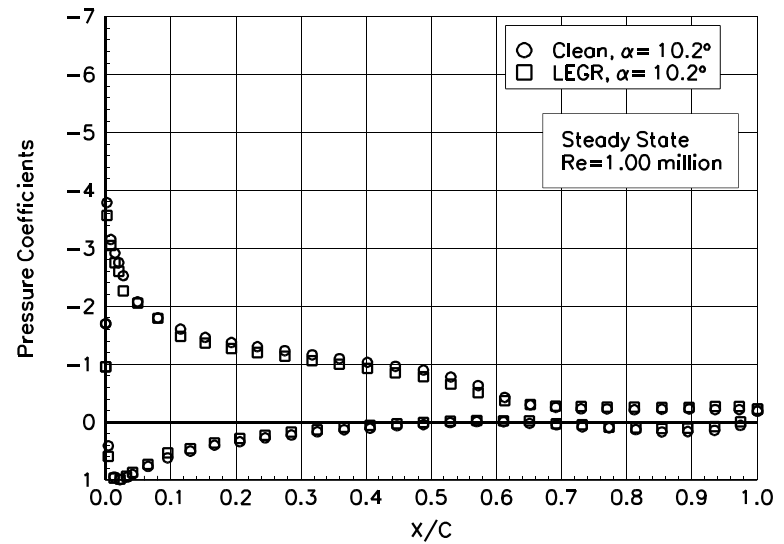


Figure 52. $\alpha = 10.2^\circ$

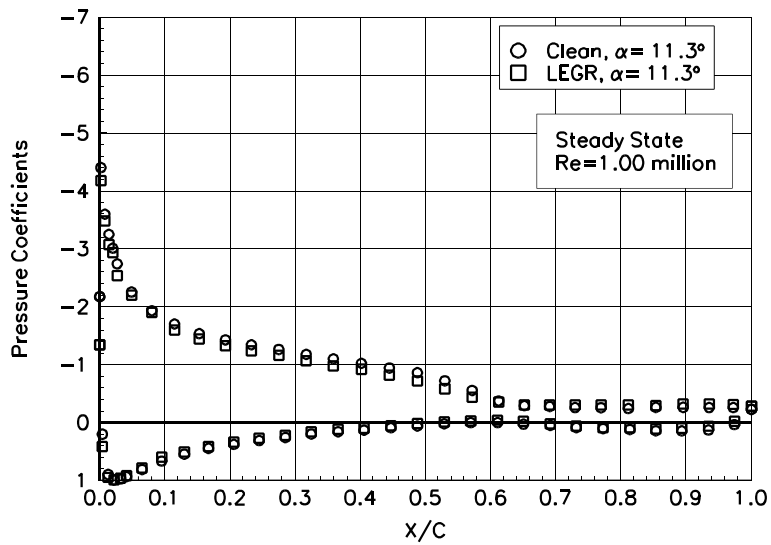


Figure 53. $\alpha = 11.3^\circ$

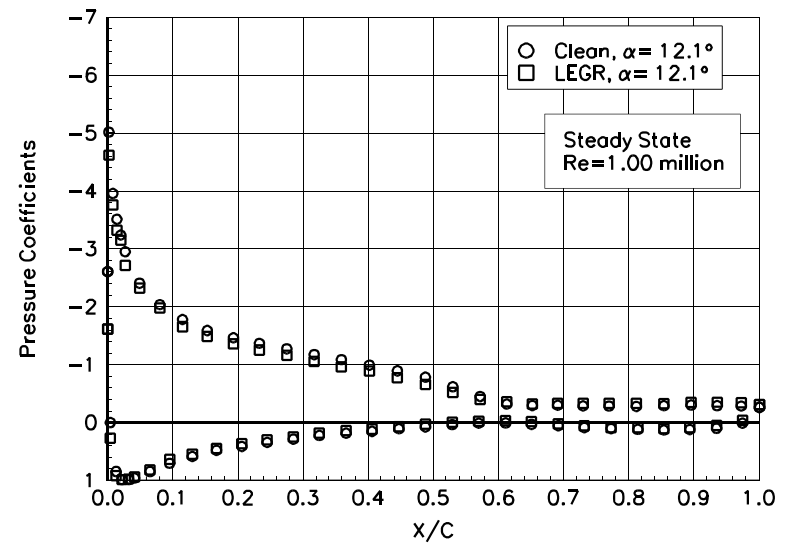


Figure 54. $\alpha = 12.1^\circ$

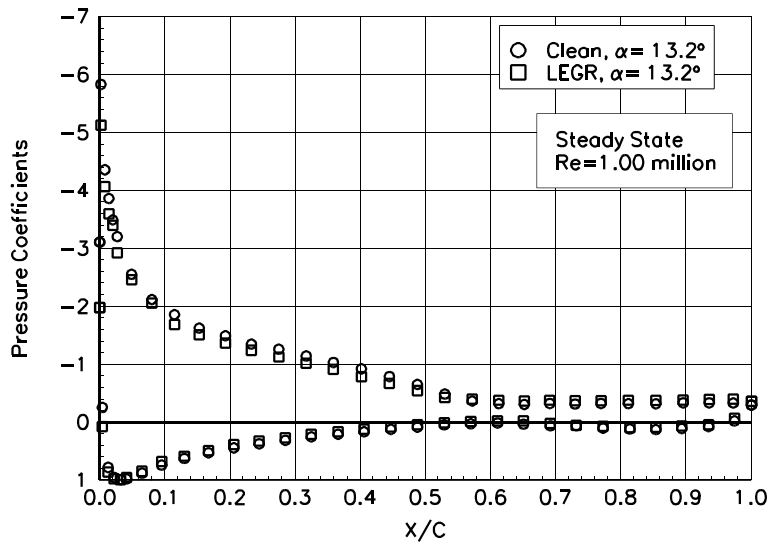


Figure 55. $\alpha = 13.2^\circ$

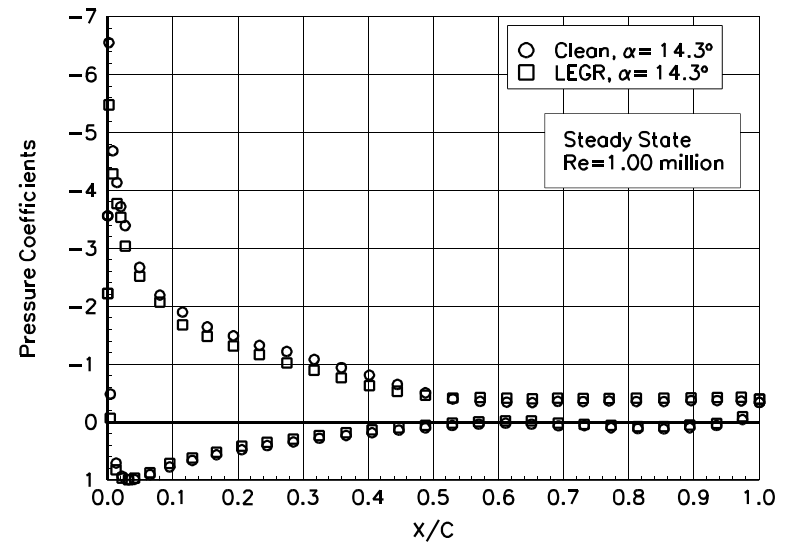


Figure 56. $\alpha = 14.3^\circ$

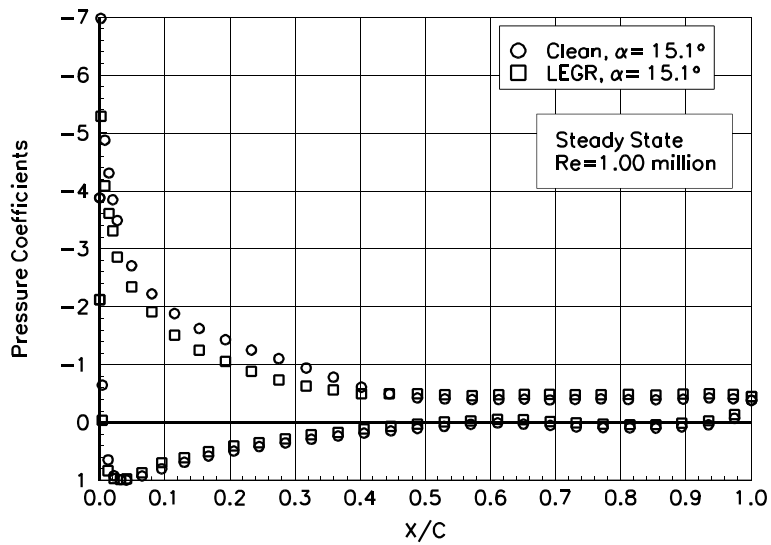


Figure 57. $\alpha = 15.1^\circ$

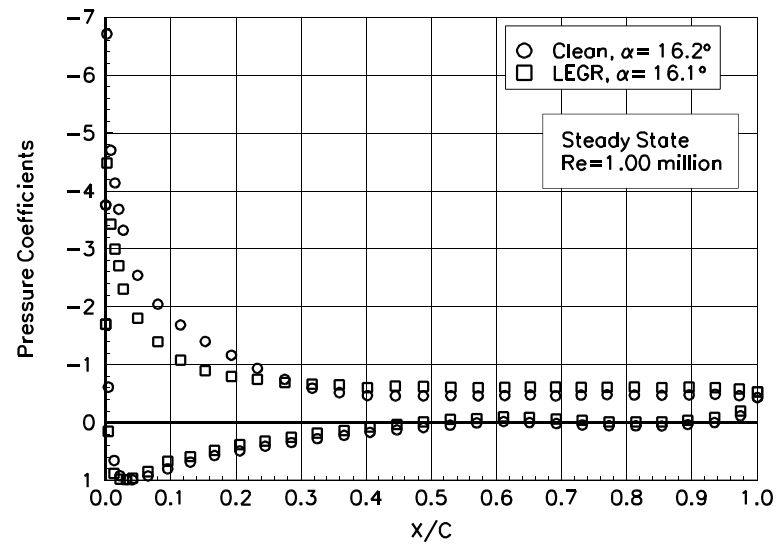


Figure 58. $\alpha = 16.2^\circ$

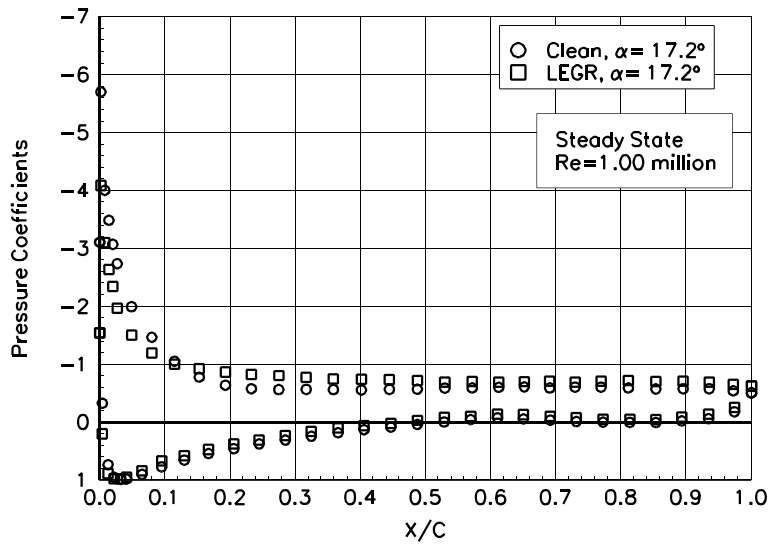


Figure 59. $\alpha = 17.2^\circ$

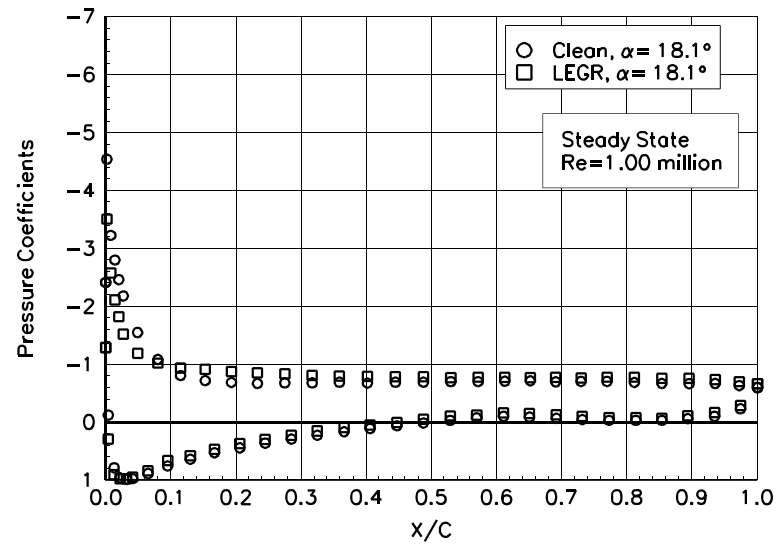


Figure 60. $\alpha = 18.1^\circ$

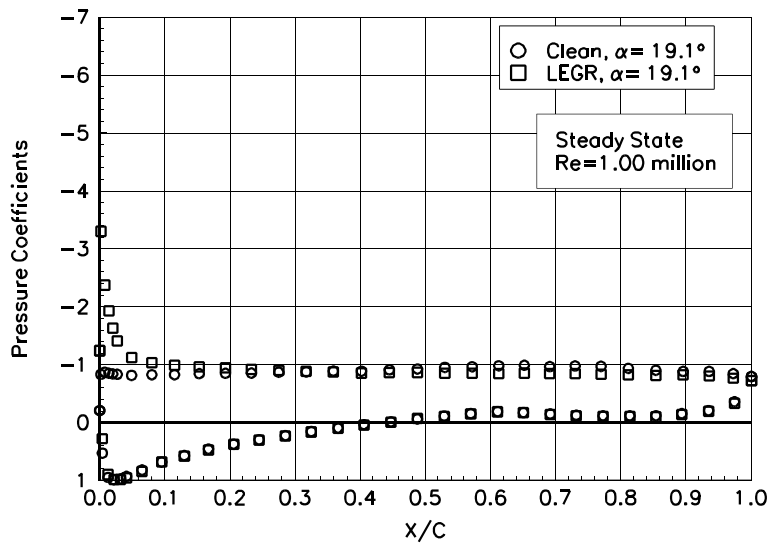


Figure 61. $\alpha = 19.1^\circ$

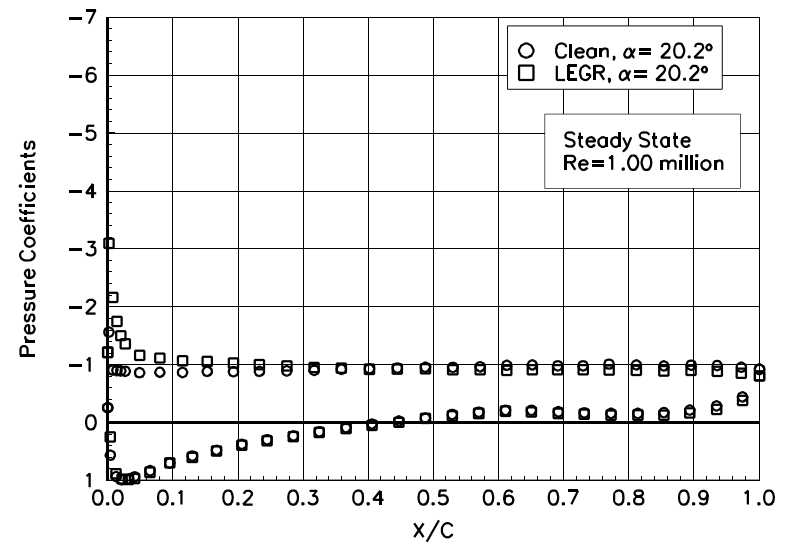


Figure 62. $\alpha = 20.2^\circ$

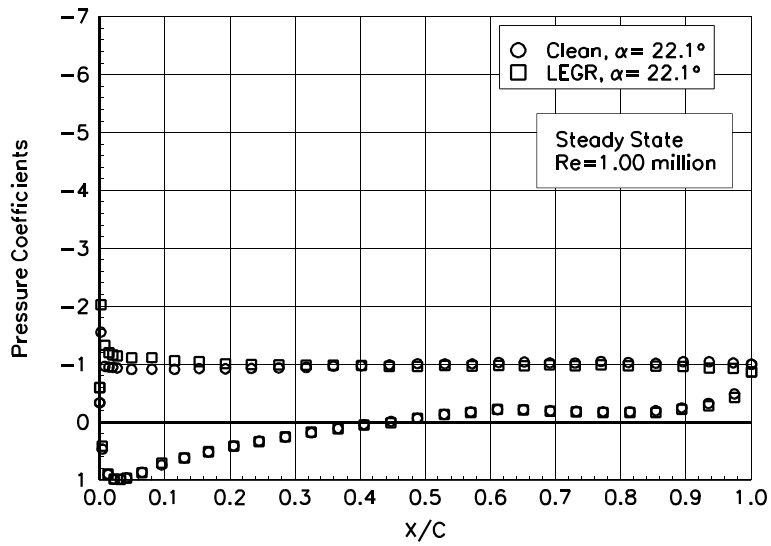


Figure 63. $\alpha = 22.1^\circ$

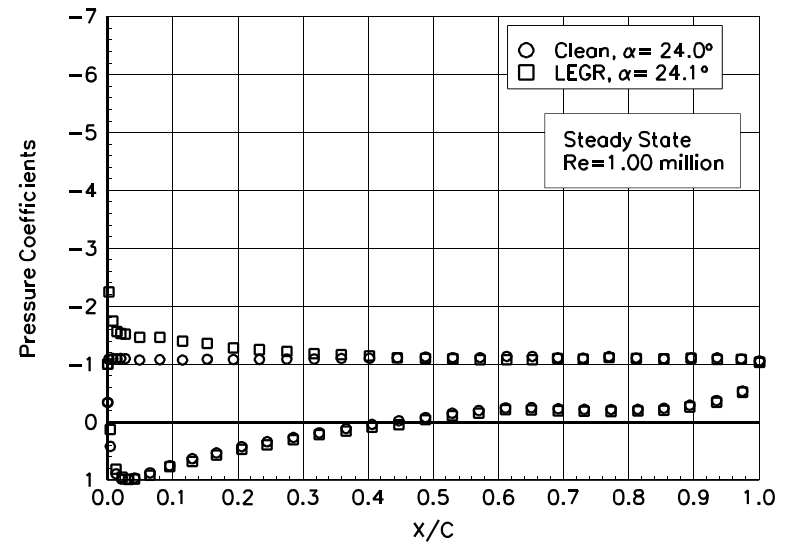


Figure 64. $\alpha = 24.0^\circ$

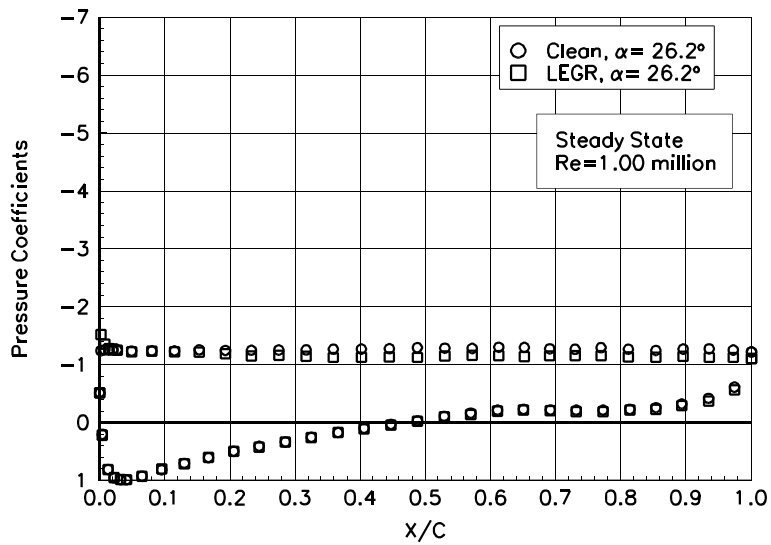


Figure 65. $\alpha = 26.2^\circ$

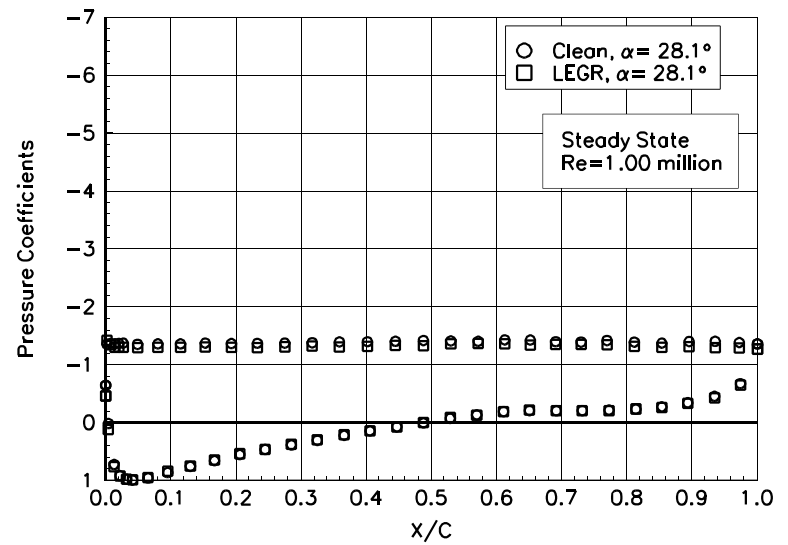


Figure 66. $\alpha = 28.1^\circ$

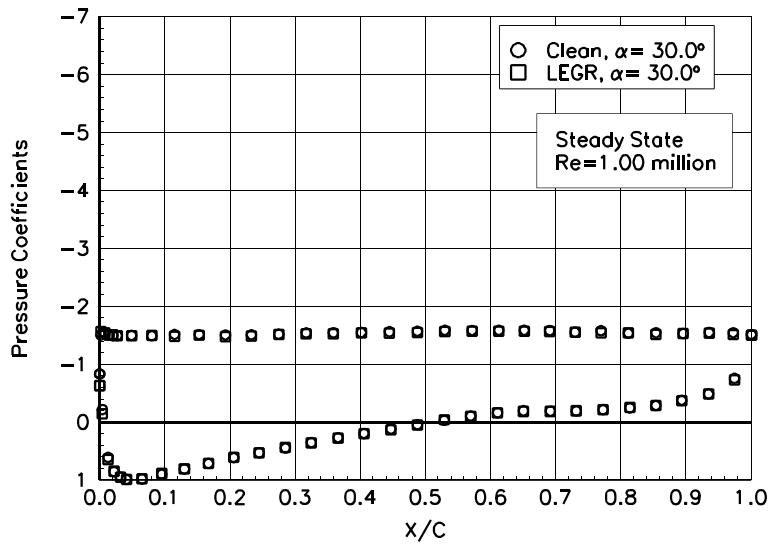


Figure 67. $\alpha = 30.0^\circ$

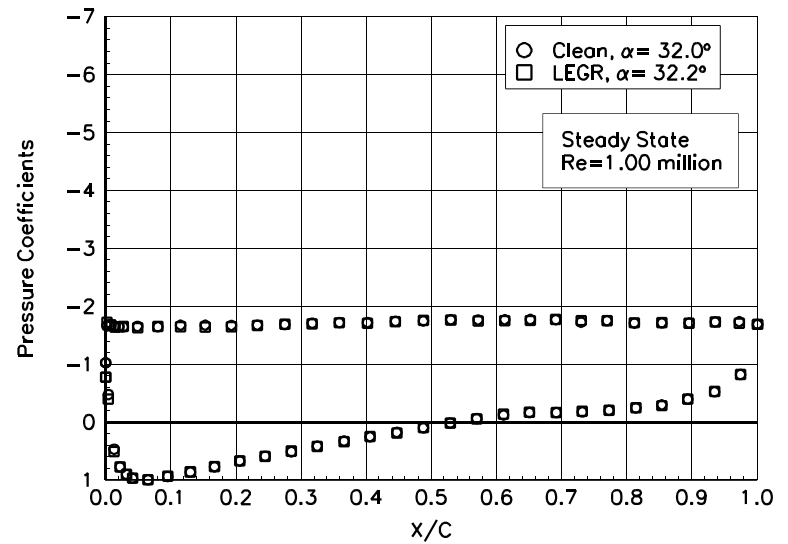


Figure 68. $\alpha = 32.0^\circ$

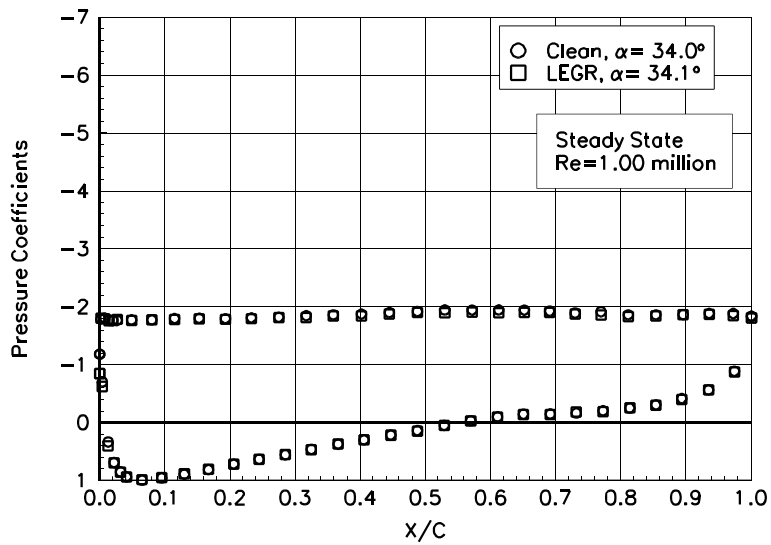


Figure 69. $\alpha = 34.0^\circ$

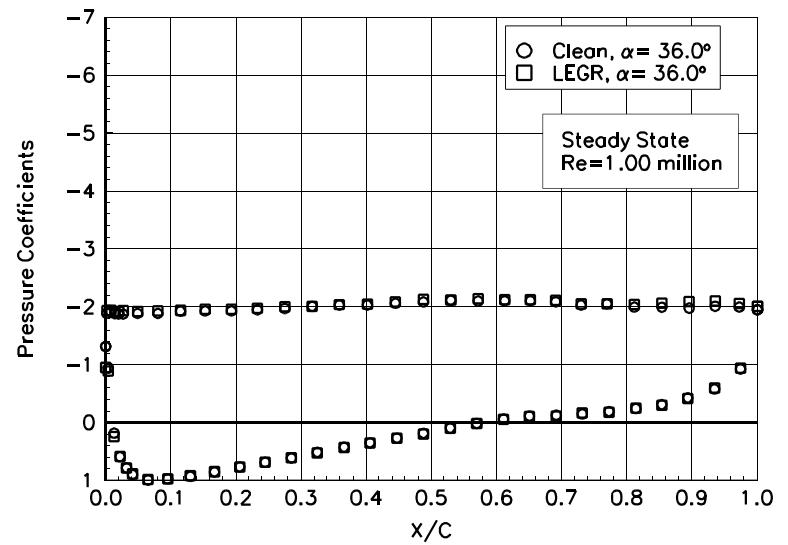


Figure 70. $\alpha = 36.0^\circ$

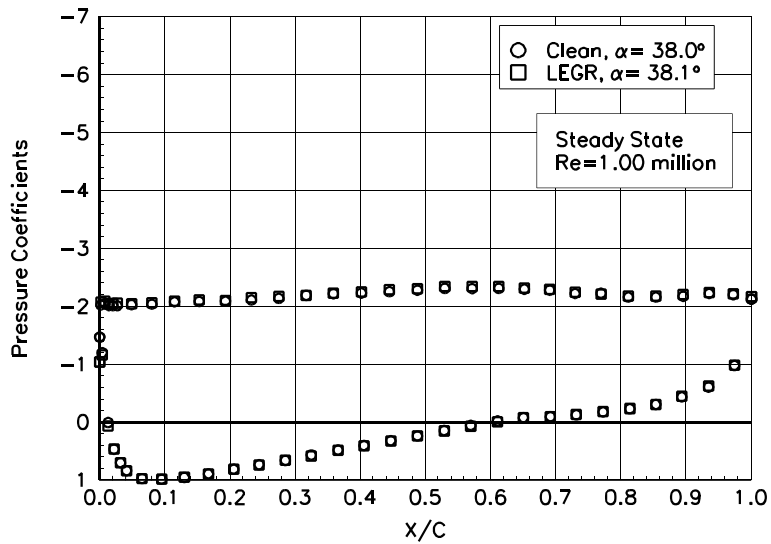


Figure 71. $\alpha = 38.0^\circ$

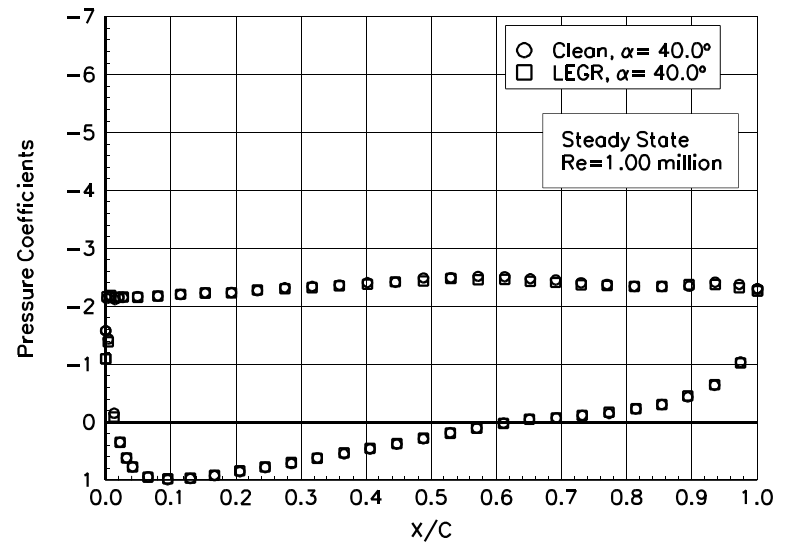


Figure 72. $\alpha = 40.0^\circ$

S813

Pressure Distributions, Steady State, Re = 1.25 million

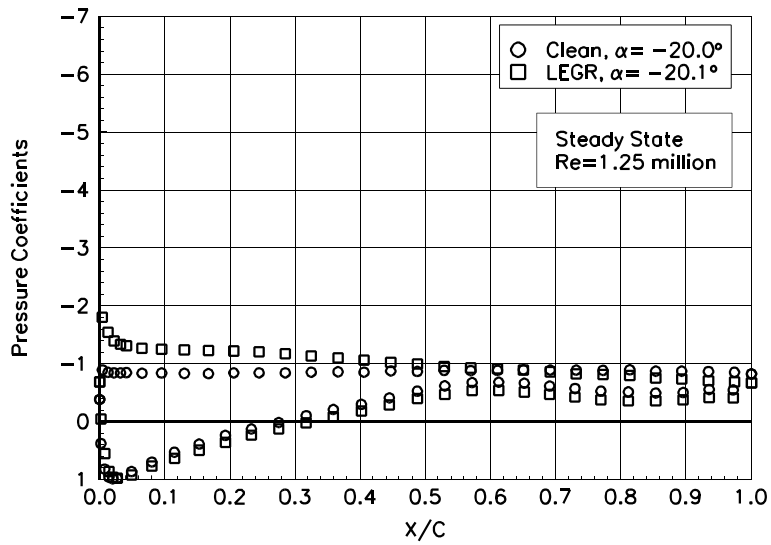


Figure 73. $\alpha = -20.0^\circ$

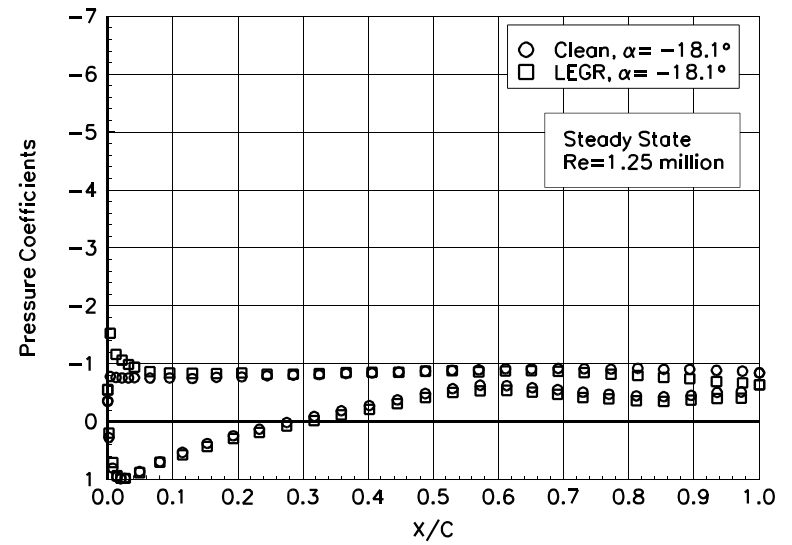


Figure 74. $\alpha = -18.1^\circ$

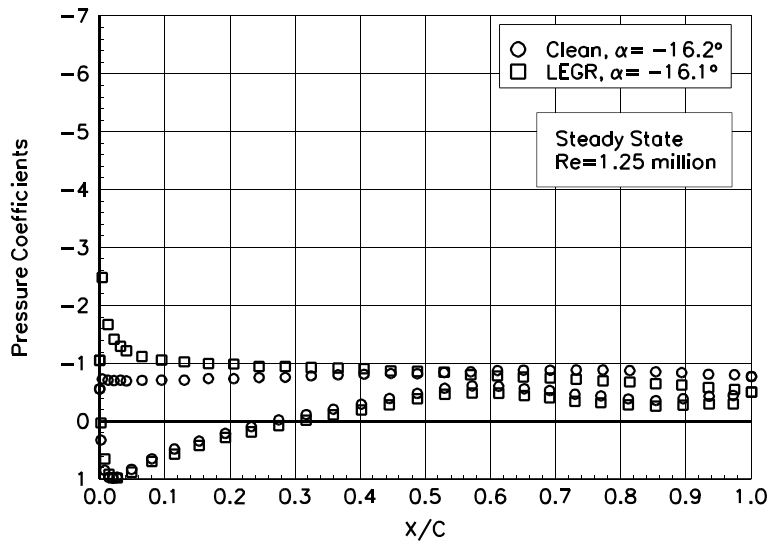


Figure 75. $\alpha = -16.2^\circ$

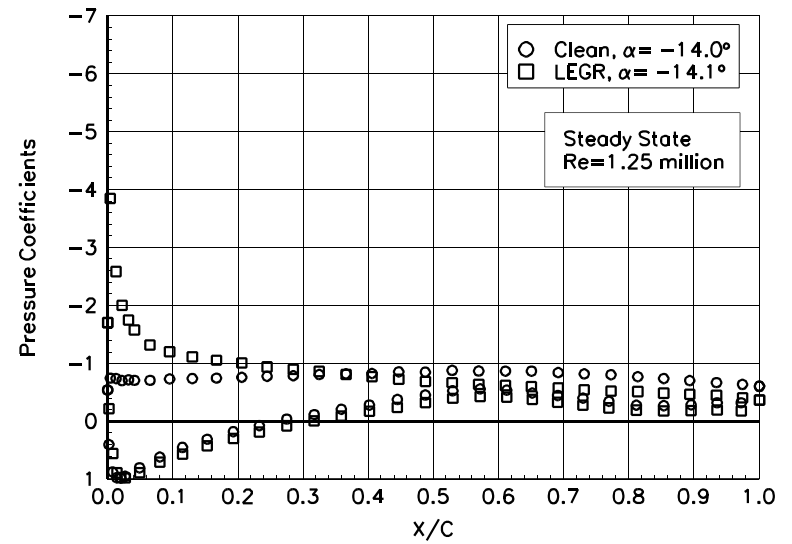


Figure 76. $\alpha = -14.0^\circ$

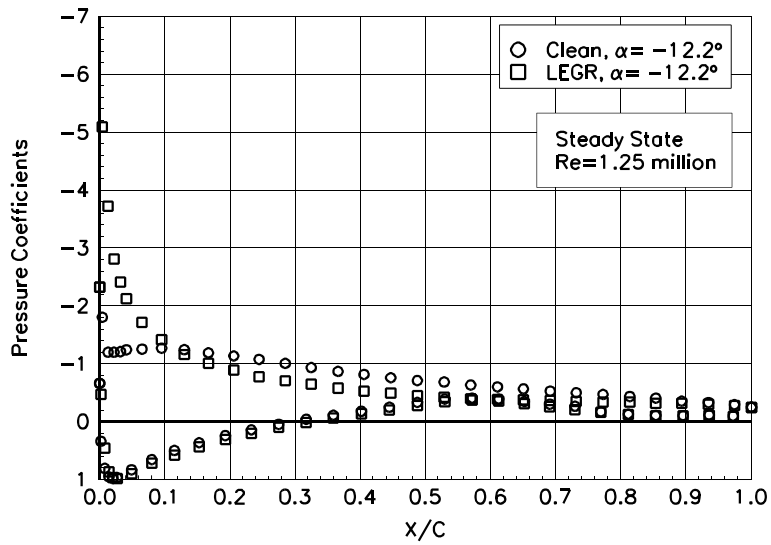


Figure 77. $\alpha = -12.2^\circ$

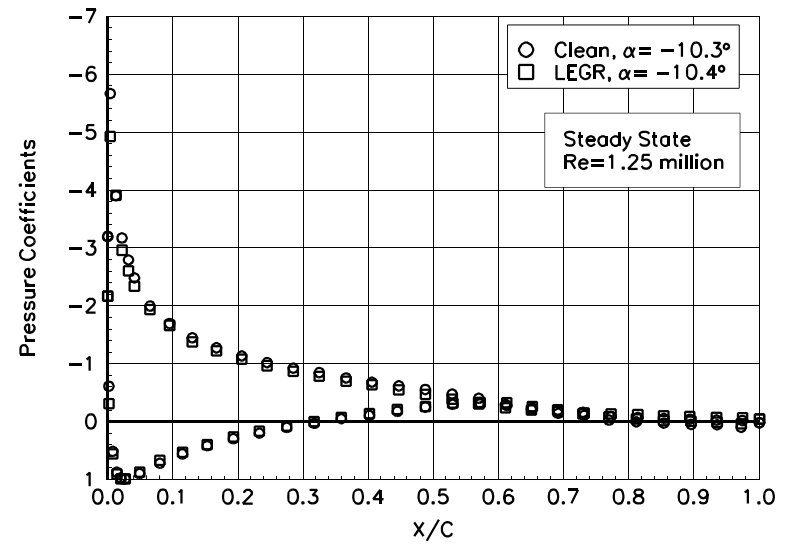


Figure 78. $\alpha = -10.3^\circ$

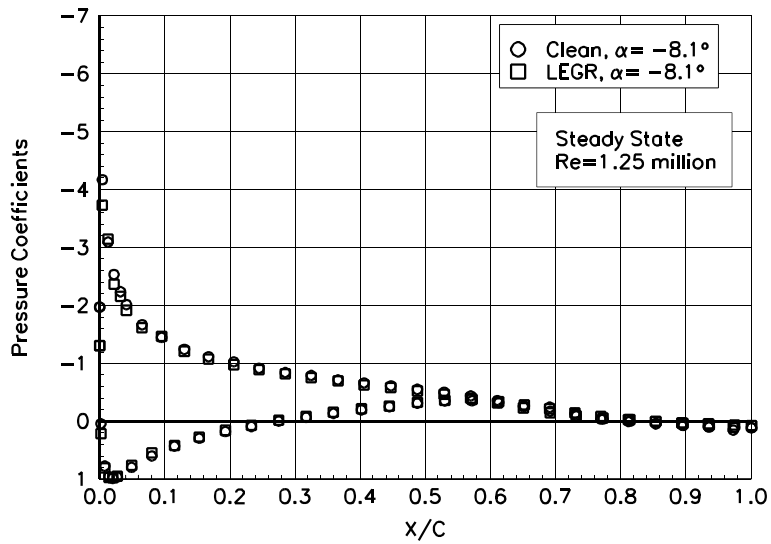


Figure 79. $\alpha = -8.1^\circ$

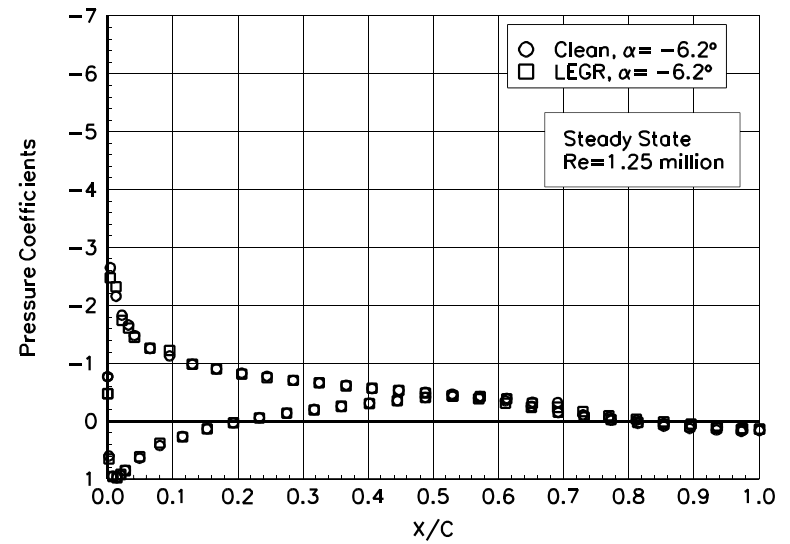


Figure 80. $\alpha = -6.2^\circ$

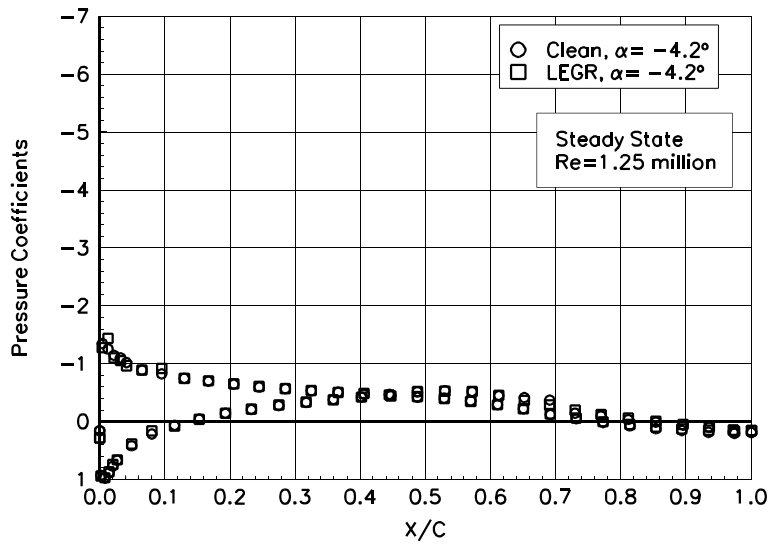


Figure 81. $\alpha = -4.2^\circ$

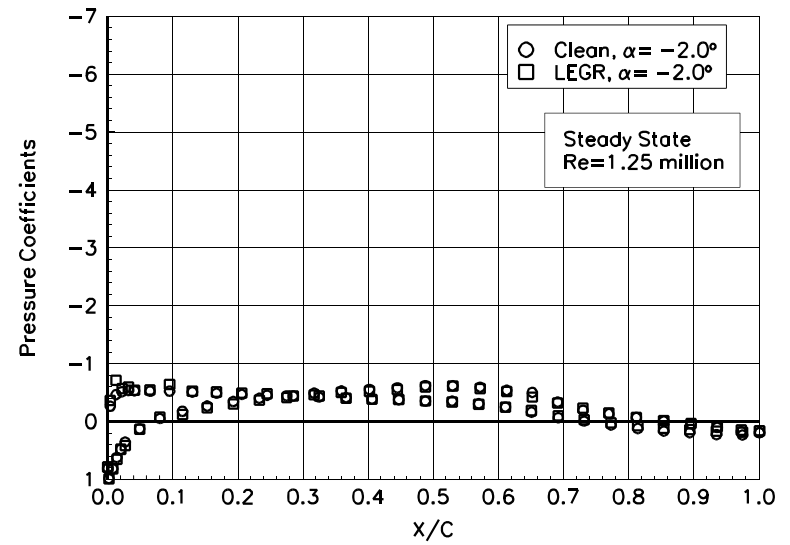


Figure 82. $\alpha = -2.0^\circ$

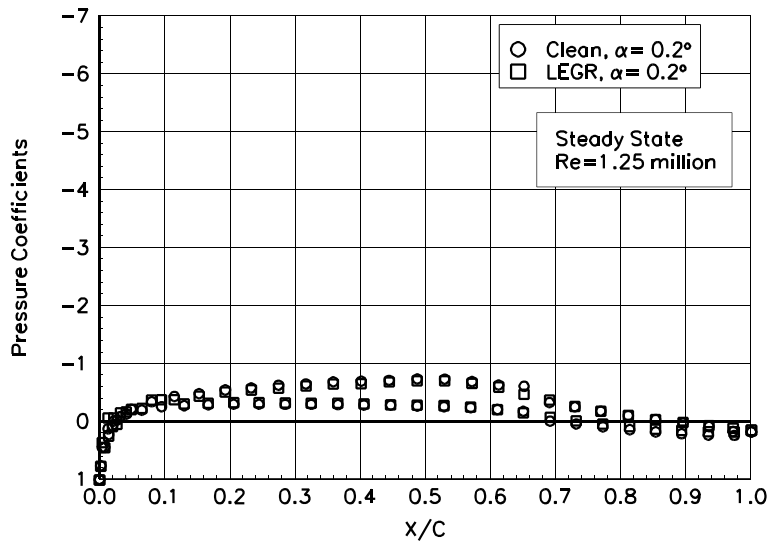


Figure 83. $\alpha = 0.2^\circ$

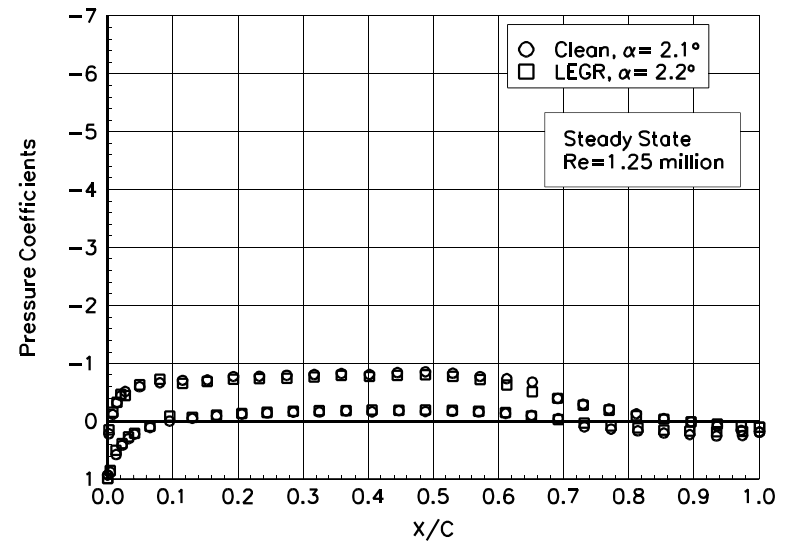


Figure 84. $\alpha = 2.1^\circ$

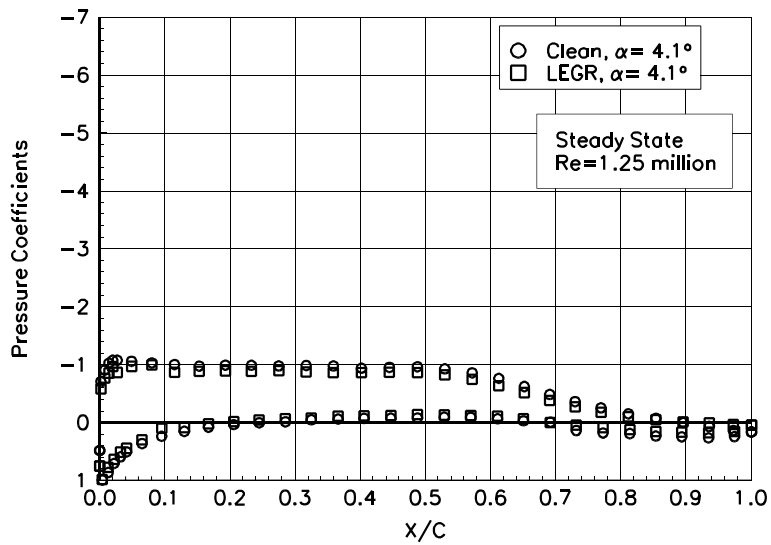


Figure 85. $\alpha = 4.1^\circ$

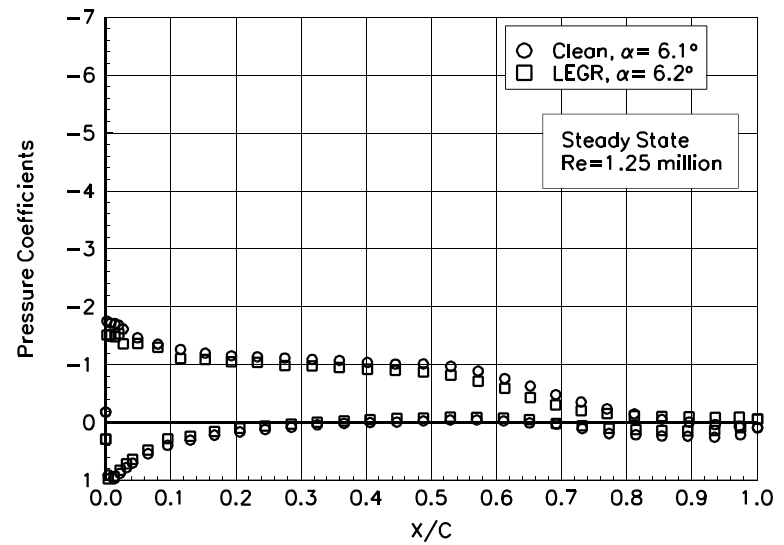


Figure 86. $\alpha = 6.1^\circ$

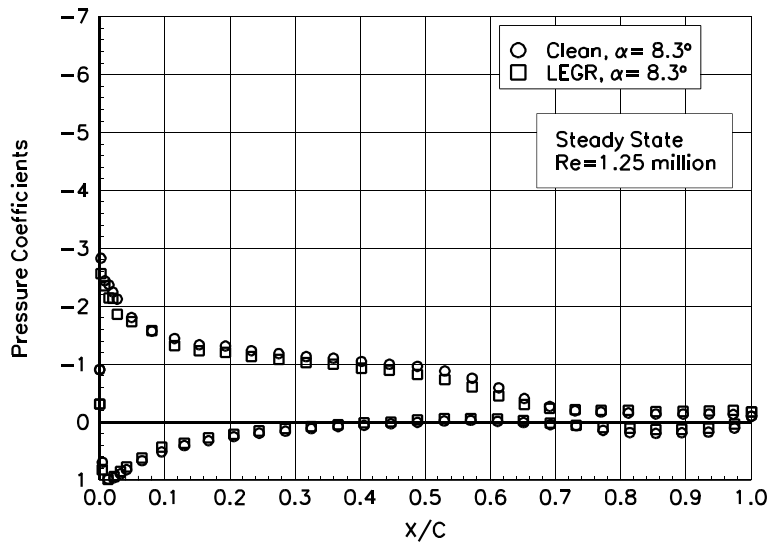


Figure 87. $\alpha = 8.3^\circ$

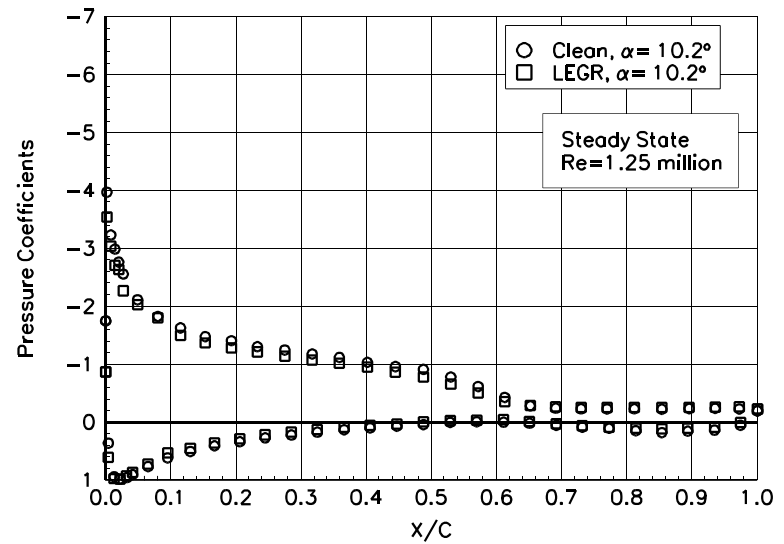


Figure 88. $\alpha = 10.2^\circ$

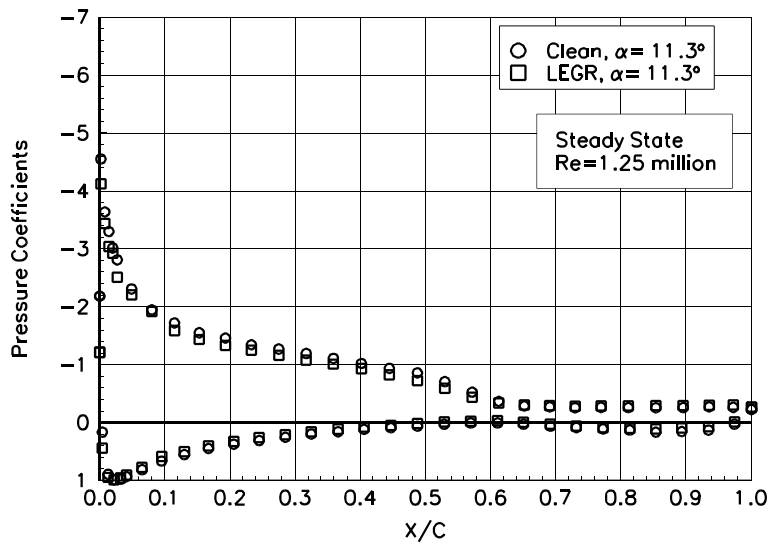


Figure 89. $\alpha = 11.3^\circ$

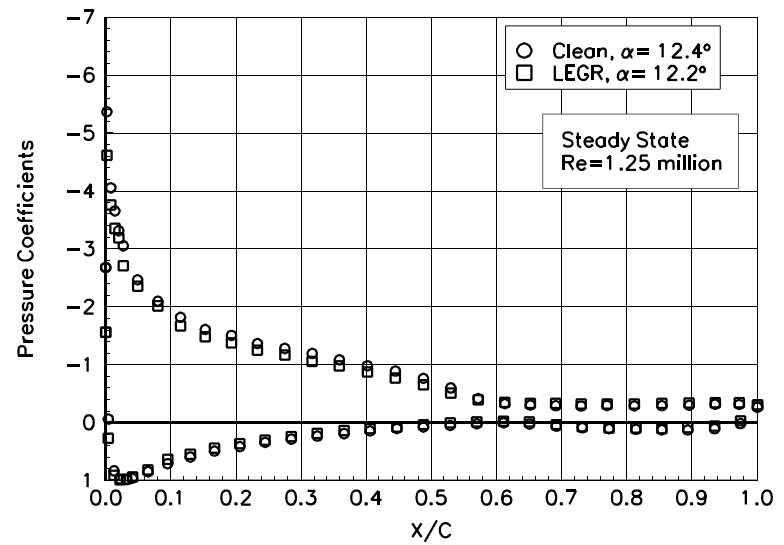


Figure 90. $\alpha = 12.4^\circ$

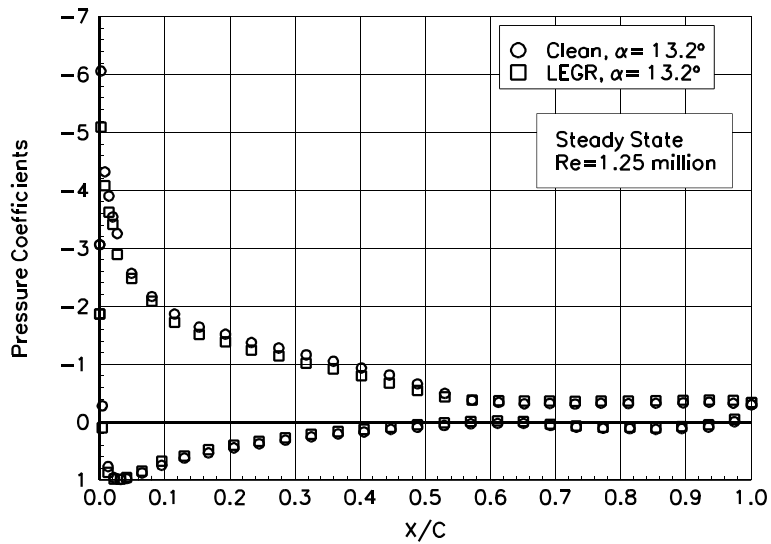


Figure 91. $\alpha = 13.2^\circ$

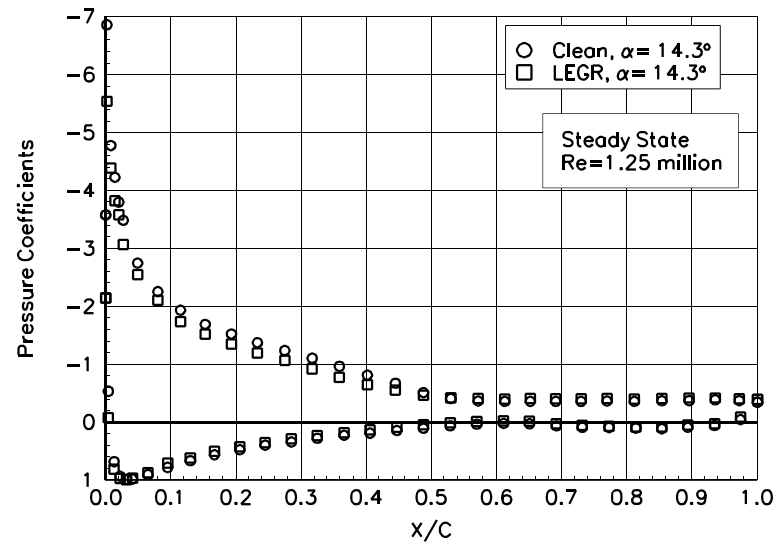


Figure 92. $\alpha = 14.3^\circ$

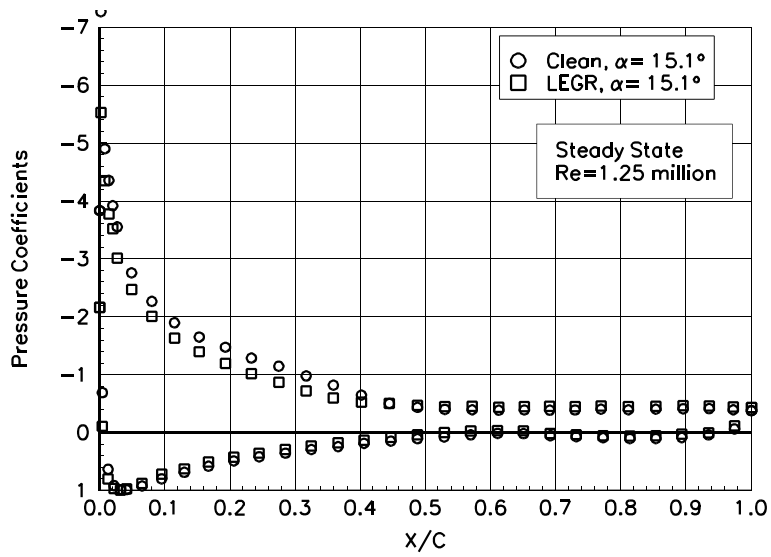


Figure 93. $\alpha = 15.1^\circ$

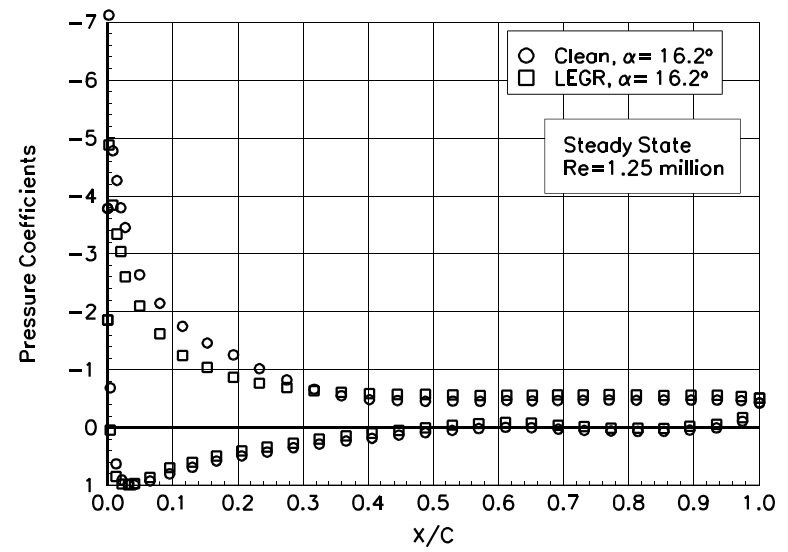


Figure 94. $\alpha = 16.2^\circ$

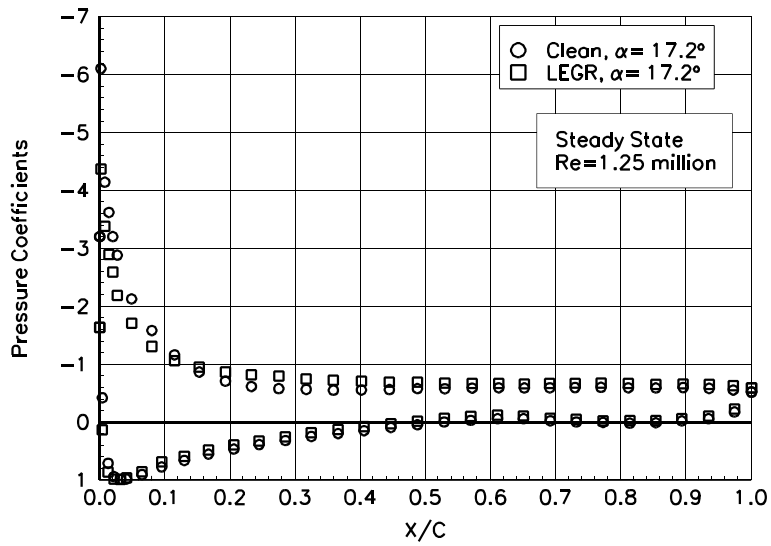


Figure 95. $\alpha = 17.2^\circ$

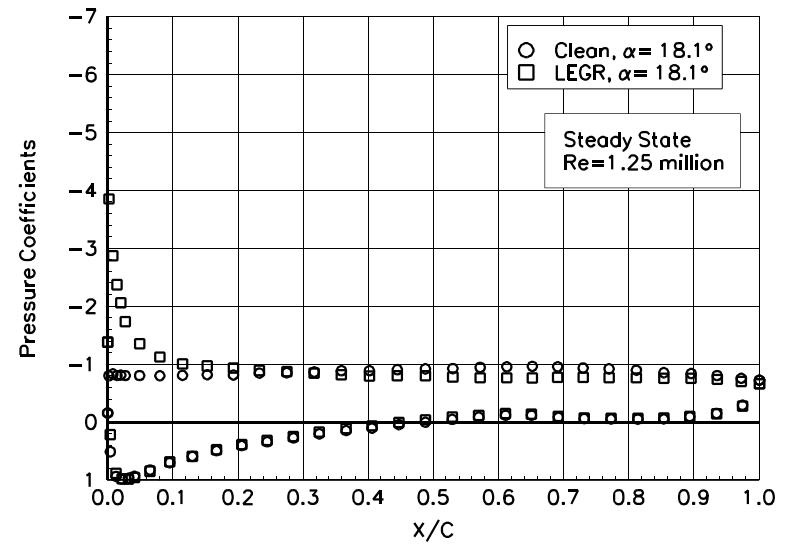


Figure 96. $\alpha = 18.1^\circ$

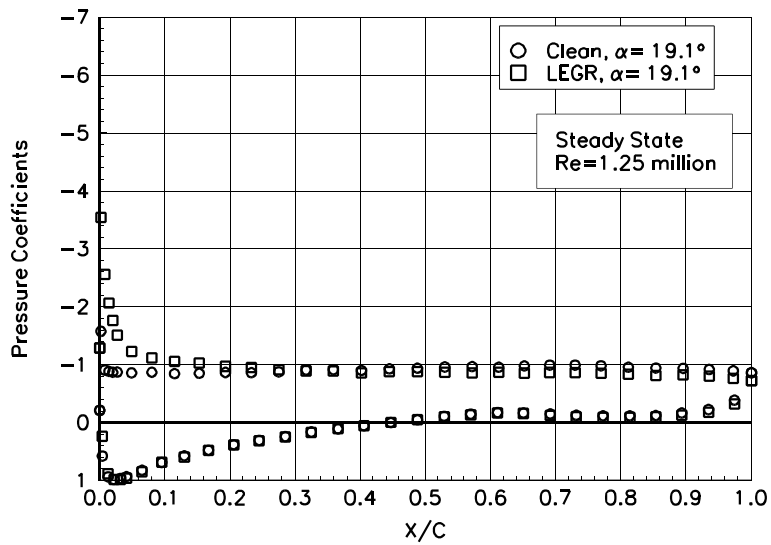


Figure 97. $\alpha = 19.1^\circ$

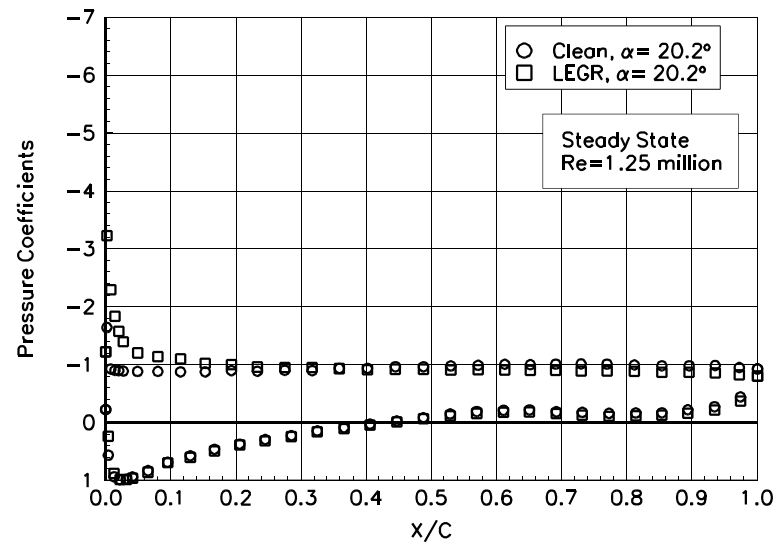


Figure 98. $\alpha = 20.2^\circ$

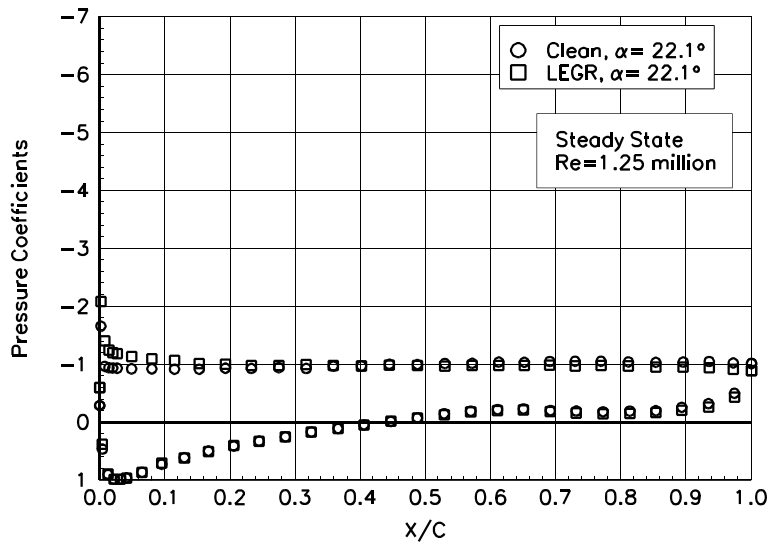


Figure 99. $\alpha = 22.1^\circ$

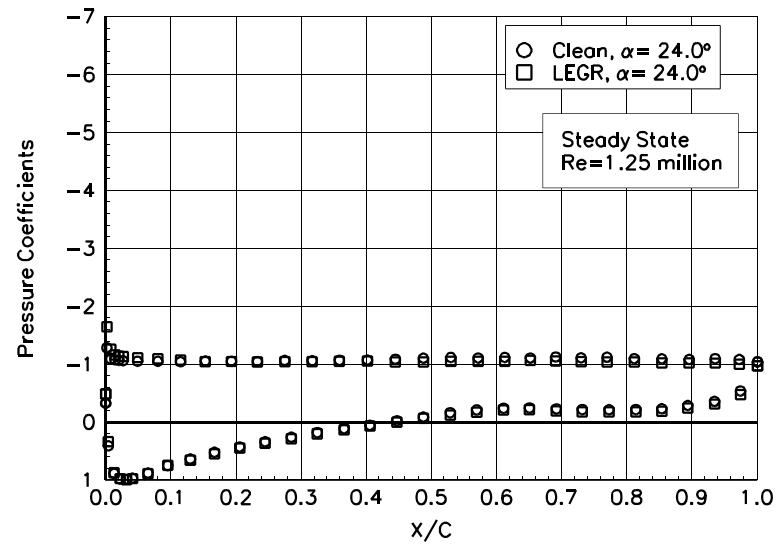


Figure 100. $\alpha = 24.0^\circ$

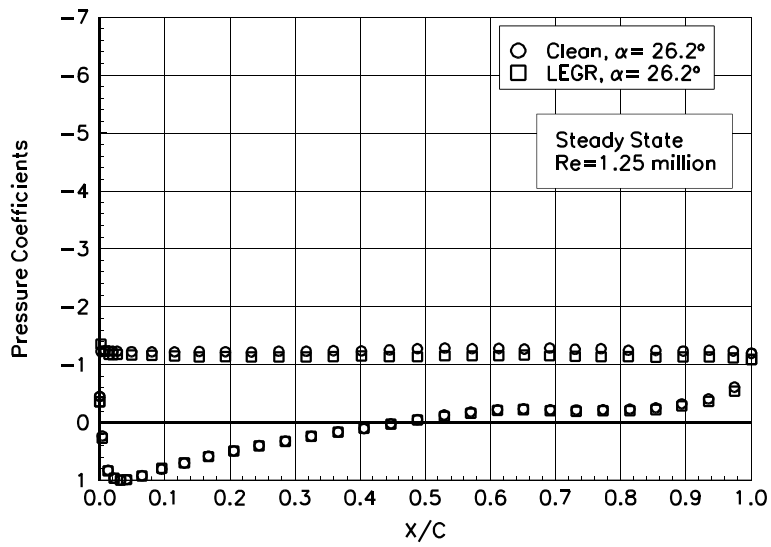


Figure 101. $\alpha = 26.2^\circ$

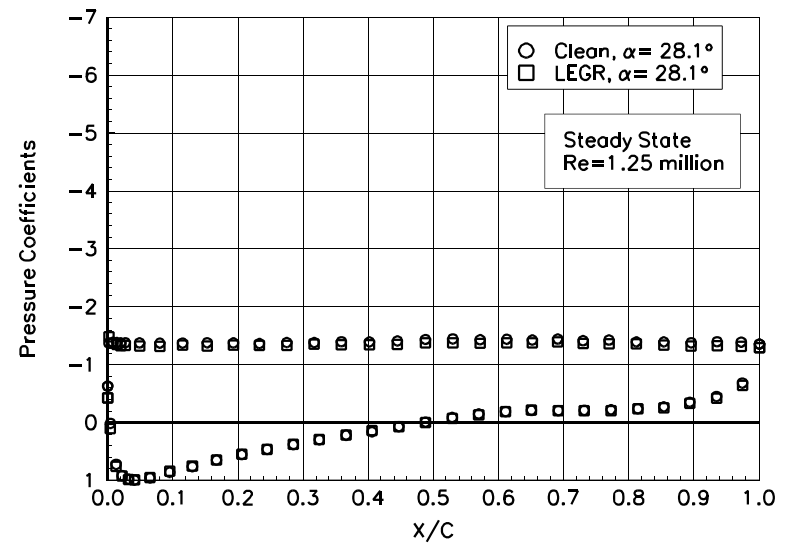


Figure 102. $\alpha = 28.1^\circ$

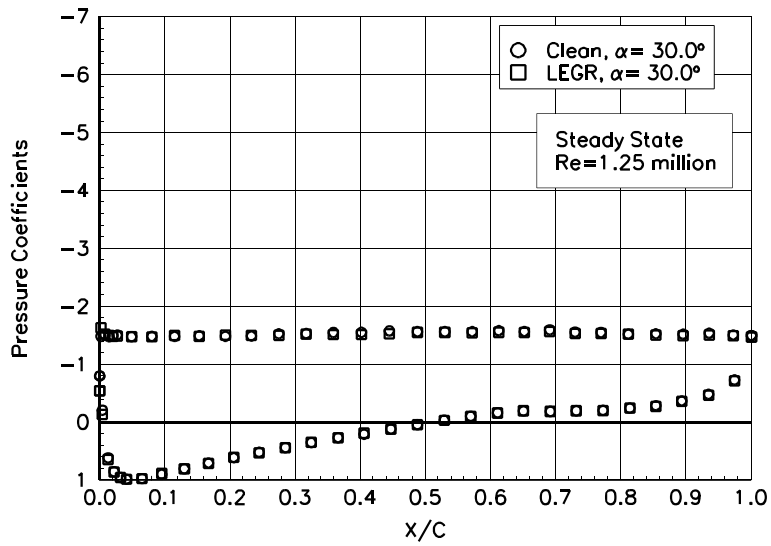


Figure 103. $\alpha = 30.0^\circ$

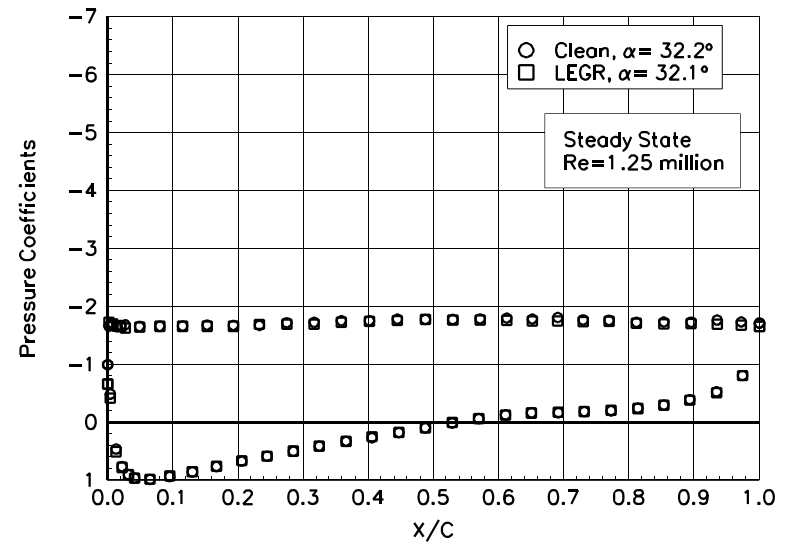


Figure 104. $\alpha = 32.2^\circ$

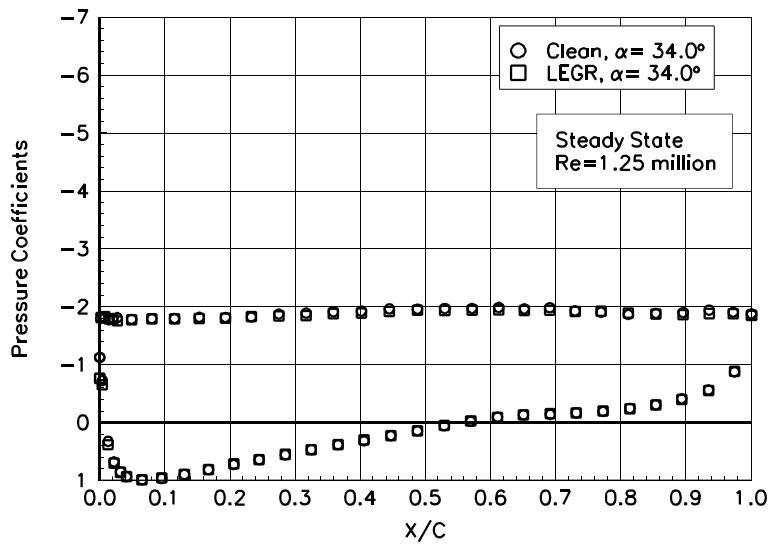


Figure 105. $\alpha = 34.0^\circ$

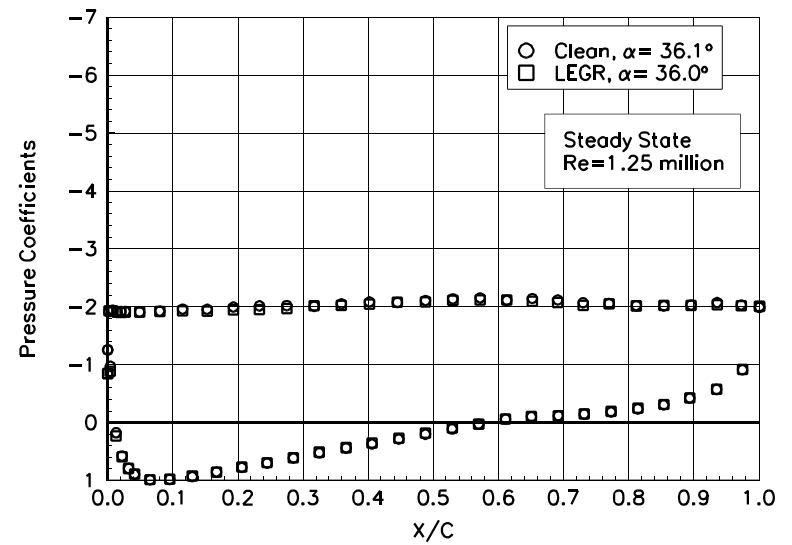


Figure 106. $\alpha = 36.1^\circ$

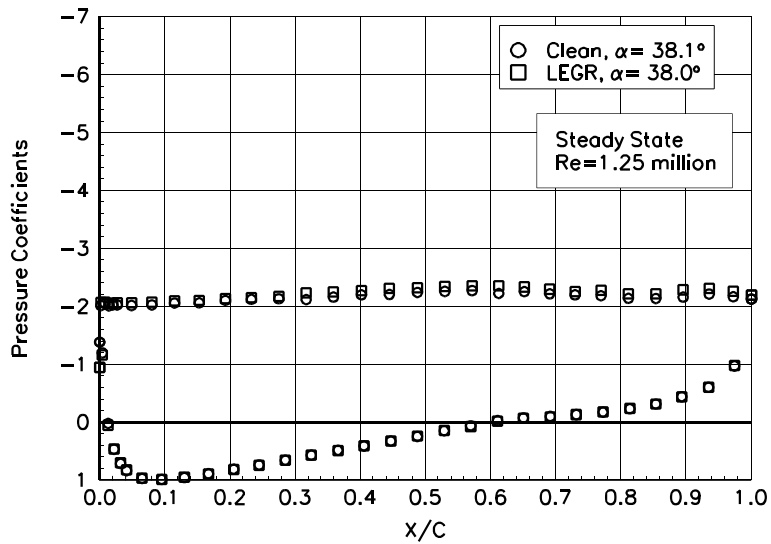


Figure 107. $\alpha = 38.1^\circ$

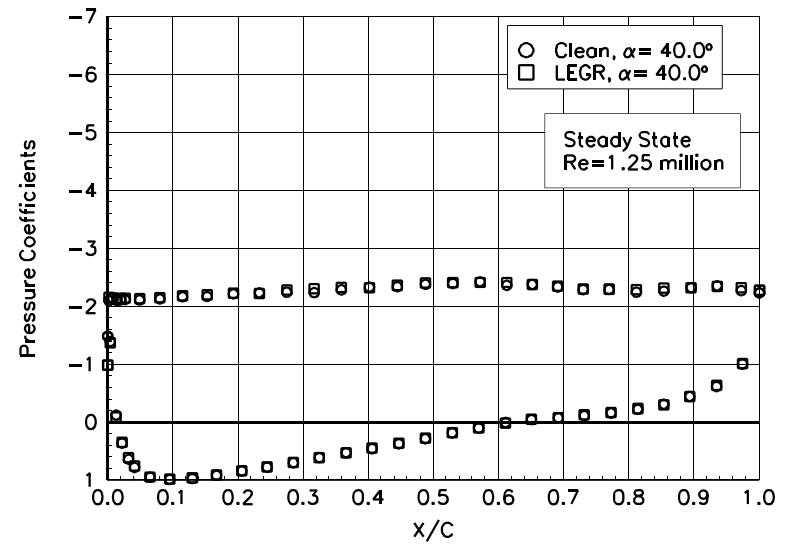


Figure 108. $\alpha = 40.0^\circ$

S813

Pressure Distributions, Steady State, $Re = 1.4$ million

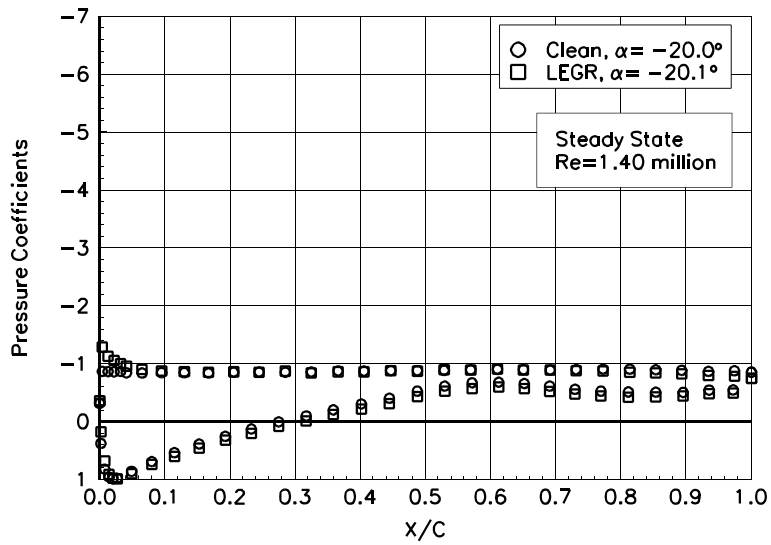


Figure 109. $\alpha = -20.0^\circ$

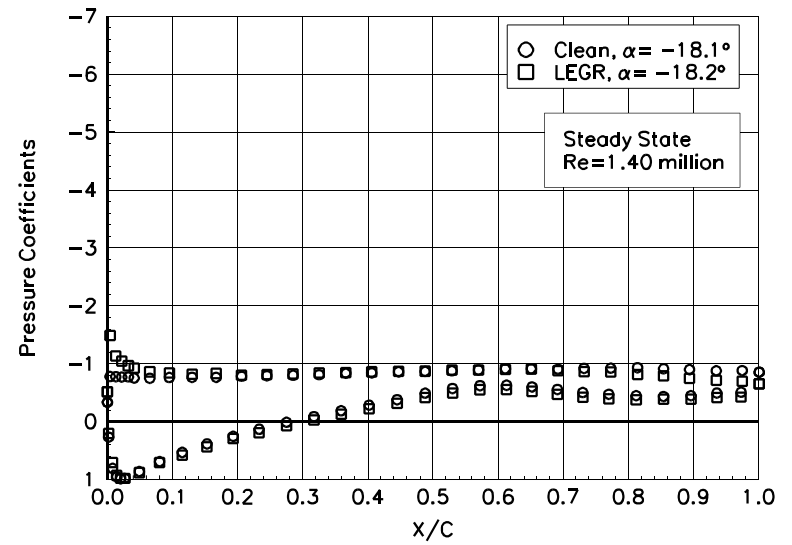


Figure 110. $\alpha = -18.1^\circ$

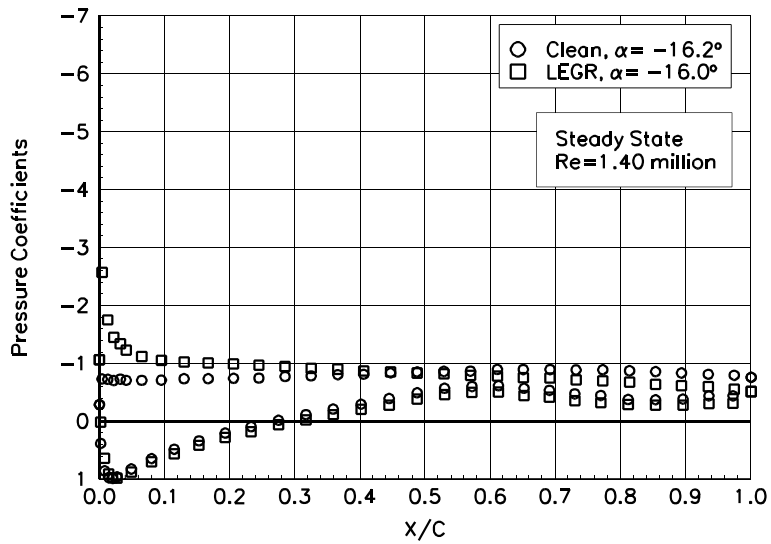


Figure 111. $\alpha = -16.2^\circ$

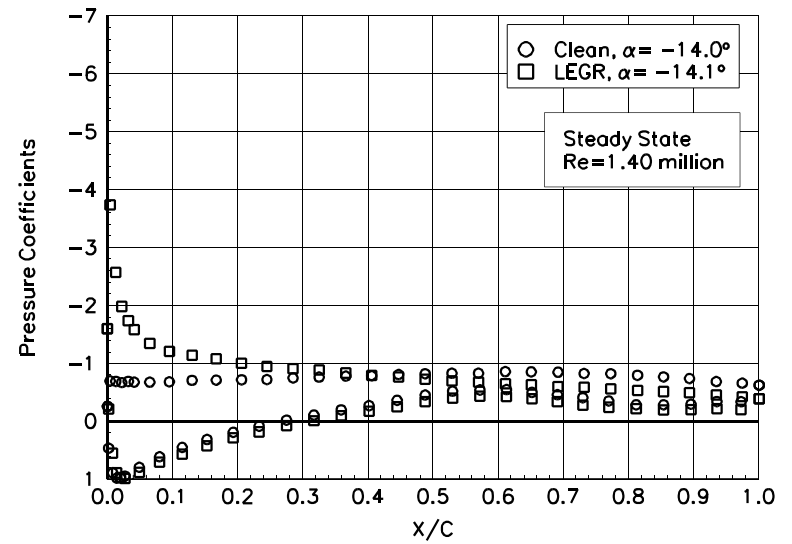


Figure 112. $\alpha = -14.0^\circ$

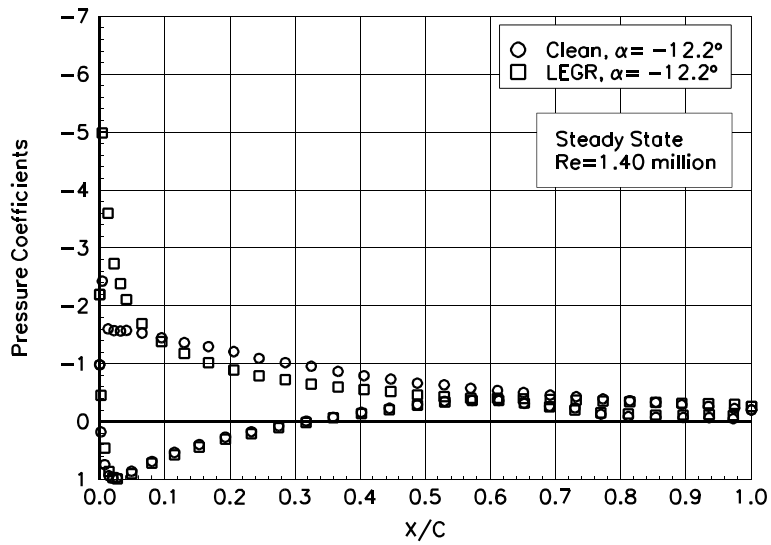


Figure 113. $\alpha = -12.2^\circ$

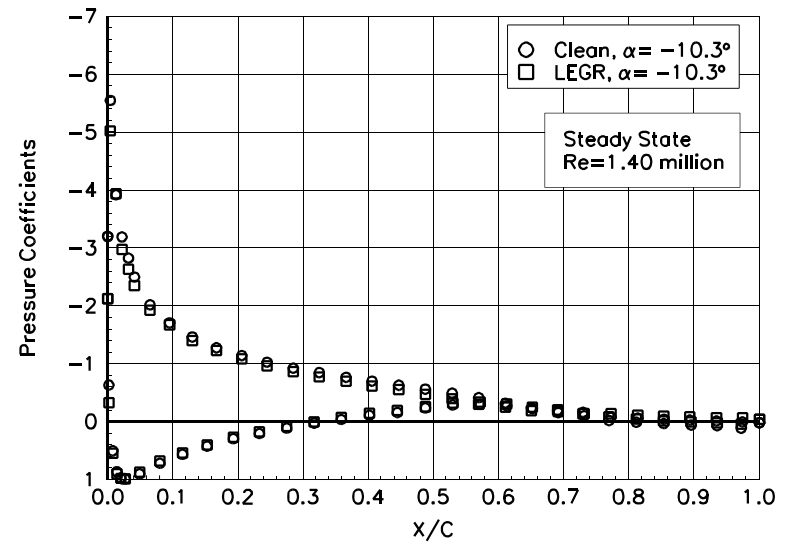


Figure 114. $\alpha = -10.3^\circ$

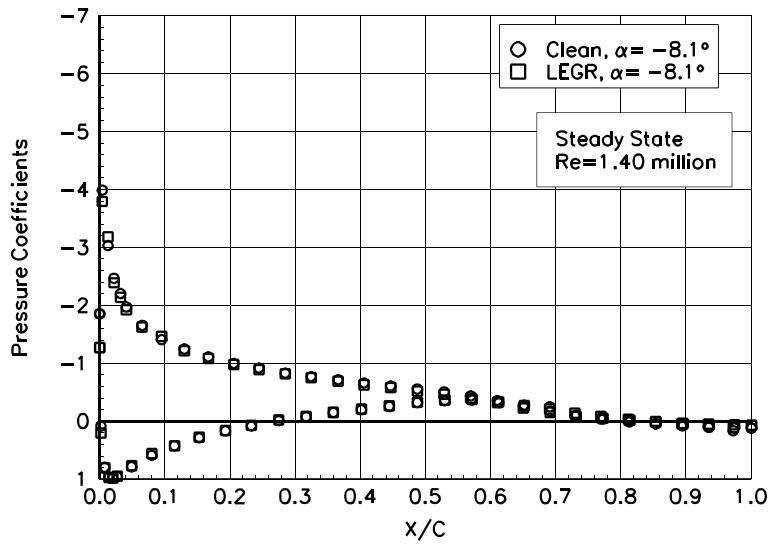


Figure 115. $\alpha = -8.1^\circ$

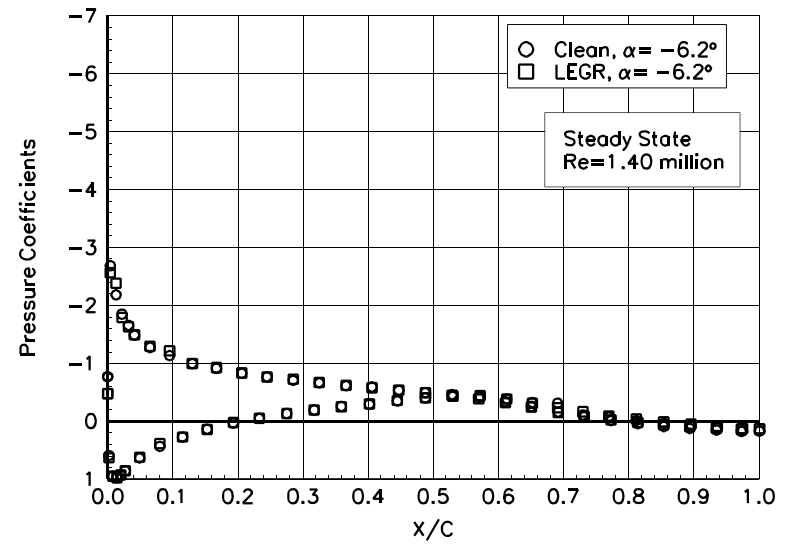


Figure 116. $\alpha = -6.2^\circ$

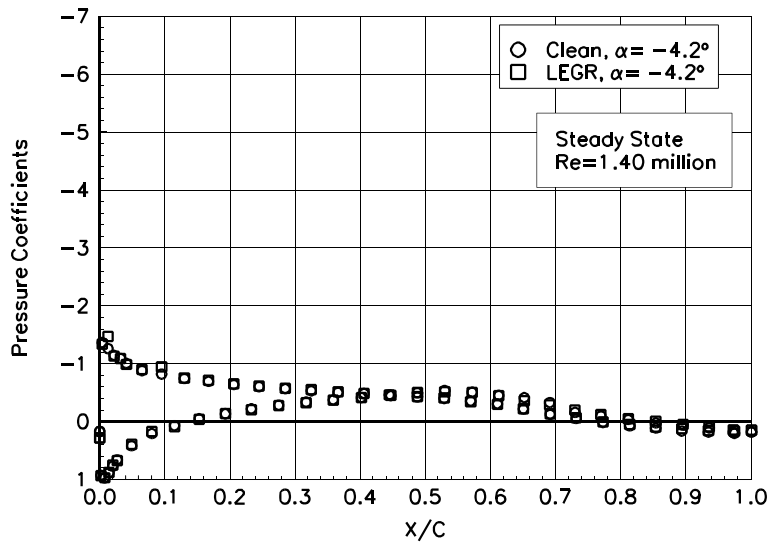


Figure 117. $\alpha = -4.2^\circ$

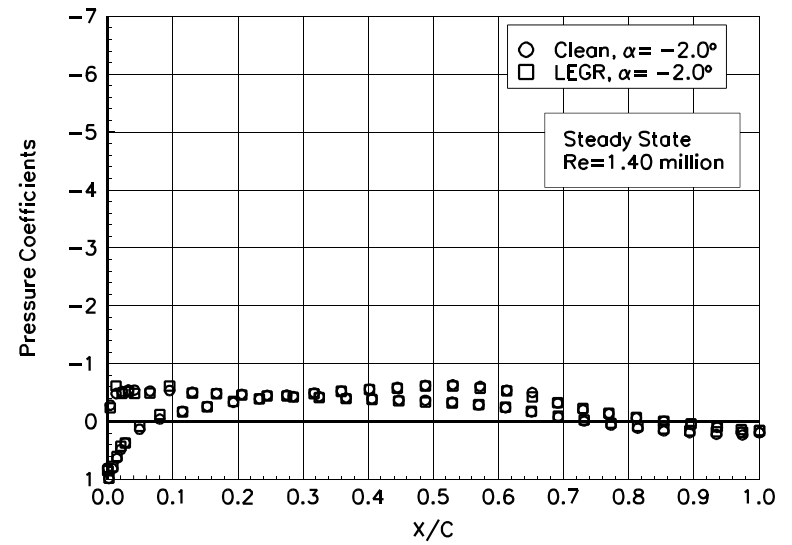


Figure 118. $\alpha = -2.0^\circ$

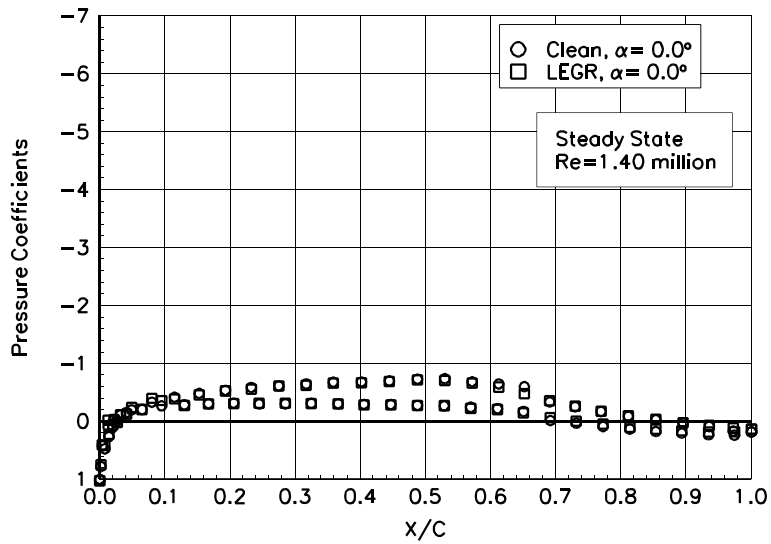


Figure 119. $\alpha = 0.0^\circ$

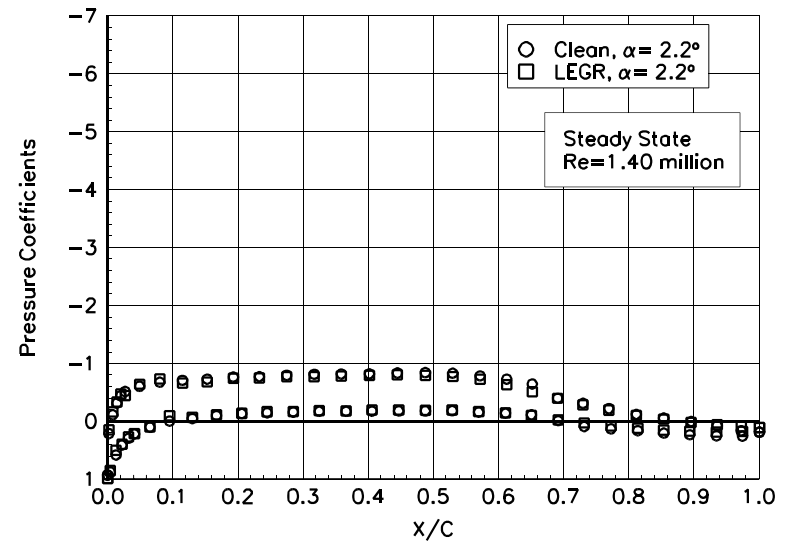


Figure 120. $\alpha = 2.2^\circ$

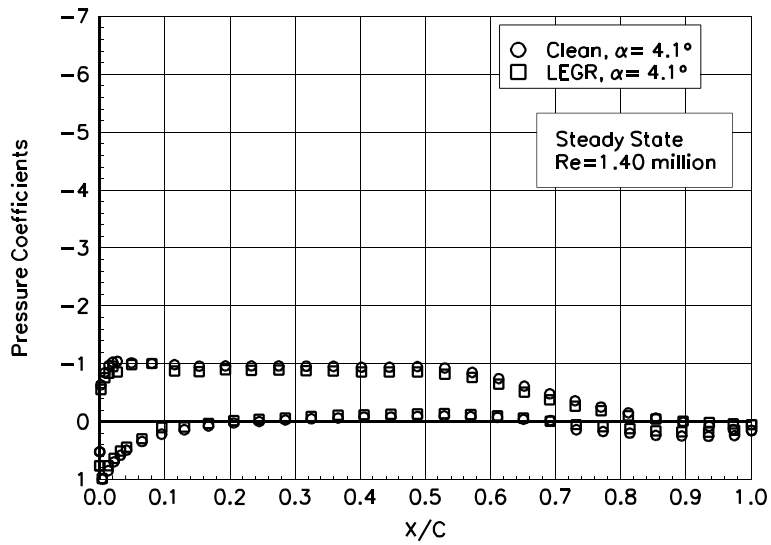


Figure 121. $\alpha = 4.1^\circ$

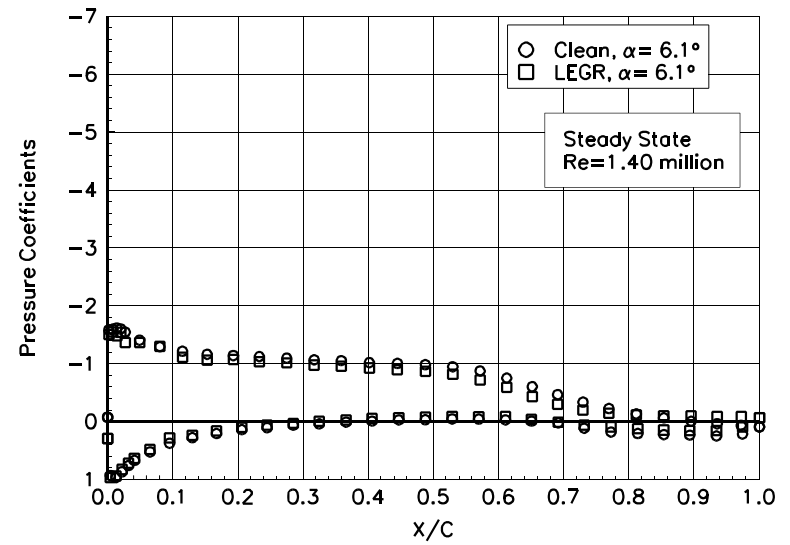


Figure 122. $\alpha = 6.1^\circ$

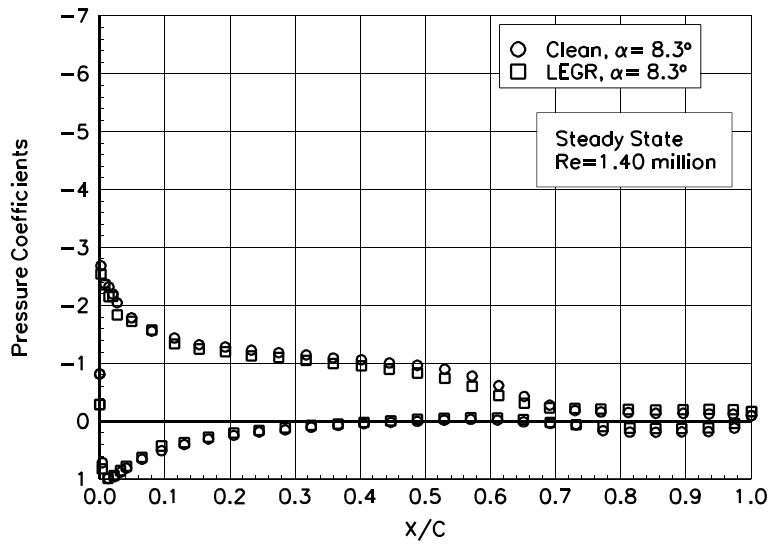


Figure 123. $\alpha = 8.3^\circ$

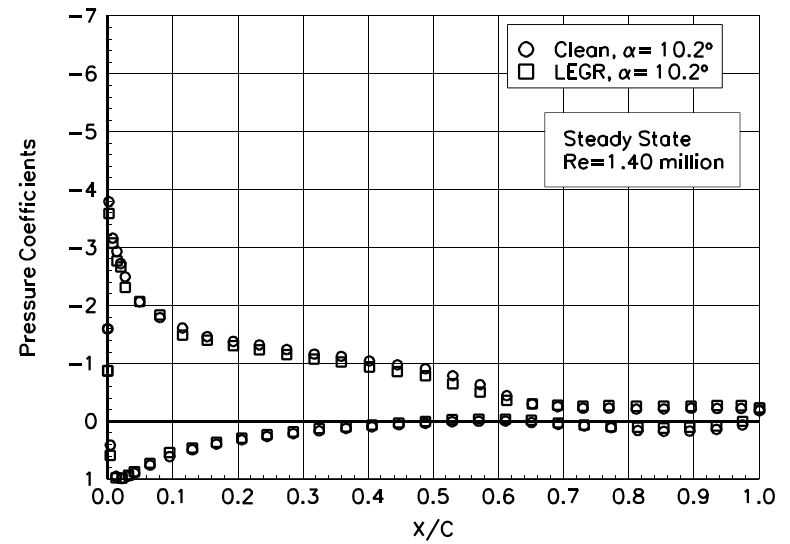


Figure 124. $\alpha = 10.2^\circ$

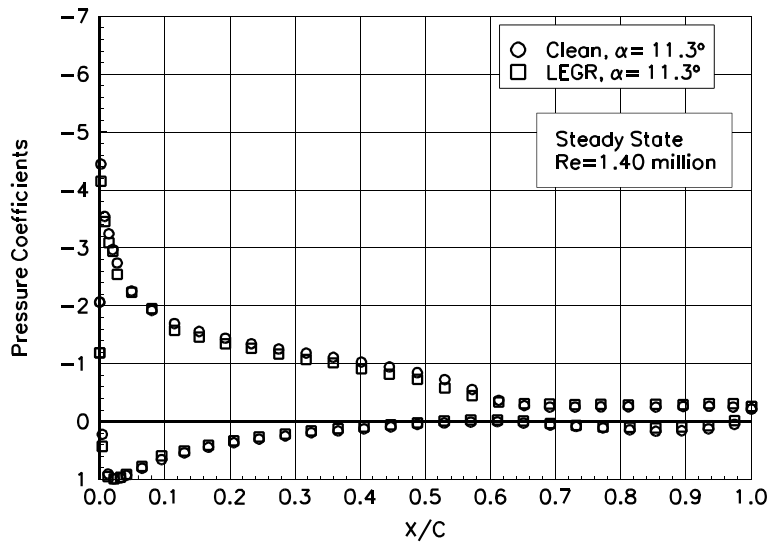


Figure 125. $\alpha = 11.3^\circ$

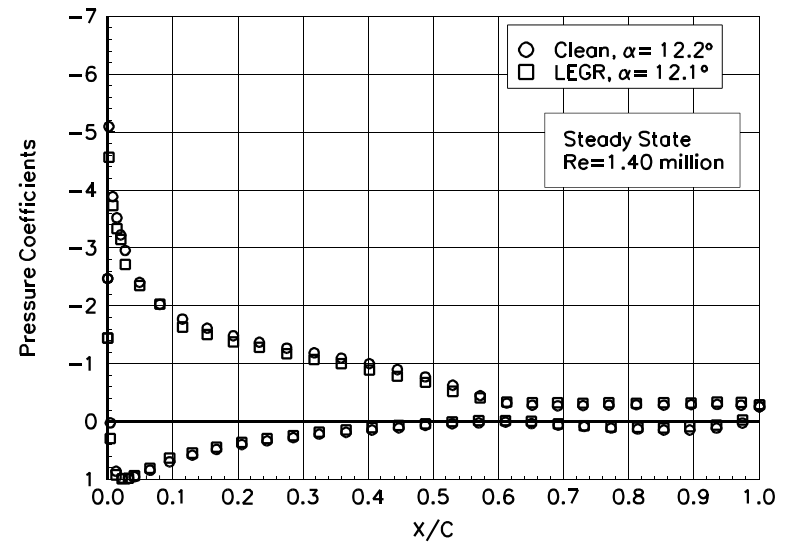


Figure 126. $\alpha = 12.2^\circ$

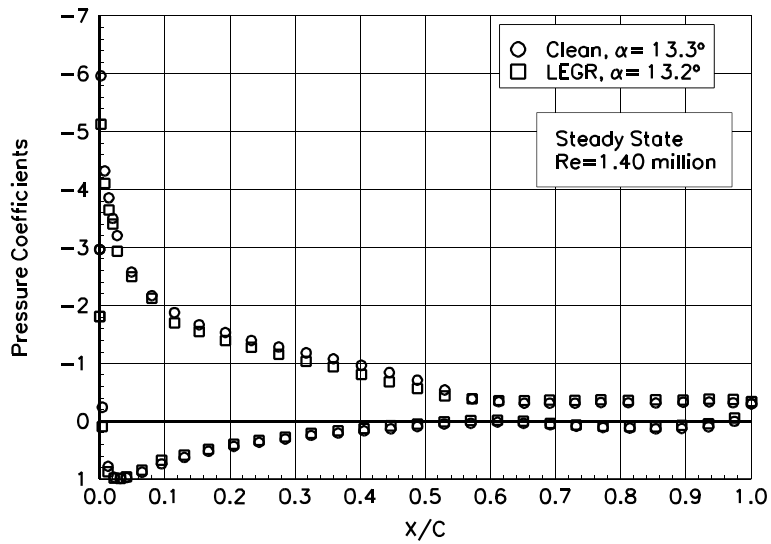


Figure 127. $\alpha = 13.3^\circ$

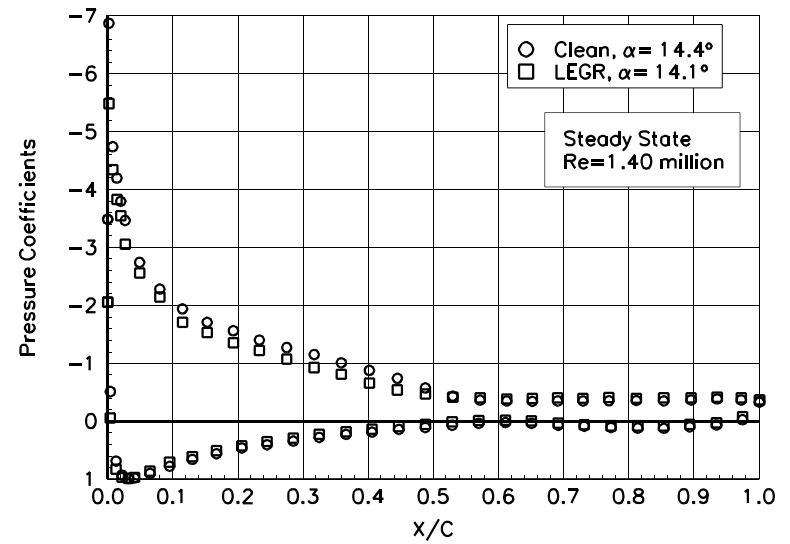


Figure 128. $\alpha = 14.4^\circ$

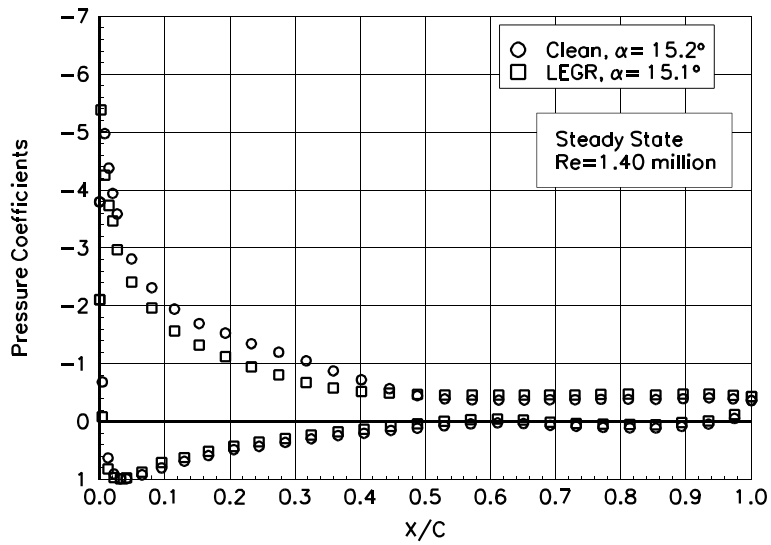


Figure 129. $\alpha = 15.2^\circ$

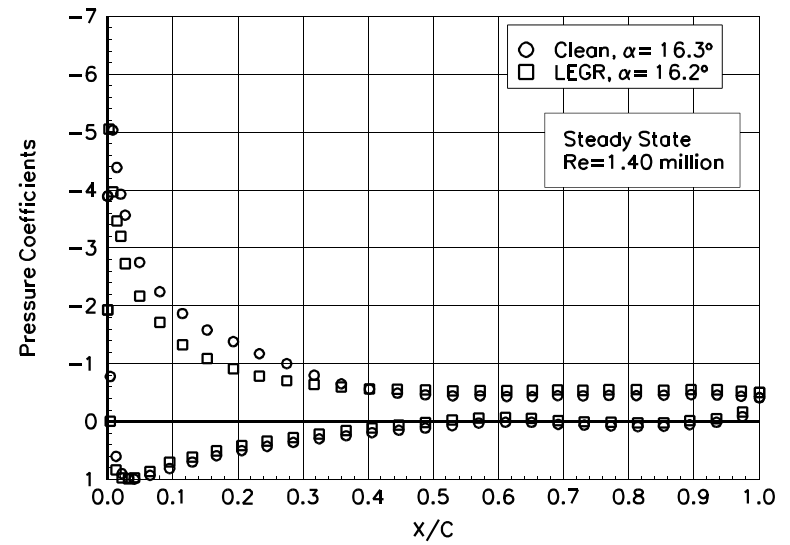


Figure 130. $\alpha = 16.3^\circ$

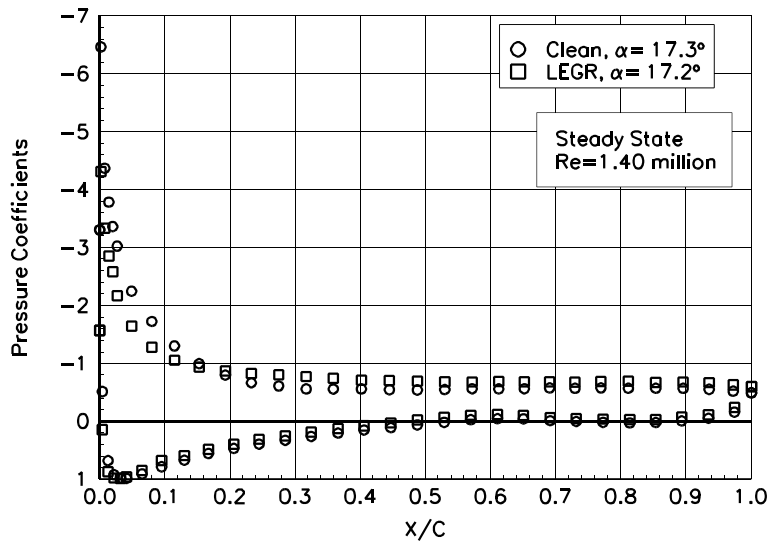


Figure 131. $\alpha = 17.3^\circ$

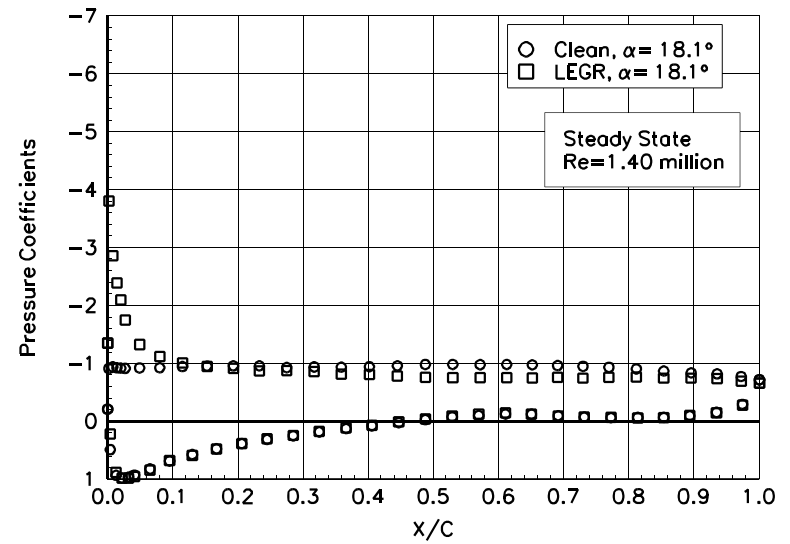


Figure 132. $\alpha = 18.1^\circ$

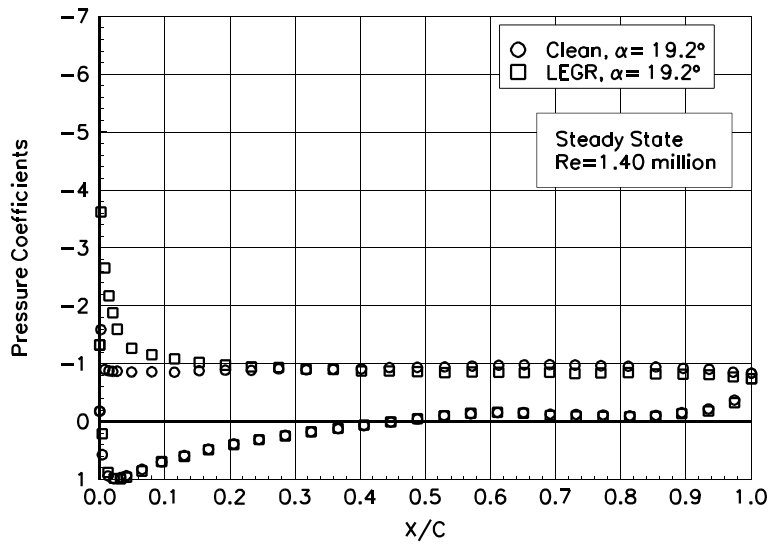


Figure 133. $\alpha = 19.2^\circ$

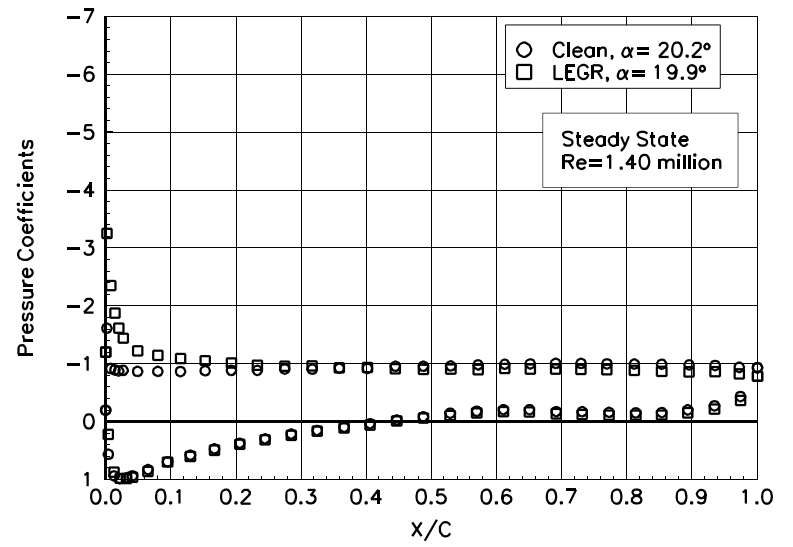


Figure 134. $\alpha = 20.2^\circ$

Appendix C: Unsteady Integrated Coefficients

List of Figures

Page

$\pm 5.5^\circ$ Sine, Re = 0.75 million	C-3
$\pm 5.5^\circ$ Sine, Re = 1 million	C-10
$\pm 5.5^\circ$ Sine, Re= 1.25 million	C-17
$\pm 5.5^\circ$ Sine, Re = 1.4 million	C-24
$\pm 10^\circ$ Sine, Re = 0.75 million	C-31
$\pm 10^\circ$ Sine, Re = 1 million	C-38
$\pm 10^\circ$ Sine, Re = 1.25 million	C-45
$\pm 10^\circ$ Sine, Re = 1.4 million	C-52

Unsteady Airfoil Characteristics

$\pm 5.5^\circ$ Sine, Re = 0.75 million

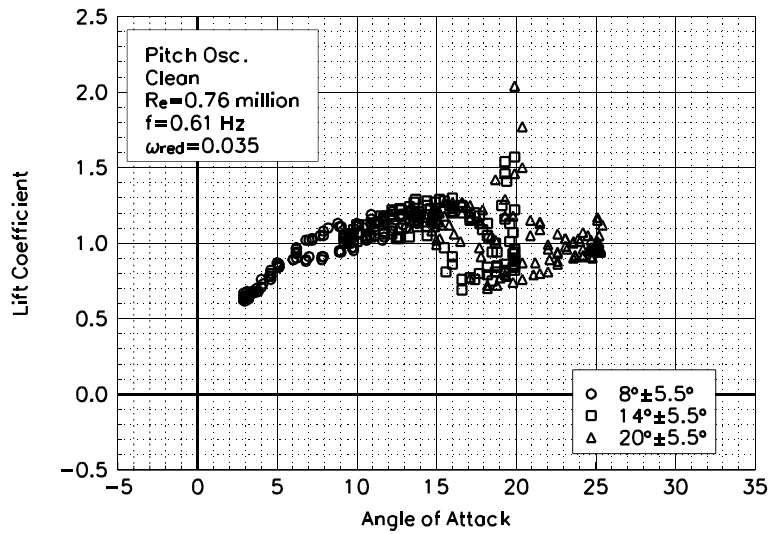


Figure C1. Lift coefficient vs α .

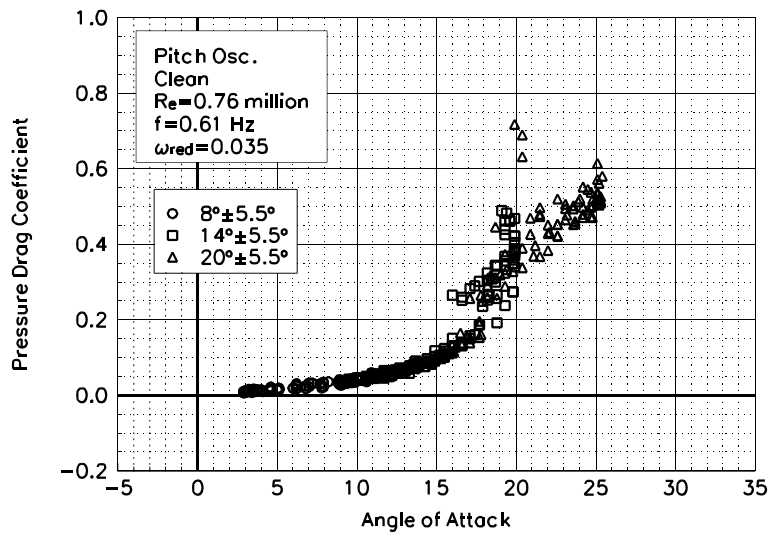


Figure C2. Pressure drag coefficient vs α .

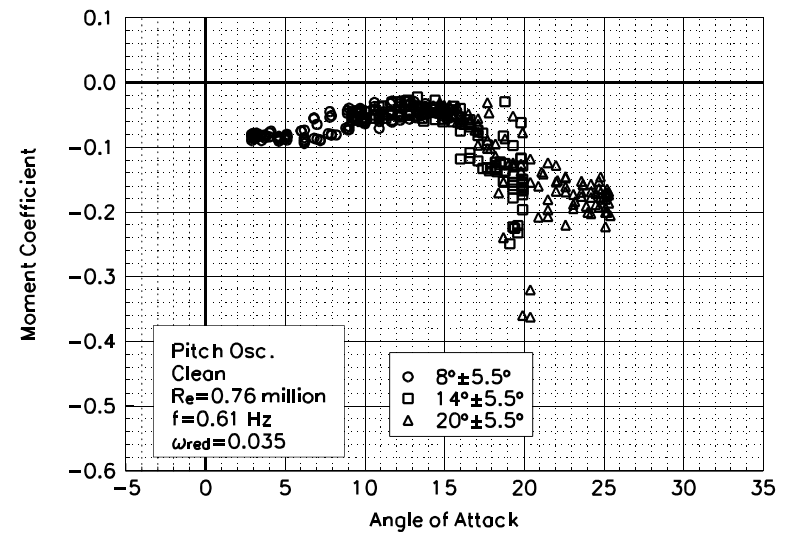


Figure C3. Moment coefficient vs α .

S813
Clean
Re=0.76 million
 $\omega_{\text{reduced}}=0.035$

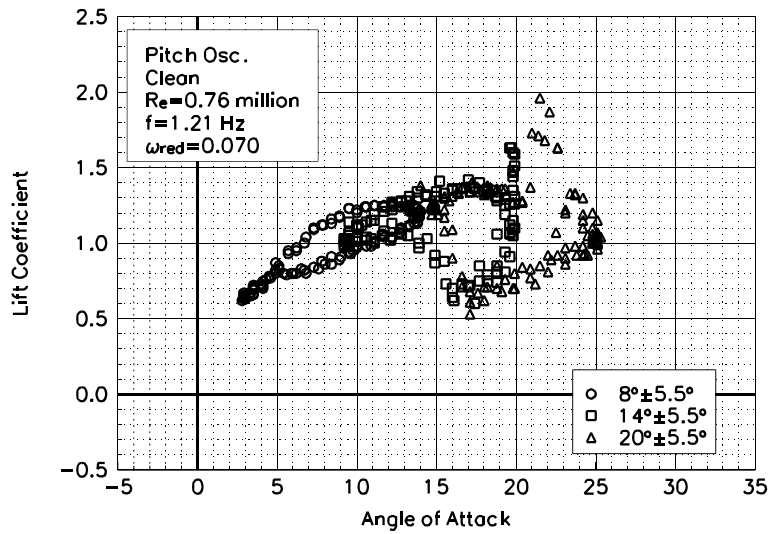


Figure C4. Lift coefficient vs α .

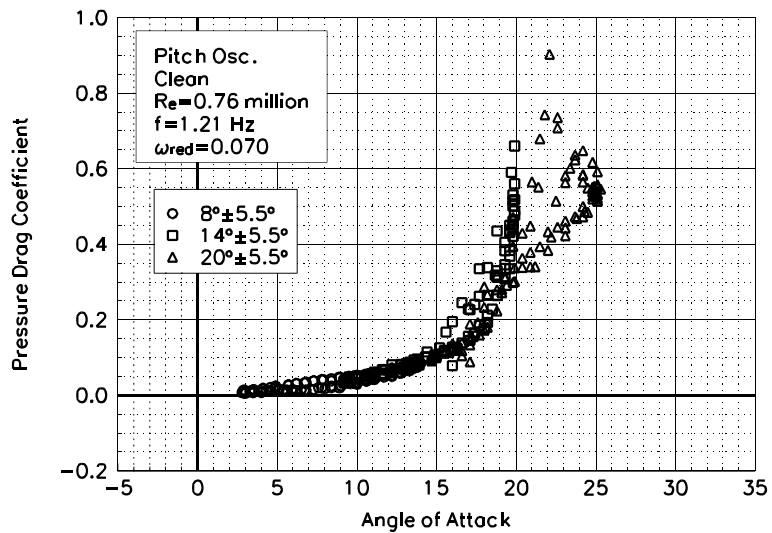


Figure C5. Pressure drag coefficient vs α .

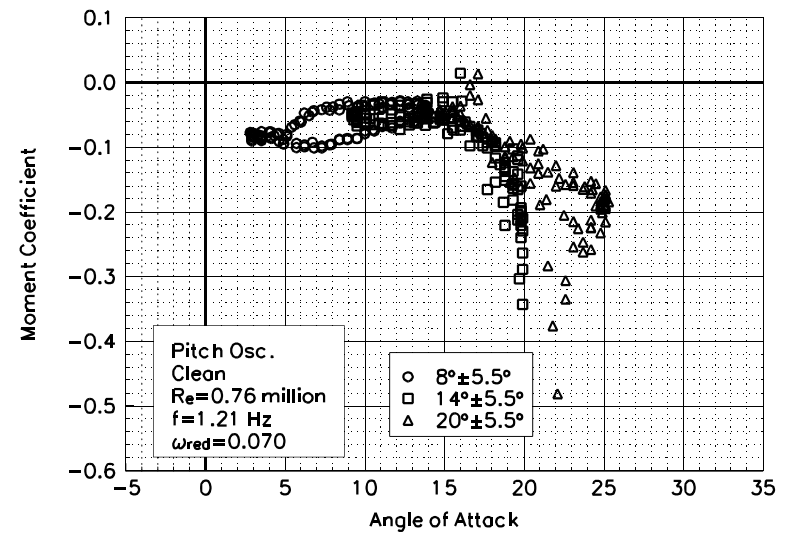


Figure C6. Moment coefficient vs α .

S813
Clean
Re=0.76 million
 $\omega_{\text{reduced}}=0.070$

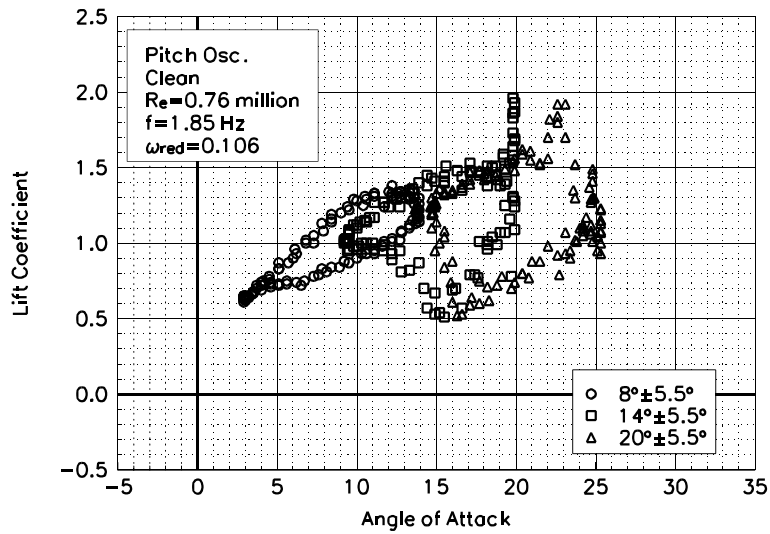


Figure C7. Lift coefficient vs α .

S813
Clean
Re=0.76 million
 $\omega_{\text{reduced}}=0.106$

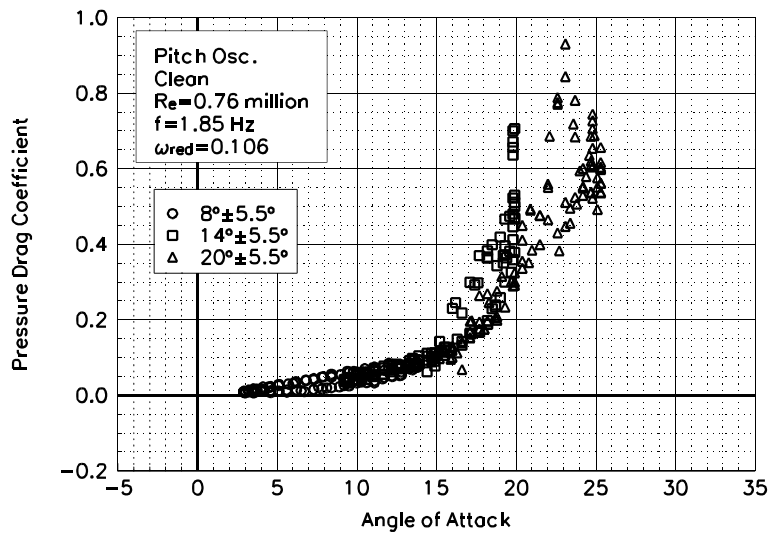


Figure C8. Pressure drag coefficient vs α .

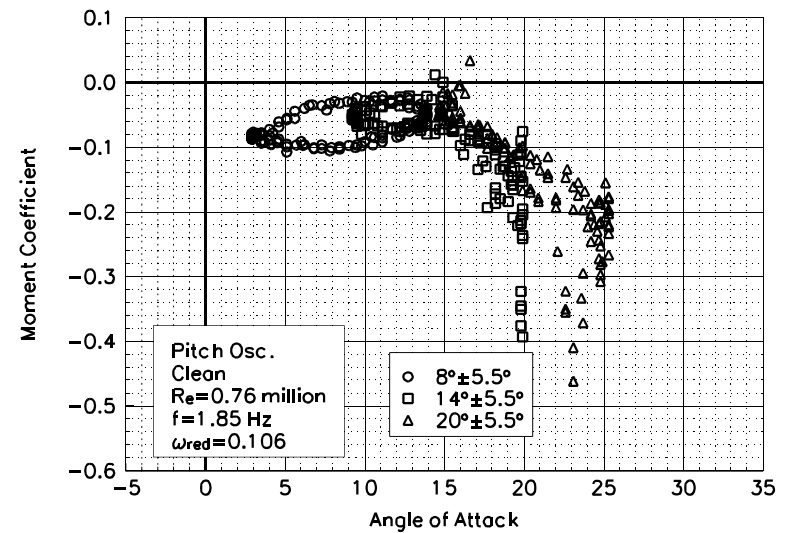


Figure C9. Moment coefficient vs α .

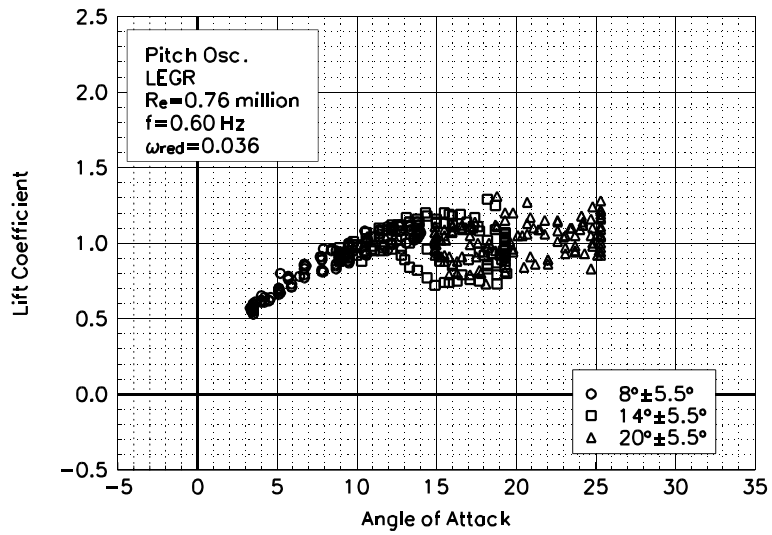


Figure C10. Lift coefficient vs α .

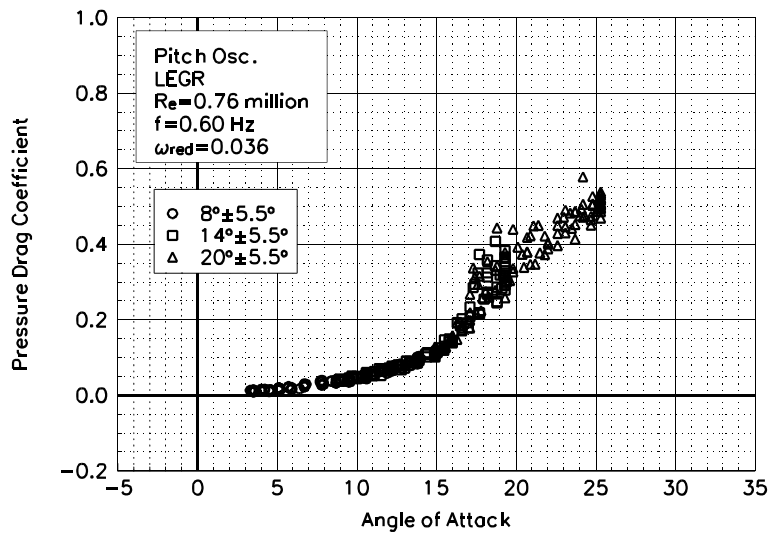


Figure C11. Pressure drag coefficient vs α .

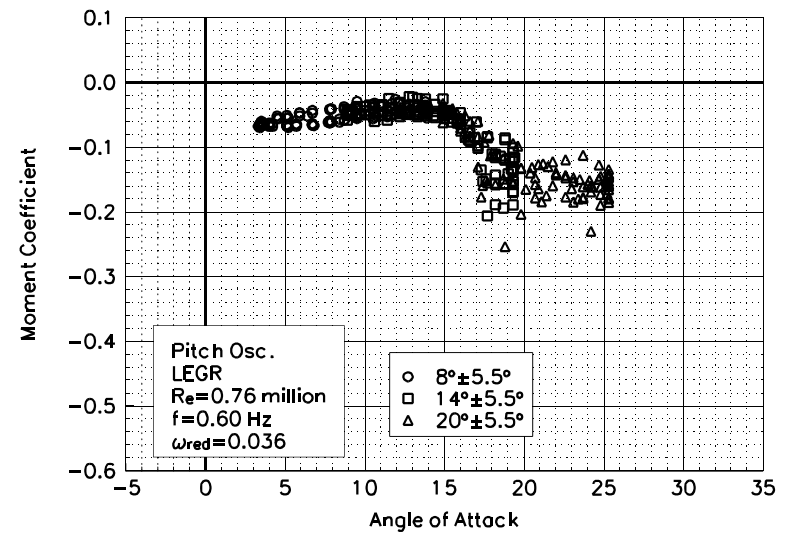


Figure C12. Moment coefficient vs α .

S813
LEGR
Re=0.76 million
 $\omega_{\text{reduced}}=0.036$

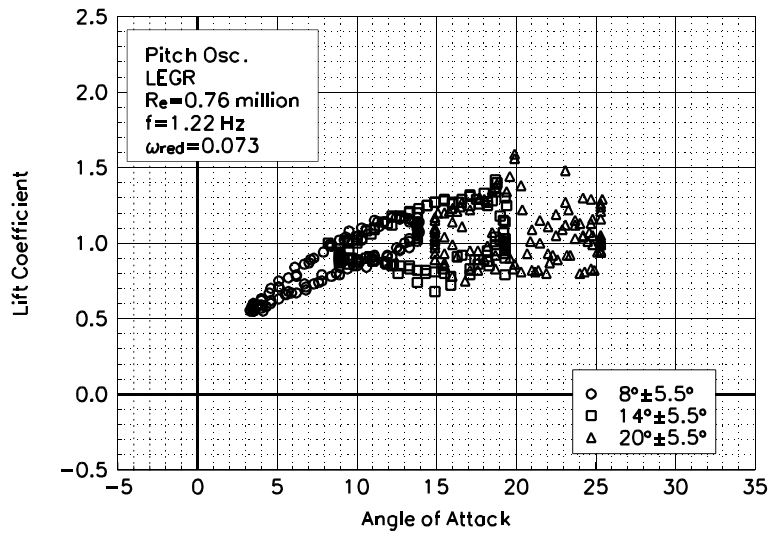


Figure C13. Lift coefficient vs α .

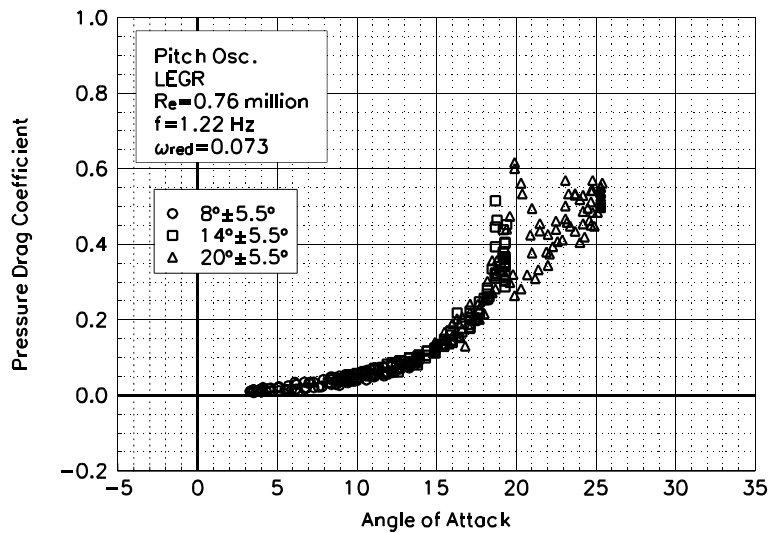


Figure C14. Pressure drag coefficient vs α .

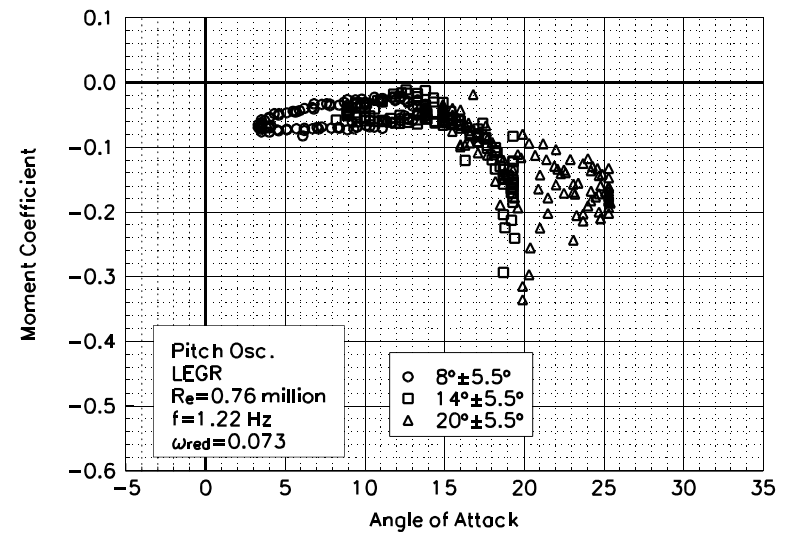


Figure C15. Moment coefficient vs α .

S813
LEGR
Re=0.76 million
 $\omega_{\text{reduced}}=0.073$

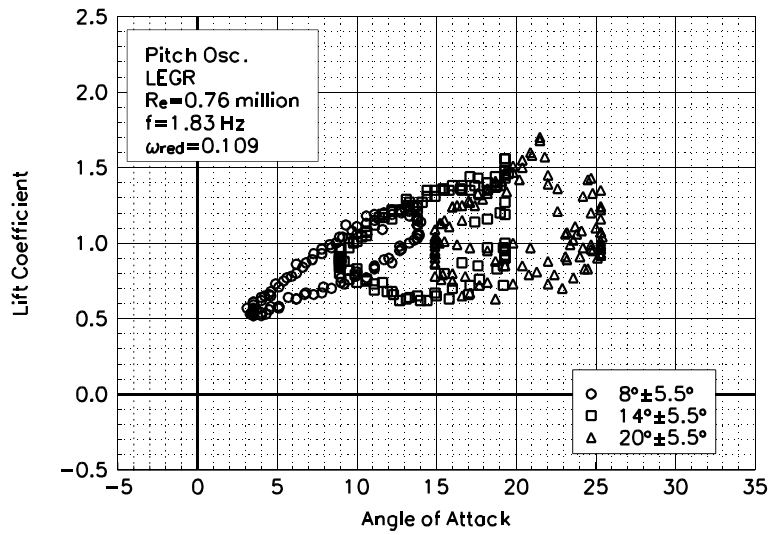


Figure C16. Lift coefficient vs α .

S813
LEGR
Re=0.76 million
 $\omega_{\text{reduced}}=0.109$

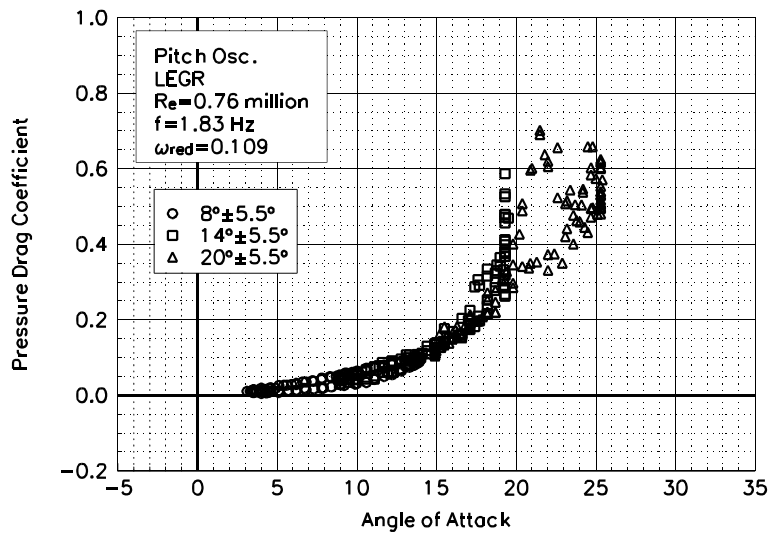


Figure C17. Pressure drag coefficient vs α .

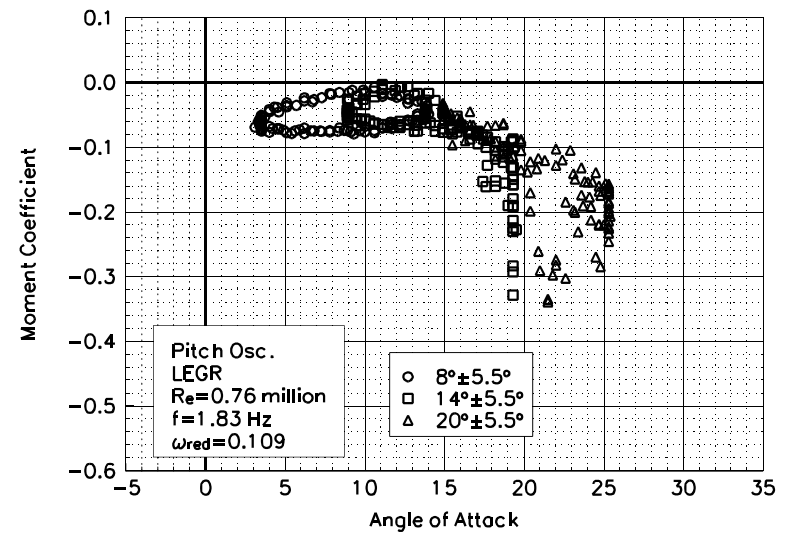


Figure C18. Moment coefficient vs α .

Unsteady Airfoil Characteristics

$\pm 5.5^\circ$ Sine, Re = 1 million

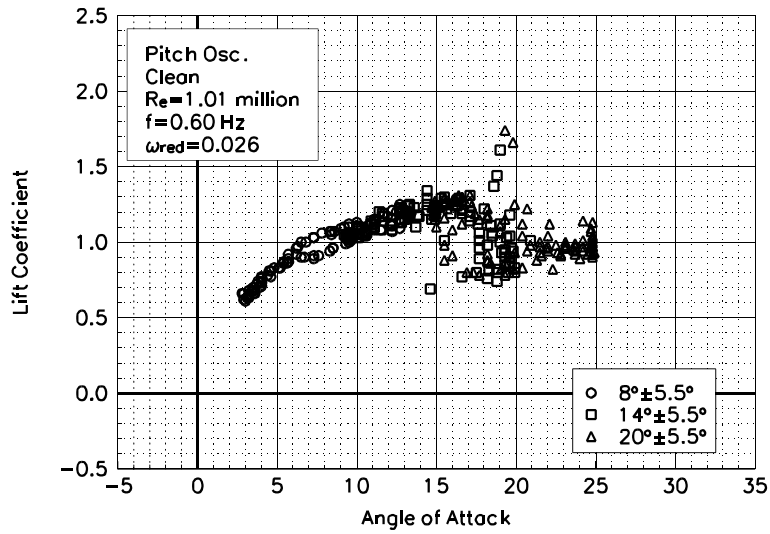


Figure C19. Lift coefficient vs α .

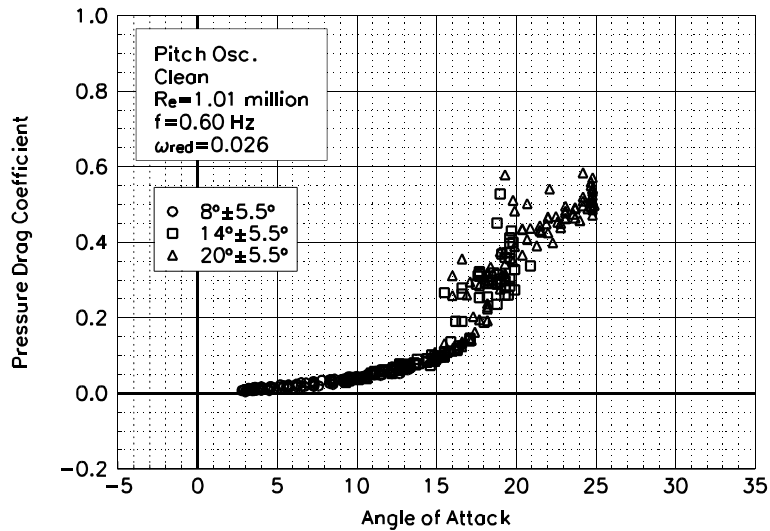


Figure C20. Pressure drag coefficient vs α .

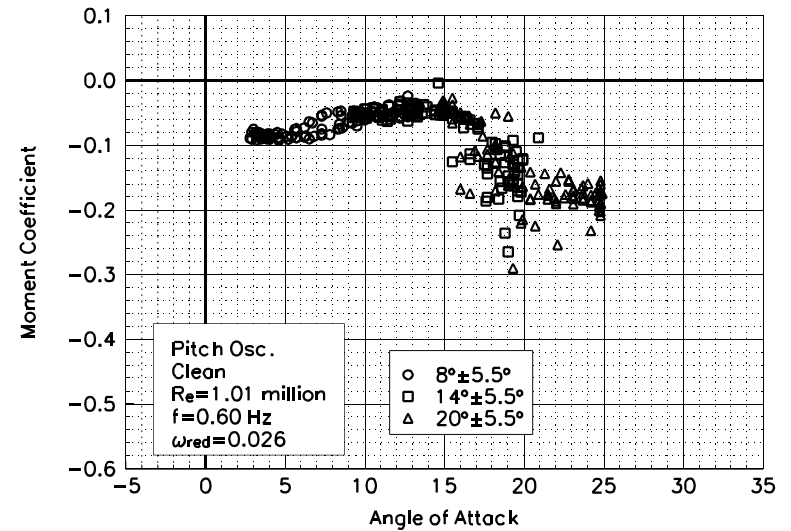


Figure C21. Moment coefficient vs α .

S813
Clean
Re=1.01 million
 $\omega_{\text{reduced}}=0.026$

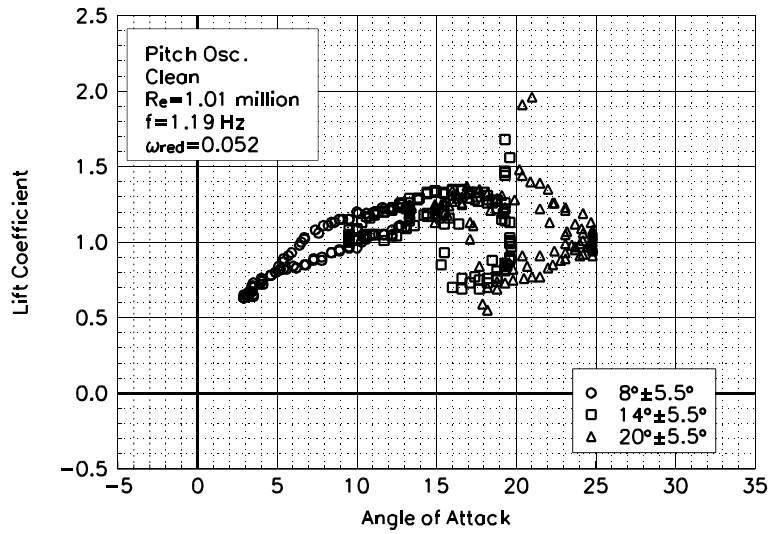


Figure C22. Lift coefficient vs α .

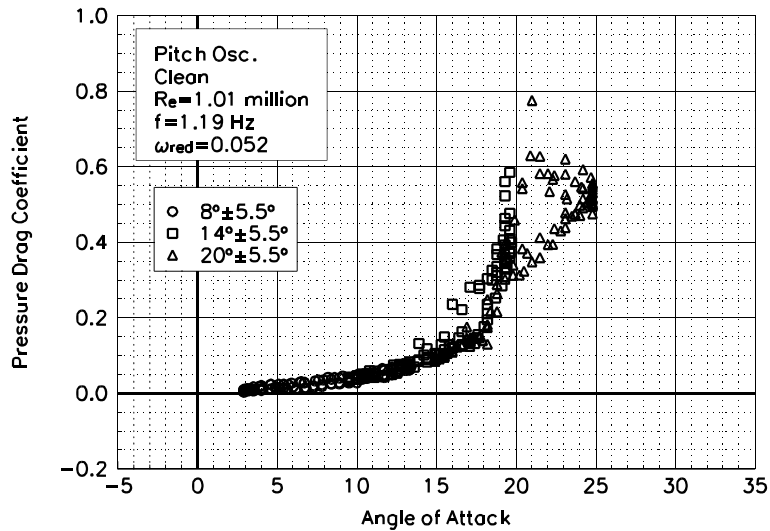


Figure C23. Pressure drag coefficient vs α .

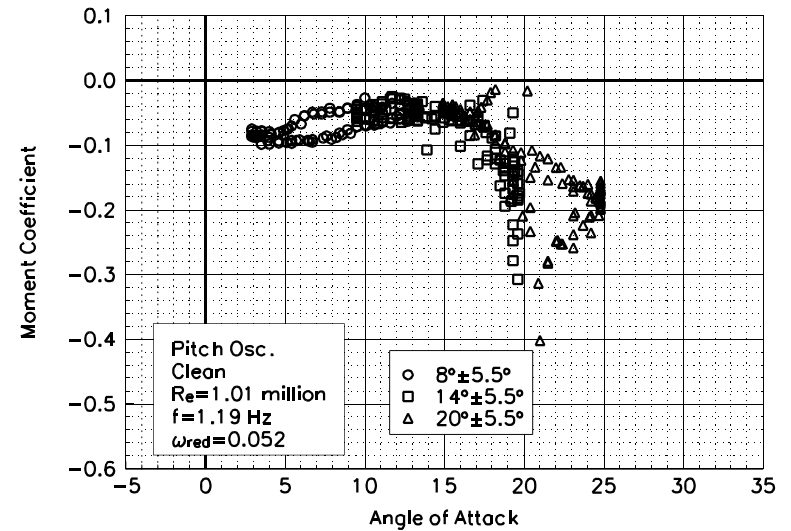


Figure C24. Moment coefficient vs α .

S813
Clean
Re=1.01 million
 $\omega_{\text{reduced}}=0.052$

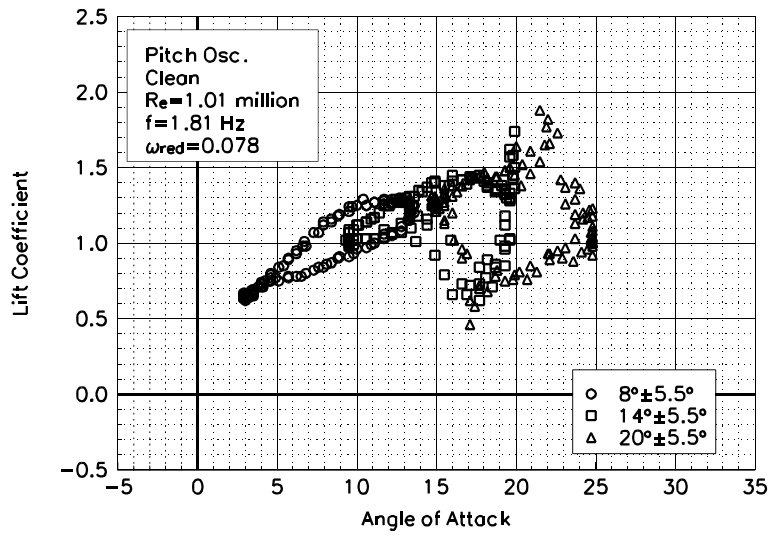


Figure C25. Lift coefficient vs α .

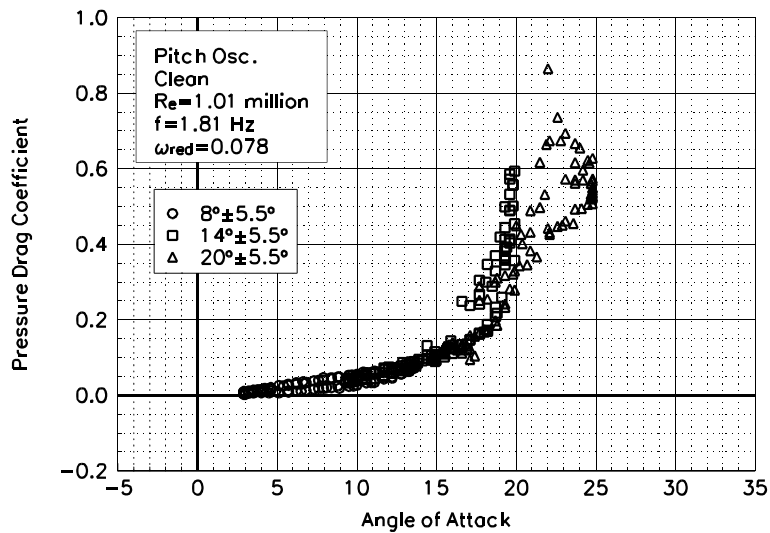


Figure C26. Pressure drag coefficient vs α .

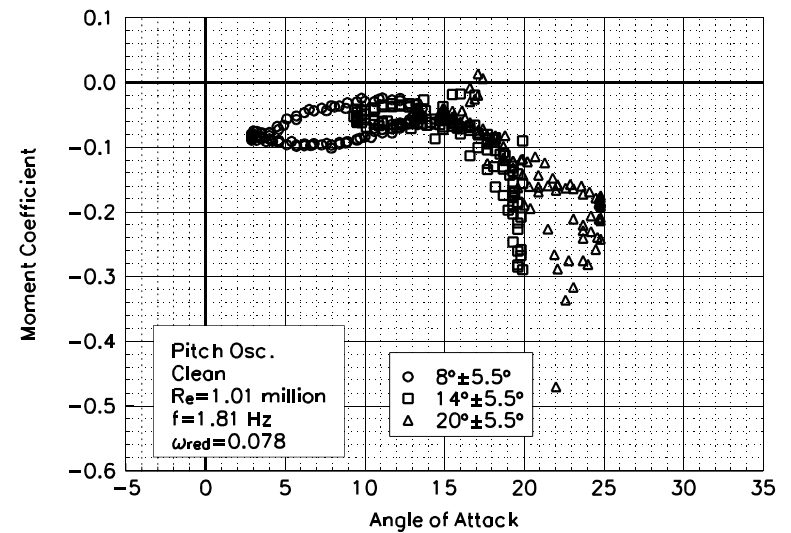


Figure C27. Moment coefficient vs α .

S813
Clean
Re=1.01 million
 $\omega_{\text{reduced}}=0.078$

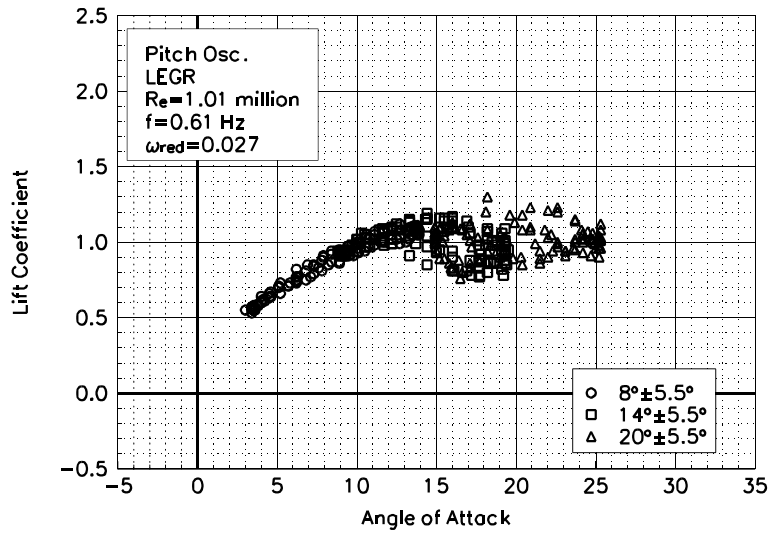


Figure C28. Lift coefficient vs α .

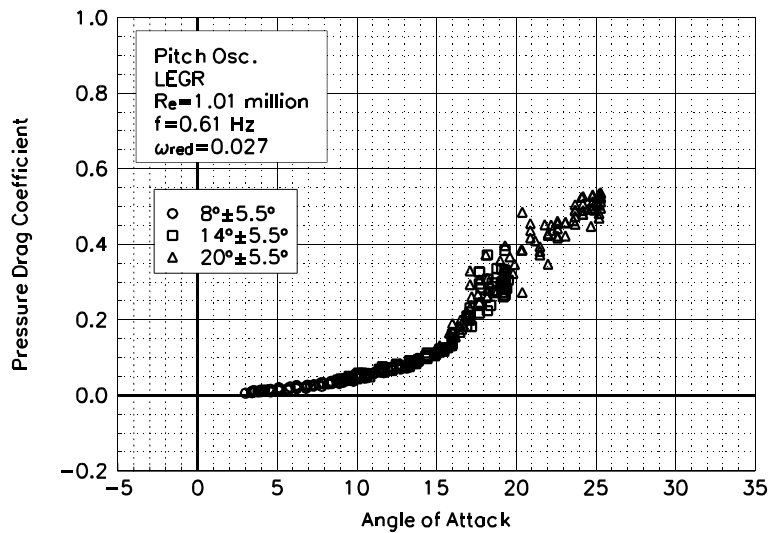


Figure C29. Pressure drag coefficient vs α .

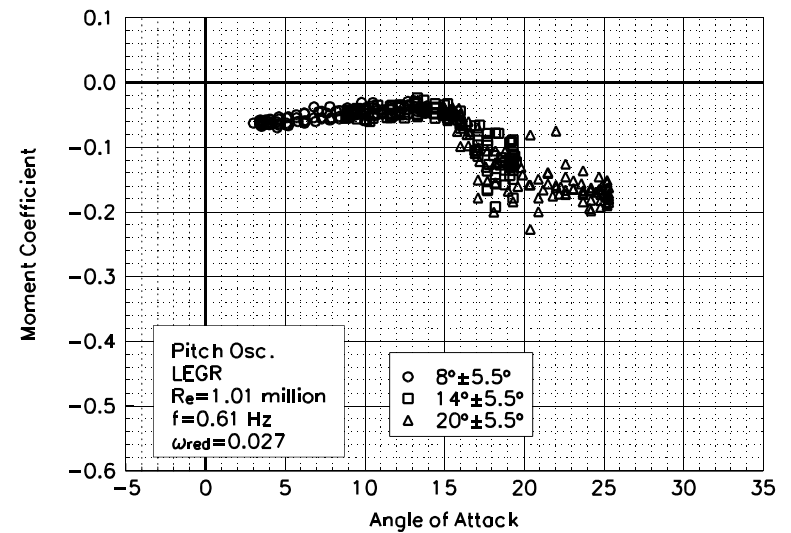


Figure C30. Moment coefficient vs α .

S813
LEGR
Re=1.01 million
 $\omega_{\text{reduced}}=0.027$

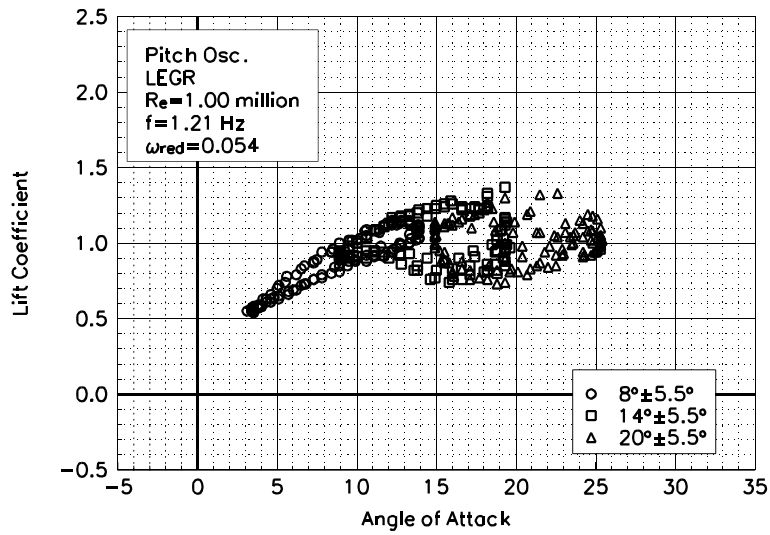


Figure C31. Lift coefficient vs α .

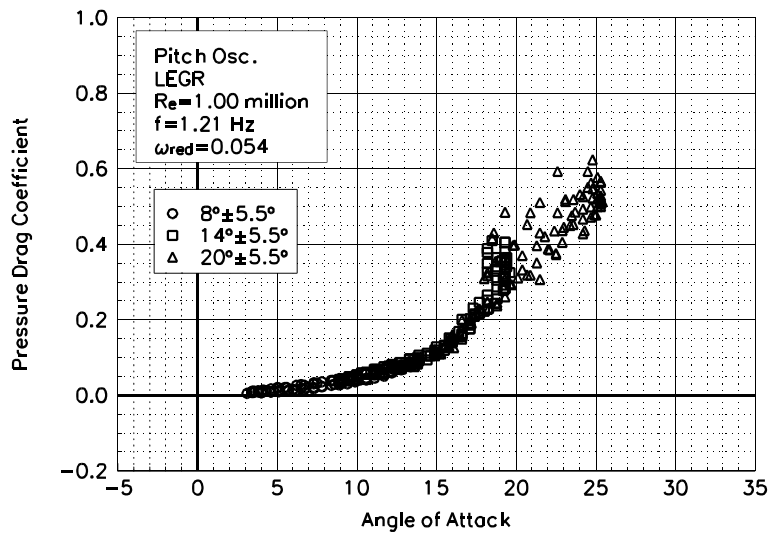


Figure C32. Pressure drag coefficient vs α .

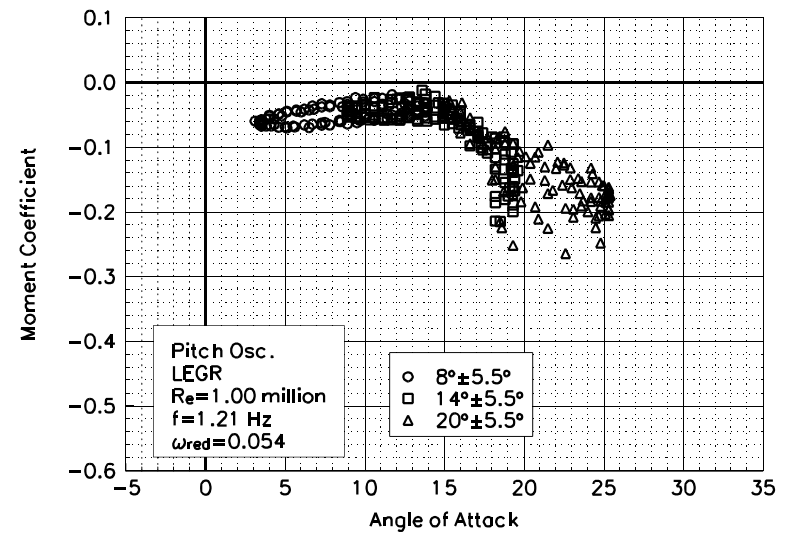


Figure C33. Moment coefficient vs α .

S813
LEGR
Re=1.00 million
 $\omega_{\text{reduced}}=0.054$

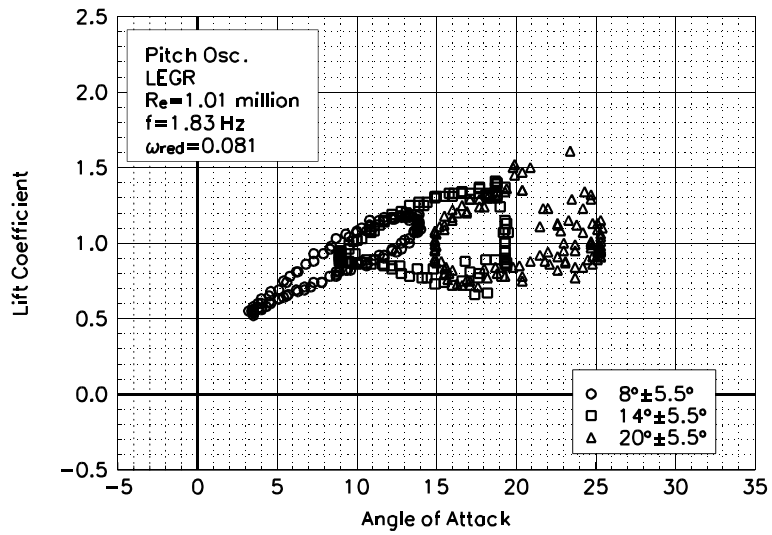


Figure C34. Lift coefficient vs α .

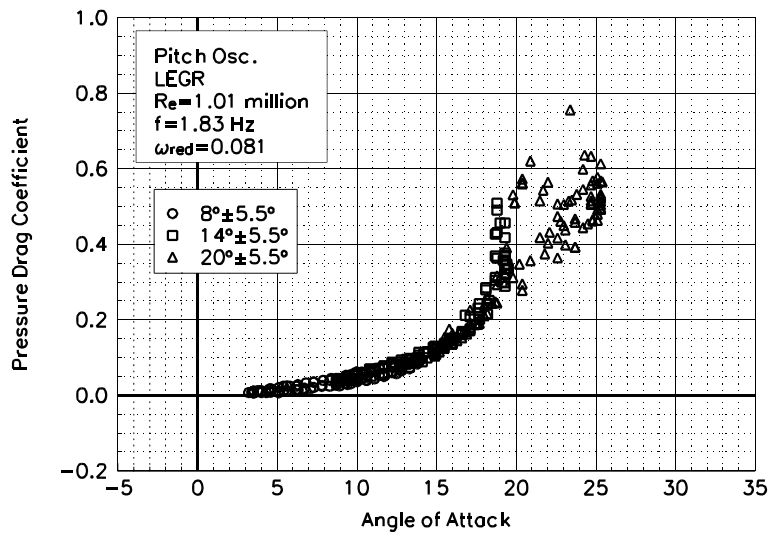


Figure C35. Pressure drag coefficient vs α .

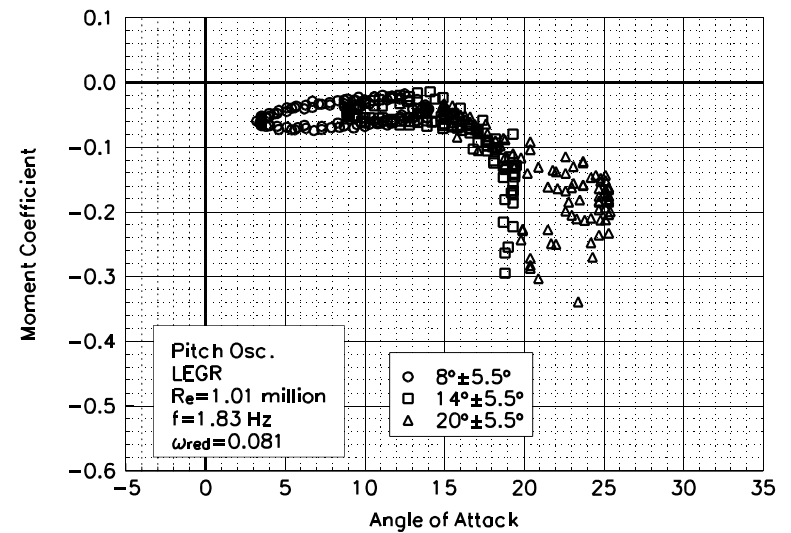


Figure C36. Moment coefficient vs α .

S813
LEGR
Re=1.01 million
 $\omega_{\text{reduced}}=0.081$

Unsteady Airfoil Characteristics

$\pm 5.5^\circ$ Sine, Re= 1.25 million

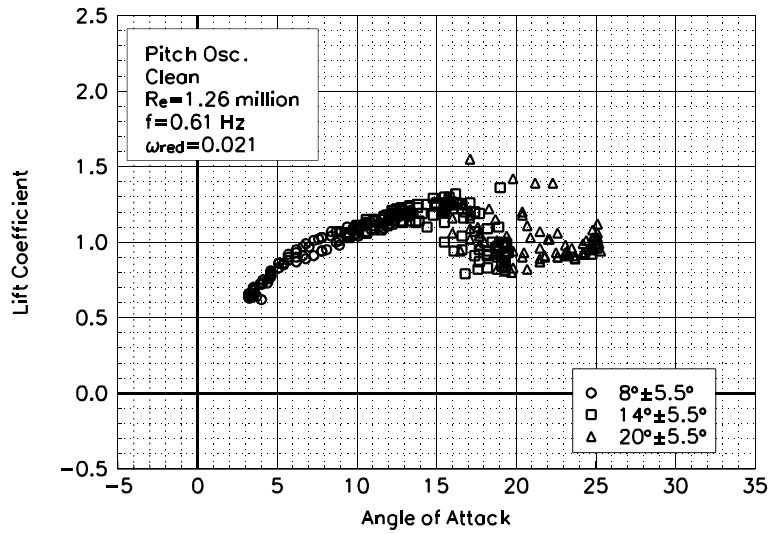


Figure C37. Lift coefficient vs α .

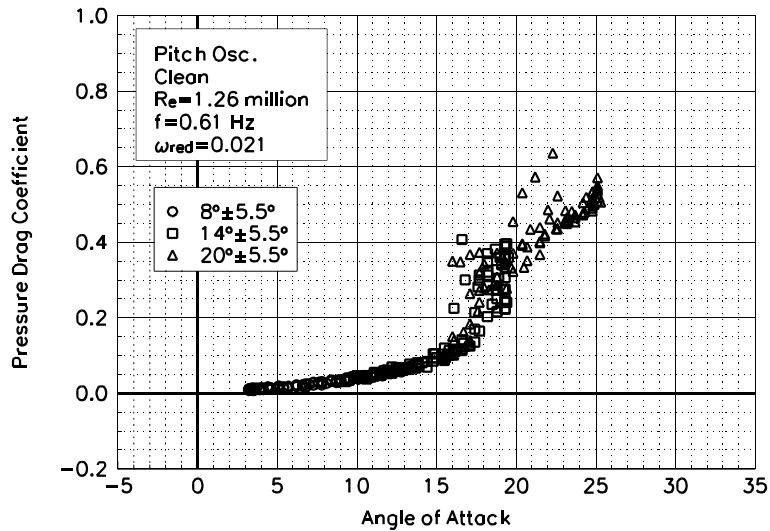


Figure C38. Pressure drag coefficient vs α .

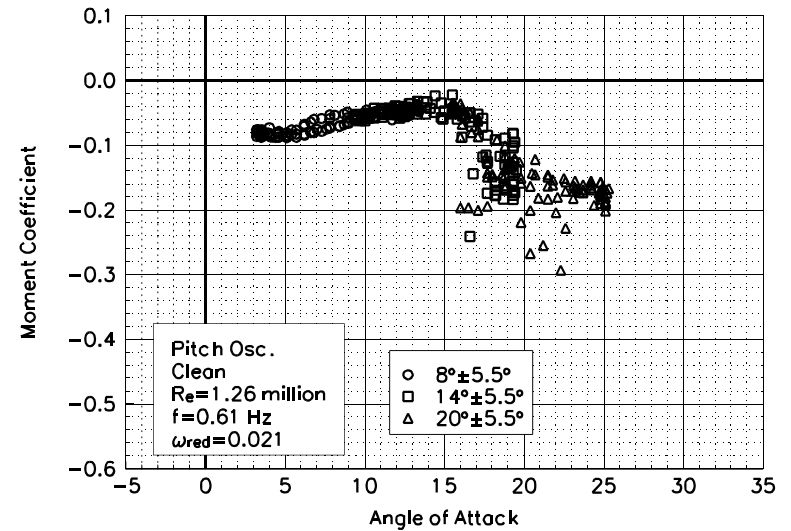


Figure C39. Moment coefficient vs α .

S813
Clean
Re=1.26 million
 $\omega_{\text{reduced}}=0.021$

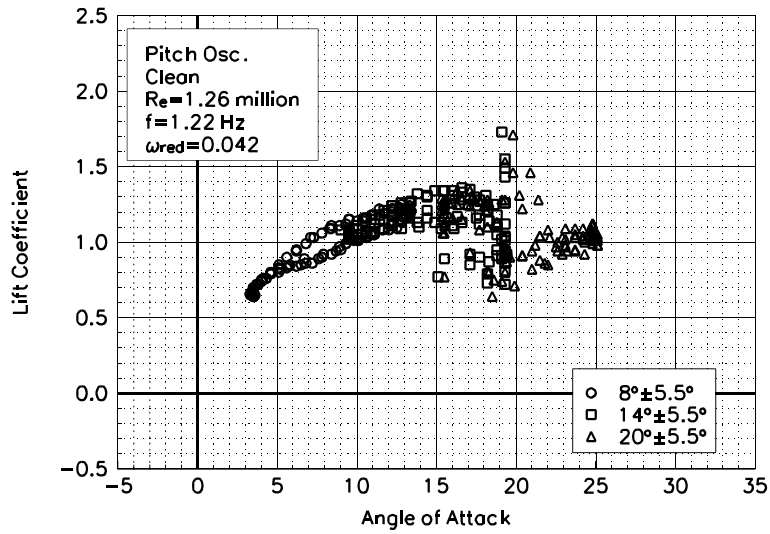


Figure C40. Lift coefficient vs α .

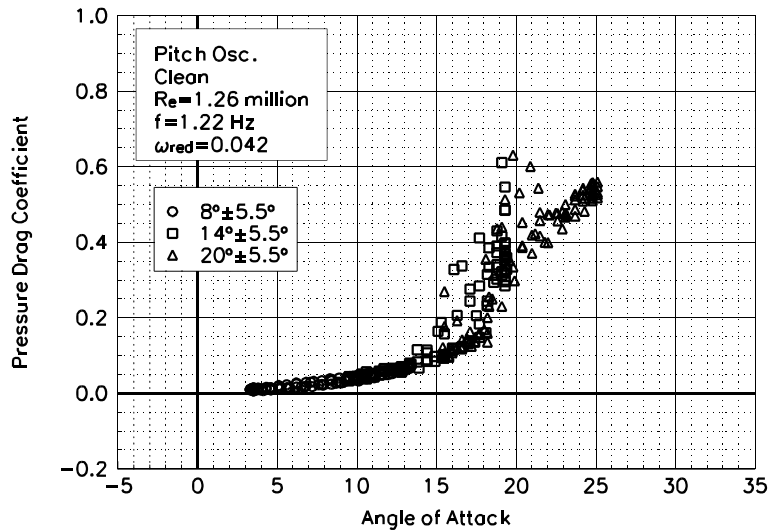


Figure C41. Pressure drag coefficient vs α .

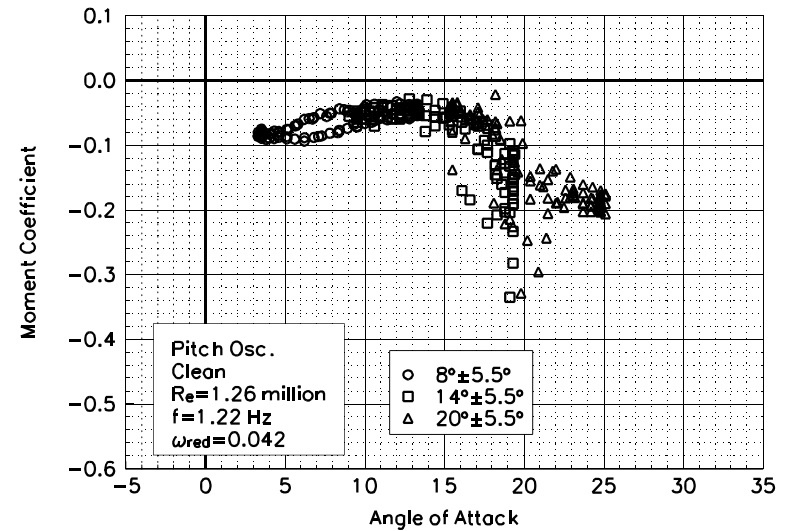


Figure C42. Moment coefficient vs α .

S813
Clean
Re=1.26 million
 $\omega_{\text{reduced}}=0.042$

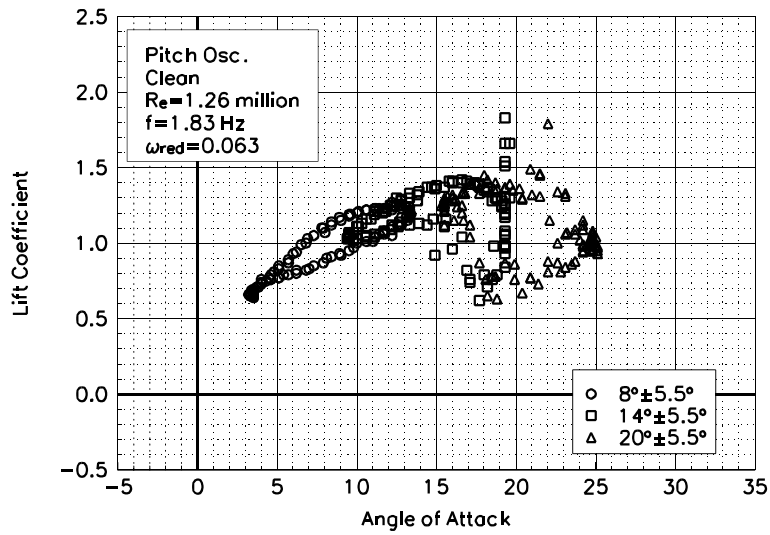


Figure C43. Lift coefficient vs α .

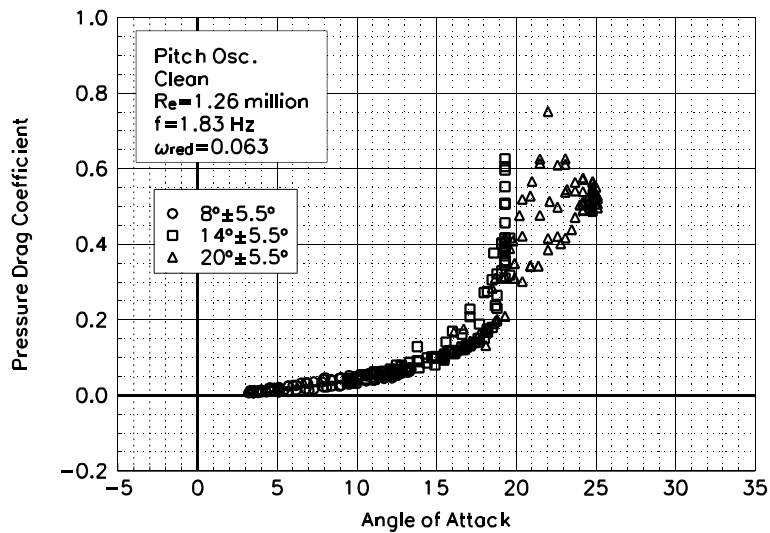


Figure C44. Pressure drag coefficient vs α .

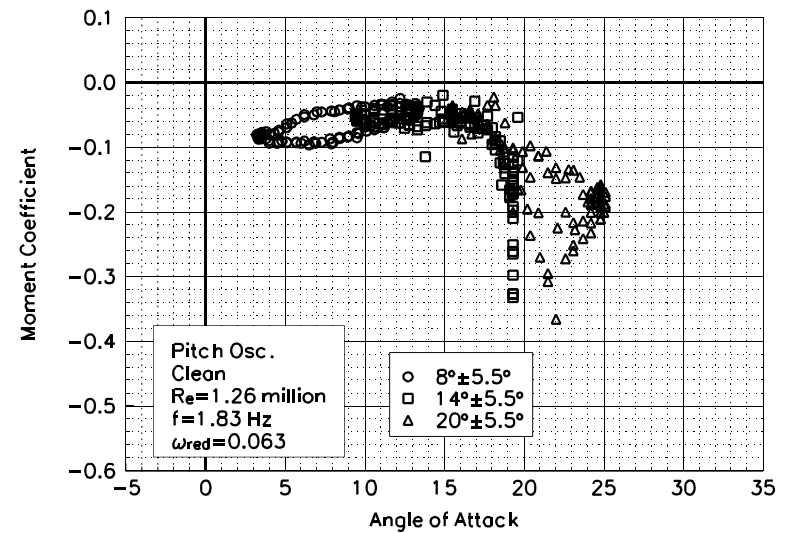


Figure C45. Moment coefficient vs α .

S813
Clean
Re=1.26 million
 $\omega_{\text{reduced}}=0.063$

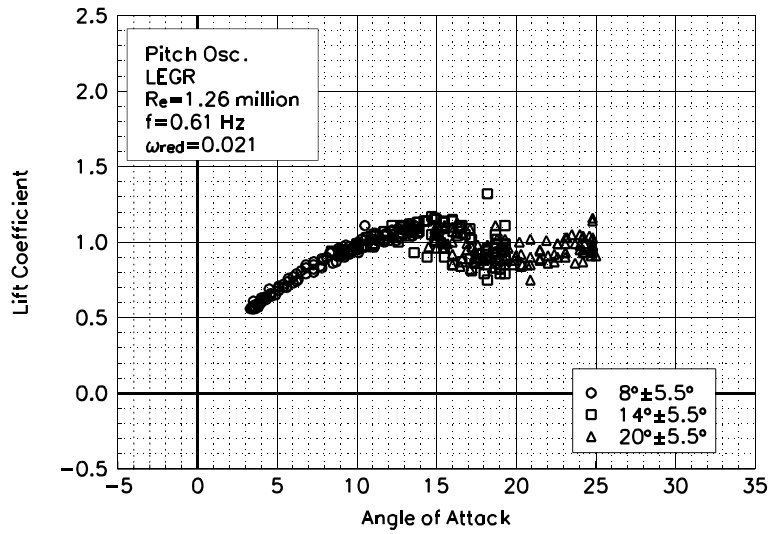


Figure C46. Lift coefficient vs α .

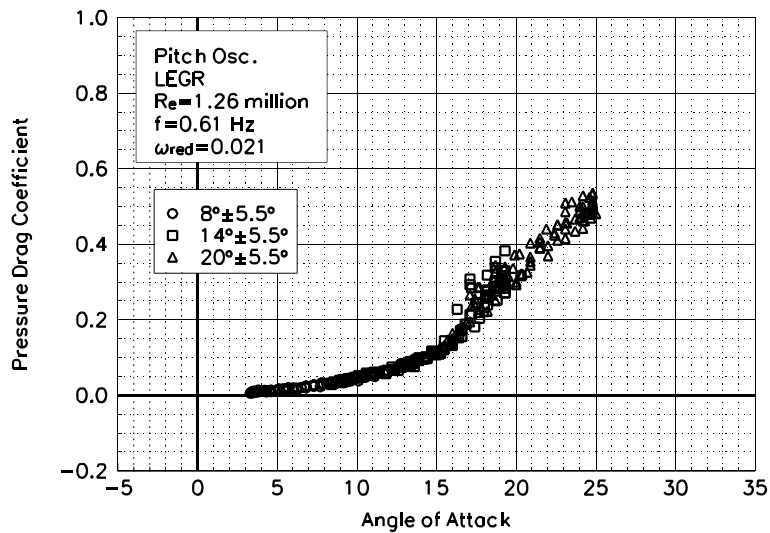


Figure C47. Pressure drag coefficient vs α .

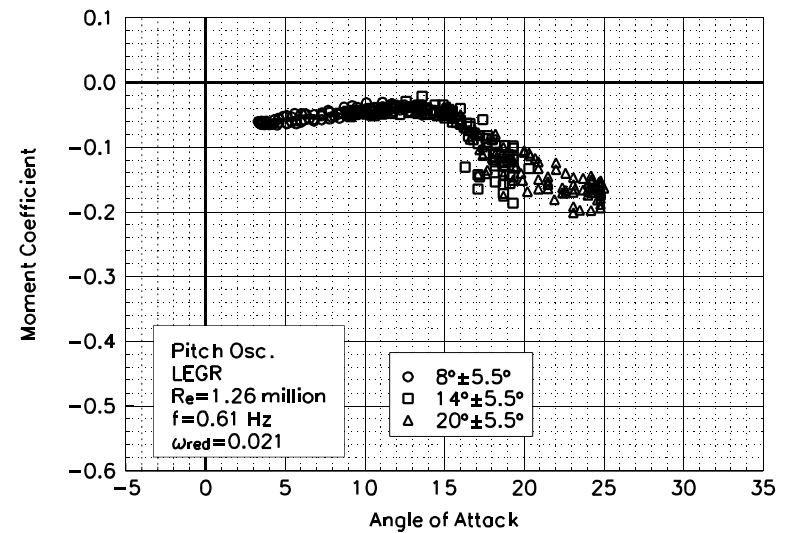


Figure C48. Moment coefficient vs α .

S813
LEGR
Re=1.26 million
 $\omega_{\text{reduced}}=0.021$

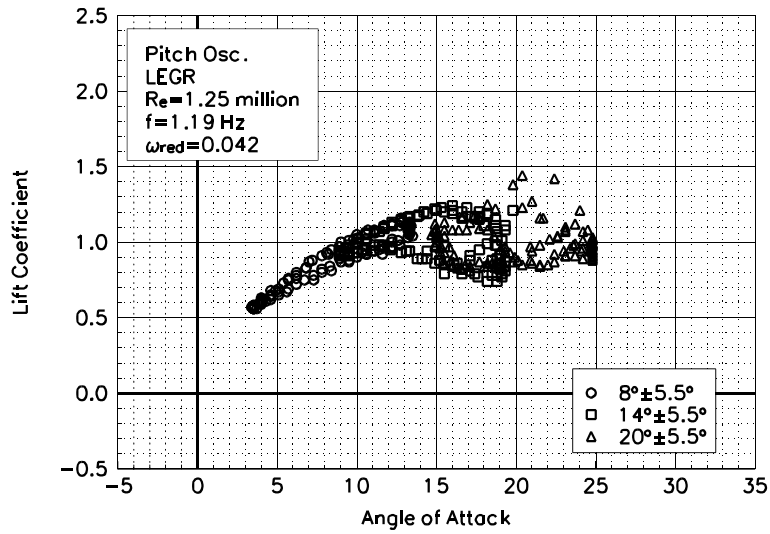


Figure C49. Lift coefficient vs α .

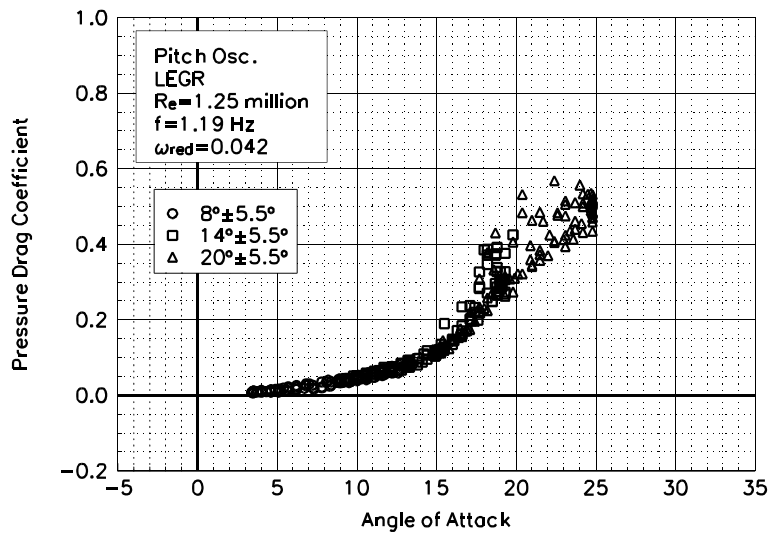


Figure C50. Pressure drag coefficient vs α .

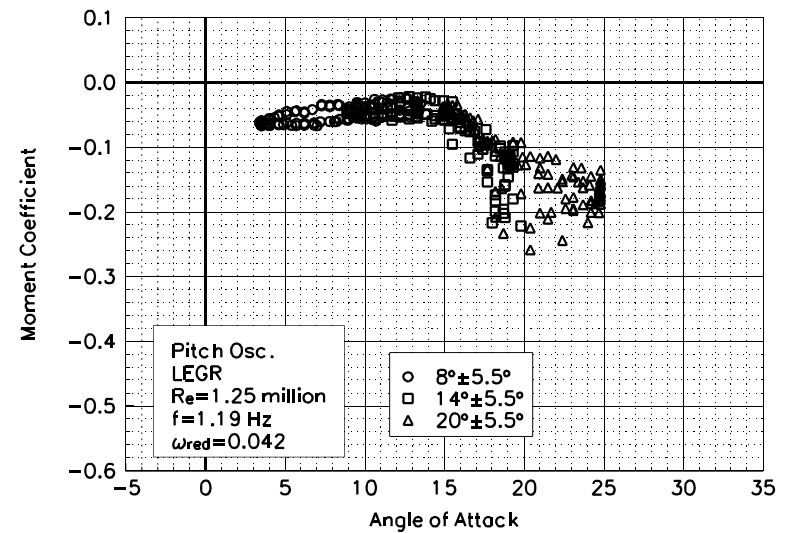


Figure C51. Moment coefficient vs α .

S813
LEGR
Re=1.25 million
 $\omega_{\text{reduced}}=0.042$

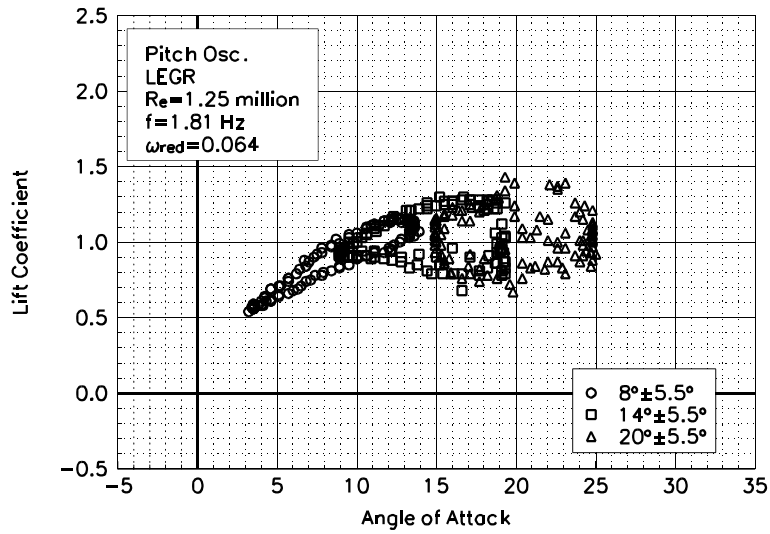


Figure C52. Lift coefficient vs α .

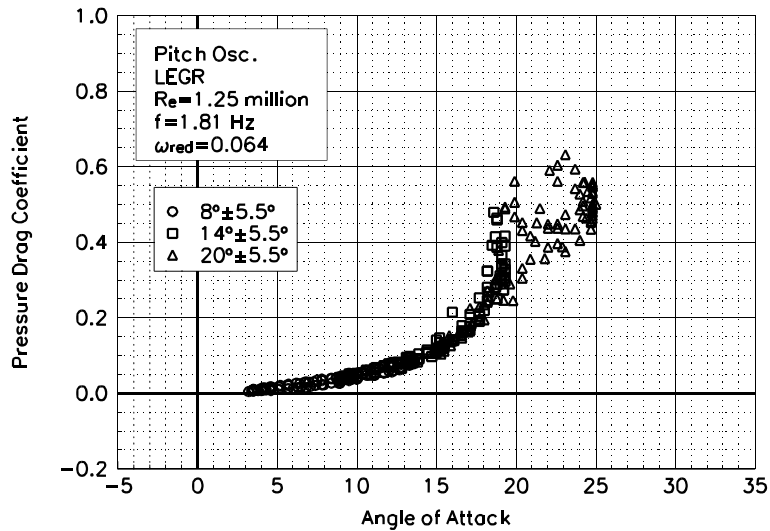


Figure C53. Pressure drag coefficient vs α .

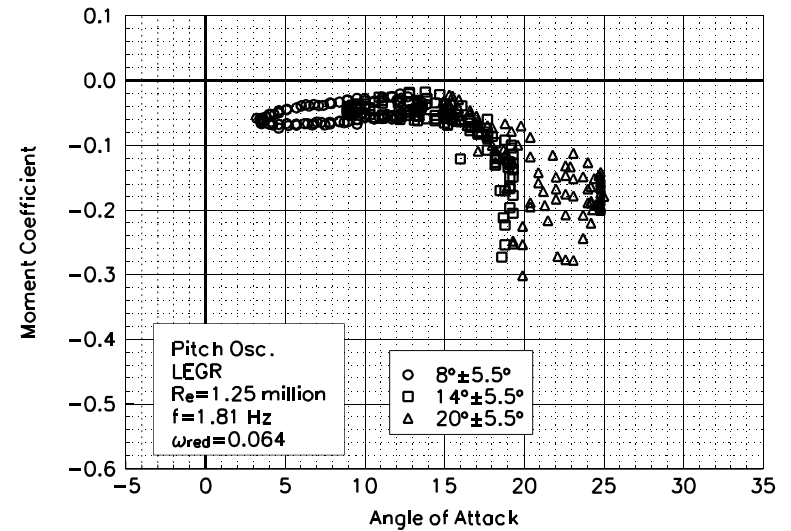


Figure C54. Moment coefficient vs α .

S813
LEGR
Re=1.25 million
 $\omega_{\text{reduced}}=0.064$

Unsteady Airfoil Characteristics

$\pm 5.5^\circ$ Sine, Re = 1.4 million

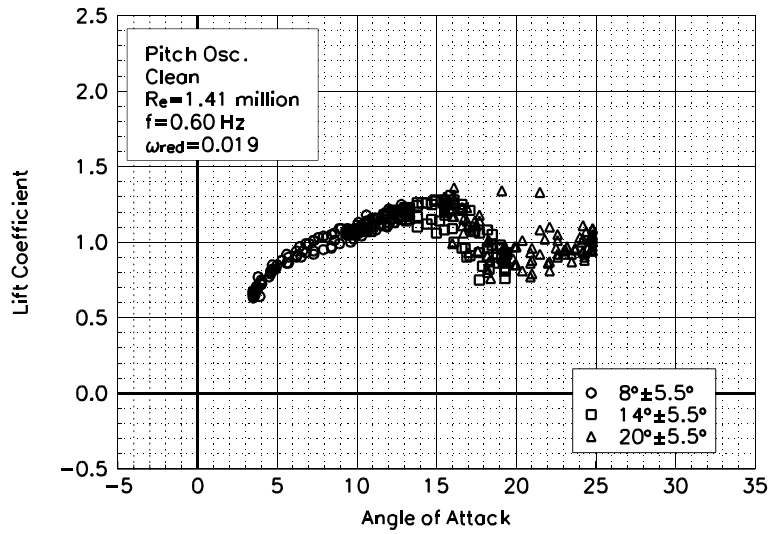


Figure C55. Lift coefficient vs α .

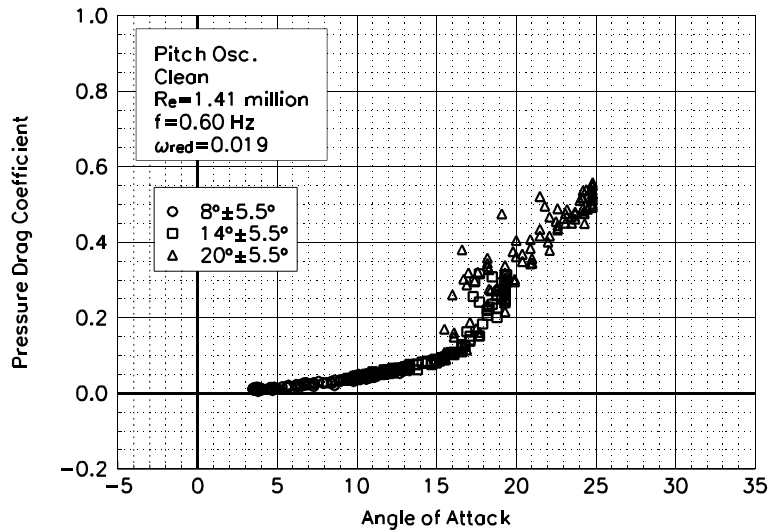


Figure C56. Pressure drag coefficient vs α .

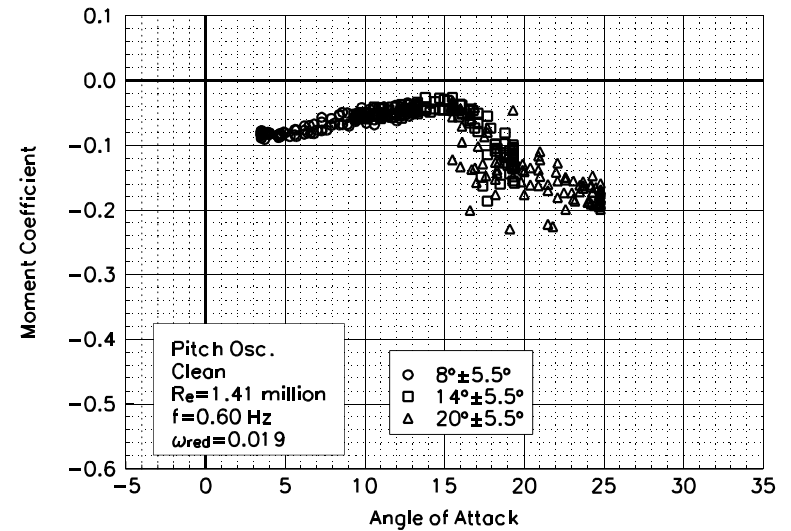


Figure C57. Moment coefficient vs α .

S813
Clean
Re=1.41 million
 $\omega_{\text{reduced}}=0.019$

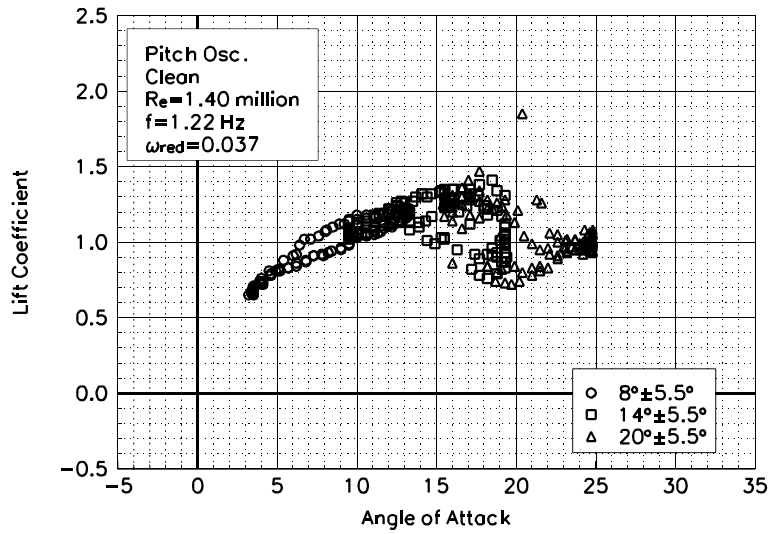


Figure C58. Lift coefficient vs α .

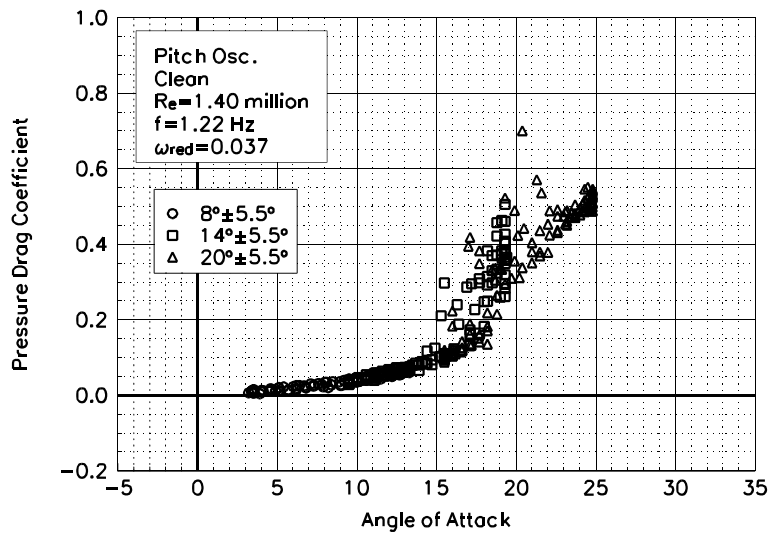


Figure C59. Pressure drag coefficient vs α .

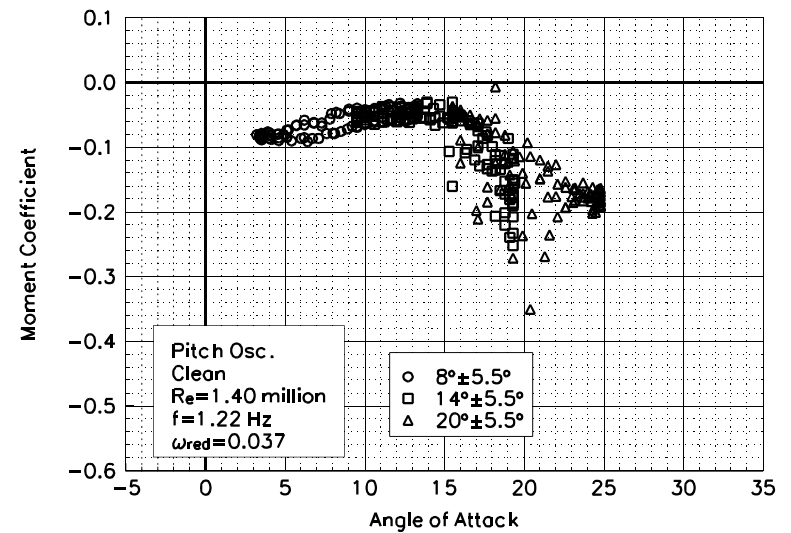


Figure C60. Moment coefficient vs α .

S813
Clean
Re=1.40 million
 $\omega_{\text{reduced}}=0.037$

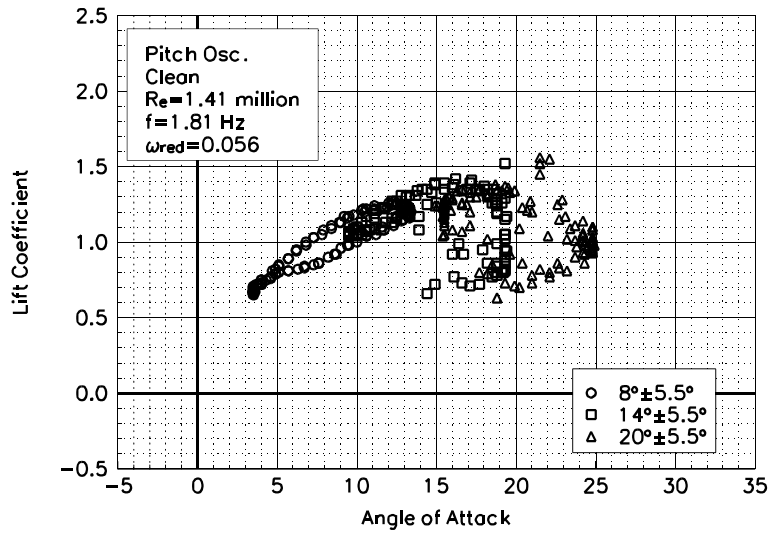


Figure C61. Lift coefficient vs α .

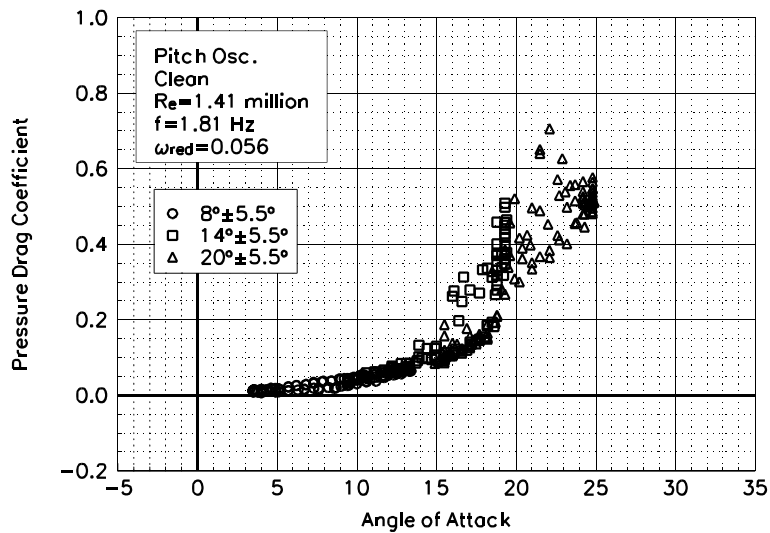


Figure C62. Pressure drag coefficient vs α .

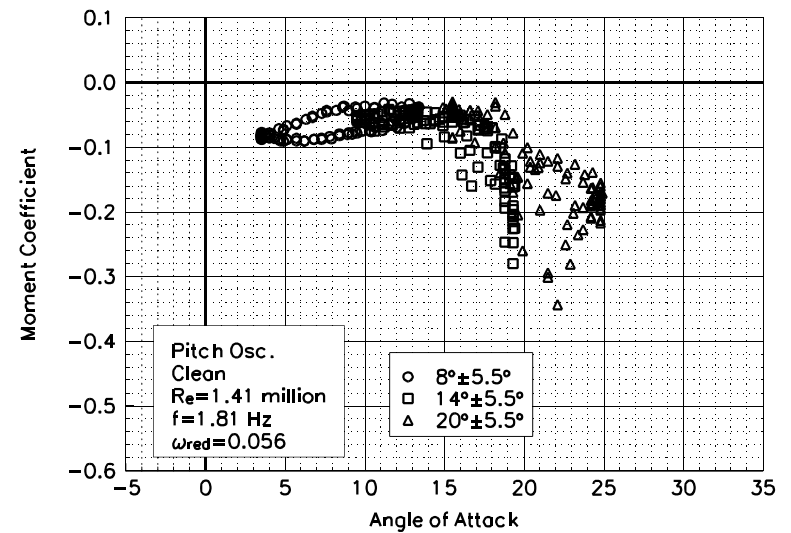


Figure C63. Moment coefficient vs α .

S813
Clean
Re=1.41 million
 $\omega_{\text{reduced}}=0.056$

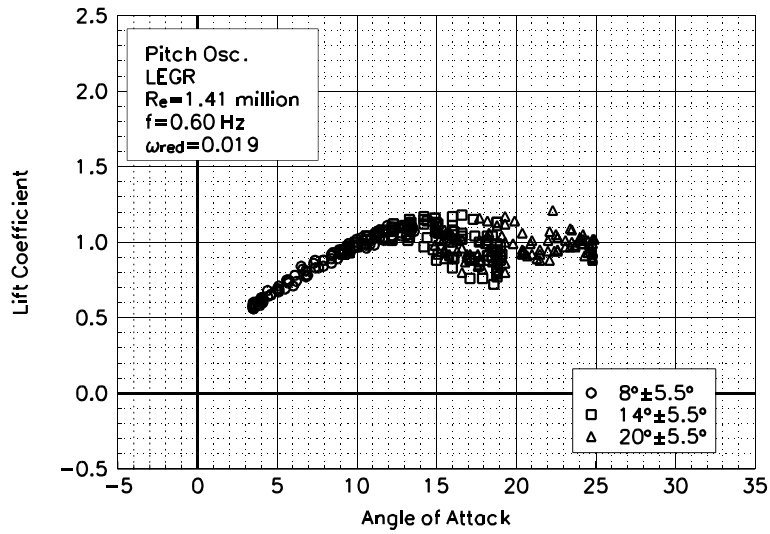


Figure C64. Lift coefficient vs α .

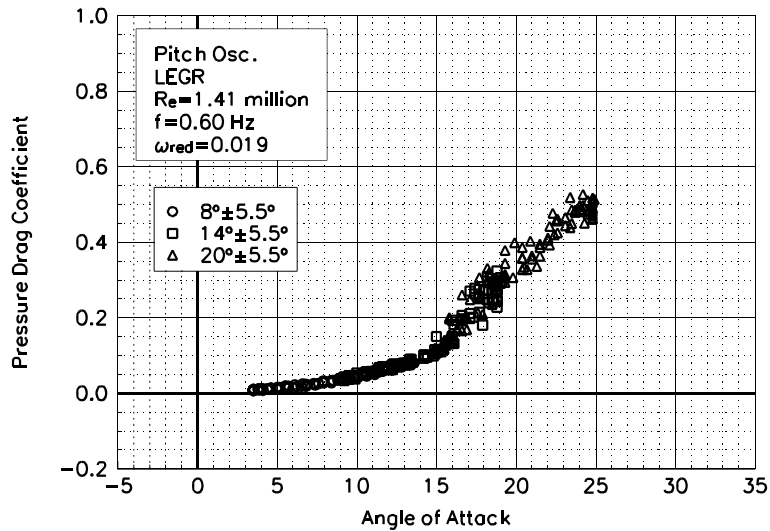


Figure C65. Pressure drag coefficient vs α .

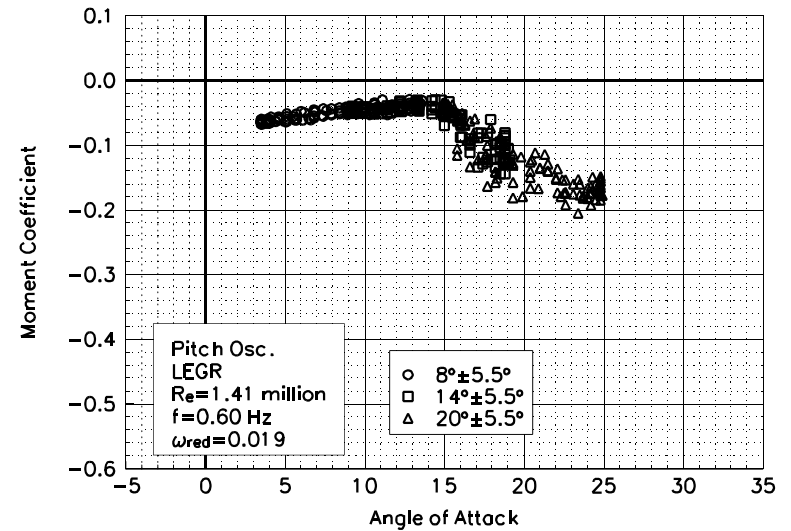


Figure C66. Moment coefficient vs α .

S813
LEGR
Re=1.41 million
 $\omega_{\text{reduced}}=0.019$

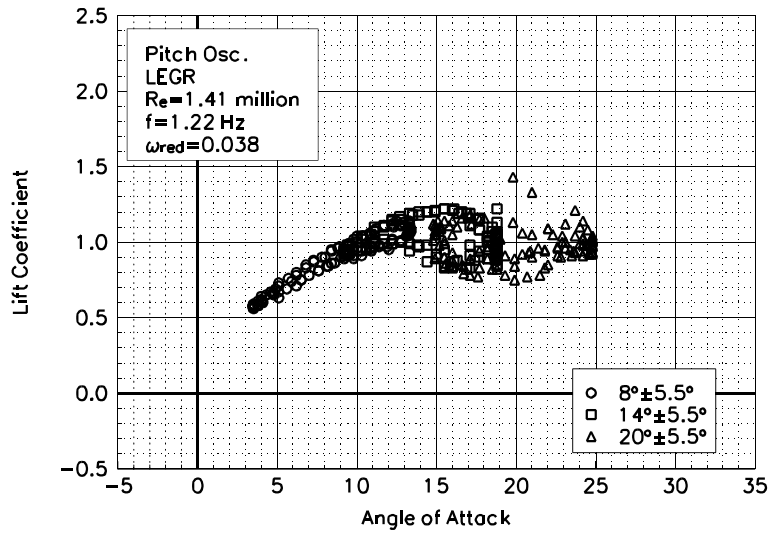


Figure C67. Lift coefficient vs α .

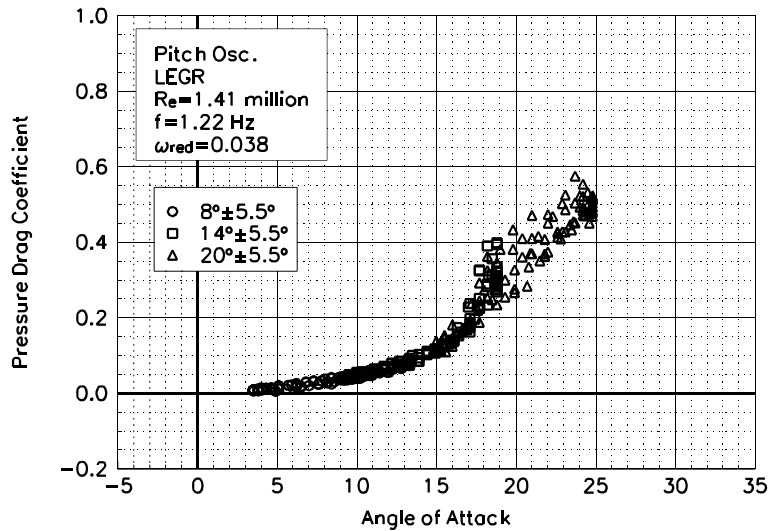


Figure C68. Pressure drag coefficient vs α .

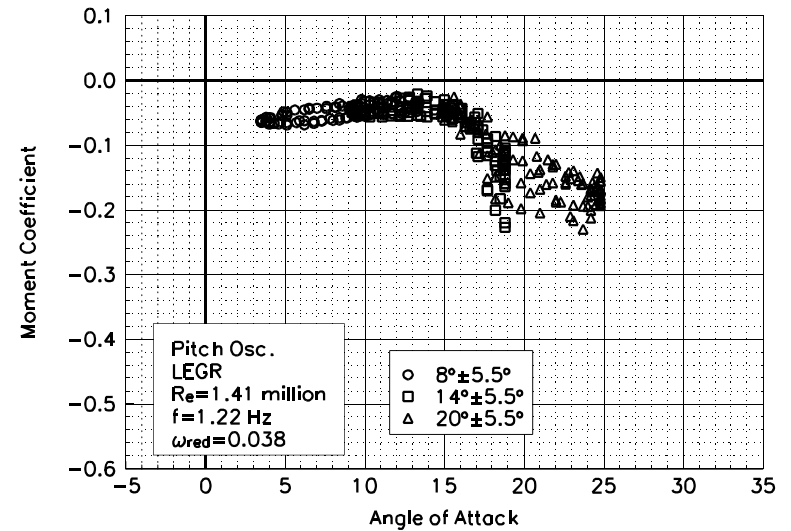


Figure C69. Moment coefficient vs α .

S813
LEGR
Re=1.41 million
 $\omega_{\text{reduced}}=0.038$

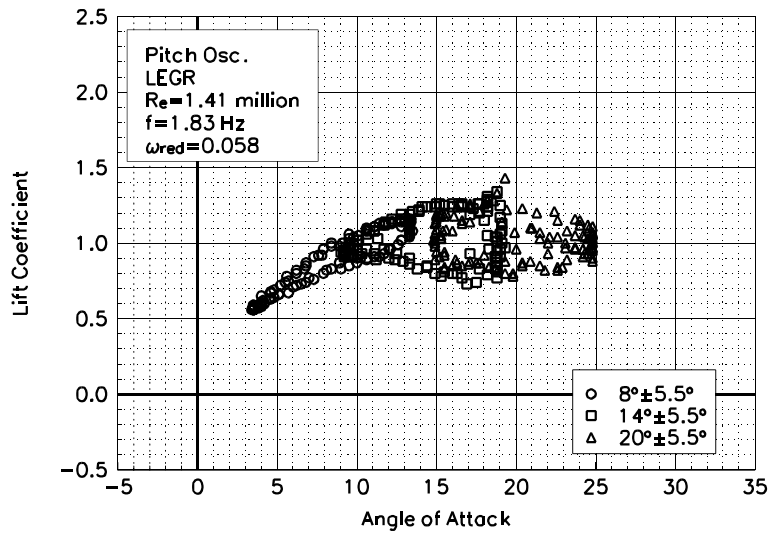


Figure C70. Lift coefficient vs α .

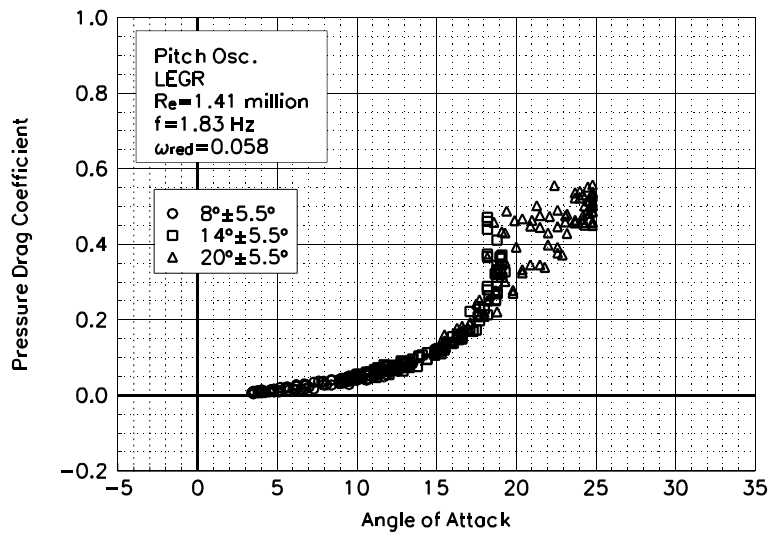


Figure C71. Pressure drag coefficient vs α .

S813
LEGR
Re=1.41 million
 $\omega_{\text{reduced}}=0.058$

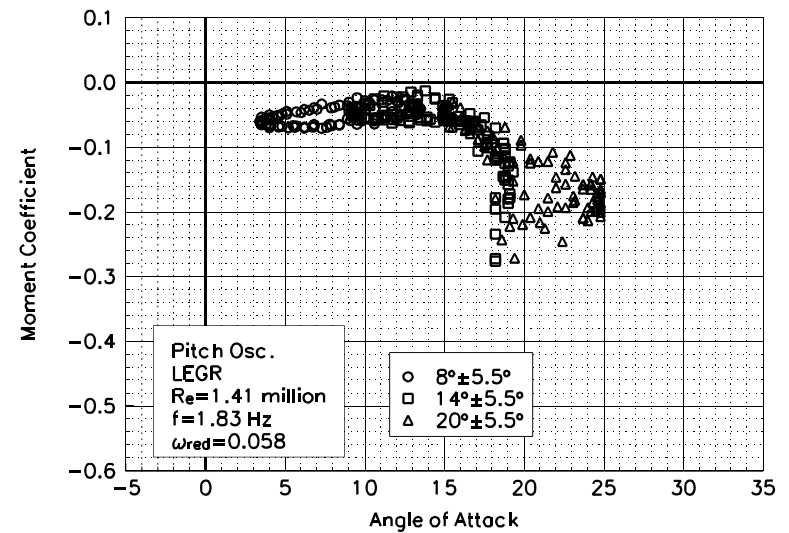


Figure C72. Moment coefficient vs α .

Unsteady Airfoil Characteristics

$\pm 10^\circ$ Sine, Re = 0.75 million

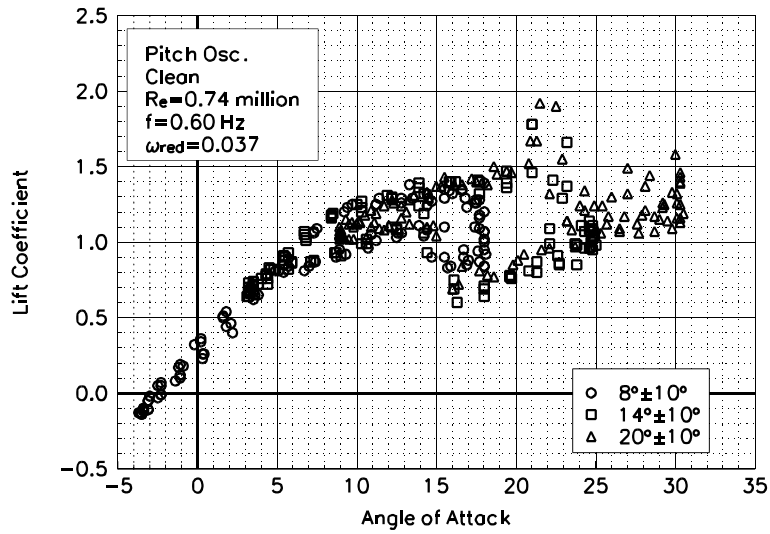


Figure C73. Lift coefficient vs α .

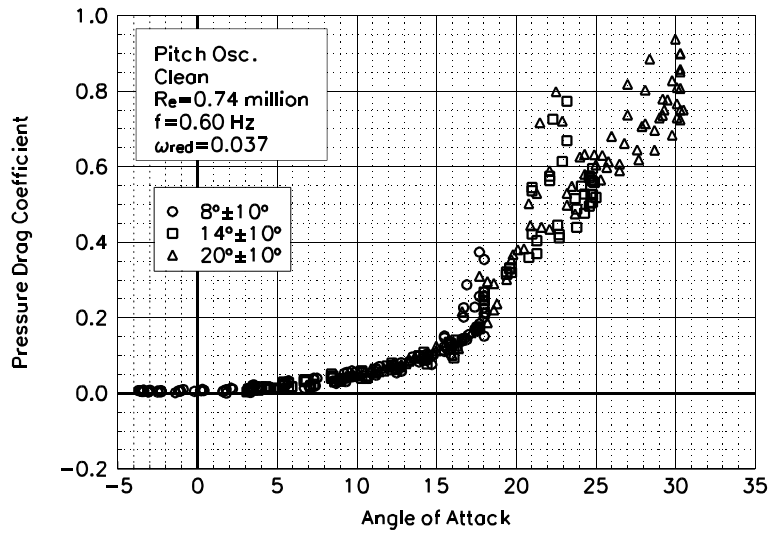


Figure C74. Pressure drag coefficient vs α .

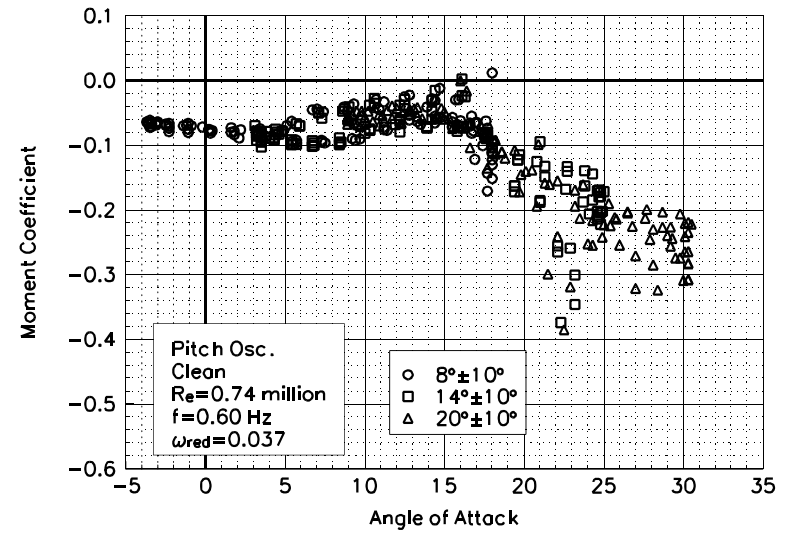


Figure C75. Moment coefficient vs α .

S813
Clean
Re=0.74 million
 $\omega_{\text{reduced}}=0.037$

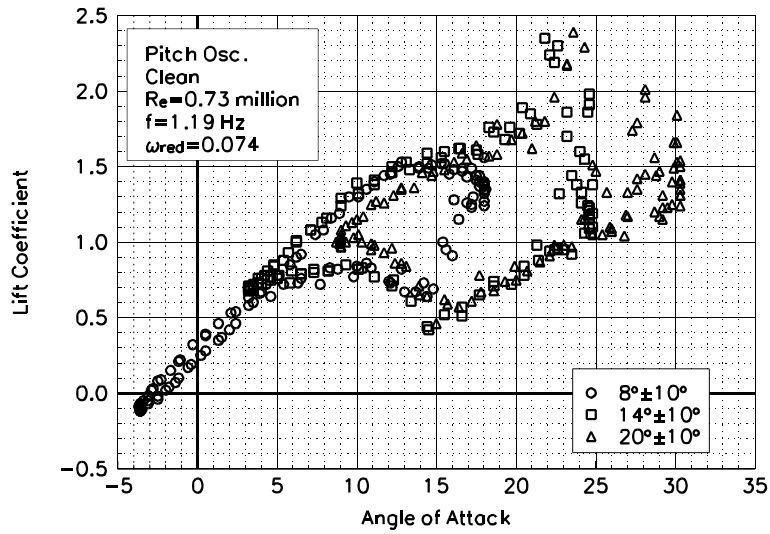


Figure C76. Lift coefficient vs α .

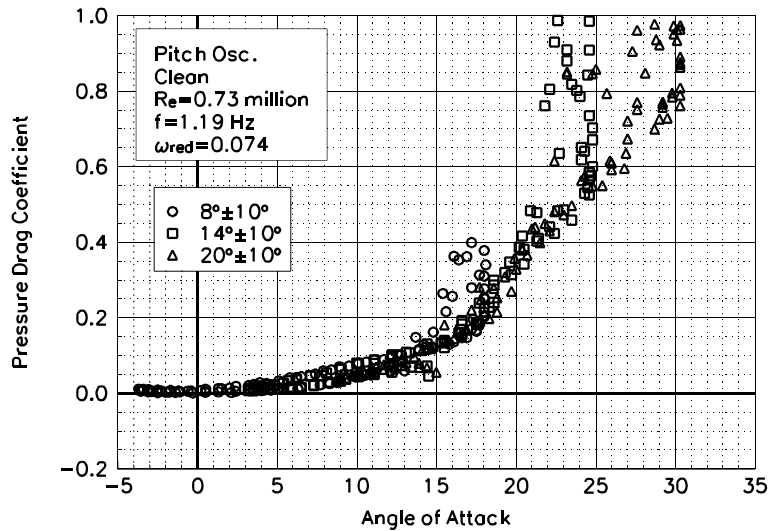


Figure C77. Pressure drag coefficient vs α .

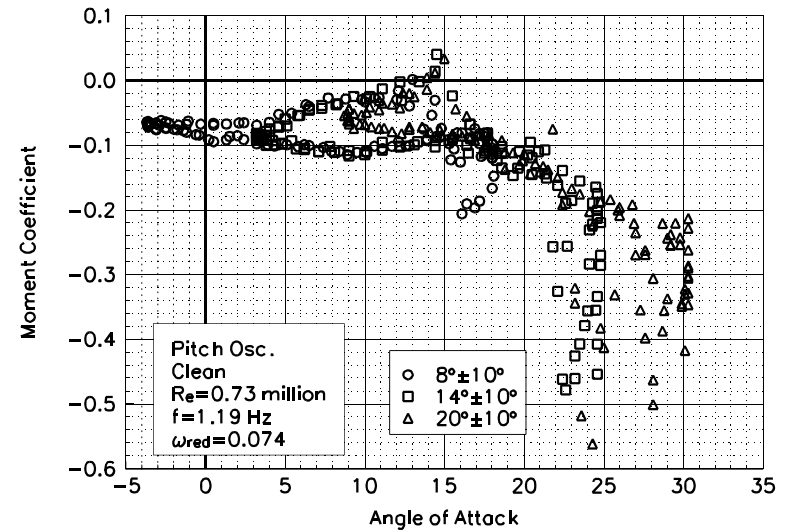


Figure C78. Moment coefficient vs α .

S813
Clean
Re=0.73 million
 $\omega_{\text{reduced}}=0.074$

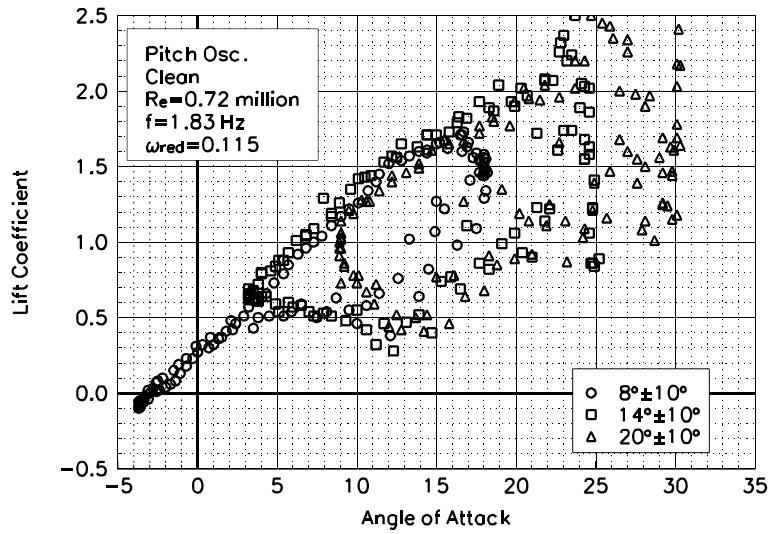


Figure C79. Lift coefficient vs α .

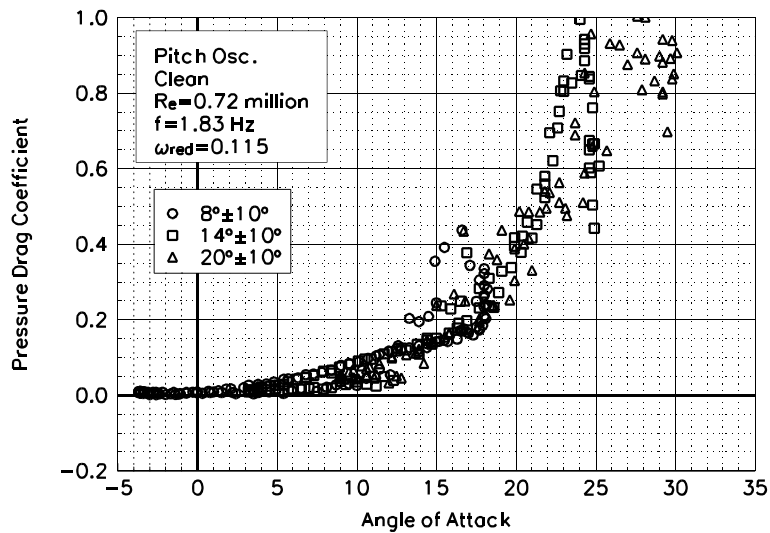


Figure C80. Pressure drag coefficient vs α .

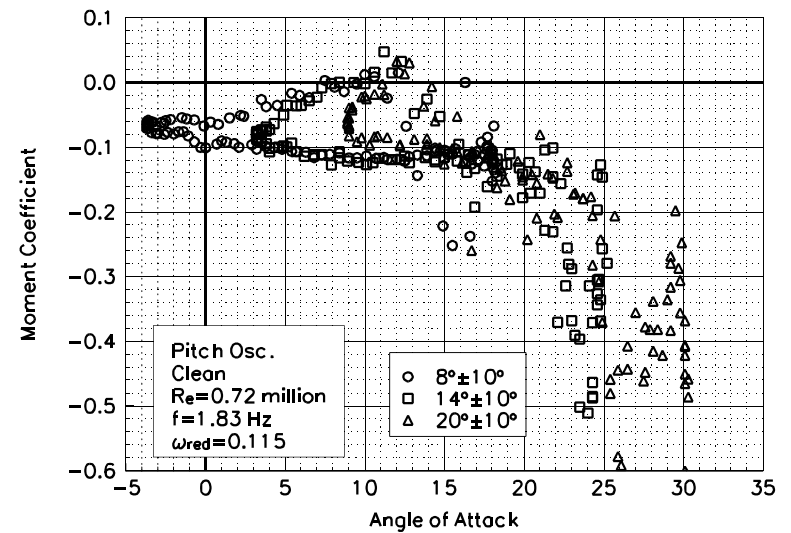


Figure C81. Moment coefficient vs α .

S813
Clean
Re=0.72 million
 $\omega_{\text{reduced}}=0.115$

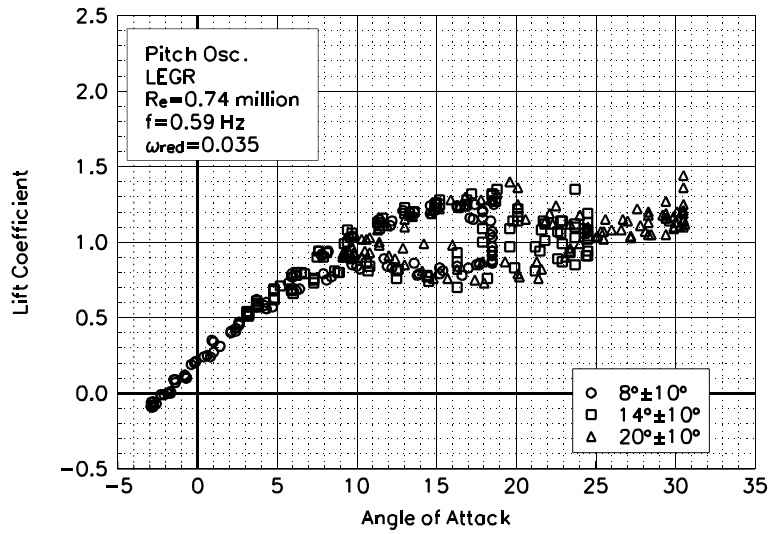


Figure C82. Lift coefficient vs α .

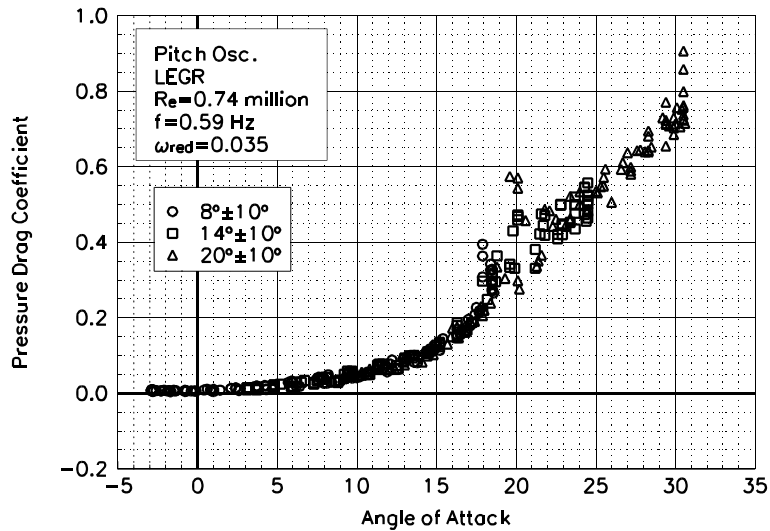


Figure C83. Pressure drag coefficient vs α .

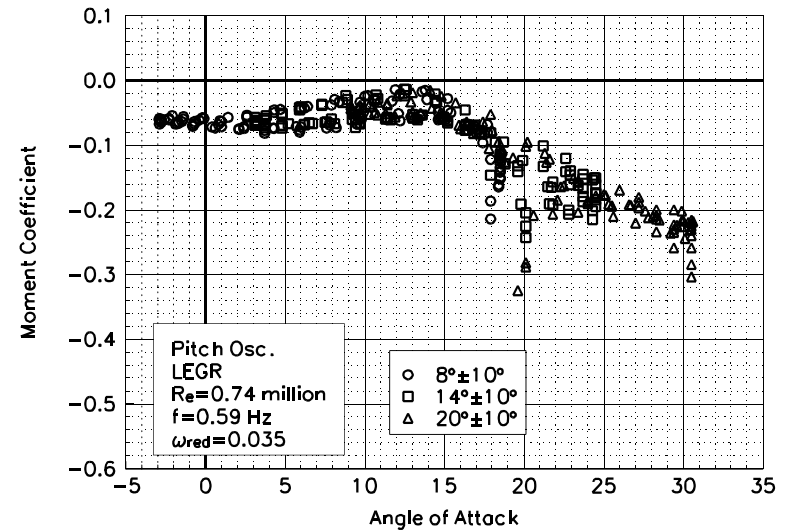


Figure C84. Moment coefficient vs α .

S813
LEGR
Re=0.74 million
 $\omega_{\text{reduced}}=0.035$

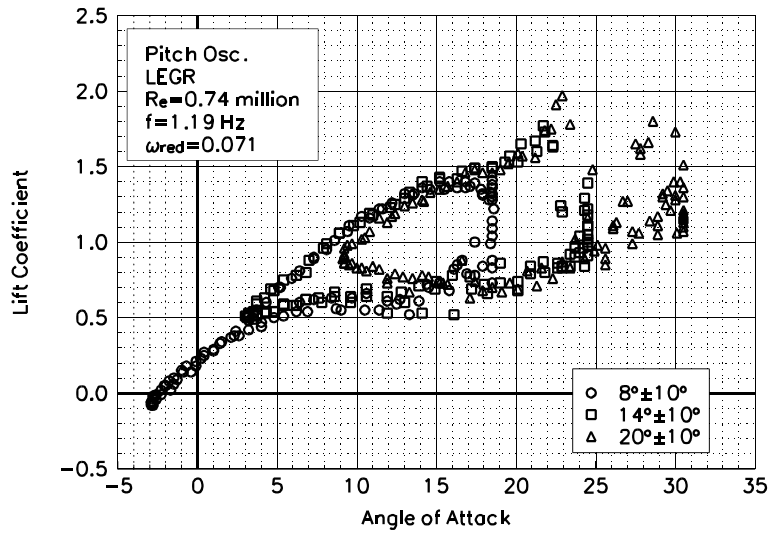


Figure C85. Lift coefficient vs α .

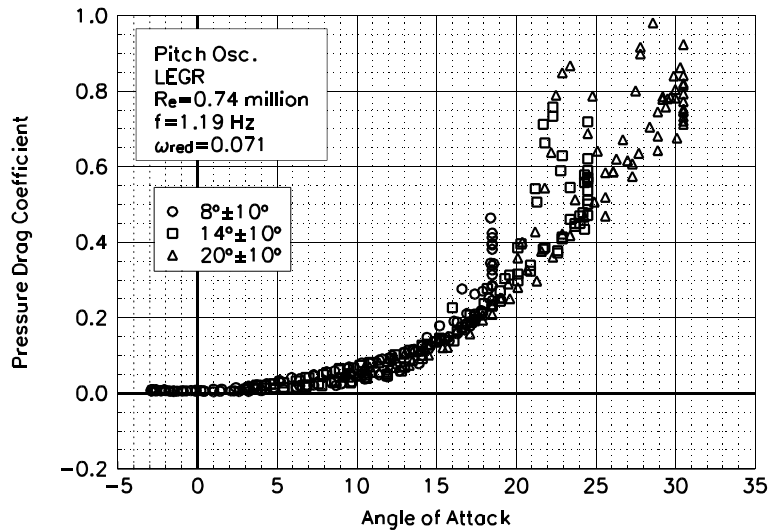


Figure C86. Pressure drag coefficient vs α .

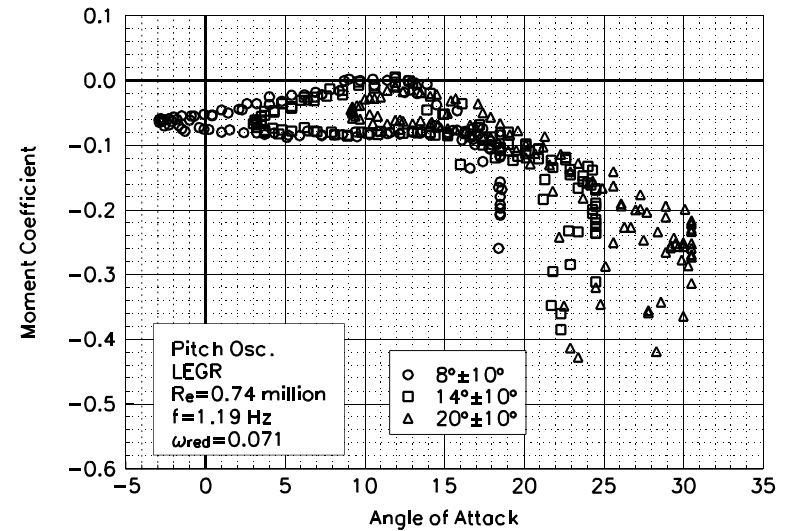


Figure C87. Moment coefficient vs α .

S813
LEGR
Re=0.74 million
 $\omega_{\text{reduced}}=0.071$

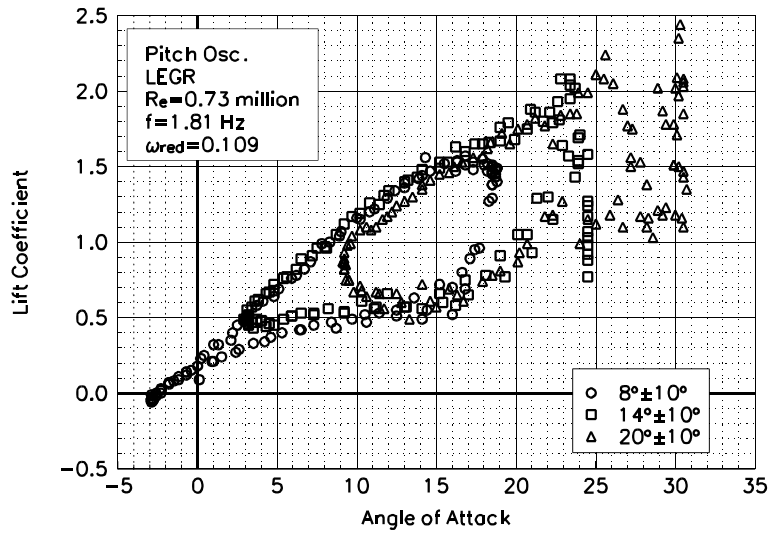


Figure C88. Lift coefficient vs α .

S813
LEGR
 $Re=0.73$ million
 $\omega_{reduced}=0.109$

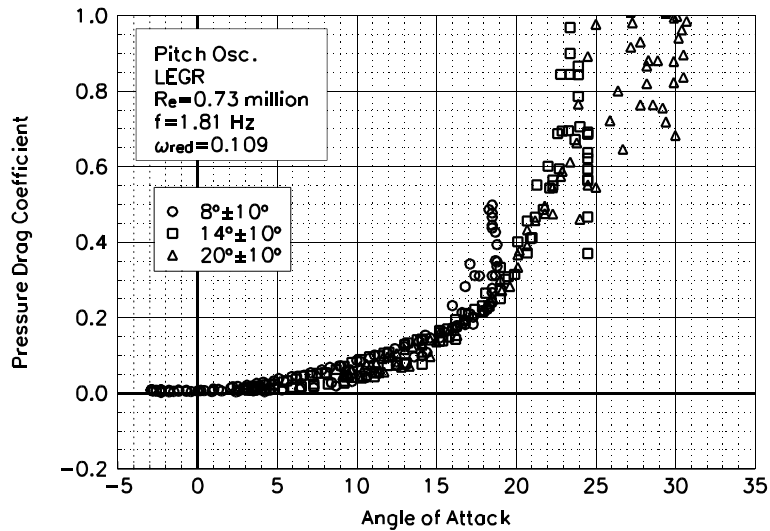


Figure C89. Pressure drag coefficient vs α .

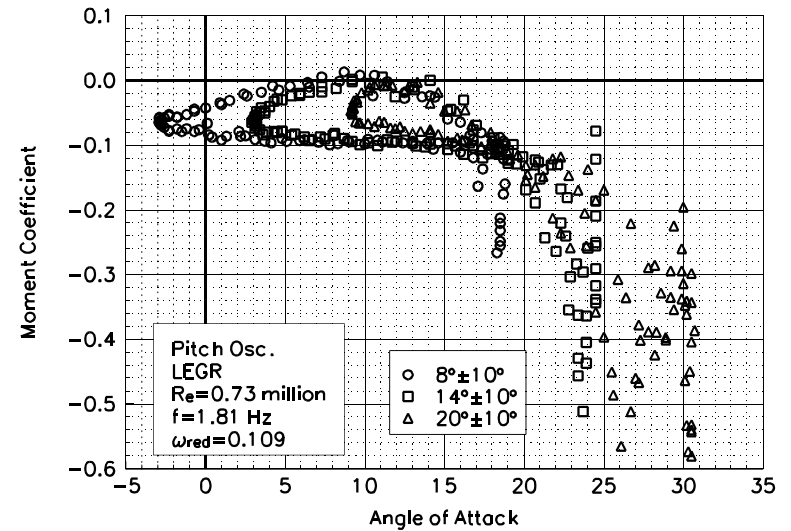


Figure C90. Moment coefficient vs α .

Unsteady Airfoil Characteristics

$\pm 10^\circ$ Sine, $Re = 1$ million

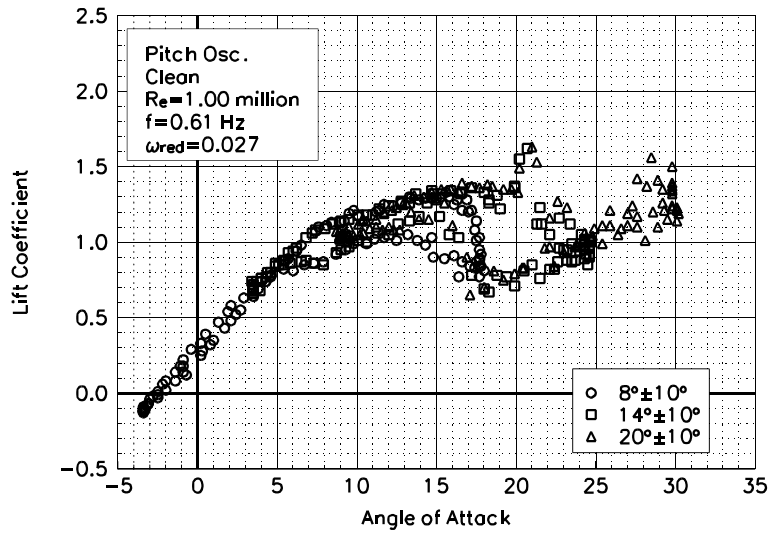


Figure C91. Lift coefficient vs α .

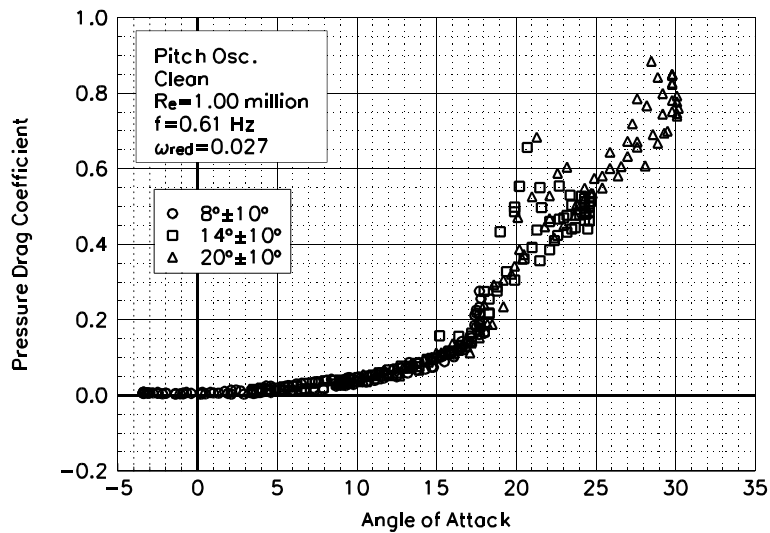


Figure C92. Pressure drag coefficient vs α .

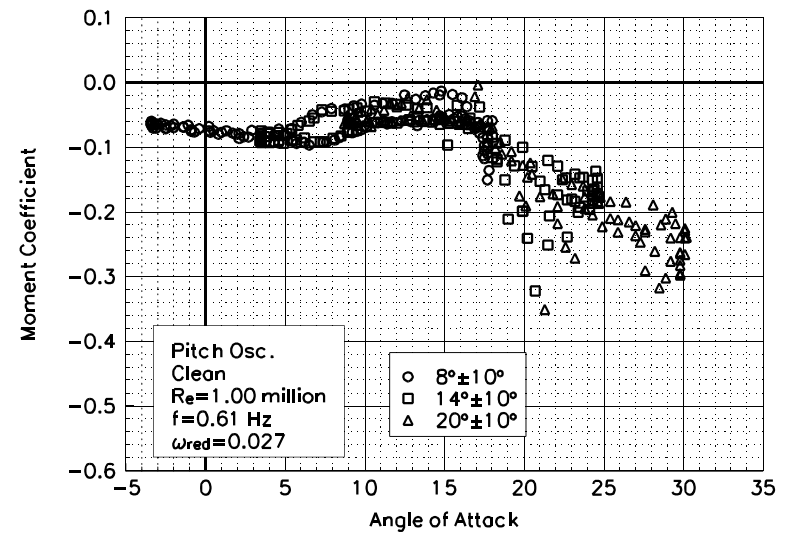


Figure C93. Moment coefficient vs α .

S813
Clean
Re=1.00 million
 $\omega_{\text{reduced}}=0.027$

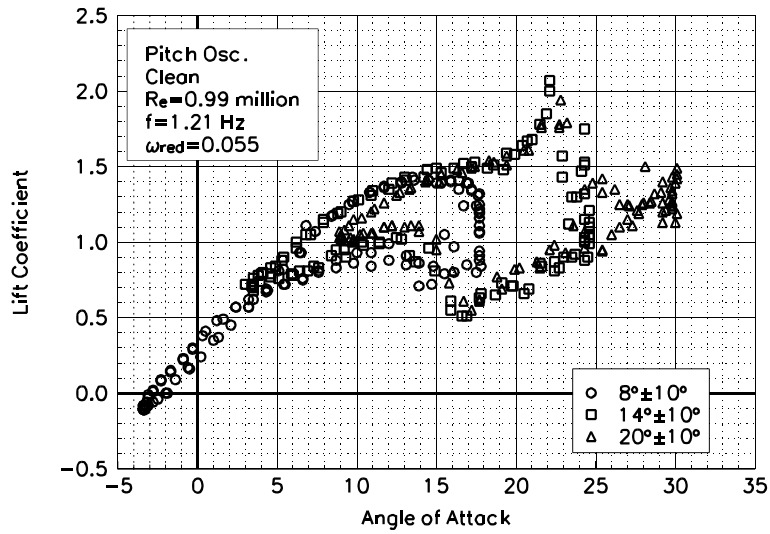


Figure C94. Lift coefficient vs α .

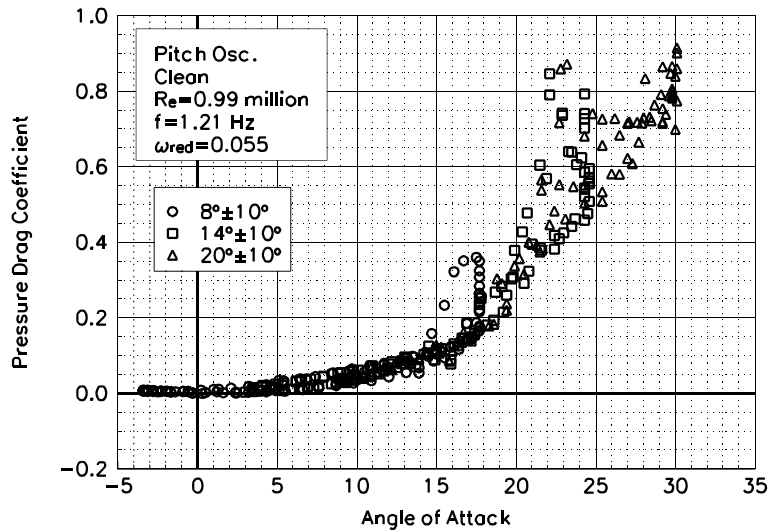


Figure C95. Pressure drag coefficient vs α .

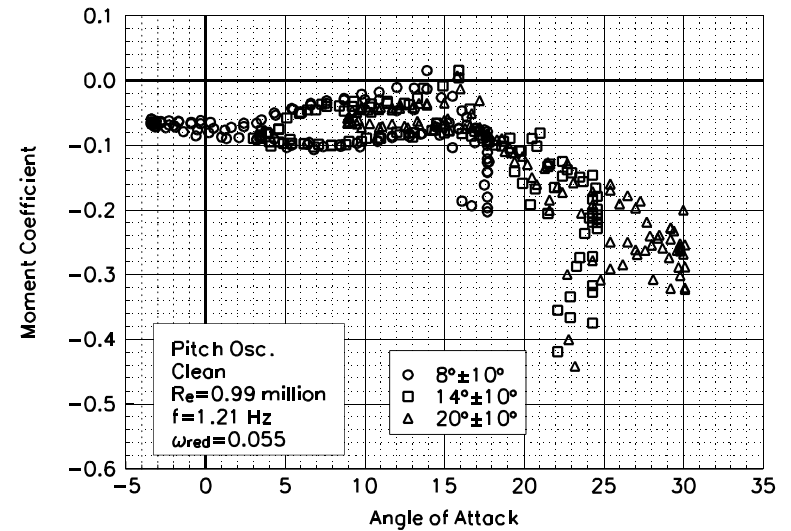


Figure C96. Moment coefficient vs α .

S813
Clean
Re=0.99 million
 $\omega_{\text{reduced}}=0.055$

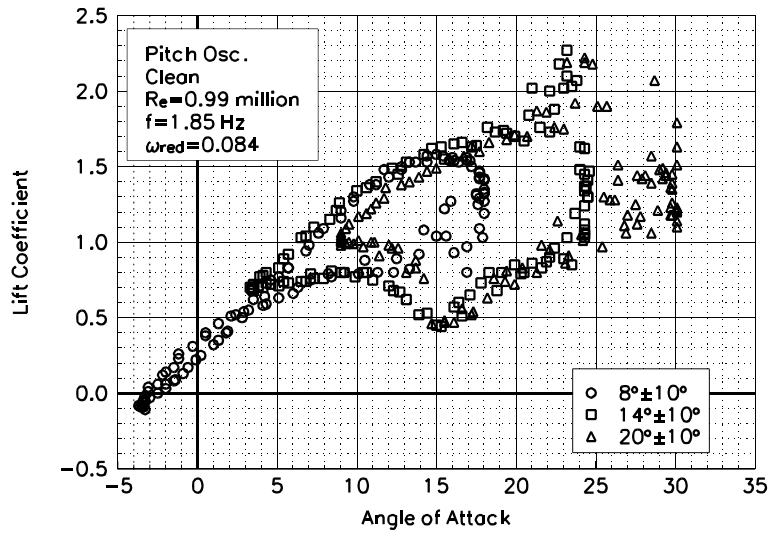


Figure C97. Lift coefficient vs α .

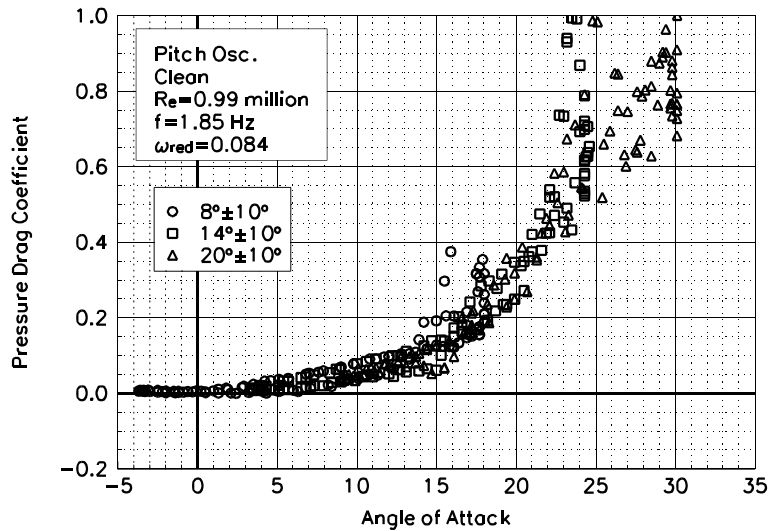


Figure C98. Pressure drag coefficient vs α .

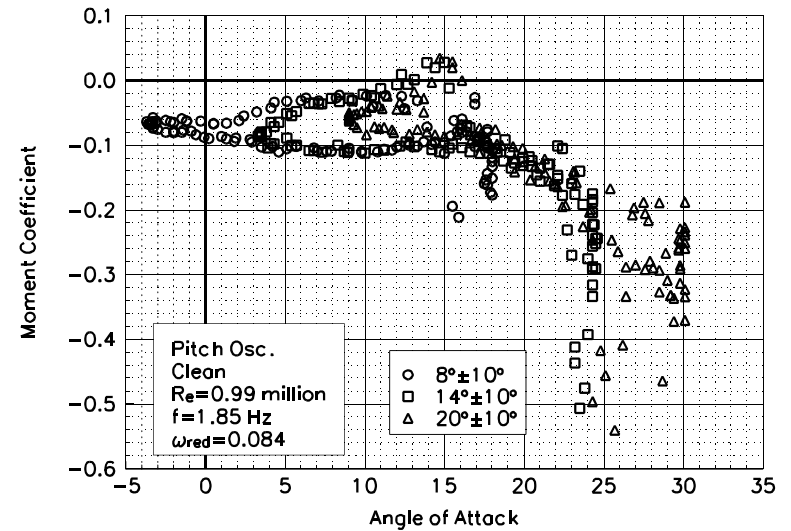


Figure C99. Moment coefficient vs α .

S813
Clean
Re=0.99 million
 $\omega_{\text{reduced}}=0.084$

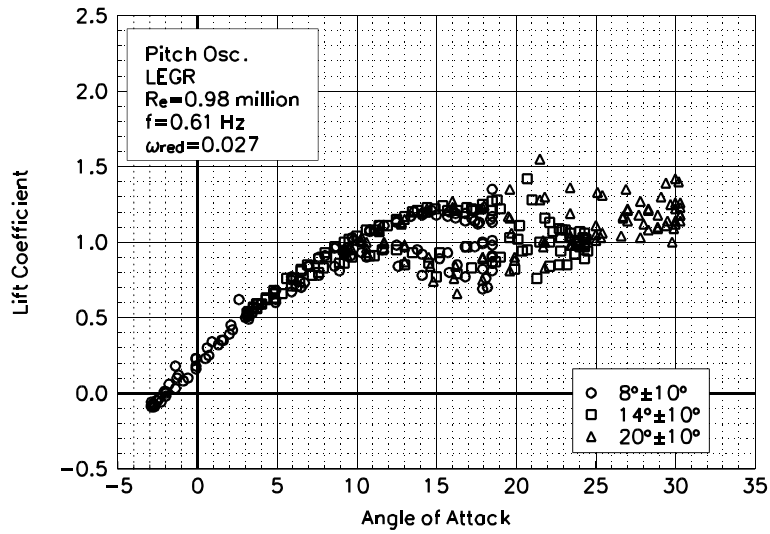


Figure C100. Lift coefficient vs α .

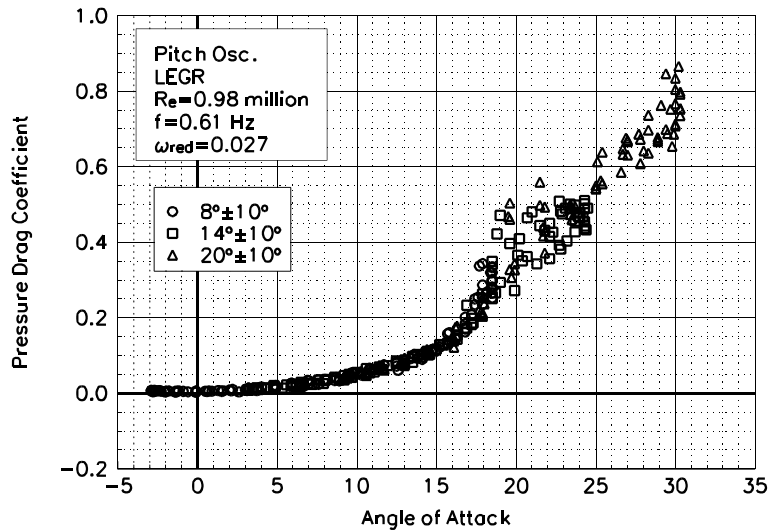


Figure C101. Pressure drag coefficient vs α .

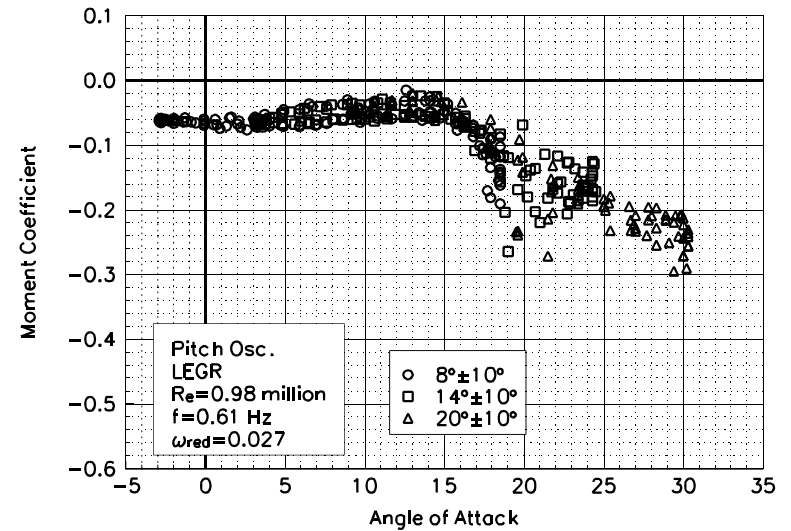


Figure C102. Moment coefficient vs α .

S813
LEGR
Re=0.98 million
 $\omega_{\text{reduced}}=0.027$

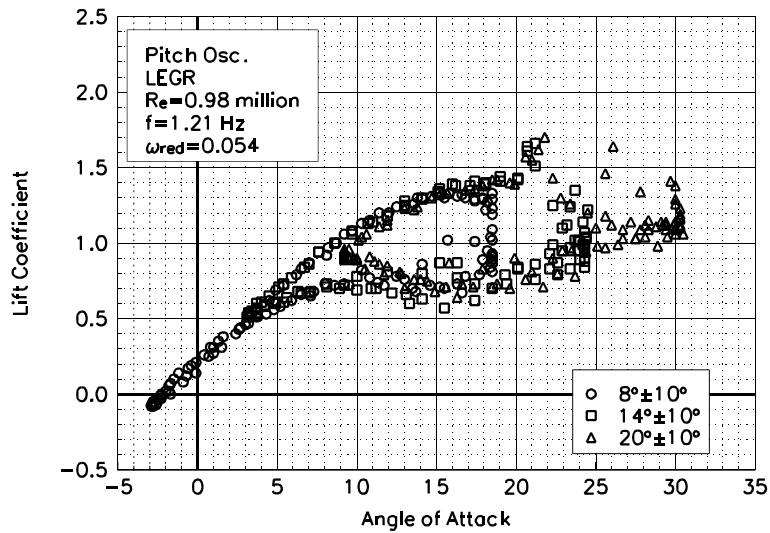


Figure C103. Lift coefficient vs α .

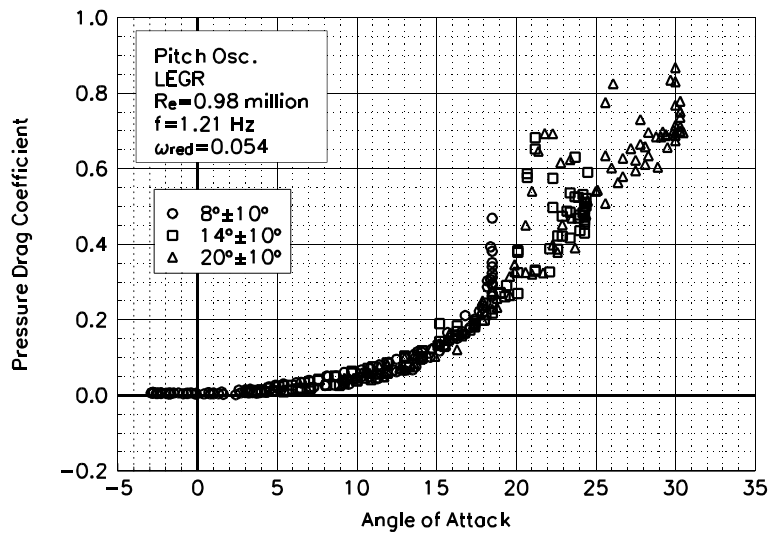


Figure C104. Pressure drag coefficient vs α .

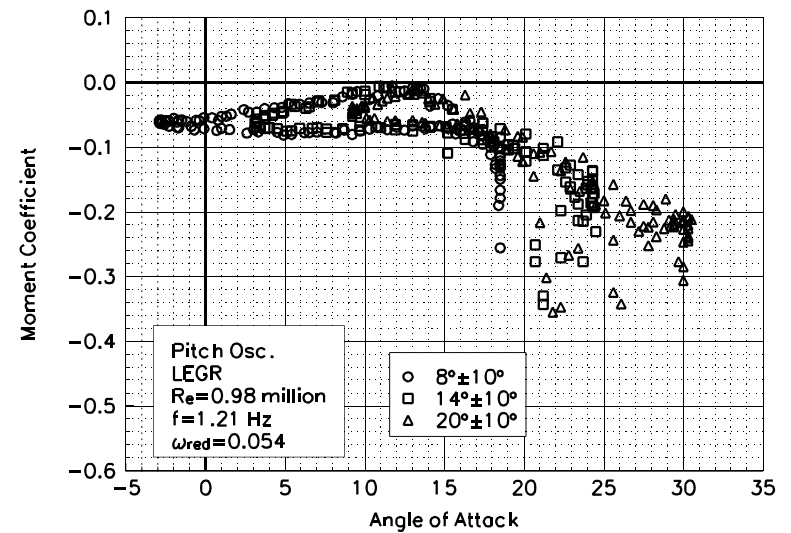


Figure C105. Moment coefficient vs α .

S813
LEGR
Re=0.97 million
 $\omega_{\text{reduced}}=0.054$

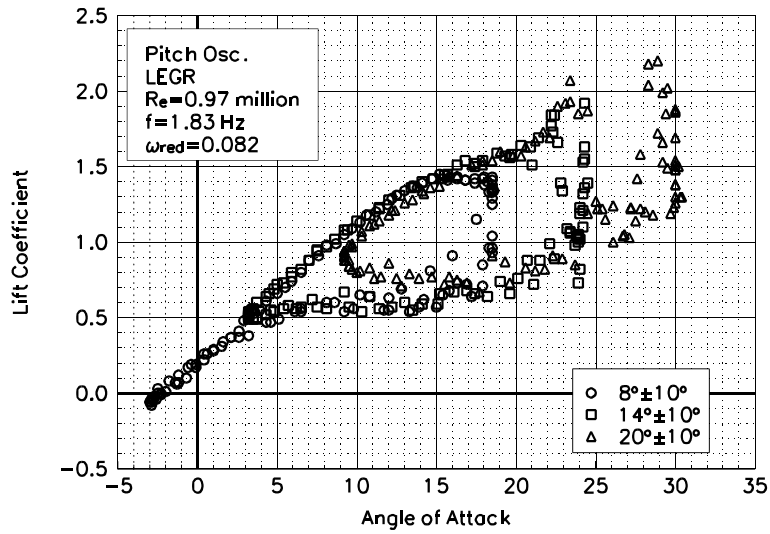


Figure C106. Lift coefficient vs α .

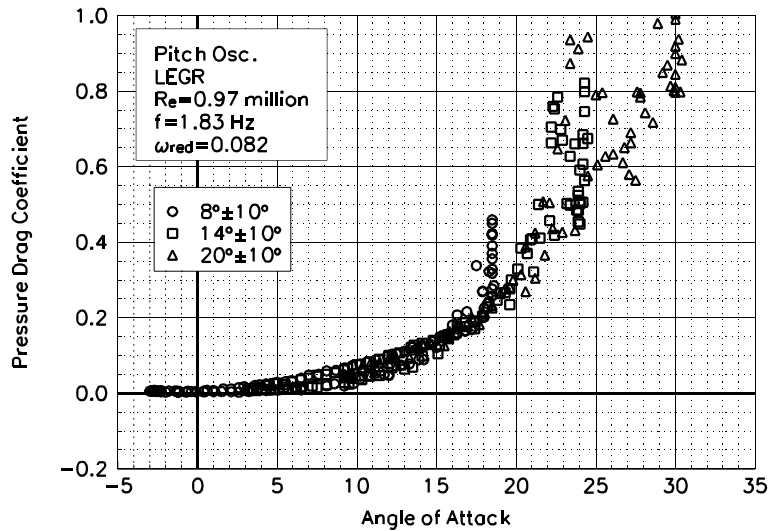


Figure C107. Pressure drag coefficient vs α .

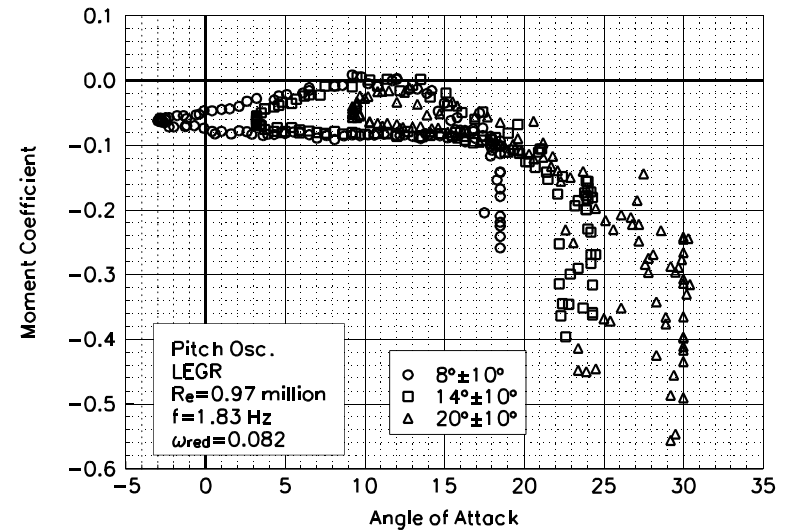


Figure C108. Moment coefficient vs α .

S813
LEGR
Re=0.97 million
 $\omega_{\text{reduced}}=0.082$

Unsteady Airfoil Characteristics

$\pm 10^\circ$ Sine, Re = 1.25 million

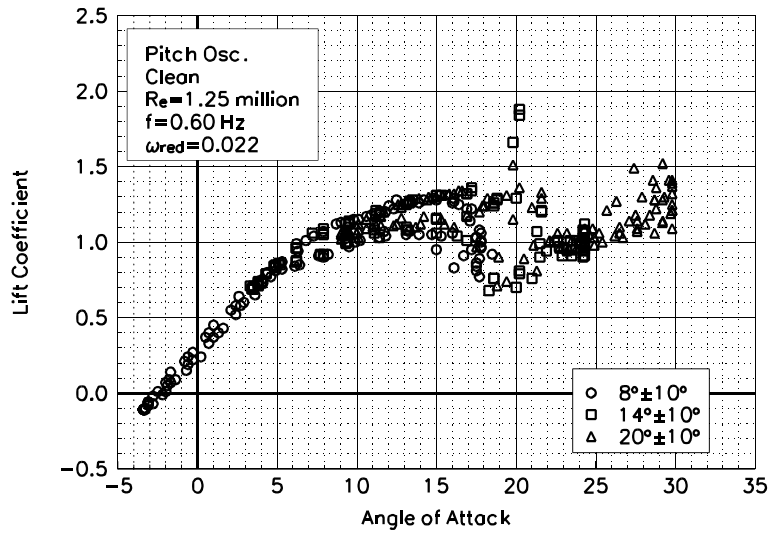


Figure C109. Lift coefficient vs α .

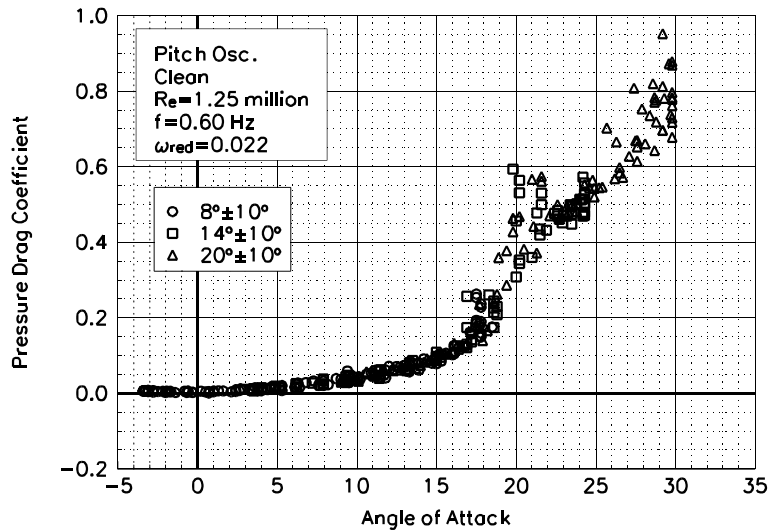


Figure C110. Pressure drag coefficient vs α .

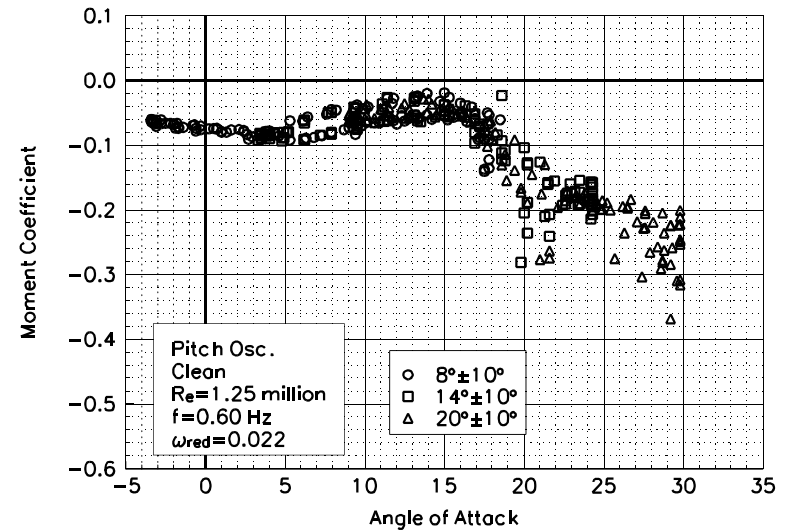


Figure C111. Moment coefficient vs α .

S813
Clean
Re=1.25 million
 $\omega_{\text{reduced}}=0.022$

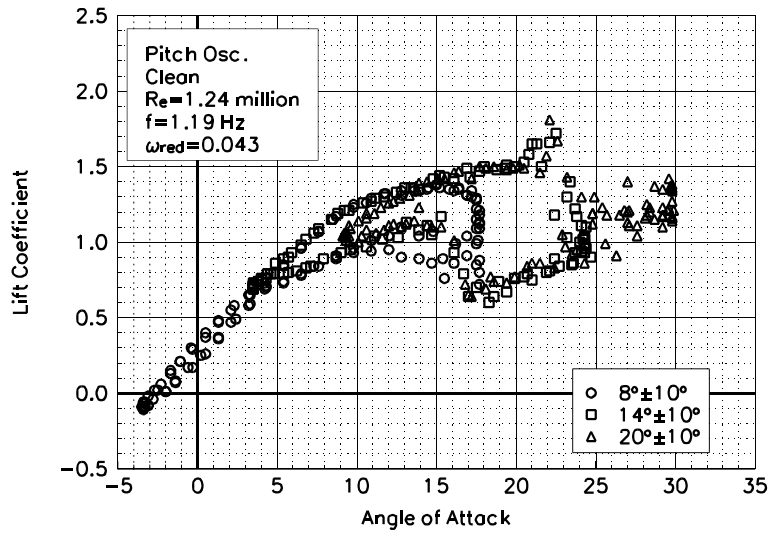


Figure C112. Lift coefficient vs α .

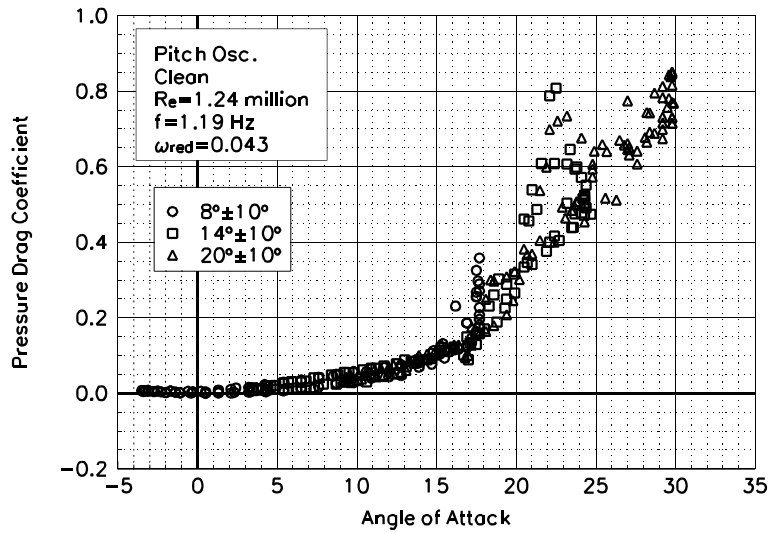


Figure C113. Pressure drag coefficient vs α .

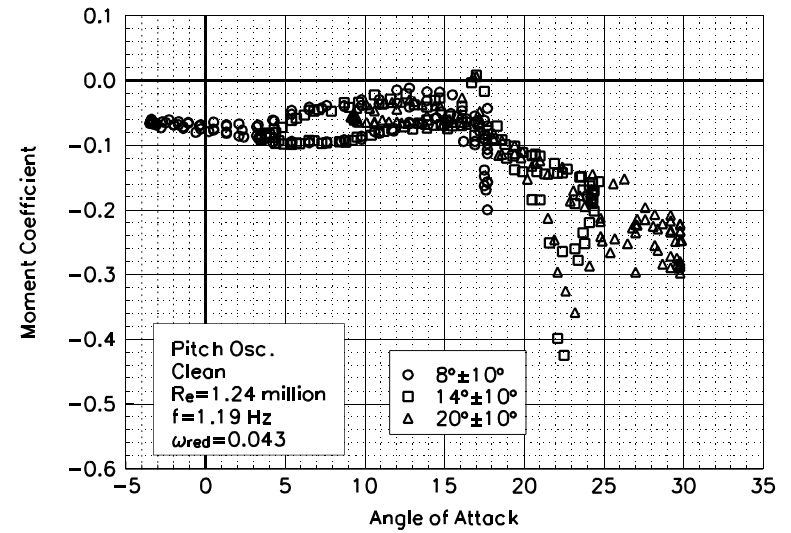


Figure C114. Moment coefficient vs α .

S813
Clean
Re=1.24 million
 $\omega_{\text{reduced}}=0.043$

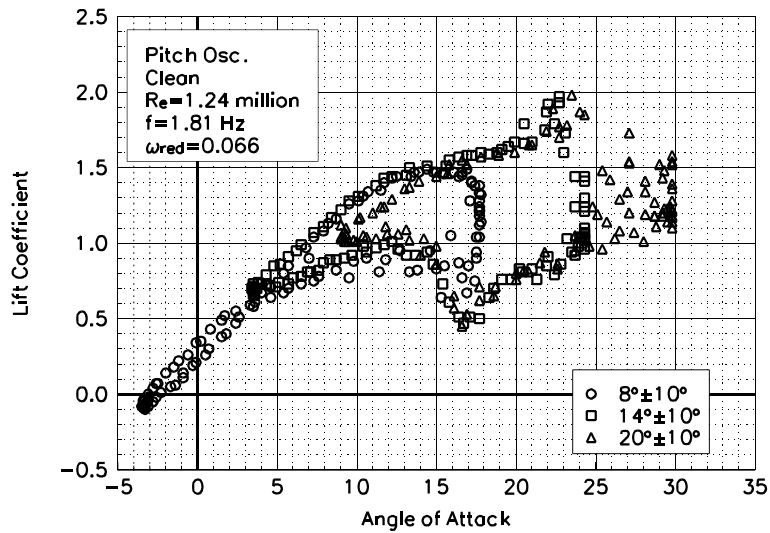


Figure C115. Lift coefficient vs α .

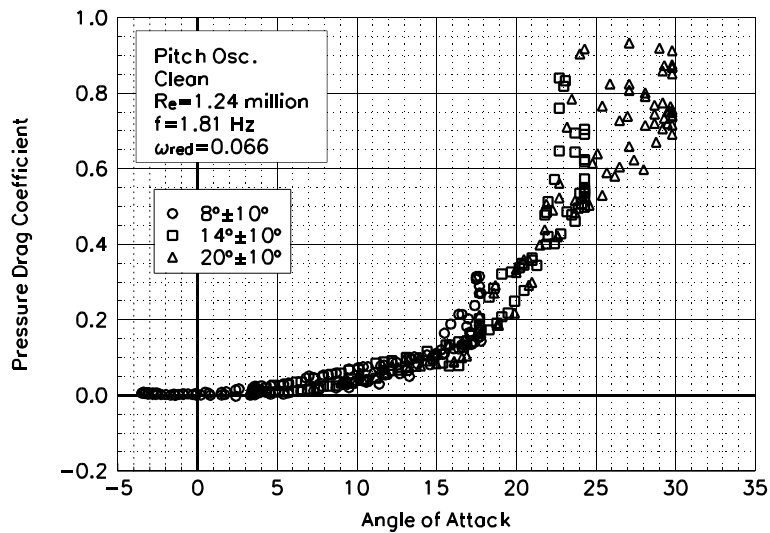


Figure C116. Pressure drag coefficient vs α .

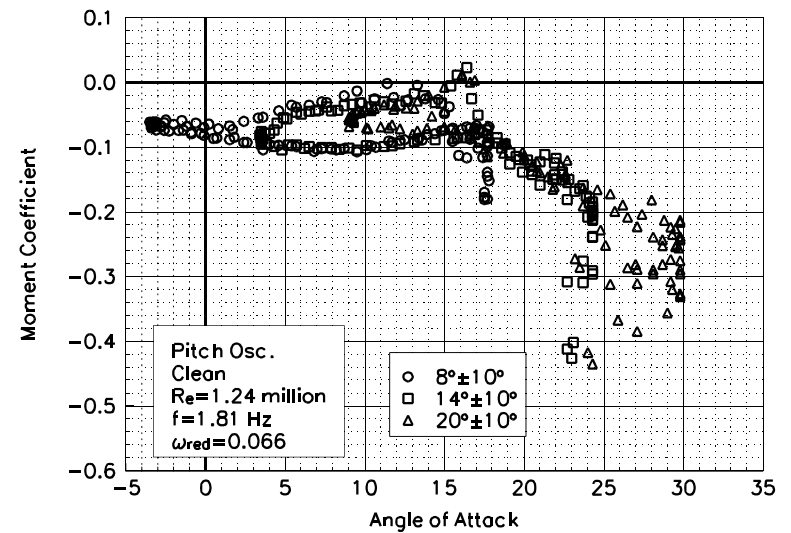


Figure C117. Moment coefficient vs α .

S813
Clean
Re=1.24 million
 $\omega_{\text{reduced}}=0.066$

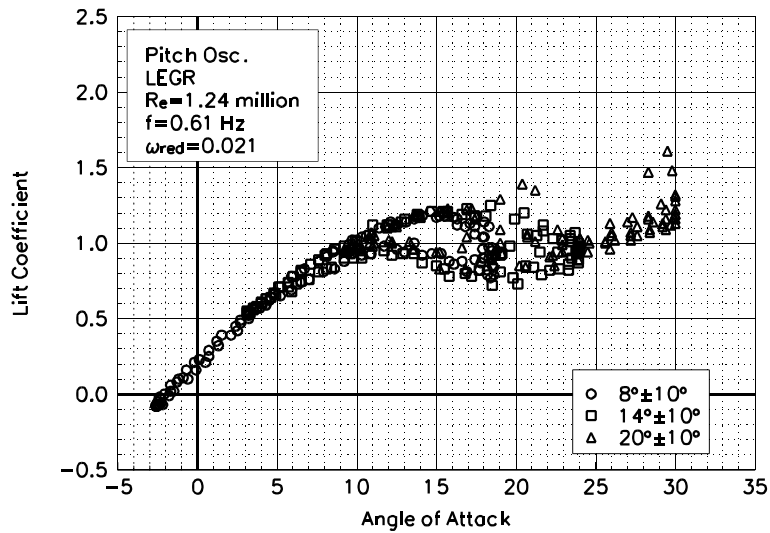


Figure C118. Lift coefficient vs α .

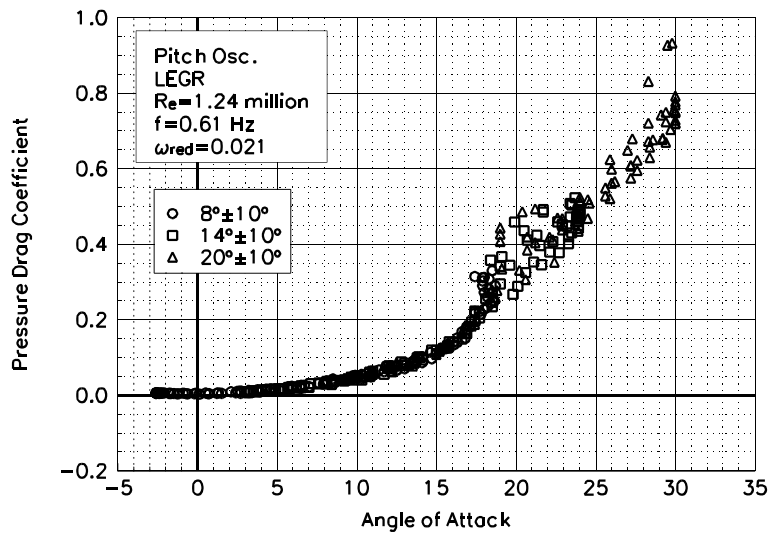


Figure C119. Pressure drag coefficient vs α .

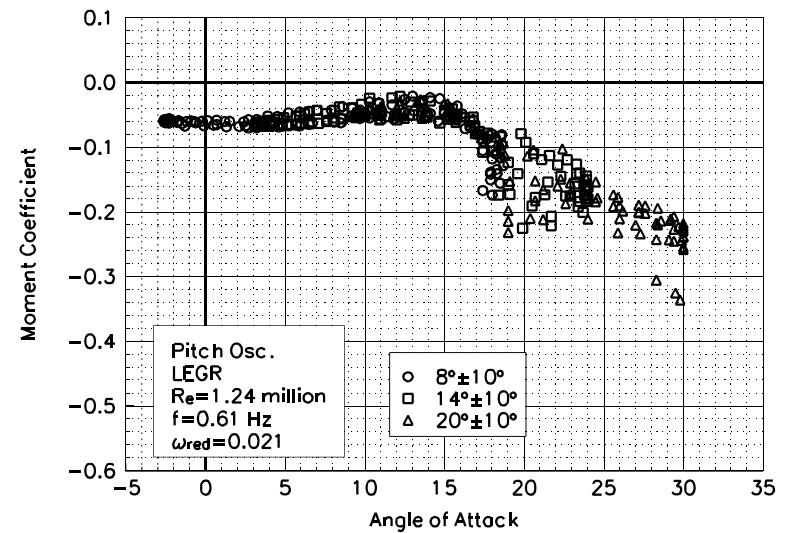


Figure C120. Moment coefficient vs α .

S813
LEGR
Re=1.24 million
 $\omega_{\text{reduced}}=0.021$

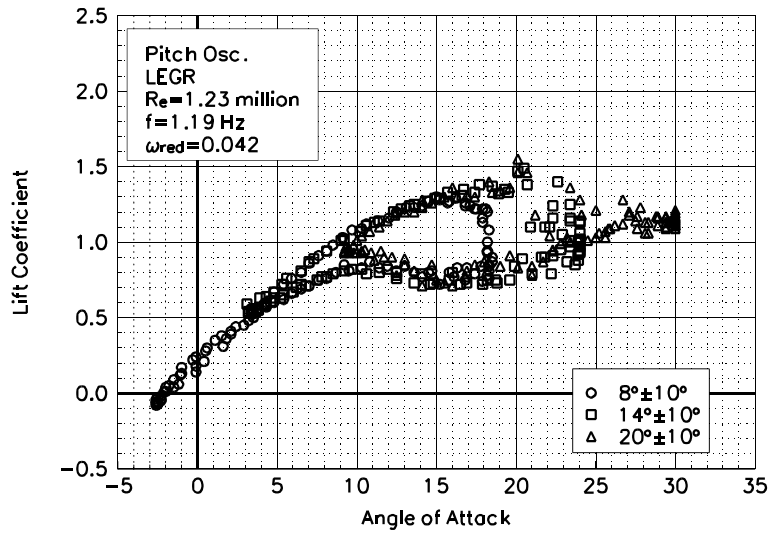


Figure C121. Lift coefficient vs α .

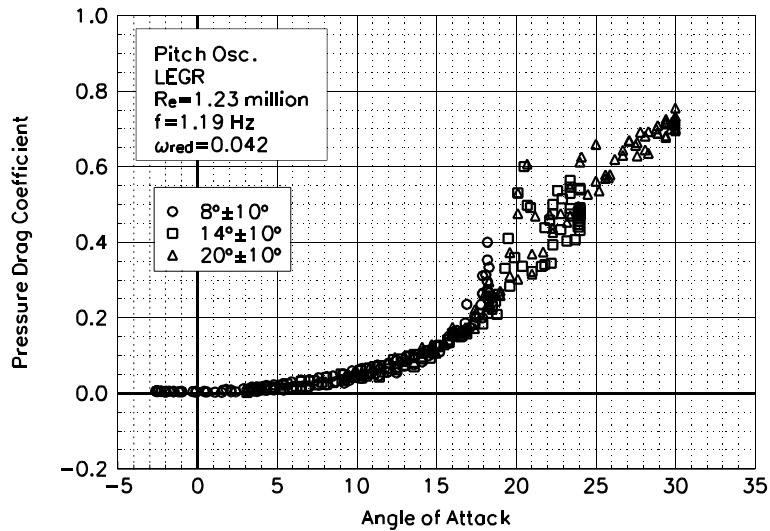


Figure C122. Pressure drag coefficient vs α .

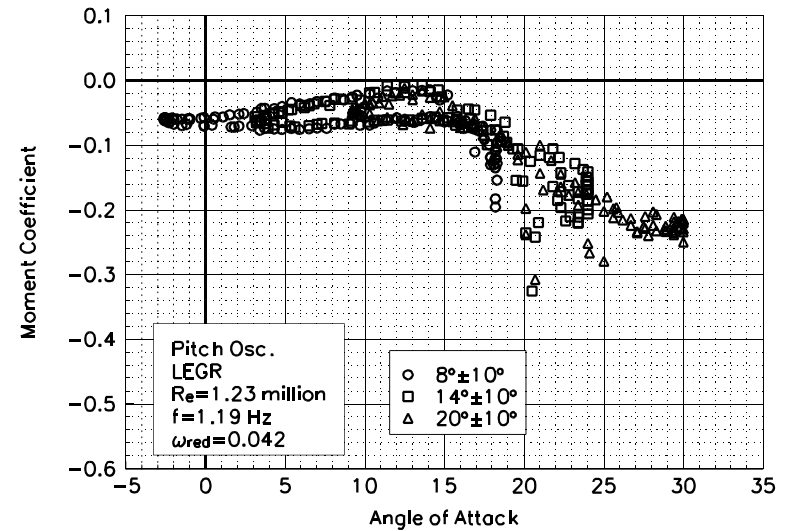


Figure C123. Moment coefficient vs α .

S813
LEGR
Re=1.23 million
 $\omega_{\text{reduced}}=0.042$

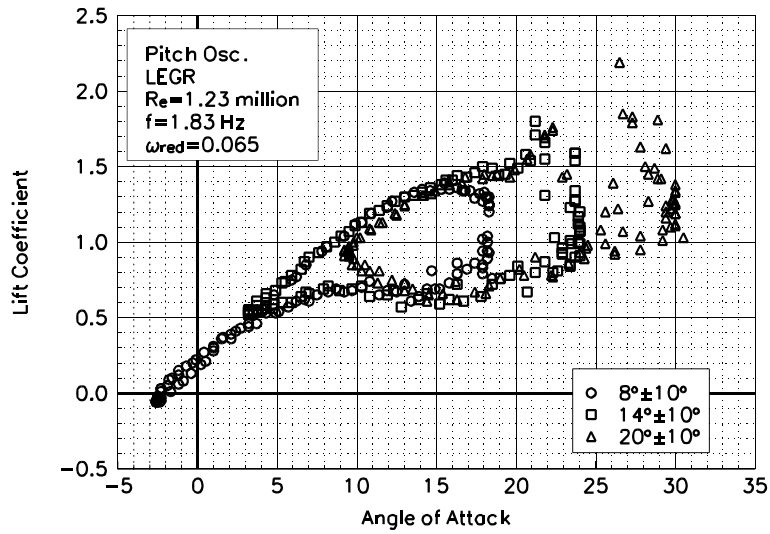


Figure C124. Lift coefficient vs α .

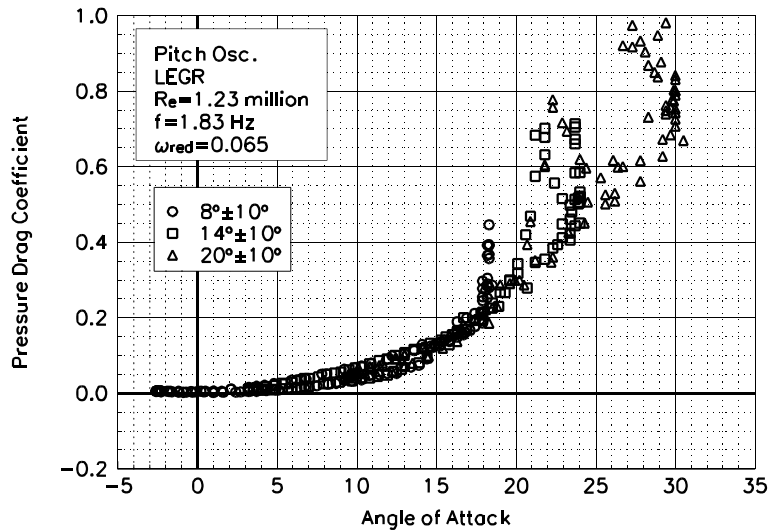


Figure C125. Pressure drag coefficient vs α .

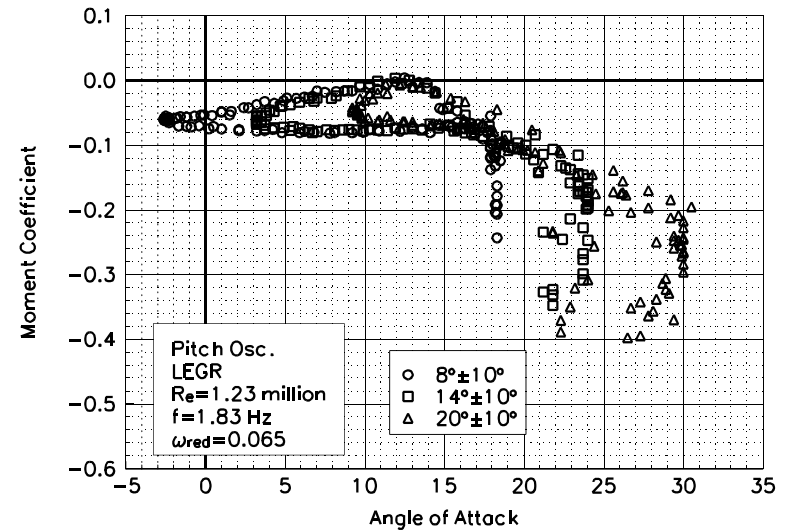


Figure C126. Moment coefficient vs α .

S813
LEGR
 $Re=1.23$ million
 $\omega_{reduced}=0.065$

Unsteady Airfoil Characteristics

$\pm 10^\circ$ Sine, Re = 1.4 million

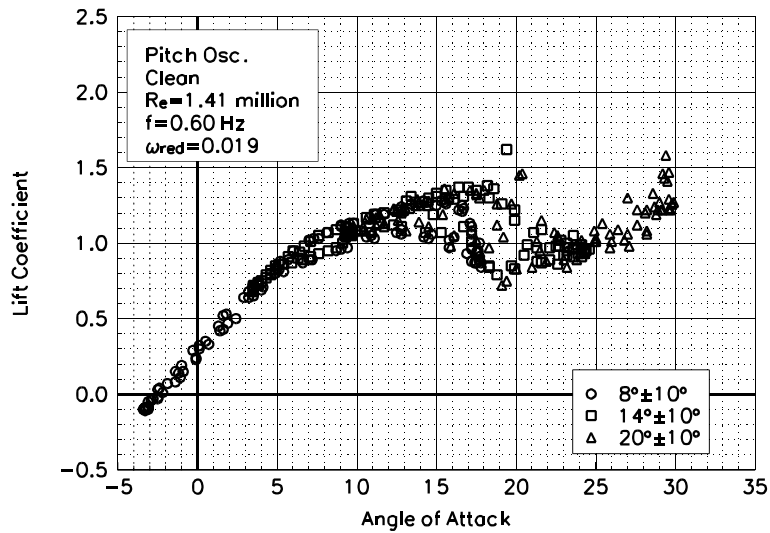


Figure C127. Lift coefficient vs α .

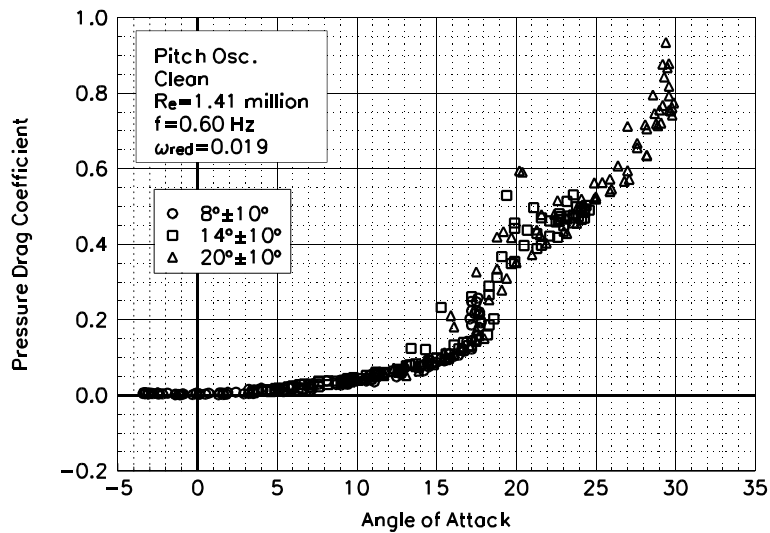


Figure C128. Pressure drag coefficient vs α .

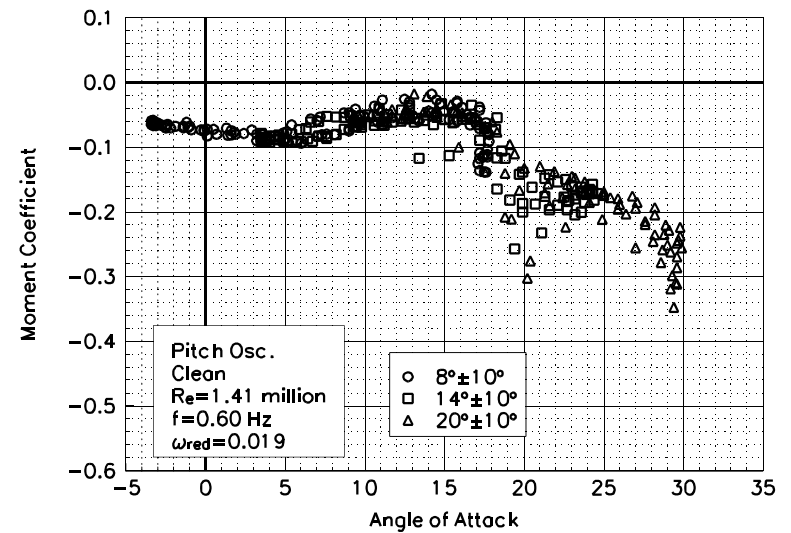


Figure C129. Moment coefficient vs α .

S813
Clean
Re=1.41 million
 $\omega_{\text{reduced}}=0.019$

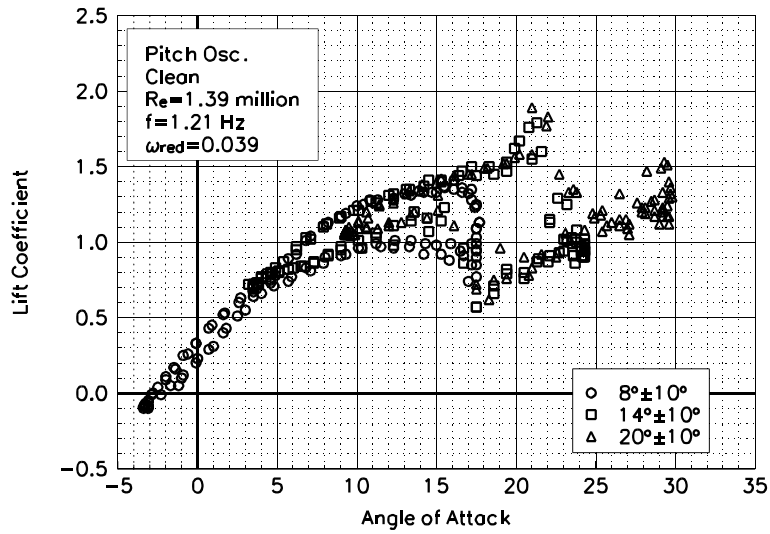


Figure C130. Lift coefficient vs α .

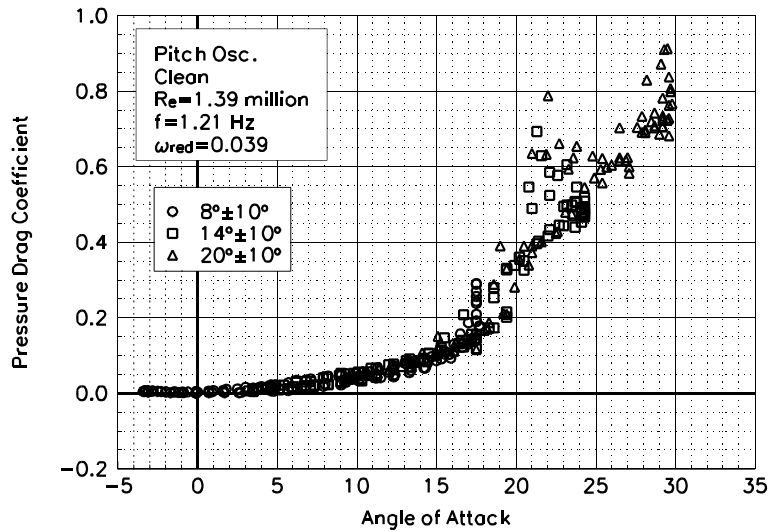


Figure C131. Pressure drag coefficient vs α .

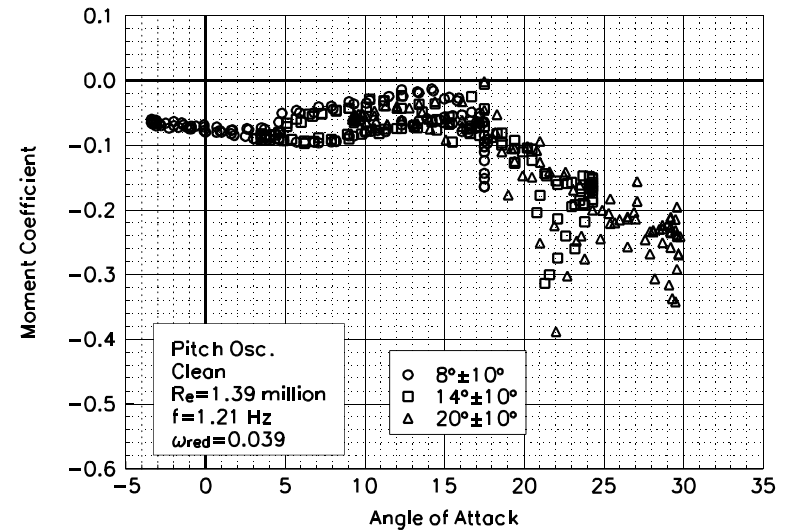


Figure C132. Moment coefficient vs α .

S813
Clean
Re=1.39 million
 $\omega_{\text{reduced}}=0.039$

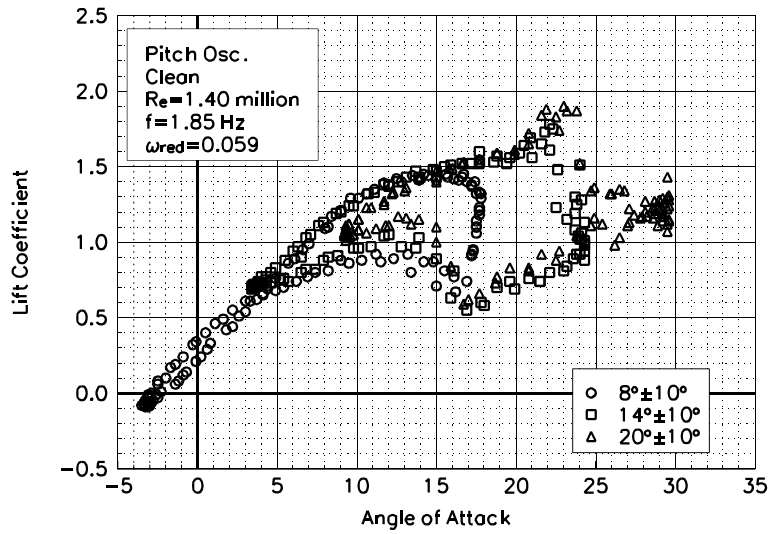


Figure C133. Lift coefficient vs α .

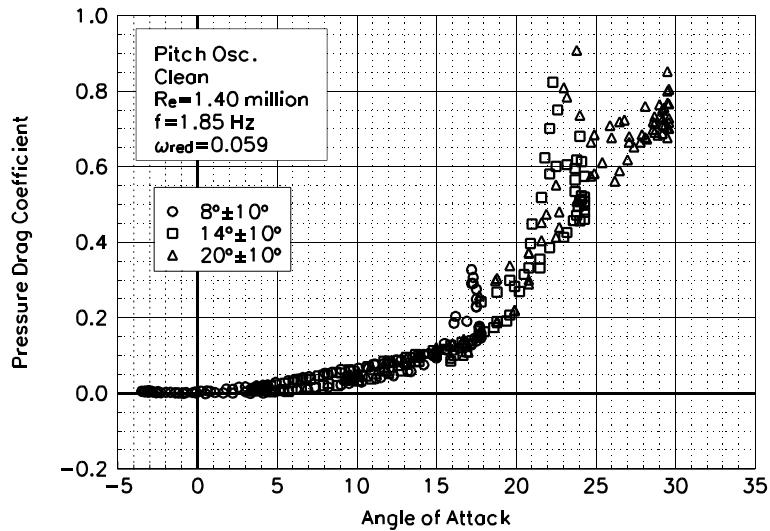


Figure C134. Pressure drag coefficient vs α .

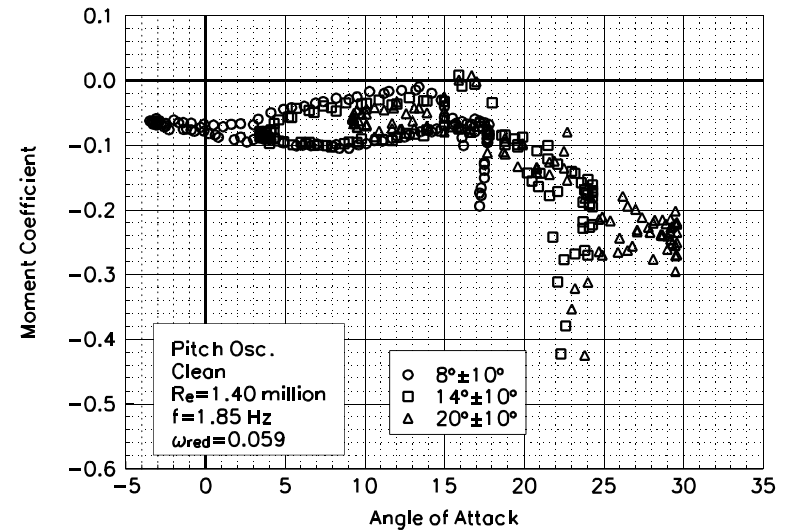


Figure C135. Moment coefficient vs α .

S813
Clean
Re=1.40 million
 $\omega_{\text{reduced}}=0.059$

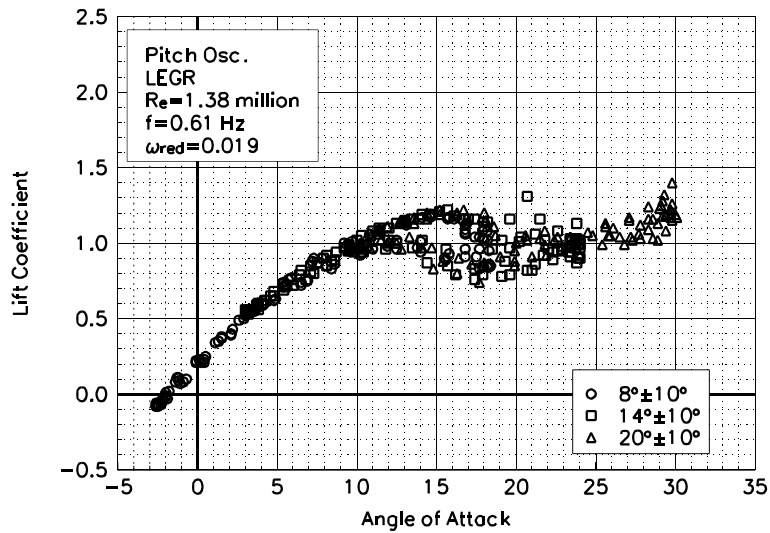


Figure C136. Lift coefficient vs α .

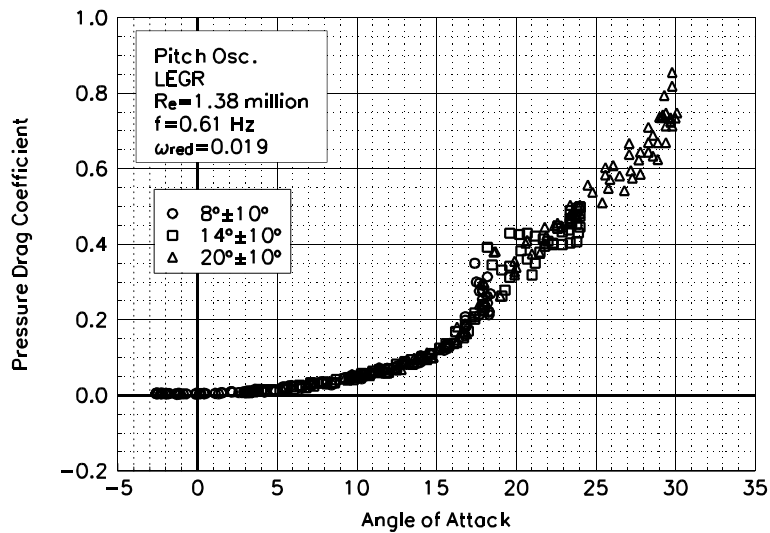


Figure C137. Pressure drag coefficient vs α .

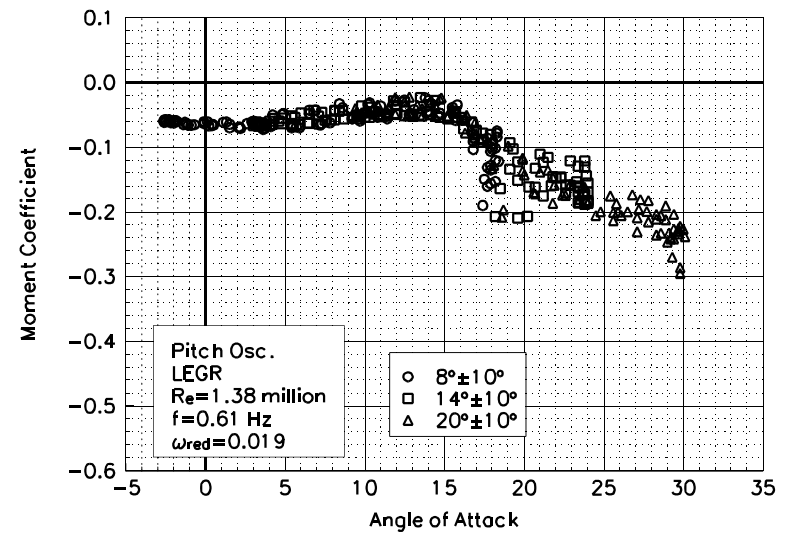


Figure C138. Moment coefficient vs α .

S813
LEGR
Re=1.38 million
 $\omega_{\text{reduced}}=0.019$

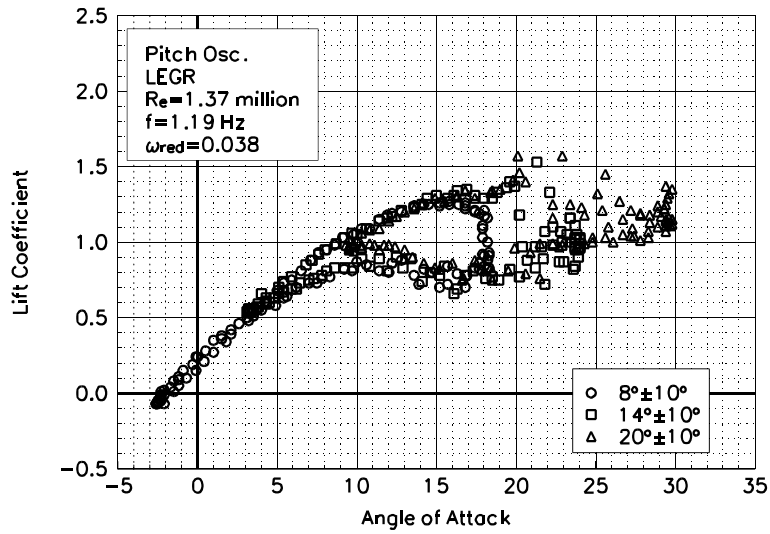


Figure C139. Lift coefficient vs α .

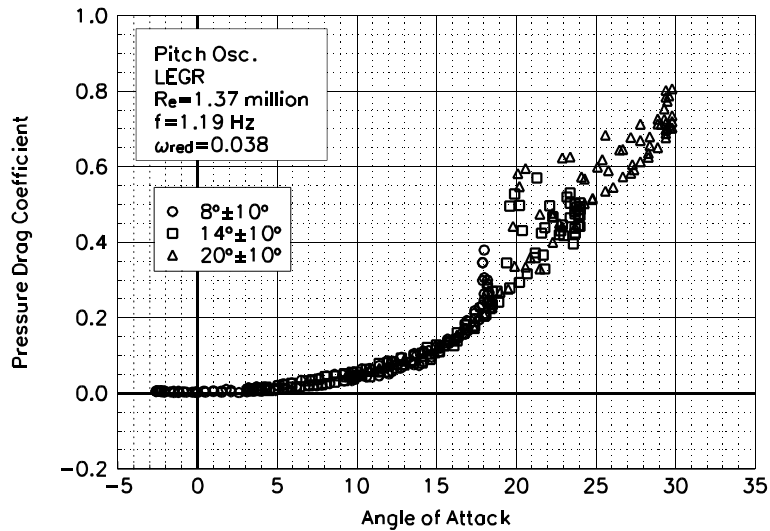


Figure C140. Pressure drag coefficient vs α .

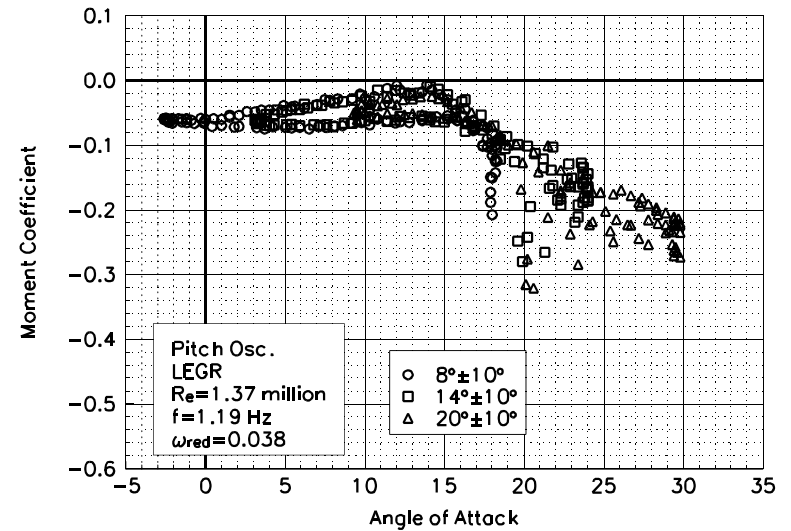


Figure C141. Moment coefficient vs α .

S813
LEGR
Re=1.37 million
 $\omega_{\text{reduced}}=0.038$

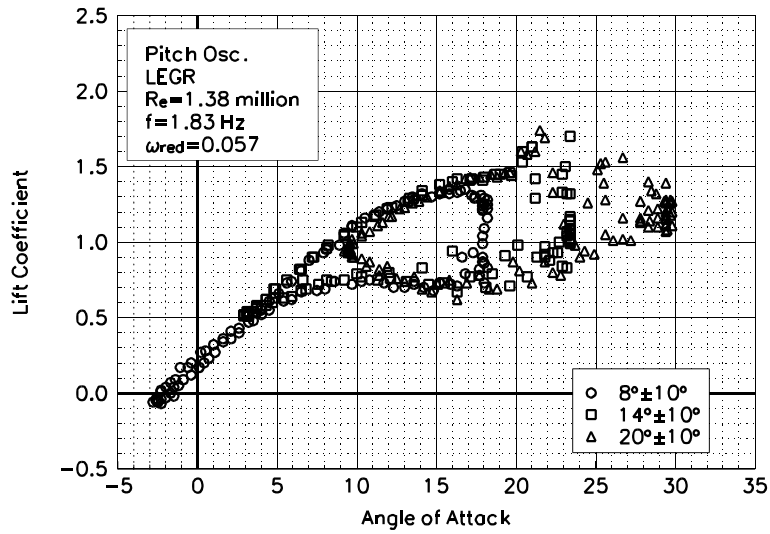


Figure C142. Lift coefficient vs α .

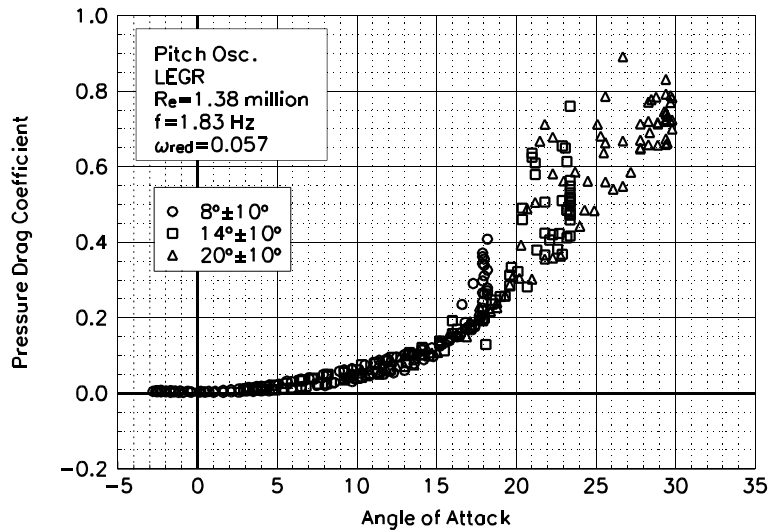


Figure C143. Pressure drag coefficient vs α .

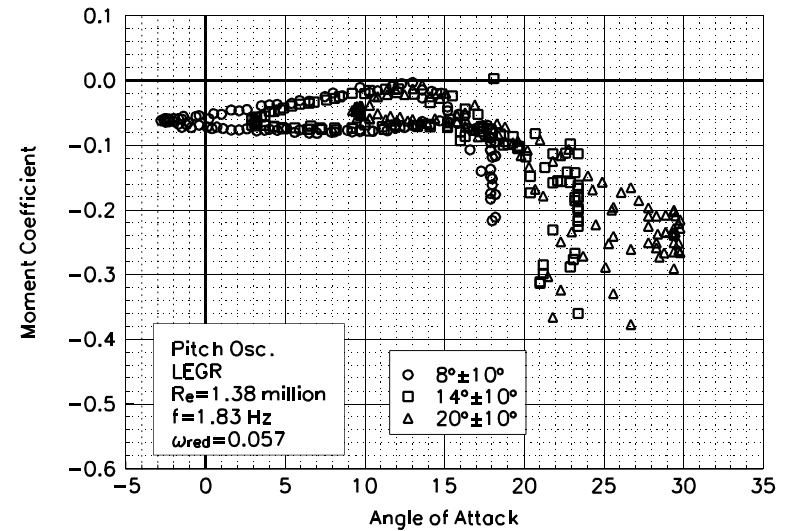


Figure C144. Moment coefficient vs α .

S813
LEGR
Re=1.38 million
 $\omega_{\text{reduced}}=0.057$